THE SOUND OF FRICTION: REAL-TIME MODELS, PLAYABILITY AND MUSICAL APPLICATIONS

A DISSERTATION
SUBMITTED TO THE DEPARTMENT OF MUSIC
AND THE COMMITTEE ON GRADUATE STUDIES
OF STANFORD UNIVERSITY
IN PARTIAL FULFILLMENT OF THE REQUIREMENTS
FOR THE DEGREE OF
DOCTOR OF PHILOSOPHY

Stefania Serafin
June 2004

I certify that I have read this dissertation and that, in my opinion, it is fully adequate in scope and quality as a dissertation for the degree of Doctor of Philosophy.

Prof. Julius O. Smith III
(Principal Adviser)

I certify that I have read this dissertation and that, in my opinion, it is fully adequate in scope and quality as a dissertation for the degree of Doctor of Philosophy.

Prof. Christopher Chafe

I certify that I have read this dissertation and that, in my opinion, it is fully adequate in scope and quality as a dissertation for the degree of Doctor of Philosophy.

Prof. Perry R. Cook

I certify that I have read this dissertation and that, in my opinion, it is fully adequate in scope and quality as a dissertation for the degree of Doctor of Philosophy.

Prof. James Woodhouse

Approved for the University Committee on Graduate Studies:

Preface

Friction, the tangential force between objects in contact, in most engineering applications needs to be removed as a source of noise and instabilities.

In musical applications, friction is a desirable component, being the sound production mechanism of different musical instruments such as bowed strings, musical saws, rubbed bowls and any other sonority produced by interactions between rubbed dry surfaces.

The goal of this dissertation is to simulate different instruments whose main excitation mechanism is friction. An efficient yet accurate model of a bowed string instrument, which combines the latest results in violin acoustics with the efficient digital waveguide approach, is provided. In particular, the bowed string physical model proposed uses a thermodynamic friction model in which the finite width of the bow is taken into account; this solution is compared to the recently developed elasto-plastic friction models used in haptics and robotics. Different solutions are also proposed to model the body of the instrument.

Other less common instruments driven by friction are also proposed, and the elasto-plastic model is used to provide audio-visual simulations of everyday friction sounds such as squeaking doors and rubbed wine glasses.

Finally, playability evaluations and musical applications in which the models have been used are discussed.

Acknowledgements

The four years spent at CCRMA have been for me a very pleasant experience not only professionally but especially for the incredible amount of wonderful people I met not just at Stanford but also at conferences all around the world.

For this reason, I want to thank first of all my advisor Julius, who gave me the possibility to study with him. Julius has a perfect combination of incredible personality and astonishing knowledge not just in signal processing. I hope we will still be able to have our catch up sessions frequently enough even if I moved back to Europe.

Thanks also to all the other people that made CCRMA a special place to be: most of all my good friends Patty and Tamara, but also all the many others I met there during those four years: Bob, Caroline, Carr, Charles, all the Chris, Ching, Fabien, Fred, Gary, Jeff, John, Jonathan, Juan, Max, Matthew, Michael, Nando, Scott, Sile, Stefan, Tim, and I certainly forgot many others. Thanks to Julien, Richard and Solvi and the lovely kids. It was great to have them around CCRMA for one year. Thanks to the other friends that were with me in California during these years: Cristiano, Helena, Nurit, Sha. Thanks also to Adrian, Agnieszka, Chloe, Jean-Marc, Rebecca, Veronique, Zacarie from the Santa Cruz side.

During the summer 2002 I spent a couple of months working at Cambridge University. Thanks to Jim Woodhouse for welcoming me there and for the incredible amount of knowledge and resources he shared with me.

During the last year of my PhD I had the opportunity to teach at the University of Virginia. I have wonderful memories of the time spent to collect fresh trashness with Juraj. Also thanks to other special people from 22903: Adina, Dave, Juraj,

Linda, Matt, Peter, Sage, Tabatha; they all made my short visit to the south quite enjoyable. Thanks also to Judith and Michael for their lovely way of making me feel welcome there.

Thanks to the people of the Analysis-Synthesis team at IRCAM that made me start working in computer music: fratellone Christophe, Diemo, Francisco, Jeoffrey, fratellone Marcelo, Philippe, fratellino Thomas and Xavier. Thanks to Elke, Kelly and Nathalie and the other people of La Residence for the nice time spent outside IRCAM. Thanks to Richard who has always been a good friend and a big supporter from the very beginning and all through these four years.

I spent most of summer 2003 in Stockholm. Thanks to Anders, Erwin, Knut and the other people at KTH who made my stay there really enjoyable. Thanks also to Diana for being not only a nice person to work with but also a good friend. The same can be said about Davide, the two Federicos, Georg and Perry; it was nice to work with you all. The end of this dissertation corresponds to be beginning of my new life in Denmark. Thanks to Jens for giving me the opportunity to move to this wonderful country and be part of the medialogy department. And thanks to that special one sitting in Copenhagen dreaming for me to be done. And finally, thanks to my family and friends in Italy. They are the ones that have been close to me for the longest time and that will always be there with their love and support.

Contents

List of Tables

List of Figures

Chapter 1

Introduction

1.1 Overview

Friction, the tangential force between objects in contact, in most engineering applications needs to be removed being a source of noise, energy loss, instabilities and undesired vibrations.

From an auditory perspective, friction is constantly present in our everyday life. The annoying sound of a brake, a squeaking door or a chalk sliding on a blackboard are only few examples of the sonorities that frictional interactions between rubbed dry surfaces can produce. Fortunately there also also pleasant sonorities that derive from frictional phenomena: few examples are skilled bowed string players, rubbed crystal wine-glasses and musical saws.

In this dissertation mathematical models that simulate friction sonorities are built, by looking at friction as a source of noise and subtle variations part of the expressive sonic phenomena considered to be desirable in music. In particular, the state of the art friction models developed in haptic and robotics are studied and applied to a musical context.

Starting from an efficient yet accurate physical model of a bowed string, simulations of different instruments that have the same excitation mechanism are presented. The ultimate goal is to provide a better understanding of the behavior of these instruments and to build real-time synthesis tools which composers and performers can

use to reproduce, explore and extend the sound of friction.

1.2 The sound of friction

Interest on friction sounds has usually been focused on the family of bowed string instruments. Most of the special quality of a violin depends on the complex and subtle range of vibrational behavior produced by a string excited by a bow. It is therefore important to achieve a better understanding of the interaction between a bow and a string, both for musical acousticians and for instrument makers.

It is also interesting to study and simulate less popular musical instruments driven by the same excitation mechanism as the bowed string. Some examples are the musical saw, the glass harmonica, the Tibetan bowl, bowed bars, bowed vibraphones and bowed cymbals. As contemporary music sees lots of these instruments in scene, mathematical and computer models of such instruments can provide a better understanding of their behavior as well as new tools for musicians and composers to experiment between real and virtual friction sounds.

1.3 Scope of the thesis

This thesis proposes physical models of friction driven instruments built using different configurations of digital waveguides [117, 114]. One dimensional digital waveguides are an efficient synthesis technique used to model quasi-harmonic resonators such as strings and tubes. One dimensional waveguides are used to simulate bowed strings. The linear string resonator is connected to different refined models of the bow-string interaction, as described in Chapter 3. While Chapter 4 focuses only on the bowed string, Chapter 5 proposes models of other friction driven instruments with the goal of obtaining computationally efficient simulations. Extensions of traditional digital waveguides are discussed, such as banded waveguides and banded waveguides meshes.

In general, the main interest of this dissertation is to look at physical models of friction driven musical instruments from different perspectives. From a scientist's

point of view, the interest is to provide a better understanding of the sound production mechanism of the instruments of the violin family and of other instruments driven by friction. From the engineer's point of view, the goal is to obtain accurate yet efficient numerical models of these instruments. From the computer scientist's point of view a real-time implementation of these instruments is provided. From the musician's point of view, the goal is to use these tools to recreate the sonorities of friction and to extend them in a compositional context.

This work therefore provides new results and discussions in musical acoustics, real-time sound synthesis, digital signal processing and musical applications, aiming both to achieve a better understanding of friction-driven musical instruments, and to build new tools that composers can use to manipulate sounds in real-time. In fact, in order to allow the possibility of reproducing all the subtleties of a complex action such as bowing and at the same time to manipulate them in real-time in a personal computer, all these models have been implemented in the Max/MSP [141], Pure Data (pd) [89] and Synthesis Toolkit (STK) [19] environments.

An accurate study of the playability of these models shows how recent discoveries on friction and bowed string interaction [138] improve the playability of virtual bowed strings. Models that incorporate recent research on the thermodynamical behavior of the bow in contact with the string, together with models for the bow-hair compliance, are also discussed.

Physical models of musical instruments are interesting for acousticians as a tool to validate the equations and theories on a particular instrument. It is a challenge to completely understand the physics of an existing instrument. This is one of the reasons why this approach to physical models is interesting to scientists. On the other end, merely focusing on a faithful reproduction of existing musical instruments is not appealing for composers and performers. This concept is well-known in computer music, yet little effort has been done to create physical models that extend the possibilities offered by traditional instruments. This thesis addresses both the acoustician's and the composer's interest, providing on one side accurate models of existing musical instruments and on the other side extended techniques to create sonorities that existing instruments cannot physically obtain.

1.4 Outline

The remaining chapters of this dissertation are organized as follows. Chapter 2 describes acoustics of friction, and describes different models to simulate frictional induced vibrations.

Chapter 3 describes acoustics and previous research on bowed strings, and Chapter 4 proposes an accurate yet efficient model of a bowed string.

Chapter 5 examines other instruments whose main excitation mechanism is friction, such as the musical saw, the glass harmonica, the Tibetan bowl and the bowed cymbal. Other everyday sounds derived by friction, such as squeaking doors and noise brake are also described.

Chapter 6 proposes methods for evaluating playability for virtual bowed string, from a musical acoustician's perspective, and Chapter 7 describes issues about musical applications and control of friction driven musical instruments. Chapter 8 presents conclusions and suggestions for future work.

Chapter 2

Friction

2.1 Introduction

Friction, the tangential force between sliding surfaces, is a phenomenon that constantly appears in our everyday life. Friction develops between sliding surfaces, and fulfills a dual role of transmitting energy from one surface to another and dissipating energy of relative motion [3].

Although friction appears in many mechanical systems, friction phenomena are not completely understood and are particularly complex since are caused by different physical mechanisms. Friction-excited vibrations common to our sonic environment, such as brake noises, chalks on blackboards, chairs sliding on a hard pavement derive from the energy that friction provides to a system and they are just a small sample of all the sonorities that hard rubbed surfaces can produce.

Friction sounds have also a slightly more appealing musical dimension, which appears, for example, in the sonorities of a bowed string or of a rubbed wineglass. Considering that friction is abundant in nature, friction research has a long history, and friction studies are still active nowadays. As a nonlinearity, friction is a challenge for researchers in dynamical systems, robotics and engineering in general.

In this chapter we examine friction induced vibrations with a focus on stick-slip oscillations. We propose an overview of the history of the study of friction in general and more specifically as a sonic phenomenon, and we describe different friction models

that will be used in the rest of this dissertation.

2.2 Historical overview of friction research

Friction is a word traceable to 15th century english, denoting the "force that resists relative motion between two bodies in contact" [73], and derives from the Latin word *fricare*, which means "to rub".

The awareness of friction existed in ancient times, although the earliest exploitations of it where not accompanied by scientific explanations [30]. Significant examples are the advent of fire making based on rubbing wood, the development of the bow as a hunting tool and the development of wheels.

Perhaps the first scientist who made some observations about friction was Aristotle, who identified the existence of this force [6]. Aristotle analyzed the motion of bodies under a constant force resisted by friction, such as a body being pulled or pushed along the ground, and stated that to obtain an uniform motion a constant force must be exerted to overcome friction.

It wasn't until the end of the 15th century, however, thanks to Leonardo da Vinci, that friction was treated in a scientific manner. The main observations made by Leonardo were that friction does not depend on the contact area but on the normal force exerted on the sliding bodies.

Leonardo's laws of friction apply to a remarkably large range of situations; Leonardo made the observation that different materials move with different ease. He claimed that this was a result of the roughness of the materials in question; thus, smoother materials have smaller friction. His results were never published; the only evidence of their existence is in his vast collection of journals.

In the late 16th century, Galileo Galilei in his *Dialogues Concerning Two New Sciences* made some observations on the act of bowing a viola string or rubbing the rim of a wineglass with a finger. He observed that "a glass of water may be made to emit a tone merely by the friction of the finger-tip around the rim of the glass". He also noted the following event: in a large glass full of water, first the waves are spaced uniformly, but, once the tone of the glass jumps one octave higher, the waves

divide in two.

Guillaume Amontons (1663-1705) rediscovered the two basic laws of friction that had been discovered by Leonardo Da Vinci, and proposed an original set of theories. He believed that friction was predominantly a result of the work done to lift one surface over the roughness of the other, or from the deforming or the wearing of the other surface. For several centuries after Amontons' work, scientists believed that friction was due to surfaces' roughness.

Chladni in 1787 published a treatise [16] in which he described a technique of sprinkling sand on vibrating plates to produce oscillations induced by friction. Exciting plates of various shapes with a bow, he obtained patterns of different shapes which were demonstrated to Napoleon in 1809.

Important improvements on the research of frictional induced vibrations were obtained by Helmholtz, who in 1860 built a vibrational microscope, using which he was able to describe the motion of a string excited by a bow, which nowadays is known as Helmholtz motion in his honor.

Helmholtz observed that the string is attached to the bow for the longest part of its period, detaching only once per period. This motion was coined as stick-slip by Bowden and Leben [9], and it is a vibratory phenomenon that is sometimes observed at frictional interfaces. Other examples of stick-slip oscillations include the squeaking of a door, the sound of a chalk on a blackboard and the rubbing of a wineglass. Stick-slip motions appear because the static friction coefficient is greater than the dynamic one. When two objects are stuck together, if a force is applied to one, the friction ramps up to the static friction limit and break away can occur. After break away the object can begin sliding for a small amount and then sticks again.

Further observations were made by Coulomb, who treated the difference between static and dynamic friction coefficients observing that static friction is always higher than dynamic friction.

Coulomb laws of friction are still used in some applications, since, although they represent a simplified version of reality, they can nevertheless provide interesting insights into the mechanics of objects in contact. It is with Coulomb that classical models of friction started to develop.

At the beginning of the 20th century, Stribeck performed some experiments on sliding bearings, showing the dependence of the friction coefficient on the sliding velocity. He created some curves, now known as Stribeck curves, in which it is clear how the frictional force drops steeply with increasing relative velocity between bodies in contact.

More recently, a new class of dynamic friction models has been developed. In these models, the dependence of friction on the relative velocity between bodies in contact is modeled using a differential equation. In the following section static and dynamic friction models are described in details.

2.3 Static friction models

In the static models, friction depends only on the relative velocity between two bodies in contact. In this section the evolution of static friction models is reviewed.

2.3.1 Coulomb's friction model

The first mathematical friction model was proposed by Coulomb in 1773 [36]. This model, despite its simplicity, is able to capture the basic physical behavior of frictionally induced vibrations.

The main idea behind the model is that friction opposes motion and its magnitude is independent of the velocity v of the contact area. The model can be described as:

$$F = F_C \times \text{sgn}(v) \tag{2.1}$$

where the friction force F_C is proportional to the normal load, i.e. $F_C = \mu F_N$, where μ represents the friction coefficient and F_N represents the normal load. This description of friction is represented in Fig. 2.1 a).

Notice how Coulomb friction does not specify the friction force for zero velocity. Notice also how F_C depends on the normal load F_N.

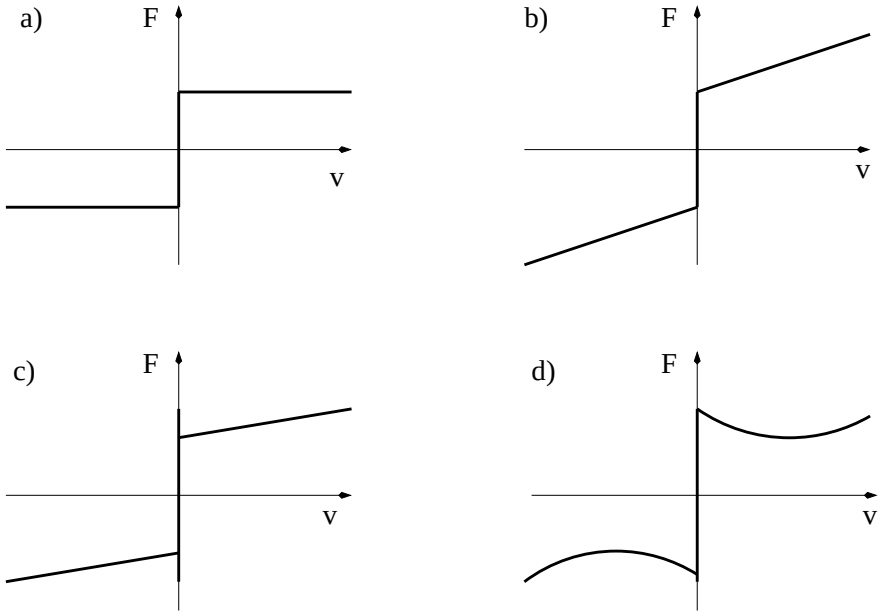

Figure 2.1: *Examples of static friction models. Figure a) shows Coulomb friction, Figure b) shows Coulomb plus viscous friction, Figure c) shows stiction plus Coulomb plus viscous friction, and Figure d) shows the Stribeck effect.*

2.3.2 Viscous friction

In the 19th century the theory of hydrodynamics was developed, leading to expressions for the friction force caused by the viscosity of lubricants [92]. The term *viscous friction* is used for this force component, and it is usually described as:

$$F = F_v v. \tag{2.2}$$

Viscous friction is often combined with Coulomb friction as shown in Fig. 2.1 b).

2.3.3 Stiction

Stiction is the short term for static friction, and describes the friction force at rest. The idea of a friction force at rest higher than Coulomb friction was introduced in 1833 by Morin [75]. Friction at rest needs to be modeled using the external force F_e,

as follows:

$$F = \begin{cases} F_e & v = 0 \quad \text{and} \quad |F_e| < F_S \\ F_S \times \text{sgn}(F_e) & v = 0 \quad \text{and} \quad |F_e| \geq F_S \end{cases}$$

where F_S is the static (breakaway) force. So at zero velocity stiction can take any value between $-F_S$ and F_S. The classical friction components can be combined in different ways, as Fig. 2.1 part c) shows.

2.3.4 Stribeck curves

At the beginning of the 20th century, Stribeck performed some experiments on sliding bearings, showing the dependence of the friction coefficient on the sliding velocity. He created some curves, now known as Stribeck curves, in which it is clear how the frictional force drops steeply with increasing relative velocity between the two bodies in contact. In his honor, the deep drop of friction while increasing the relative velocity is known as **Stribeck effect**. As Fig. 2.1 part d) shows, friction does not decrease discontinuously as in Fig. 2.1 part c), but the velocity dependence is continuous. So a more general description of friction is

$$F = \begin{cases} F(v) & \text{if} \quad v \neq 0 \\ F_e & v = 0 \quad \text{and} \quad |F_e| < F_S \\ F_s \times \text{sgn}(F_e) & v = 0 \quad \text{and} \quad |F_e| \geq F_S \end{cases}$$

where $F(v)$ is an arbitrary function that looks like in Fig. 2.1 part d).

Different parametrizations have been proposed for $F(v)$. In chapter 3 the parametrizations proposed to simulate a bowed string are described. Let us now examine more general parametrizations of this function.

A common form for the friction function is given by [80]

$$F(v) = f_c + (f_s - f_c)e^{-|v/v_s|^{\delta_s}} + f_v v \tag{2.3}$$

where v_s is called Stribeck velocity and F_v represents viscosity. Fig. 2.2 shows the shape of $F(v)$ for $f_c = 0.3$, $f_s = 0.8$, $\delta_S = 2$, $v_s = 0.5$ m/s for different values of the

parameter F_v.

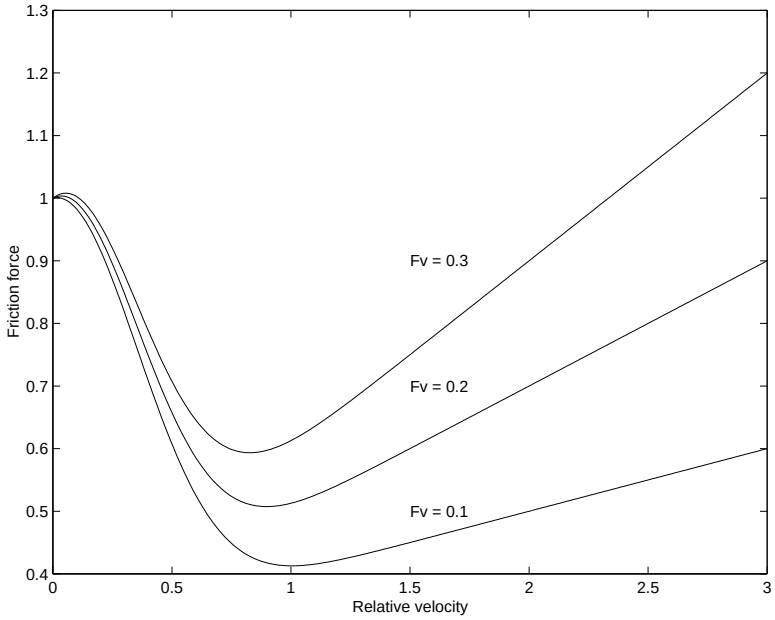

Figure 2.2: *Friction model of Eq. 2.3 for different values of F_v.*

2.3.5 Rate and state friction models

In the rock mechanics community, rate and state friction models have been developed [25] to simulate dynamics of earthquakes. Tectonic earthquakes, in fact, occur by sudden slippage along a pre-existing fault or plate surface. The observation that earthquakes must be the result of a stick-slip frictional instability was made in 1966 by Brace and Byerlee [11].

2.4 Dynamic friction models

More recently, a new class of dynamic friction models has been developed. In these models, the dependence of friction on the relative velocity between the two bodies in contact is modeled using a differential equation. Dynamic models are also able to take into account pre-sliding displacement, i.e., displacement that occurs just before

a complete slip takes place.

2.4.1 The Dahl model

The Dahl model and more general dynamic friction models are better understood considering Fig. 2.3 [43]. Let us consider two objects connected by a spring; let x be the moving object and w the adhesion point. Moreover, let $z = x - w$ describe micromovements between the two objects. Dynamic models define the friction force to be proportional to z, as is the two objects were attached by a spring. The quantity $|z|$ is not allowed to exceed a small value $z_{max} > 0$ called breakaway distance (which corresponds to the breakaway force). When $|z|$ reaches z_{max}, the contact becomes fully tense and w relocates. While the contact is fully tense, $\dot{x} = \dot{w}$ and $\dot{z} = 0$. This is when sliding takes place.

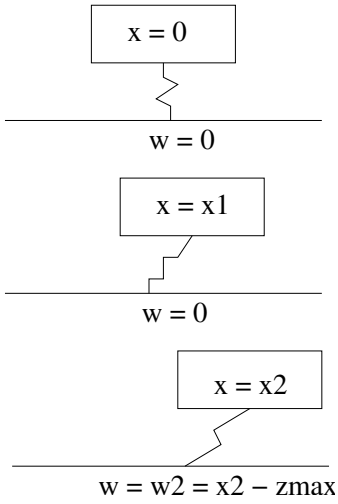

Figure 2.3: *Two objects connected by a spring.*

The first dynamic model, proposed by Dahl in 1968 [22], has as starting point the stress-strain curve in classic solid mechanics shown in Fig. 2.4. Dahl modeled the stress-strain curve using the following differential equation:

$$\frac{\partial F}{\partial x} = \sigma \left(1 - \frac{F}{F_C}\text{sgn}(v)\right)^{\alpha} \tag{2.4}$$

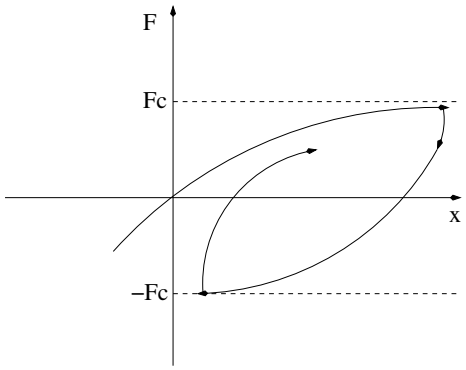

Figure 2.4: *Friction force as a function of displacement in the Dahl model.*

where x is the displacement, F is the friction force, F_C is the Coulomb friction force, σ is the stiffness coefficient and α determines the shape of the stress-strain curve.

By multiplying Eq. (2.4) by v, it results:

$$\frac{\partial F}{\partial x} = \frac{\partial F}{\partial x}\frac{\partial x}{\partial t} = \frac{\partial F}{\partial x}v = \sigma\left(1 - \frac{F}{F_C}\text{sgn}(v)\right)^{\alpha} v \tag{2.5}$$

For $\alpha = 1$ this gives:

$$\frac{\partial F}{\partial t} = \sigma v - \frac{F}{F_C}|v| \tag{2.6}$$

introducing $F = \sigma z$ the equation becomes:

$$\frac{\partial z}{\partial t} = v - \frac{\sigma|v|}{F_C}z \tag{2.7}$$

in steady state ($\dot{z} = 0$) it becomes:

$$z = \frac{F_C}{\sigma}\text{sgn}(v)F = F_C\text{sgn}(v) \tag{2.8}$$

so the steady state version of the Dahl model is Coulomb friction.

Dahl's model is a simple dynamic model that captures many phenomena such as hysteresis. In this model, friction depends only on displacement. Dahl's model, however, does not account for the Stribeck effect.

2.4.2 The LuGre model

An extension to the Dahl model is the LuGre model, whose name comes from the two laboratories in which it was developed (Lund and Grenoble), in which the Stribeck effect is included [24, 43]. The LuGre model is related to the bristle interpretation of friction as in [41]. The idea behind the bristle interpretation of friction is shown in Fig. 2.5. Let's consider two facing surfaces with bristles extending from each, as

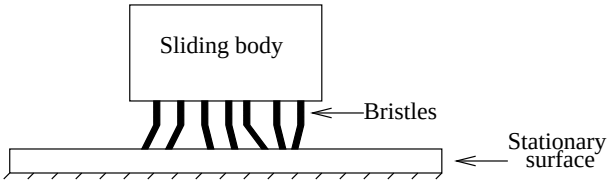

Figure 2.5: *Bristle model.*

shown in Fig. 2.5. The friction between the two surfaces is assumed to be caused by a large number of bristles, each contributing a fraction of the total friction load. The load contributed by each bristle is proportional to the strain of the bristle. When the strain exceeds a certain level the bond is broken, as shown in Fig. 2.6. In LuGre

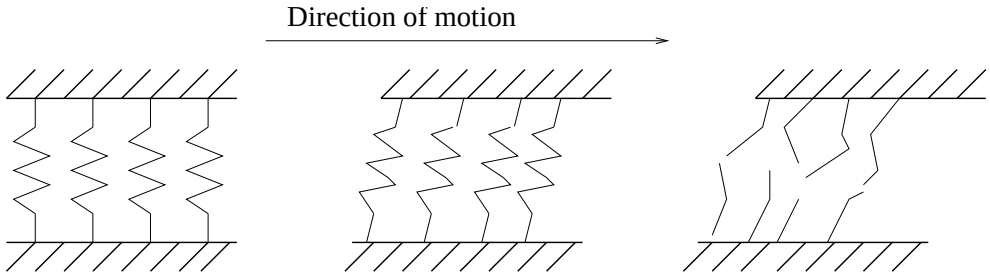

Figure 2.6: *Contacting asperities act as small stiff springs with dampers, giving rise to microscopic displacements (stick) and return forces. If the displacement becomes too large, the junctions break. At this break-away displacement true, macroscopic sliding (slip) starts.*

model, friction is modeled as the average deflection of the bristles. When a tangential force is applied, the bristles deflect like springs. If the deflection is large enough, the bristles start to slip. Denoting by z the average bristle deflection, the model is given

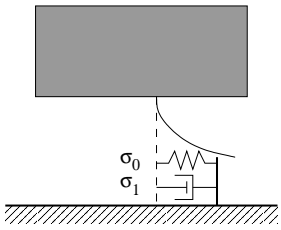

Figure 2.7: *The LuGre single-state averaged model.*

by:

$$\frac{\partial z}{\partial t} = v - \sigma_0 \frac{|v|}{g(v)} z \tag{2.9}$$

$$F = \sigma_0 z + \sigma_1(v) \frac{\partial z}{\partial t} + f(v) \tag{2.10}$$

where σ_0 is the stiffness of the bristles, and $\sigma_1(v)$ is the damping. So the physical interpretation of this model is as follows. Contact surfaces are very irregular at microscopic level. This can be visualizes as two rigid bodies that make contact through elastic bristles. When a tangential force is applied, the bristles will deflect like springs and dampers which gives rise to the friction force. The average deflection of the bristles corresponds to the internal state of the dynamic friction model z.

The idea of the LuGre model, is to generalize the Dahl model to obtain the Stribeck effect.

In steady state, the LuGre model is given by:

$$z = \frac{g(v)}{\sigma_0} \text{sgn}(v) F = g(v)\text{sgn}(v) + f(v) \tag{2.11}$$

The LuGre model is described in Fig. 2.7. This model is as simple as the Dahl model, and captures many aspects of friction such as the Stribeck effect and stick-slip motion. However, LuGre exhibits drift for arbitrarily small external forces, which is spurious. This effect has been explained in [26] by observing that LuGre does not allow a purely elastic regime for small displacements. Therefore, a class of *elasto-plastic* models has been proposed in [26], where the drawbacks of LuGre are overcome. These models have been applied in [42] to haptic rendering applications.

2.4.3 Elasto-plastic models

In order to improve the LuGre model and allow a purely elastic regime, a class of *elasto-plastic* models has been proposed [26]. In these models, the drawbacks of the LuGre model are overcome using the following formulation for the bristle displacement

$$\dot{z}(v,z) = v\left[1 - \alpha(z,v)\frac{z}{z_{ss}(v)}\right] \tag{2.12}$$

where $\alpha(z,v)$ is an adhesion map which controls the rate of change of z in order to avoid drift.

The elasto-plastic model will be used extensively in this dissertation, and therefore it requires a more detailed description. Eq. (2.12), together with:

$$f(z,\dot{z},v,w) = \sigma_0 z + \sigma_1 \dot{z} + \sigma_2 v + \sigma_3 w, \tag{2.13}$$

summarizes the elasto-plastic modeling approach. Eq. (2.12) defines the averaged bristle behavior as a first-order system: z and $\dot{z}$ can be interpreted as the mean bristle displacement and velocity, respectively, while v is the relative velocity between the two bodies in contact. Eq. (2.13) states that the friction force f results from the sum of three components: an elastic term $\sigma_0 z$, an internal dissipation term $\sigma_1 \dot{z}$, and a viscosity term $\sigma_2 v$ which appears in lubricated systems. As explained in [79], the viscosity term needs not be linear and may be a more complicated function of the relative velocity. A fourth component $\sigma_3 w$ is added here to Eq. (2.13), which is not part of the original formulation by Dupont *et al.* [26]. The term $w(t)$ is a pseudo-random function of time which introduces noise in the force signal, and is therefore related to surface roughness. The auxiliary functions α and z_{ss} can be parametrized in various ways. Following [24], z_{ss} is defined as

$$z_{ss}(v) = \frac{\mathrm{sgn}(v)}{\sigma_0}\left[f_c + (f_s - f_c)e^{-(v/v_s)^2}\right], \tag{2.14}$$

where f_c, f_s, and v_s are defined as before, and the subscript ss in z_{ss} stands for

"steady-state". Following [26] α is defined as:

$$\alpha(v,z) = \begin{cases} \left.\begin{array}{ll} 0 & |z| < z_{ba} \\ \alpha_m(v,z) & z_{ba} < |z| < z_{ss}(v) \\ 1 & |z| > z_{ss}(v) \end{array}\right\} & \text{if } \operatorname{sgn}(v) = \operatorname{sgn}(z) \\ 0 & \text{if } \operatorname{sgn}(v) \neq \operatorname{sgn}(z) \end{cases} \tag{2.15}$$

The function $\alpha_m(v,z)$, which describes the transition between elastic and plastic behavior, is parametrized as

$$\alpha_m(v,z) = \frac{1}{2}\left[1 + \sin\left(\pi \frac{z - \frac{1}{2}(z_{ss}(v) + z_{ba})}{z_{ss}(v) - z_{ba}}\right)\right]. \tag{2.16}$$

and is shown in Fig. 2.8. Therefore the parameter z_{ba} defines the point where α starts to take non-zero values, and is termed *breakaway displacement*.

Suppose that a constant relative velocity v is applied, starting from zero conditions.

1. As far as z remains small ($z < z_{ba}$), then $\alpha = 0$ and the first equation in (2.13) states that $\dot{z} = v$. This describes *presliding elastic* displacement: the (mean) bristle deflection rate equals the relative velocity and the bristle is still anchored to the contact surface.

2. When z exceeds z_{ba}, the mixed *elastic-plastic* regime is entered, where $|\dot{z}| < |v|$.

3. After the transient mixed regime, the first-order equation in (2.13) converges to the equilibrium $\dot{z} = 0$, and steady-state is reached with purely *plastic* bristle displacement. Note that $\dot{z} = 0$ means $z = z_{ss}$. It is now clear why z_{ss} (z at steady-state) has been given this name.

Note how in steady state $f(v) = \sigma_0 z_{ss}(v)$. In other words, at steady-state the elasto-plastic model converges to the kinetic model.

In the following chapters, the friction models introduced will be applied to an accurate bowed string physical model, and to other friction driven musical instruments. It is especially interesting to analyze the transient behavior of these friction

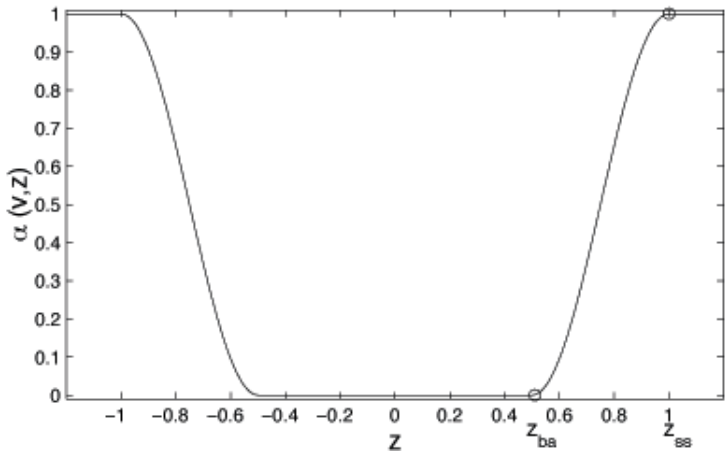

Figure 2.8: *The shape of the α function*

models, and how they affect the playability of virtual instruments. This is the topic of Chapter 6.

Chapter 3

The bowed string

3.1 History of the violin

The violin as known nowadays evolved from different musical instruments including the Greek lira, the Indian rabab, the renaissance fiddle and several other instruments dating back to a few thousand years B.C.

By the Middle Ages, around the eleventh century, the vielle and the rote had come into existence. Around this time, a fingerboard was added to such instruments.

The 12th century brought the last evolution of the vielle which, at that time, looked similar to a modern guitar. It was a widely used instrument during that period due to its ease of handling and its big tonal range. Throughout the 11th and 12th centuries ribs were added, as well as the tailpiece and a bridge. Three other instruments appeared before the 15th century, one called the *viola da gamba*, since it was held on or between the knees, the *lira da braccio*, and the *viola da braccio*.

The viola da braccio, which had originally three or four strings, became a four-stringed instrument and it is likely the closest predecessor of the contemporary violin [32]. The sound holes changed their shape toward the f shape used nowadays, from which the name f-holes derives.

3.2 The violin

The different components of a violin which contribute to the resulting sonorities are shown in Fig. 3.1.

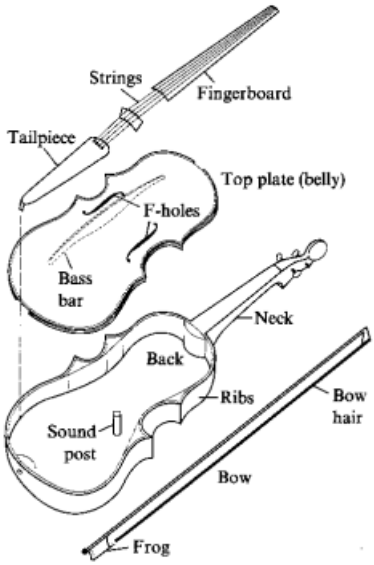

Figure 3.1: *Different components of a violin, from [32].*

The sound of a violin depends on the transfer of vibrations from the bowed string through the bridge to the body of the instrument. All these components, together with the way they are coupled, contribute to the characteristic sound of this instrument. First of all, the role of the strings is essential. The strings provide the driving force that brings the body into vibration.

3.2.1 The Helmholtz motion

As the bow is drawn across the strings, strings move back and forth in a motion similar to the one shown in Fig. 3.2. This motion is known as *Helmholtz motion*, in the honor of the scientist who discovered it.

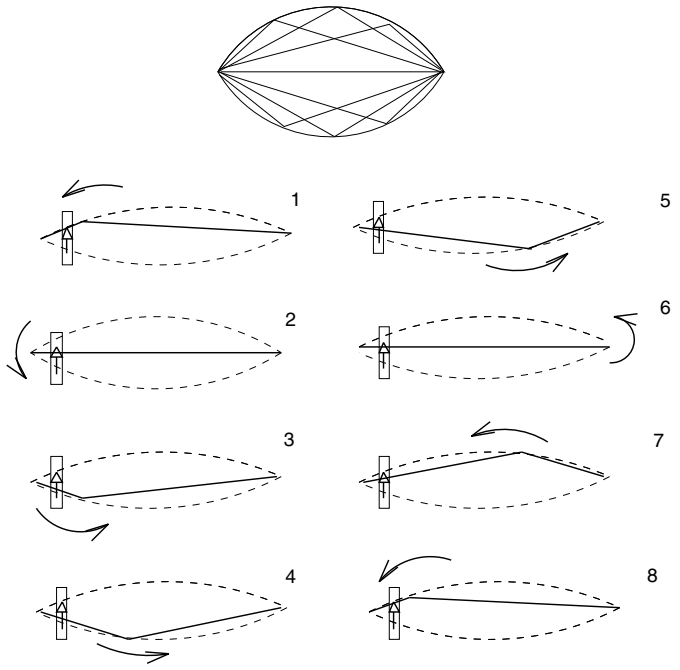

Figure 3.2: *The idealized Helmholtz motion. The string moves in time from position 1 to position 8. The rectangle represents the bow.*

The Helmholtz motion considers an ideal flexible string, rigidly terminated. The bow is assumed to be perfectly rigid and to be in contact with the string in a single point. In this idealized situation, the shape of the string consists of two straight lines joined by a corner known as "Helmholtz corner". Helmholtz studied the motion of the bowed string at the bowing point and at other points along the string by observing an illuminated speck of starch attached to an otherwise blackened string, using what he called a vibration microscope. This instrument allowed him to observe the characteristic "sawtooth" motion of a bowed string. In normal conditions the string remains "stuck" to the bow hair and travels along with it for a considerable fraction of each vibratory cycle, after which it flies back abruptly to begin the next cycle, which takes place at very nearly the first-mode frequency of the string.

Although every player is trying to achieve the Helmholtz motion, different perturbations from this ideal situation exist, and will be discussed in Chapter 6. In that chapter the different kinds of regimes produced by the physical models described in chapter 4 will be examined.

3.3 The violin body

The violin body acts as a resonator for the vibration generated from the strings. The coupling of air cavity modes and top and back plate modes produces the complex filtering which contributes strongly to the characteristic timbre of the violin.

The impulse response of a violin body is shown in Fig. 3.3.[1] The bottom of Fig. 3.3 shows the input admittance. At low frequencies, the resonances of the whole body dominate, except for the 460 Hz resonance and the air resonance [55]. With increasing frequency, a large number of top and back plate resonances will dominate the body vibration of a violin. At high frequencies the bridge will give a major contribution. The sound post gives a large asymmetry at low frequencies. The violin body therefore acts as an acoustical amplifier which gives two kinds of amplification. First the vibration of the strings results in the vibration of the body walls, since the vibrating string produces a vibration force on the bridge, which is transmitted via the bridge to the top plate and thereafter to the complete body. Secondly, the resonances of the violin body give extra amplification at specific frequencies.

3.4 Research on bowed strings

The first scientific investigations of vibrating strings are credited to the Greek philosopher Pythagoras, who, in the 6th century B.C., noticed some important relationships between string length and pitch.

Preliminary observations regarding the sound of friction for bowed objects were made by Galileo Galilei in the 16th century [35]. Galileo noticed that when a brass plate is scraped with an iron chisel, the scraping produces a sharp whistling sound.

In the 18th and 19th century, Savart directly experimented with violin construction and form. He studied modes and vibration of violin's plates, using the technique previously developed by Chladni [16], which consisted of sprinkling plates with fine powder and putting them into vibration using a violin bow. This technique was also used to study the vibrational modes of a trapezoidal violin such as the one shown in

[1] Courtesy of Jim Woodhouse.

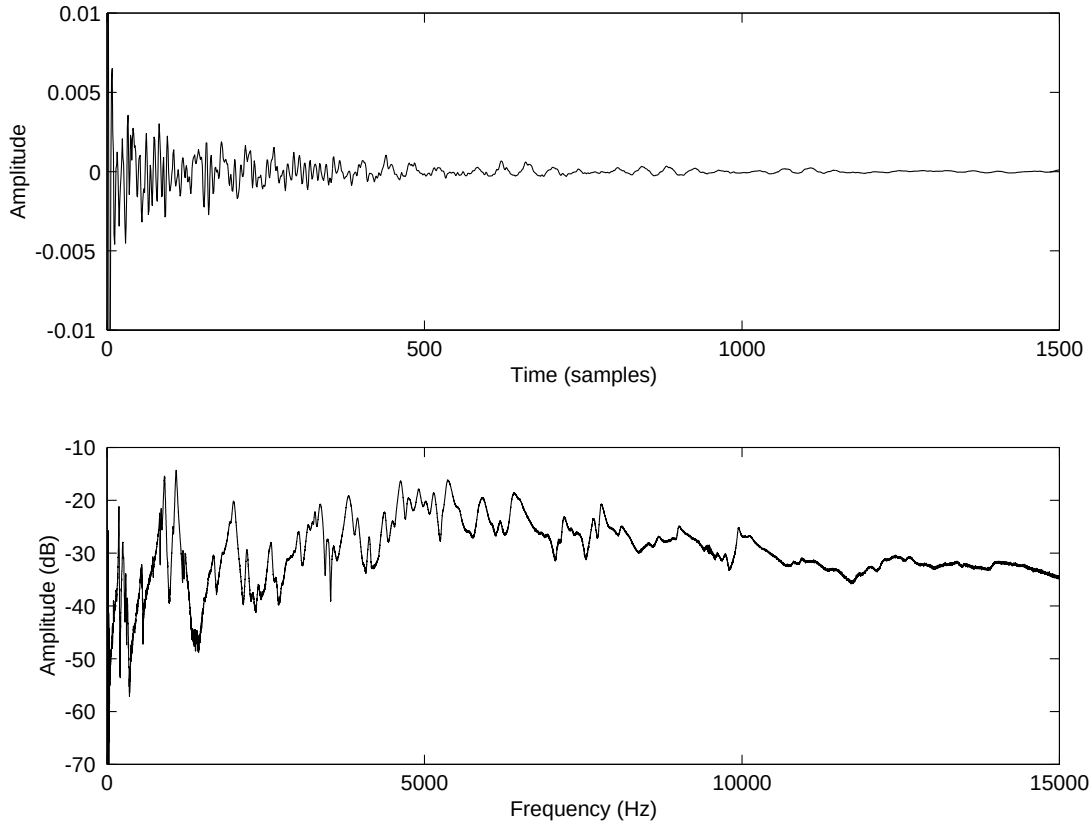

Figure 3.3: *Top: impulse response of a violin body. Bottom: input admittance of a violin body.*

Fig. 3.4.

Elements of the violin as a musical instrument were extensively studied by Helmholtz in [130]. In his monumental work he described the motion of a bowed string as explained in the previous section, and he also dealt with psychological investigations of the tones produced by the instrument.

Later on, Lord Rayleigh [91] explored vibrational characteristics of many media and developed one of the first mathematical descriptions of the vibration of a bowed string.

During the period from 1909 through 1921, the Indian physicist C. V. Raman published a series of papers on the properties of bowed strings [90]. Raman's analysis of string vibrations confirms and greatly extends Helmholtz's work, since the effect

Figure 3.4: *Savart's original trapezoidal violin. From the Ecole Polytechnique collection, France.*

of string damping was for the first time taken into account.

The technological developments of the 20th century made it possible for different researchers to investigate the motion of a bowed string and to analyze the body of the instrument in greater detail. In particular, Schelleng used electrical circuit methods to formulate the behavior of string-body vibration, as well as to derive the first explicit mathematical formulas for the limits of maximum and minimum bow force in violin playing. This issues will be discussed in detail in Chapter 6.

In the second half of the 20th century, mathematical descriptions of vibrating strings were combined with computer simulations, as described in the following section.

3.5 Physical models of bowed strings

Starting in the second half of the 20th century, improvements in hardware technology allowed the development of synthesis techniques to simulate the sound of musical instruments on a computer. In particular, digital sound synthesis by physical models started to develop. Sound synthesis by physical models requires two main steps: the description of a vibrating structure by the principles of physics and the transformations of these laws into discrete-time and discrete-space models which can be

implemented in software.

The bowed string is a complex nonlinear dynamical system. Mathematical formulations that describe its behavior have seen lots of improvements also thanks to the availability of computers which allow to digitally visualize and reproduce the behavior of such instruments.

A simple mathematical model of a bowed string was proposed by Rayleigh [91]. Rayleigh compared the behavior of a bow driving a string to the one of a mass moving in a conveyor belt, as shown in Fig. 3.5. This model has been used in many simulations of different dynamical systems driven by friction [88]. As shown in Fig. 3.5, a conveyor belt is moving at constant speed v_0. Coulomb friction between a block of mass m and the belt opposes the mass motion. The block is restrained by a spring with constant k. The equations of this model are derived in [96].

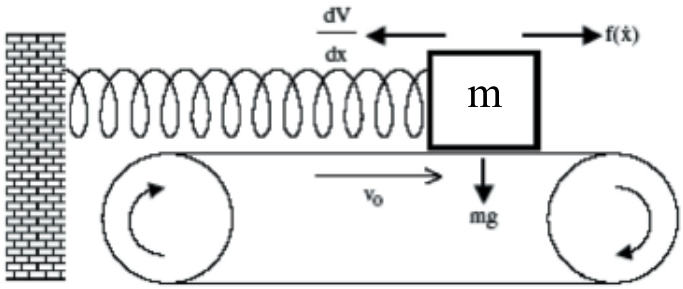

Figure 3.5: *Rayleigh's mass-spring model of a bowed string. A mass m sits upon a conveyor belt which moves with uniform velocity* v_0.

Friedlander [34] and Keller [60] explored the mathematical properties of simple bowed string models which assumed a perfectly sharp Helmholtz corner.

The impossibility for the Helmholtz corner to be perfectly sharp, due to losses and dispersion of the string was first pointed out by Cremer, who also wrote a landmark book on violin research which at the time represented the state of the art in the field [21].

Starting from these pioneering research efforts, and thanks to advances in hardware and software technology, different physical modeling techniques have developed during the past 20 years.

Physical modeling methods can be divided into five categories [125]:

1. Exciter-resonators models.
2. Vibrating mass-spring models.
3. Modal synthesis.
4. Numerical solution of partial differential equations.
5. Digital waveguides.

In the remaining part of this chapter the use of such five types to simulate a bowed string is described.

3.5.1 Exciter-resonators models

"Exciter-resonator" is a general term used to represent a system in which a source of energy (the exciter) is fed into a resonating structure. In a general sense, all the physical modeling techniques mentioned above can be seen as belonging to the exciter-resonator paradigm. In the case of the bowed string, the exciter is the bow when interacting with the string, and the resonator is given by the vibrating strings coupled to the body.

In [71], McIntyre, Schumacher and Woodhouse describe a general class of so-called *self-sustained oscillators*, i.e., systems in which sound is produced as long as a source of energy is fed into a system. Examples of self-sustained oscillators examined in [71] are a flute, a violin and a clarinet. These instruments are distinguished from the so-called *transient instruments*, i.e., instruments in which a transient source of energy is fed into a system, at which point the system starts and continues to oscillate until damped. Examples of transient instruments are percussion instruments, plucked and struck strings.

In [71], a simple time-domain simulation of a bowed string is proposed as follows. This algorithm is nowadays known as MSW algorithm, in the honour of the researchers who developed it. Let us consider velocity traveling waves that propagate to and from

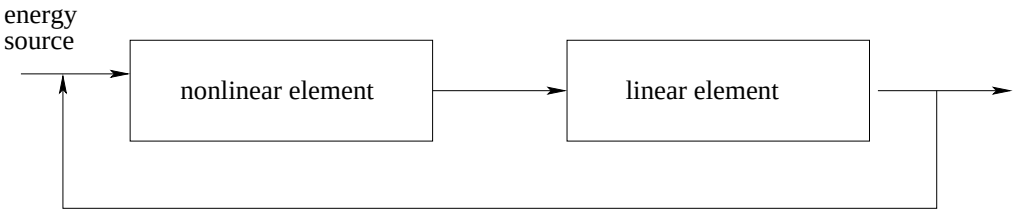

Figure 3.6: *A general oscillator made of a linear and nonlinear component connected in a feedback loop.*

the two extremities of a string, which are called the bridge and the nut, and meet at the bow point.

First of all, the contribution of the reflected waves v_{in} and v_{ib} coming from the nut and the bridge respectively are summed at the bow contact point:

$$v_h = v_{in} + v_{ib}$$

where v_h is the notation used in [71] to denote the historical (i.e., known) string velocity. At this point, two variables are considered, which are the transverse string velocity v and the frictional force f. These quantities are connected in two different ways, represented by the following equations:

$$f = 2Z(v - v_h) \tag{3.1}$$

$$f = \mu(v - v_b)f_b \tag{3.2}$$

where Z is the wave impedance of the string, v_b is the bow velocity, f_b is the bow force, v is the velocity of the string at the contact point and μ is the frictional force. As shown in Eq. (3.2), to a first approximation it is possible to assume that the frictional force simply depends on the relative velocity between the bow and the string $(v - v_b)$ and on the bow force f_b. Once the friction force f has been calculated, two traveling waves v_{on} and v_{ob} resulting from the bow string interaction propagate toward the nut

and the bridge and are calculated as follows:

$$\begin{aligned} v_{on} &= v_{ib} + f/(2Z) \\ v_{ob} &= v_{in} + f/(2Z) \end{aligned} \tag{3.3}$$

since

$$\begin{aligned} v &= v_{on} + v_{in} \\ &= v_{ob} + v_{ib}. \end{aligned}$$

Such outogoing velocities reflect again at the two extremities of the string and meet at the bow point, where it is possible to calculate the historical velocity v_h which at this time step is given by the sum of the two new contributions. This algorithm, which will be widely used in Chapter 4, is summarized in the following box.

for $n = 1 \ldots$ samples
1) Compute v_h from v_{in} and v_{ib}
2) Solve $f = 2Z(v - v_h)$
and $f = \mu(v - v_b)f_b$
with f and v as unknown
3) Compute $v_{on} = v_{ib} + f/(2Z)$
$v_{ob} = v_{in} + f/(2Z)$
end

TIme domain simulation of bow-string contact is also used in the digital waveguide approach, which will be described in Sec. 3.5.5.

3.5.2 Vibrating mass-spring models

Another approach to simulate the vibration of a string as well other vibrating systems is the one developed by Cadoz and coworkers [13]. They suggest to create complex physical models by connecting basic mechanical elements such as masses, dampers and springs.

In 1985 the first real-time bowed string simulation based on such particle-interaction systems was proposed [13]. In it, the string was represented by a set of 25 to 60 masses linked by visco-elastic elements.

The system implementing bowed string physical models as well as other vibrating structures is called *Cordis-Anima*. In it elements that receive forces and calculate positions are found, and interaction elements that calculate a force according to the positions of the other elements.

The basic elements of the Cordis-Anima system are:

1. point masses
2. ideal springs
3. ideal dampers

The Cordis-Anima system is still widely used and developed at the center Acroe in Grenoble, where Cadoz and coworkers can now take advantage of the development in hardware technology to create complex vibrating systems that work in real-time. The Cordis-Anima environment presents a powerful combination of physically-modeled audio-visual simulations used in virtual reality and computer music compositions.

3.5.3 Modal synthesis

Another powerful synthesis technique inspired by the physics of vibrating objects with a strong link to spectral models is *modal synthesis*. The modal synthesis approach has been widely adopted in the sound synthesis community. As few important examples, Klatt used it to simulate a formant based speech synthesizer [61], Serra adopted it to simulate bar percussion instruments [111], Wawrzynek used modal synthesis for

VLSI computation [131]. Other applications of modal synthesis to the simulation of musical instruments were proposed by Adrien [2, 1].

Modal synthesis is based on the premise that many sound-producing objects can be represented as a set of vibrating substructures which are defined by modal data.

Recently modal synthesis has been widely adopted in the computer music community for simulation of audio effects and sounding objects in general [20, 93, 83].

Concerning the bowed string, in [5] a detailed simulation of how a modal resonator can be coupled to a friction excitation is described. The approach derived in [5] is described in the following.

Let us consider the equation of an ideal vibrating string:

$$m\frac{\partial^2 y}{\partial t^2} = T\frac{\partial^2 y}{x^2} - \eta\frac{\partial y}{\partial t} + F(x,t) \tag{3.4}$$

of mass m, length L and dissipation η, where $c^2 = T/m$, and F represents external forces on the string. All the solutions of Eq. (3.4) can be formulated in terms of the modal parameters $m_n = \mu L/2$ $(\forall n)$, $\omega_n = n\pi c/L$, η_n, and modeshapes $\phi_n(x) = \sin(n\pi x/L)$, for $n = 1, 2, ..., N$, where the mode number N is arbitrarily chosen.

In the modal domain, the response of the string can be expressed as:

$$[M]\ddot{Q}(t) + [C]\dot{Q}(t) + [K]Q(t) = \Xi(t) \tag{3.5}$$

where

$$\begin{aligned}
[M] &= \mathrm{diag}(m_1, ..., m_N), \\
[C] &= \mathrm{diag}(2m_1\omega_1\zeta_1, ..., 2m_N\omega_N\zeta_N), \\
[K] &= \mathrm{diag}(m_1\omega_1^2, ..., m_N\omega_N^2), \\
\{Q(t)\} &= < q_1(t), ..., q_N(t) >^T, \\
\{\Xi(t)\} &= < \chi_1(t), ..., \chi_N(t) >^T
\end{aligned}$$

At any time, the response of the system can be calculated by modal superposition:

$$y(x,t) = \sum_{n=1}^{N} \phi_n(x) q_n(t) \tag{3.6}$$

For given external excitation and initial conditions, the previous system of equations can be integrated using an adequate time-step integration algorithm. It is possible to show [83] that modal synthesis can be implemented by using resonant filters in parallel.

The right side of Eq. (3.5) contains all the nonlinearities of the system. In the case of the bowed string, therefore, the second term contains the frictional interaction between the bow and the string.

3.5.4 Numerical solution of partial differential equations

In [44], Hiller and Ruiz proposed a numerical solution to the partial differential equation representing a bowed string. They were the first to take the approach of numerically solving the equation of a vibrating string for sound synthesis purposes.

A similar approach which uses finite differences to simulate a bowed string was proposed in [85]. The starting point is a variation of the wave equation of Eq. (3.4):

$$m\frac{\partial^2 y}{\partial t^2} = T\frac{\partial^2 y}{x^2} - \eta\frac{\partial y}{\partial t} + S_j\frac{\partial^3}{\partial x^2 \partial t} \tag{3.7}$$

in which the last term represents energy losses due to internal viscous friction.

In order to integrate Eq. (3.7), the authors decompose the instantaneous shape of the string into a set of harmonic functions up to a certain order that is the highest allowable spatial frequency for the string. The solution for the integration of spatial variables is similar to the use of finite elements, since it is based on the decomposition into orthonormal functions. As in [5], the shape of the string is obtained by a sinusoidal decomposition. For the integration of the time variables, finite differences are used.

The model described was used by the Italian composer Michelangelo Lupone in

the piece called *Corda di Metallo* premiered by the Kronos Quartet in Rome in 1997.

3.5.5 Waveguide synthesis

Digital waveguide models [113, 116, 114] have become popular in the last two decades as an efficient synthesis technique suitable for real-time implementation.

The starting point of digital waveguides [71] is the ideal wave equation as solved by D'Alembert [23]

$$\frac{\partial^2 y}{\partial x^2} = c^2 \frac{\partial^2 y}{\partial t^2} \tag{3.8}$$

where y is the displacement of the string, x the position along the string and c the wave speed. D'Alembert showed that the wave equation has an explicit solution given by:

$$y(x,t) = y_r(x - ct) + y_l(x + ct) \tag{3.9}$$

where y_l and y_r are interpreted as left-going and right-going traveling waves respectively. Therefore, it is possible to consider the solution to the wave equation as a sum of traveling waves, in which a single traveling wave is simulated using one delay line. Therefore, an ideal vibrating string is simulated using a pair of delay lines, one for each direction of traveling. In order to obtain a digital implementation, the traveling waves are sampled in interval T is time and X in space as follows:

$$\begin{aligned} x \rightarrow x_m &= mX \\ t \rightarrow t_n &= nT \end{aligned} \tag{3.10}$$

where m and n represent the new space variables. The following relationship yields simplest results:

$$c = \frac{X}{T} \tag{3.11}$$

Substituting Eq. (3.11) into Eq. (3.9) we obtain, following [114]

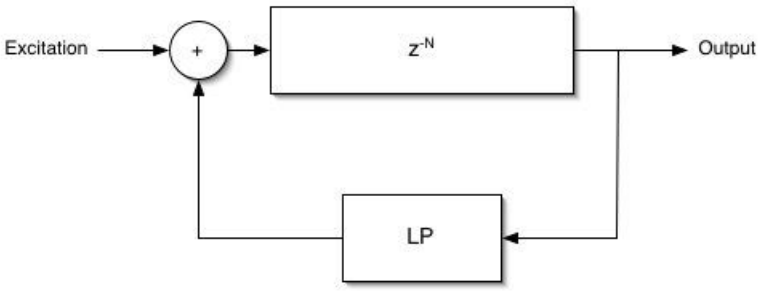

Figure 3.7: *A simplified waveguide physical model of a vibrating string. The delay line of N samples represents two traversals of the string, and LP represents the low-pass filter that accounts for all losses during two traversals.*

$$\begin{aligned} y(t_n, x_m) &= y_r(t_n - x_m/c) + y_l(t_n + x_m/c) && (3.12)\\ &= y_r\left(nT - \frac{mX}{c}\right) + y_l\left(nT + \frac{mX}{c}\right) && (3.13)\\ &= y_r(T(n-m)) + y_l(T(n+m)) && (3.14) \end{aligned}$$

If $y^+(n) = y_r(nT)$ and $y^-(n) = y_l(nT)$, the two discrete functions $y^+(n-m)$ and $y^-(n+m)$ can be interpreted as the output of an m-sample delay line whose input are $y^+(n)$ and $y^-(n)$ respectively [114].

3.5.6 Accounting for losses

The previous derivations assume a lossless wave propagation. Such a situation does not occur in reality. As a first approximation to real propagation losses, the substitution

$$z^{-1} \leftarrow gz^{-1},$$

where $|g| \leq 1$, is possible. Because the system is linear and time-invariant, the distributed loss factors g can be commuted or lumped together and implemented at discrete points. For a delay line of length N, the commuted factor would equal g^N.

In general, since damping increases with frequency, a more accurate representation of propagation losses is frequency-dependent. To implement frequency-dependent

losses, each scale factor g is replaced by an appropriately designed digital filter. Because the system is linear and time-invariant, these filter responses can also be commuted and implemented as a single string loop filter $G(z)$. In Fig. 3.7 the low-pass filter LP which accounted for losses while traversing the string was introduced. The role of LP is to simulate frequency-dependent attenuation. By using a linear-time-invariant filter, it is possible to provide an independent gain at each frequency, as described in [114]. Digital filters which allow to simulate losses in a violin and cello string are described in Chapter 4.

Before describing different bow-string interaction models proposed in the literature, the characteristics of the described synthesis techniques are summarized in Table 3.1.

3.6 Comparisons between the different techniques

The different synthesis techniques used to synthesize a bowed string are summarized in Table 3.1. Until recently, finite differences and mass-spring systems could not be implemented in real-time due to computational issues. However, improvements in hardware technology are allowing such techniques to see real-time implementations. The choice of the discretization technique to model resonators is usually based on the structure of the resonator itself. For example, for quasi-harmonic systems such as violin strings, usually digital waveguides are the preferred choice. However, for systems which show a strongly inharmonic spectrum, usually other techniques such as modal synthesis are preferred.

Technique	**Characteristics**	**Reference**
Finite differences	Numerical solution of the wave equation.	[85]
The MSW algorithm	Precursor of digital waveguides.	[71, 38, 39]
Digital waveguides	Efficient for quasi-harmonic systems.	[119, 14, 124, 45]
Modal synthesis	Efficient for systems with few modes.	[2, 5]
Mass-spring systems	High computational cost.	[13]

Table 3.1: *Summary of physical modeling techniques used to simulate a bowed string.*

3.7 The bow-string interaction

"Classic" models of the bow-string interaction assume that friction depends only on the relative velocity between the bow and the string, in a dependence similar to the one shown in Fig. 3.8, in which friction exponentially decreases while the relative bow-string velocity increases. The different shapes which the friction curve of Fig. 3.8 can assume are discussed in Chapter 4.

In order to solve the interaction between the bow and the string, a graphical solution to the system in Eq. (3.2) was first proposed in [34] and is represented in Fig. 3.8 part a). Notice how, in a situation such as Fig. 3.8 part b) three intersections can occur, as pointed out by Friedlander [34]. This ambiguity is solved using the hysteresis rule proposed in [72] and described in Fig. 3.8, part c) and d): as the string velocity increases, the bow remains in slipping mode until it reaches the capture velocity v_c. The string velocity then jumps to the bow velocity v_b. The string remains in stick velocity until it decreases to v_r, at which point the maximum sticking force is exceeded. The hysteresis rule therefore means that the solution point traverses a different path for increasing relative bow spring speeds than for decreasing speeds.

The shape of the "classic" friction curve has been mathematically expressed in different ways, which are described in the following section.

3.7.1 Mathematical formulations of the friction curve

Hyperbolic friction model

The hyperbolic model for the coefficient of bow-string friction is given by:

$$\mu = \mu_d + \frac{(\mu_s - \mu_d)v_0}{v_0 + v - v_b} \tag{3.15}$$

where v, v_b and v_0 are the string velocity, bow velocity and initial bow velocity, respectively, and μ_d and μ_s are the dynamic and static coefficients of friction, respectively. Notice that $\mu_s > \mu_d$. Typical values used in the literature are $\mu_s = 0.8$ and $\mu_d = 0.3$ [100]. This model has been used for many years as a convenient mathematical approximation which yields closed-form results for the bow-string interaction

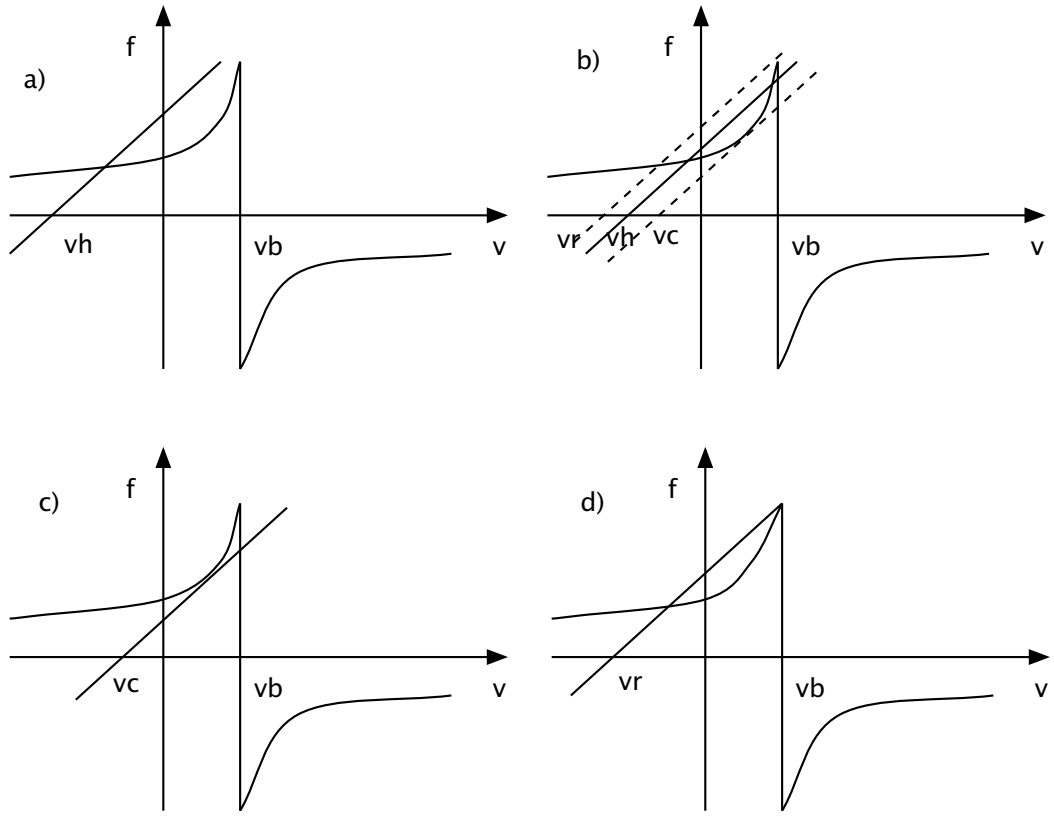

Figure 3.8: *a) The solution of the bow-string interaction. b) Friedlander ambiguity. c) Hysteresis rule for capture. d) Hysteresis rule for release.*

[72, 71, 134].

Double exponential friction model

The exponential model is given by [112]

$$\mu = 0.4\, e^{\frac{v-v_b}{0.01}} + 0.45\, e^{\frac{v-v_b}{0.1}} + 0.35 \tag{3.16}$$

where, as before, v and v_b represent the velocity of the string and the bow, respectively. This model fits a sum of two exponentials to friction measurements made during steady sliding. As a result, any dynamic behavior is neglected in the establishment of frictional force after a velocity change.

Other formulations of similar velocity dependent friction models have also been proposed. For example, the friction model suggested in [5] is the following:

$$f_s(x_A, t) = -\mu(v - v_b) f_b \text{sgn}(v - v_b) \qquad \text{if} \qquad |v - v_b| > 0 \tag{3.17}$$

$$|f_b(x_A, t)| < \mu_S f_b \qquad \text{if} \qquad |v - v_b| = 0 \tag{3.18}$$

where, as before, f_b represents the bow pressure, μ_s is the static friction coefficient and $\mu(v - v_b)$ represents the friction force ($f = \mu_d f_b$). The shape of μ proposed in [5] is given by:

$$\mu(v - v_b) = \mu_d + (\mu_s - \mu_d) e^{-C|v - v_b|} \tag{3.19}$$

with $0 \leq \mu_d \leq \mu_s$, and C is a parameter that controls the decay time of the friction coefficient.

The shape of the friction curve of Eq.(3.19) with $\mu_s = 0.4$, $\mu_d = 0.2$ and $C = 5$ is shown in Fig. 3.9.

In [121] and efficient simulation of the bow-string interaction problem is proposed, in order to facilitate a real-time implementation. The bow-string interaction is simulated by using a memoryless table lookup.

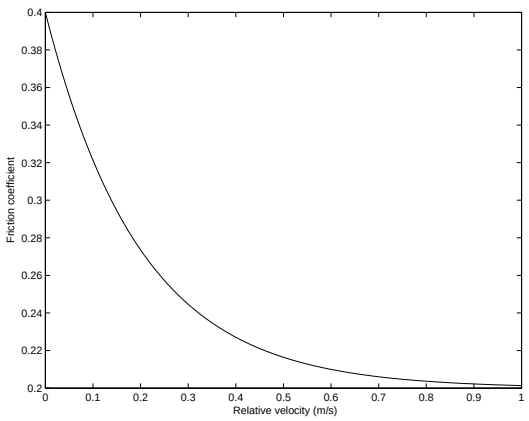

Figure 3.9: *Friction curve used in the simulations of [5].*

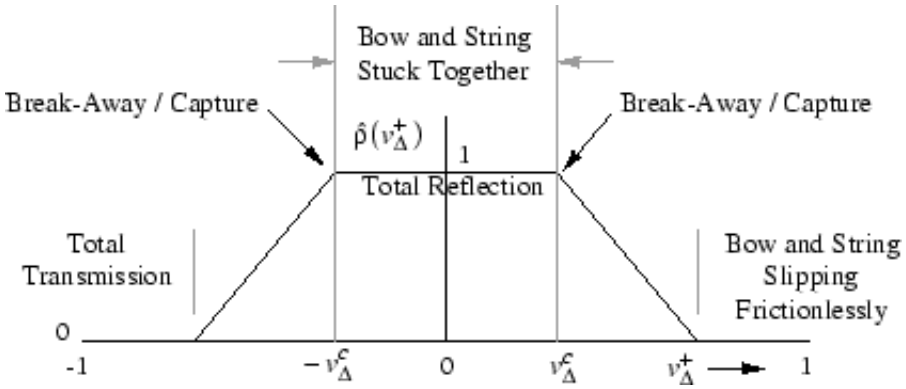

Figure 3.10: *Simplified bow table ρ proposed in [118].*

Using the same notation as in Sec. 3.5.1, the equations of the model are given by

$$\begin{aligned} v_{on} &= v_{ib} + \rho(v_b - v_h)(v_b - v_h) \\ v_{ob} &= v_{in} + \rho(v_b - v_h)(v_b - v_h) \end{aligned} \tag{3.20}$$

where

$$\rho(v_b - v_h) = \frac{r(v_\Delta(v_b - v_h))}{1 + r(v_\Delta(v_b - v_h))} \tag{3.21}$$

where $v_\Delta = v_b - v$, and $r(v_\Delta) = 0.25R_b(v_\Delta)/R_s$, R_b represents the static friction coefficient, R_s is the wave impedance of the string, $v_h = v_{in} + v_{ib}$ represents the

historical (past) velocity at the bow point and R_b is the friction coefficient of the bow against the string. R_b is constant for $|v_\Delta| \leq v_\Delta^c$, where v_Δ^c is the capture and breakaway differential velocity.

For $|v_\Delta| > v_\Delta^c$, R_b falls quickly to a low dynamic friction coefficient. The bow table chosen in [121] is shown in Fig. 3.10. These equations are justified by the fact that velocity input (which is injected equally in the left- and right-going directions) must be found such that the transverse force of the bow against the string is balanced by the reaction force of the moving string. If bow-hair dynamics are neglected, the bow-string interaction can be simulated using a memoryless table lookup or segmented polynomial such as the one shown in Fig. 3.10.

The flat portion corresponds to the portion of the bow "stuck" to the string, while the outer section corresponds to the slipping part. The outer sections of the curve give a smaller reflection coefficient corresponding to the reduced bow-string interaction force while the string is slipping under the bow. Using this simplified bow table, it is possible to avoid the iterative solver required when the bow-string interaction is expressed through a nonlinear function. This friction model does not account for hysteresis.[2]

Following Smith's approach, other researchers recently proposed waveguide-based bowed string physical models. For example, in [124] a waveguide bowed string physical model is driven by a rule-based parameters' engine, in order to increase its expressivity. In [45] variations to the original waveguide models are also proposed. The addition of random noise to the friction curve in order to simulate the characteristic noise of a bowed string instrument was first proposed in [15], and recently used in [85].[3]

Dynamic bow models

An interesting approach in order to obtain a dynamic model of the bow was proposed in [2] and shown in Fig. 3.11.

[2] A nonlinear function generation apparatus which comprises hysteresis was developed by Yamaha in a patent filled in 1990, patent number 613163.

[3] The addition of random noise to the friction curve was also suggested to the author by Knut Guettler [37].

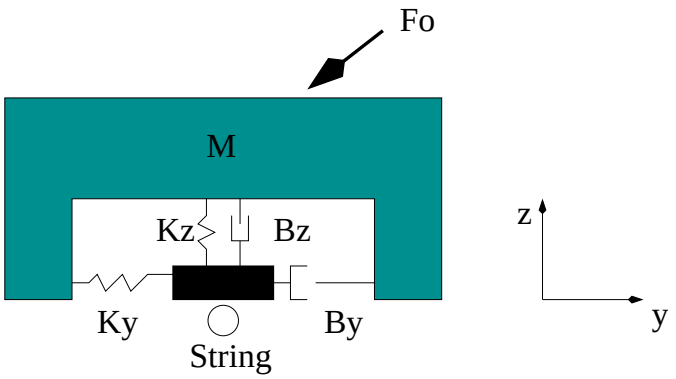

Figure 3.11: *Mechanical model for the bow as proposed in [2]. M represents the bow wood, on which the player applies a force F_0.*

In it M represents the bow wood, on which the player applies a force F_0, and m represents the bow hair.

The equations proposed in [2] are given by

$$(F_{oy}, F_{cy}) = [Z_Y](V_y, v_y) \tag{3.22}$$

$$(F_{oz}, F_{cz}) = [Z_Z](V_Z, v_z) \tag{3.23}$$

where F_{oy} and F_{cy}, F_{oz} and F_{cz} represent the external forces applied on the masses M and m, and V_y, v_y and V_z, v_z represent the velocities of the masses M and m in the Oy and Oz directions.

In addition, the following relationship holds:

$$F_{cy} = -||F_{cz}||\Delta\mu/[(1 + v_y - v_{sy})/\beta] \tag{3.24}$$

where F_{cy} is the sliding force applied by the string on the bow hair in the O_y direction, F_{cz} is the sticking force applied in the O_z direction and $v - v_{sy}$ is the velocity of the string relative to the bow hair, and β is a coefficient related to the bow hair rosin. In this model, however, the friction curve is still represented using a velocity dependent friction curve.

3.7.2 Plastic friction models

The previous friction models assume that friction depends only on the relative velocity between the bow and the string.

Recently, Smith and Woodhouse discovered that the behavior of friction at the bow point is more complicated than a simple friction versus velocity dependence [112]. If the force f and sliding velocity v are measured during stick-slip motion with rosin at the interface, the results of the plots in the $f - v$ plane are shown in Fig. 3.12. This plot was obtained by rubbing two crossed cylinders of perspex loaded together to give an approximatively circular contact area. One of the cylinders was stationary, while the other was moving carrying a layer of rosin. In the plot the dotted exponential curve represents the classic friction model, while the other curve represents the measurements. From this plot, it is evident how the *classic* friction models that consider friction as depending only on the relative velocity between the bow and the string are not correct.

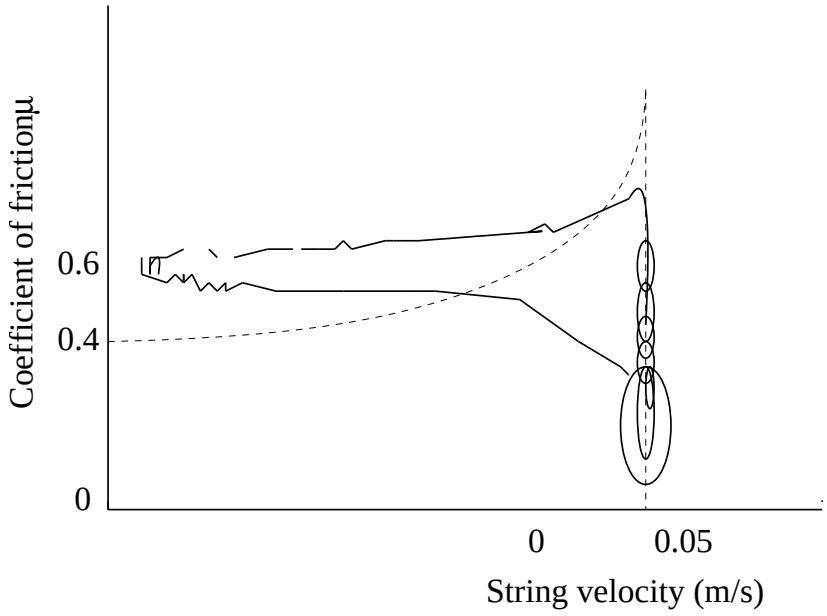

Figure 3.12: *Solid curve: coefficient of friction between two rosin coated surfaces, adapted from [112]. Dashed line: steady state relationship.*

In [112] it has been suggested that friction depends on the variations of temperature in the interfacial rosin layer. The explanations for this behavior are as follows: during sticking the contact region cools by heat conduction into the bulk materials behind the contact. This allows the shear strength of the interface and the friction coefficient to reach a high value. Once sliding begins, the contact region is heated by the work done against friction, the rosin layer weakens and the friction coefficient falls.

In order to model this behavior, let's consider T as an "average" contact temperature, a circular contact of radius a and an uniform layer thickness δ. The friction force can be expressed as

$$f = F_N \mu(T) \text{sgn}(v_b - v) \tag{3.25}$$

where F_N is the normal bow force, v_b is the bow velocity, v is the string velocity and $\mu(T)$ is the temperature dependent friction coefficient plotted in Fig. 3.13. This model

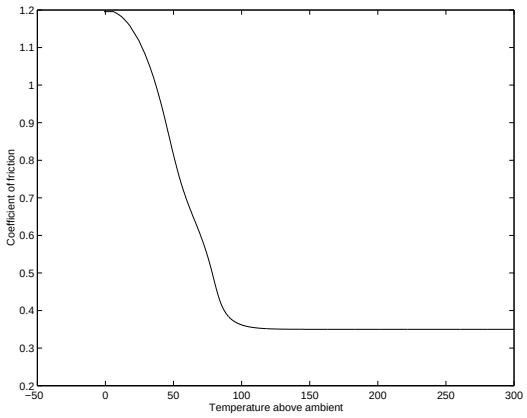

Figure 3.13: *Coefficient of friction as a function of contact temperature (in Celsius above ambient), assuming a normal force of* $3N$ *and a contact radius of 0.5 mm. Courtesy of Jim Woodhouse.*

behaves better than the "classic" models [106]. Moreover, further investigations on reconstructing the bowing point friction force [138], confirm the fact that friction does not depend only on the relative bow string velocity. Measuring the force at the two extremes of the string using force transducers, it is possible to reconstruct the force at the bowing point and observe the same hysteresis loop obtained by using the two

coated cylinders.

3.7.3 The bow hair compliance

Another element that seems to have a strong effect on the frictional interaction between a bow and a string is bow hair compliance.

The bow hair-compliance was investigated by Raman [90], who stated that, while it is possible for a single point on the string to have absolutely the same velocity as the bow in every part of its forward motion, kinematical theory shows that it is not possible for every element on a finite region to have absolutely the same velocity as the bow in every part of its forward motion.

The first line of evidence comes from analyzing experimental results presented by Cremer [21] of the reflection and transmission behavior of transverse waves on a string incident on a bow at rest. The second line of evidence comes from simulations of the bowed string taking into account the finite width of the bow. The nature of the "differential slipping" which may arise due to the kinematic incompatibility of uniform bow velocity across the width of the bow and the string velocity in standard bowed string motion (Helmholtz motion) is strongly dependent on bow hair compliance. Simulations also demonstrate that suitable tilting of the bow can reduce the extent to which "differential slipping" is detrimental to the establishment of the desired string motion. The incompatibility of finite width and idealized Helmholtz motion is shown in Fig. 3.14, borrowed from [70].

In position 1, the Helmholtz corner has just travelled past the bow from left to right. While the entire section of the string under the bow sticks to the bow-hair, it is carried forward parallel to its initial position, leading to position 2. The displacement of the string force by the finite width of the bow is in disagreement with the ideal Helmholtz motion, in which the shape of the string consists only of two straight lines.

As explained in [70], the the finite width of the bow creates a phenomenon called *differential slipping*, in which the string occasionally slips at one side of the bow continuing to stick at the other side.

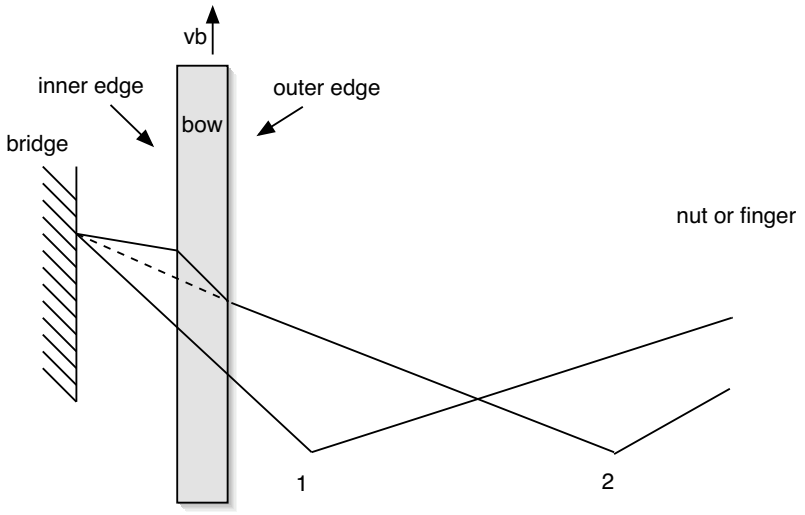

Figure 3.14: *Incompatibility between the ideal Helmholtz motion and the finite width of the bow, from [70].*

Pitteroff [87] proposes an accurate yet efficient model of the bow hair compliance, using a velocity dependent friction model.

A still unexplored result in bowed string synthesis is the combination of the plastic friction model with accurate models of the bow hair compliance. Combining these two refinements should provide a bowed string model that reproduces with a larger accuracy the behavior of real instruments.

3.8 Modeling the body of the instrument

As mentioned before, an important element of a violin is its body, which filters vibrations that propagate from the string through the bridge. In real-time synthesis of a violin, there is some difficulty in modeling the body because of a tradeoff between accuracy and computational cost. If all the resonances of the body are accounted for by modeling each one with its own pair of filter poles, the computational cost is too high. On the other hand, one cannot implement too few filter poles and neglect the large number of resonances, because the complex filtering of the body contributes strongly to the characteristic timbre of the violin.

3.8.1 Previous research on body models

Electronic simulation of body's resonances

In [69] Mathews and Kohut proposed a technique to simulate electronically the body resonances of a violin. The authors used twenty resonant circuits in parallel, tuned to the main resonances of the violin body. Using this setup, they made some interesting discoveries concerning the body of a violin:

- The peak frequencies must be irregularly spaced with respect to the harmonic frequencies of any violin tone.
- The Q factors of the resonances must be sufficiently large so that the response curve is steep almost everywhere.
- The peaks must be sufficiently closed together so the depth of the intervening valleys does not exceed about 15 dB.

Mathews and Kohut claimed that a violin tone can be achieved with 20 or 30 resonances distributed either randomly or exponentially over the frequency range 200-5000 Hz. Small damping gave unresponsive sound, while too high damping gave an hollow and uneven tone, in which some pitches were stronger than others.

Commuted synthesis

An efficient implementation of the body in a synthesis model can be based on a technique called commuted synthesis [122, 59]. In the commuted synthesis approach, the body response is read from a wavetable and injected into a waveguide string as the excitation source. Commuted waveguide synthesis is an efficient yet high quality synthesis technique which avoids explicit modeling of the violin body. The idea behind commuted synthesis is the following. In the real acoustic world, the string of a violin couples via the bridge into a resonating body, which imposes a frequency response of its own to the radiated sound. This situation is shown in Fig. 3.15, part a).

Since the string and the body constitute a linear system, they can be commuted as shown in Fig. 3.15, part b). Moreover, the body and the excitation can be combined

in a single excitation unit, for computational purposes. This means that the string is fed with the traditional excitation combined with the impulse response representing the body resonances.

There are various ways of combining the body excitation into the system. Morever the low frequencies least damped modes can be factored out using, for example, second order filters. This is useful to reduce the length of the excitation table and to achieve interesting effects with the parametric modes [114].

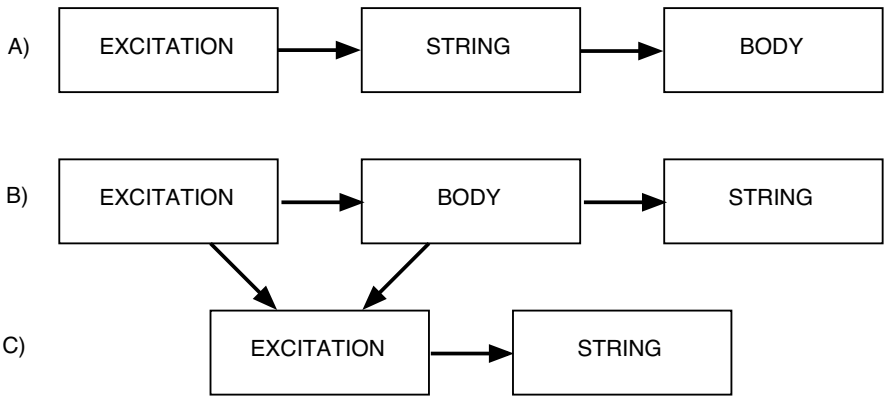

Figure 3.15: *The commuted synthesis approach. A) The excitation is fed through the strings and then through the body. B) By using the linearity of the system, string and body are commuted. C) The excitation and the body are combined together creating the final excitation of the system.*

The basic commuted synthesis solution is applicable only to linear, time-invariant (LTI) systems, such as plucked and struck strings. In the case of a bowed violin, the nonlinearity of the bow/string interaction does not allow this method to be used in a precise way, although approximations are possible [52].

Since the computational power of computers in constantly strongly increasing, it is possible to adopt other techniques which explicitly model the instruments' body, instead of sampling. In the following chapter different approaches to model a violin body based on the waveguide mesh are proposed.

Chapter 4

Computational models for bowed strings

In the previous chapter the acoustics of bowed string instruments was described, and on overview of the bowed string models proposed in the literature was presented.

In this chapter an efficient yet accurate model of a bowed string is proposed. Starting by discretizing the ideal wave equation, different solutions for solving the interaction between a bow and a string are proposed. Sec. 4.1 describes the technique adopted to design filters for different violin strings; Sec. 4.3 proposes a basic bowed string physical model, Sec. 4.4 describes how to improve the model, Sec. 4.5 proposes models to account for the finite width of the bow, and Sec. 4.6 describes how to model the body of the instrument.

4.1 Measuring Decay Times in Pizzicato Recordings

As a first step, plucked violin strings were simulated. In an anechoic room, the four violin strings were recorded while plucked at five different positions placed at equal distance along the fingerboard. The energy decay relief (EDR) was calculated.

The EDR at time t and frequency ω is defined as the sum of all remaining energy

at that frequency from time t to infinity. It is a frequency-dependent generalization of Schroeder's Energy Decay Curve [57].

More precisely, the EDR is given by

$$EDR(t_n, f_k) = \sum_{m=n}^{M} |H(m,k)|^2, \tag{4.1}$$

where $H(m,k)$ denotes bin k of the Short-Time Fourier Transform (STFT) at time-frame m, and M denotes the total number of time frames. An example of EDR for the violin D string ($f_0 = 196$ Hz) is shown in Fig. 4.1, while the summed EDR, obtained by summing power within bands, is shown in Fig. 4.2. The analysis was performed using a FFT of 2048 points, with a Hanning window and no overlap. As a comparison, Fig. 4.3 shows the EDR for a violin D string using the same parameters as before, but damping the fingerboard side. Notice how the higher damping is clearly visible in the resulting EDR. For each string, lowpass filters were estimated [1], which

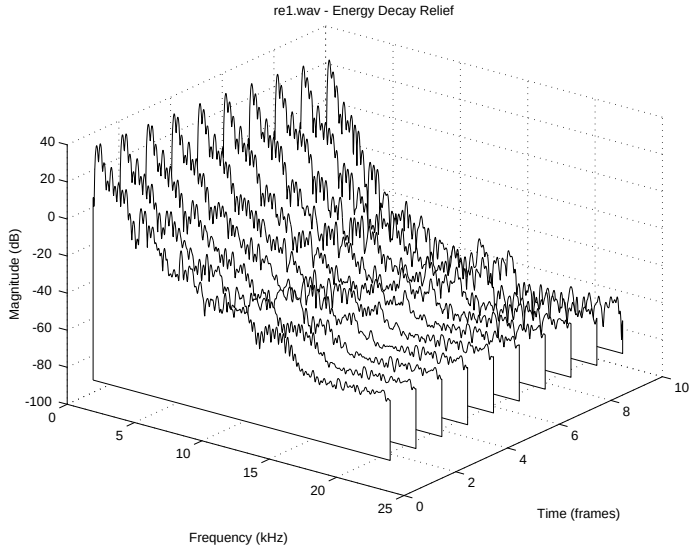

Figure 4.1: *EDR for the violin D string, without finger for damping the fingerboard side.*

matched the corresponding EDR. A different starting point to estimate low-pass filters

[1]The estimation of the lowpass filter was performed using the Matlab function invfreqz.

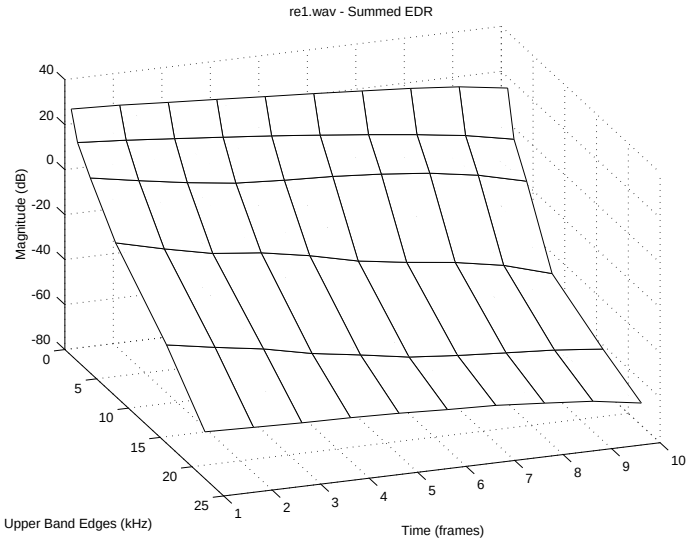

Figure 4.2: *Summed EDR for the violin D string, without finger for damping the fingerboard side.*

which simulate losses is the assumption of constant-Q reflection functions at the two extremities. This approach is described in Sec. 4.3.

4.2 Accounting for bending stiffness

. When an ideal string such as the one introduced in Eq. (3.4) is bowed, a sawtooth waveform with a sharp corner is produced. This waveform is known as the ideal Helmholtz motion. In reality, strings are not perfectly flexible, but they exhibit a certain amount of stiffness. This is expressed by adding a fourth order term to Eq. (3.4). Eq. (3.4), in fact, is a simplification of the following equation for a lossless stiff string:

$$m\frac{\partial^2 y(x,t)}{\partial t^2} - T\frac{\partial^2 y(x,t)}{x^2} + B\frac{\partial^4 y(x,t)}{x^4} = 0 \tag{4.2}$$

where $B = (\pi/\kappa L)^2$ is the bending stiffness, $\kappa = (T/EI)^{1/2}$, E is the Young modulus, I is the second moment of area. Partial solutions of this equation are plane waves of the form:

$$y(x,t) = Ae^{j(\omega t + kx)} \tag{4.3}$$

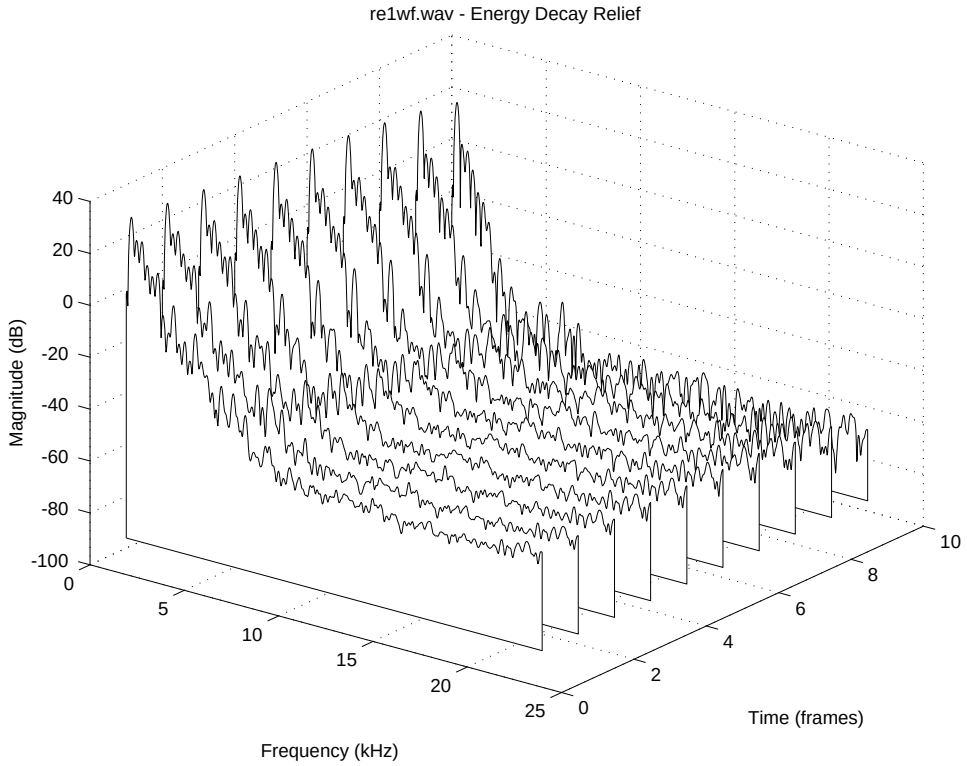

Figure 4.3: *EDR for the violin D string, with a finger damping the fingerboard side.*

in case the dispersion relation

$$\omega = c_t k \sqrt{1 + (k/\kappa)^2} \tag{4.4}$$

is satisfied, where ω is the angular frequency. Since the string is attached at both ends, k, the wave number, can take only the discrete values $k_n = n\pi/L$. The frequency of the wave vibrations is therefore discretized as [32]

$$\omega_n = n\omega_c \sqrt{1 + Bn^2} \tag{4.5}$$

for $n = 1, 2 \ldots$, where $B = (\pi/\kappa L)^2$ denotes the inharmonicity factor of the string and $\omega_c = \pi c_t / L$ is the fundamental frequency in case of no stiffness.

The relationship in Eq. (4.5) states that the modes of transversal vibration are not in harmonic frequency ratio. An example of this situation is shown in Fig. 4.5. In it,

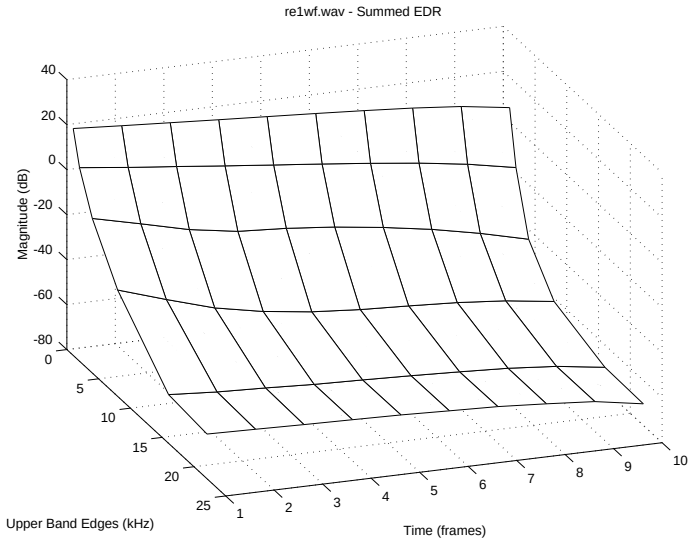

Figure 4.4: *Summed EDR for the violin D string, with finger damping the fingerboard side.*

the location of the partials of a cello D string with fundamental frequency $f_0 = 147$ Hz and inharmonicity factor $B = 0.0004$ is compared to the location of the partials of the same string with $B = 0$. Notice how, according to Eq. (4.5), the shift increases at higher frequencies.

Designing allpass filters for dispersion simulation

In order to model dispersion a numerical filter made of a delay line $q^{\tau-\tau_0}$, and a n-order stable all-pass filter $H(q) = q^{-n}P(q^{-1})/P(q)$ is considered, where $P(q) = p_0 + \ldots + p_{n-1}q^{n-1} + q^n$, and τ and n are appropriately chosen.

As proposed in [66], the goal is to minimize the ∞-norm of a particular frequency weighting of the error between the internal loop phase and its approximation by the filter cascade:

$$\delta_D = \min_{p_1,\ldots,p_m} \|W_D(\Omega)[\varphi_d(\Omega) - (\varphi_D(\Omega) + \tau\Omega)]\|_\infty$$

where $\varphi_D(\Omega)$ is the phase of $H(e^{j\Omega})$, and $W_D(\Omega)$ is the frequency weighting. The

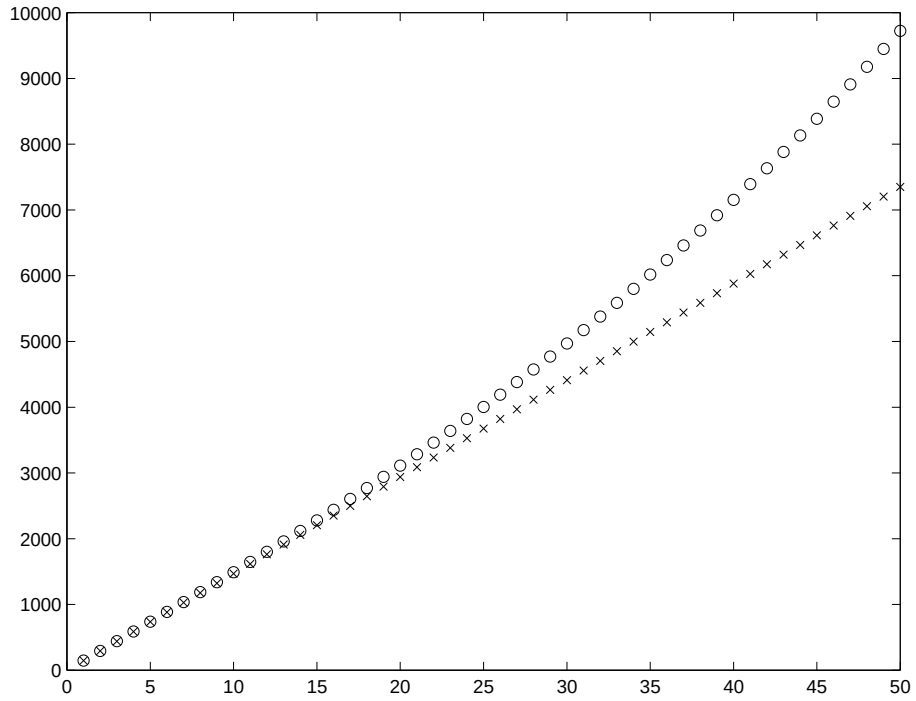

Figure 4.5: *Shift of partials for a stiff string (∘) with $f_0 = 147$ Hz, $B = 4e^{-4}$, versus a non stiff string ($B = 0$) (x). Horizontal axis: partial number. Vertical axis: frequency (Hz).*

following weighting function is chosen:

$$W_D = \frac{1}{\Delta\phi_i} \Big/ \omega_i \tag{4.6}$$

where ϕ_i is the prescribed loop phase response at frequency ω_i. Moreover, $W_D(\Omega)$ is zero outside the frequency range, i.e., $[\Omega_c, \Omega_N]$.

From an acoustical point of view, it is important to have a frequency weighting that approximates the way the auditory system perceives the difference between original and simulated phase dispersion.

Järveläinen et at. [56] conducted listening tests in order to find out the audibility of inharmonicity in string instruments. The threshold of audibility of inharmonicity was measured as a function of the inharmonicity coefficient B. Results showed that

the detection of inharmonicity is strongly dependent on the fundamental frequency.

Fig. 4.6 shows the frequency error in cents for the cello D string ($f_0 = 147$ Hz). Inharmonicity was simulated by using three 4-th order allpass filters in cascade, at a sampling rate $F_s = 44100$ Hz. Notice the small error of the approximation up to about 5000 Hz.

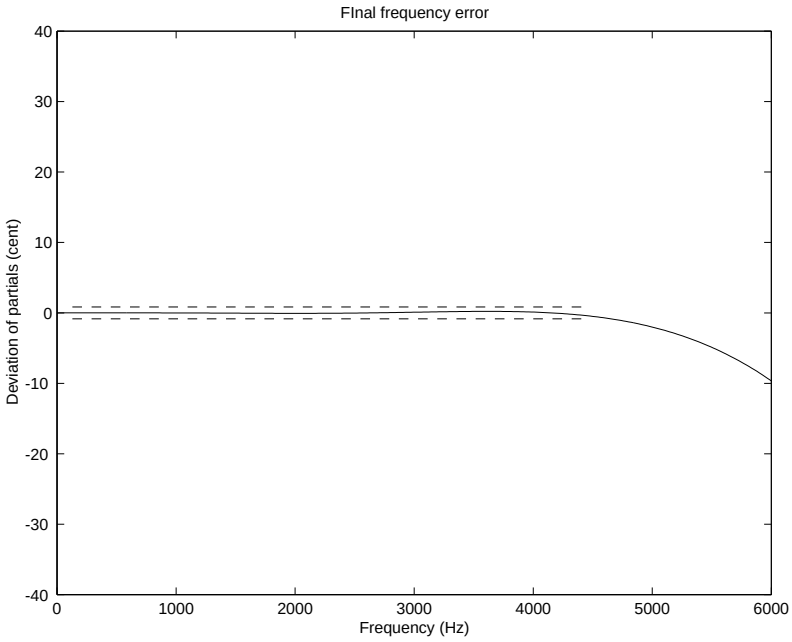

Figure 4.6: *Result of the filter design example for a cello D string ($f_0 = 147$ Hz), $F_s = 44100$ Hz, using three 4-th order filters in cascade. Notice how the approximation is precise up to 5000 Hz.*

Fig. 4.7 shows the result of simulating the impulse response of a cello D string with and without stiffness. Notice how the effect of stiffness is clearly visible. Fig. 4.8 shows mode number versus frequency over mode number for the first 25 partials of a cello D string. The circles represent the ideal location of the partials; the plus signes represent the location of the partials according to the technique suggested by Woodhouse in [134], and the stars represent the location of the partials which results by simulating dispersion using three 4-th order alpass filters in cascade, estimated

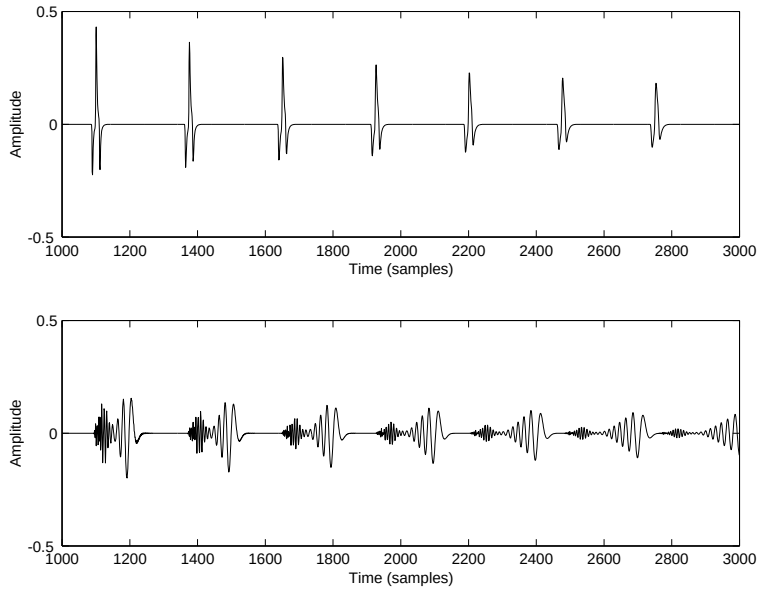

Figure 4.7: *Impulse response of a cello D string. Top:* $B = 0$*, bottom:* $B = 4e^{-4}$*. Notice how stiffness breaks the regularity of the impulse response.*

using the technique described in Sec. 4.2. Notice how there is a good agreement between ideal location and location obtained with the simulations. For each mode number, the relative error (frequency/mode number) is only 1 Hz, which is not perceivable. The computational cost of the technique described in this chapter is lower that the cost of the technique described in [134], and therefore suitable for a real-time implementation.

In this section a stiff cello D string has been simulated. In the following sections different friction models are applied to the same string.

4.3 A basic bowed string physical model

In order to simulate the action of a bow rubbing a string, an hyperbolic model for the coefficient of bow-string friction is chosen, given by

$$\mu = \mu_{\mathrm{d}} + \frac{(\mu_{\mathrm{s}} - \mu_{\mathrm{d}})v_0}{v_0 + v - v_{\mathrm{b}}} \tag{4.7}$$

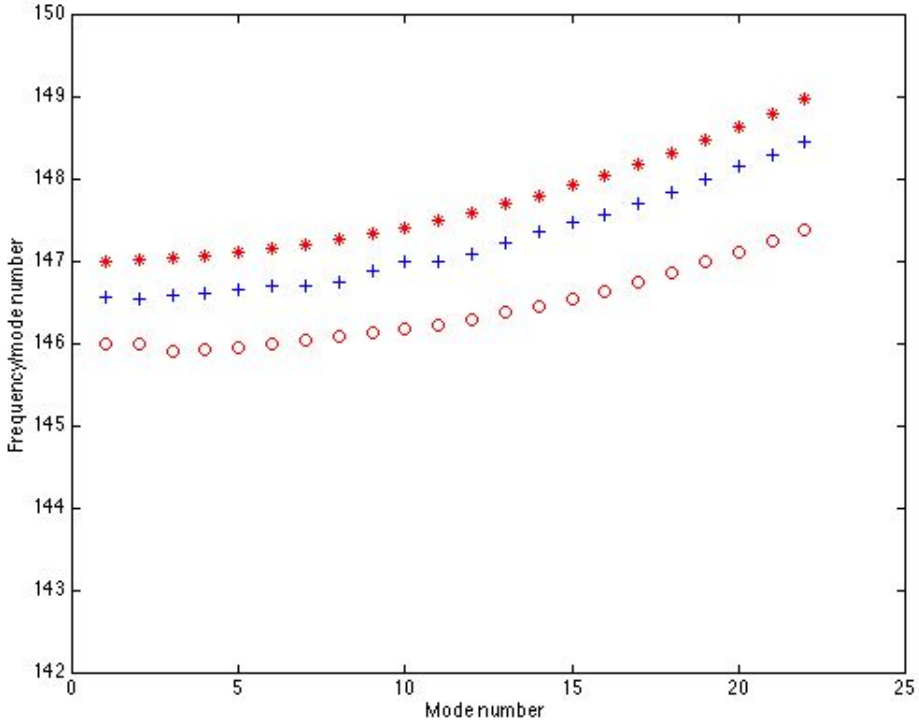

Figure 4.8: *Mode number versus frequency over mode number for the cello D string. o= desired location of the partials, += location according to the technique described in [134], *= location using the technique described in Sec. 4.2. Notice how there is a good match between desired location and the two techniques.*

where v, v_b and v_0 are the string velocity, bow velocity and initial bow velocity, respectively, and μ_d and μ_s are the dynamic and static coefficients of friction, respectively. For a bow interacting with a string, $\mu_d = 0.3$ and $\mu_s = 0.8$. Using such parameters, the shape of μ is shown in Fig. 4.9. This model has been used for many years as a convenient mathematical approximation which yields closed-form results for the bow-string interaction [72, 71, 134]. The hyperbolic friction model is coupled to a waveguide string model as described in Sec. 3.7 and represented in Fig. 4.10.

In it, v_{ob} and v_{on} represent the outgoing traveling waves from the bow point, propagating toward the bridge and nut respectively. Traveling waves are filtered by the

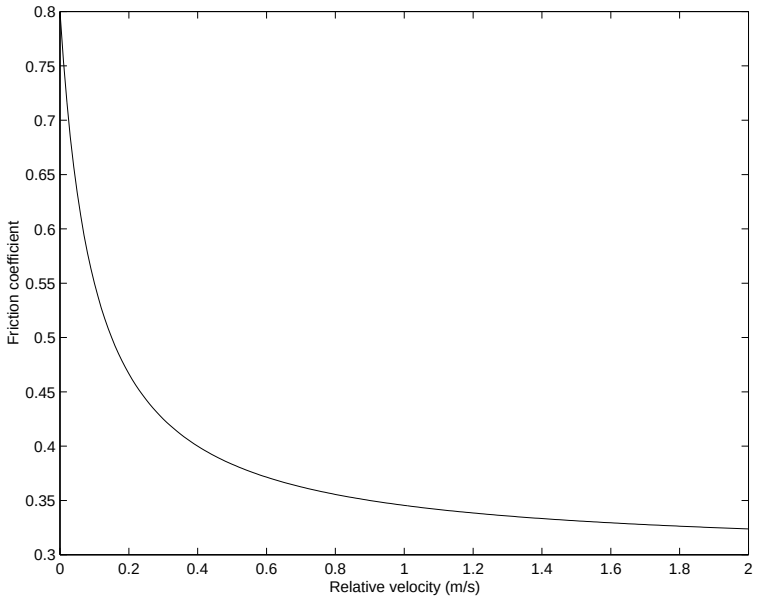

Figure 4.9: *The hyperbolic friction model. Horizontal axis: relative bow-string velocity. Vertical axis: coefficient of friction.*

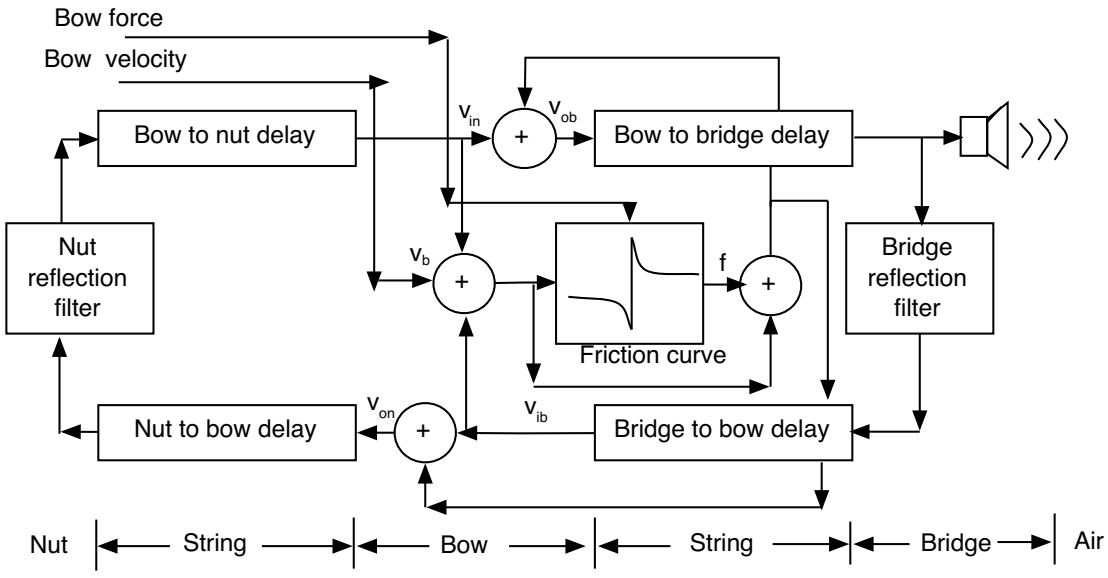

Figure 4.10: *Block diagram of a basic bowed string physical model which uses an hyperbolic friction model.*

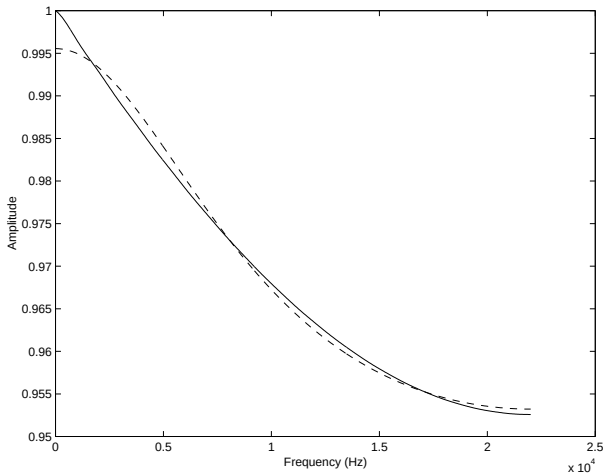

Figure 4.11: *Frequency response of the reflection filters at the bridge side for a cello D string. Solid line: frequency response obtained using a 600 points FIR filter ($F_s = 44.1$ kHz), using the technique described in [134]. Dotted lines: frequency response of the estimated second order low-pass IIR filters.*

bridge and nut reflection filters, which lump losses along the string and at the two extremities. For computational efficiency, the reflection functions described in [134], are represented by using second order low-pass filters, estimated using the **invfreqz** function provided by Matlab. More precisely, assuming an average Q factor for transversal modes of 500, reflection FIR filters for the bridge and nut side can be calculated, using the technique described in [134]. The frequency response of the reflection FIR filters is calculated, and second order IIR filters which best approximate such frequency response are calculated by using the **invfreqz** function provided by Matlab.

Fig. 4.11 shows the frequency response of the reflection filters at the bridge side for a cello D string. The solid line represents the frequency response obtained using an FIR filter with 600 coefficients at a sampling rate $F_s = 44.1$ kHz, calculated using the technique described in [134]. The dotted line represents the frequency response of the estimated second order low-pass filters. Notice how the low-pass filter provides a good approximation of the FIR filter, and is at the same time efficient enough to be used in a real-time implementation of a bowed string synthesizer.

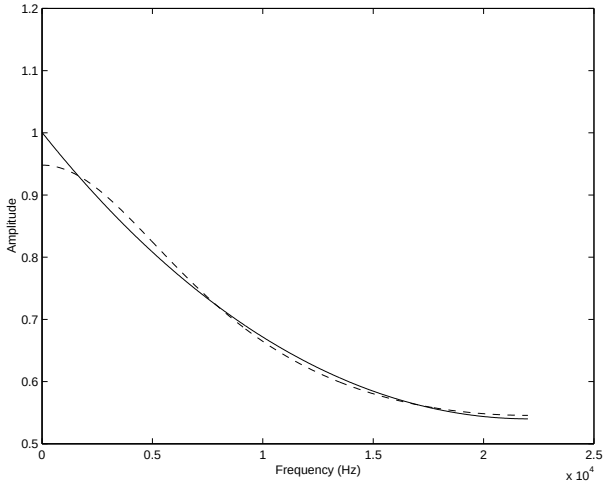

Figure 4.12: *Frequency response of the reflection filters at the nut side for a cello D string. Solid line: frequency response using the reflection filters described in [134], dotted lines: frequency response of the estimated second order low-pass filters.*

Fig. 4.12 shows the frequency response of the reflection filters at the nut side for a cello D string. As in Fig. 4.11, the solid line represents the frequency response obtained by using the FIR filters described in [134], while the dotted line represents the estimated second order IIR filters. Notice how the second order IIR filter matches closely the frequency response of the FIR filter.

4.4 Improving the model

4.4.1 Accounting for torsional waves

A first improvement in modeling the string resonator consists of accounting for torsional waves. It is well known that string losses are required for stability of the Helmholtz motion [34, 135, 100]. The transduction of transverse waves into (more highly damped) torsional waves represents a significant loss on the string. The most intuitive way to account for torsional waves is by adding an additional pair of delay

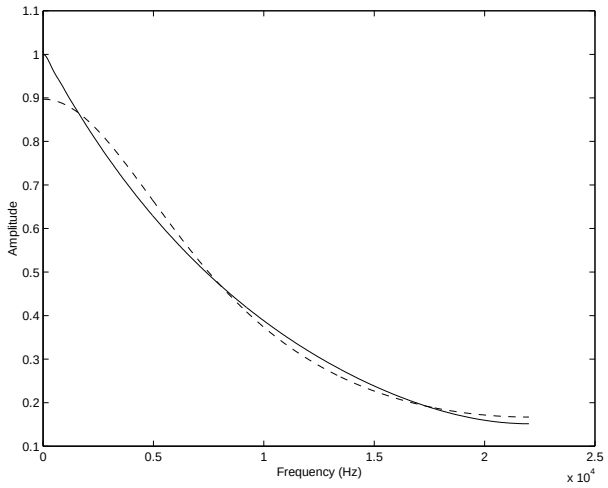

Figure 4.13: *Frequency response of the reflection filters at the fingerboard side for a cello D string, torsional waves. Solid line: frequency response using the reflection filters described in [134], dotted lines: frequency response of the second order low-pass filters.*

lines travelling in the same way as transversal waves but about 5.2 times faster. Reflection functions for torsional waves are calculated with the same technique used for transversal waves. In this case, the average Q factor for torsional modes is 45 [137]. The frequency responses for the finger and bridge side of the reflection functions for torsional waves are shown in Fig. 4.13 and Fig. 4.14 respectively. As before, the FIR filters proposed in [134] have been approximated by using second order low-pass IIR filters. Notice how, as it was the case for transversal waves, the approximation provides satisfactory results.

The structure of the model that accounts for torsional waves is shown in Fig. 4.15. Compared to Fig. 4.10, the model presents two additional pair of delay lines containing torsional traveling waves toward the nut and the bridge. Transversal and torsional waves are summed at the bow point where, as before, the coupling between the bow and the string is solved.

It is also natural to ask whether the basic model might be improved by including only the (real) losses corresponding to torsion-wave creation, since this costs little or nothing extra in the simulation. In other words, the model generates torsion

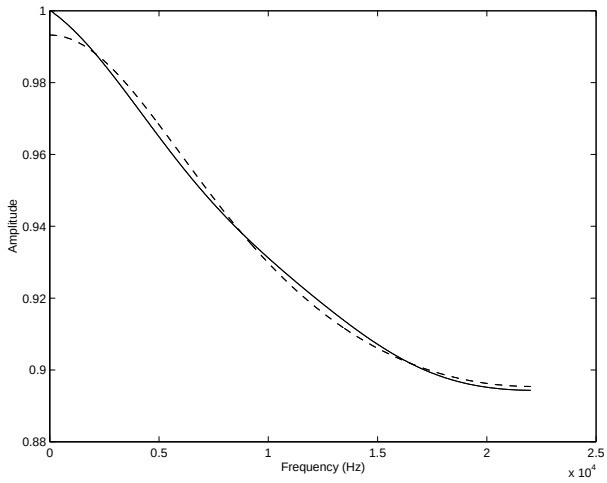

Figure 4.14: *Frequency response of the reflection filters at the bridge side for a cello D string, torsional waves. Solid line: frequency response using the reflection filters described in [134], dotted lines: frequency response of the second order low-pass filters.*

waves realistically, but they are treated as if they are fully absorbed by the string terminations. This simplified torsion-wave simulation was suggested as a possibility in [21], implemented in [71] and investigated in [106].

4.4.2 Accounting for string stiffness

As a further improvement, allpass filters were added, which accounted for the string bending stiffness, as described in the previous section. The bowed string physical model that accounts for string stiffness is represented in Fig. 4.16. The three allpass filters in cascade are added to the trasversal waves in the delay lines on the nut side.

This model is able to simulate the rounding off of the idealized waveform by introducing more dissipative terms and dispersive terms. Fig. 4.17 and Fig. 4.18 illustrate this situation. Fig. 4.17 displays the time domain waveform of a bowed cello D string without bending stiffness, bowed with a constant bow velocity $v_b = 0.05$ m/s, bow force $f_b = 0.3162$ N and normalized bow position $\beta = 0.07$. The waveforms were

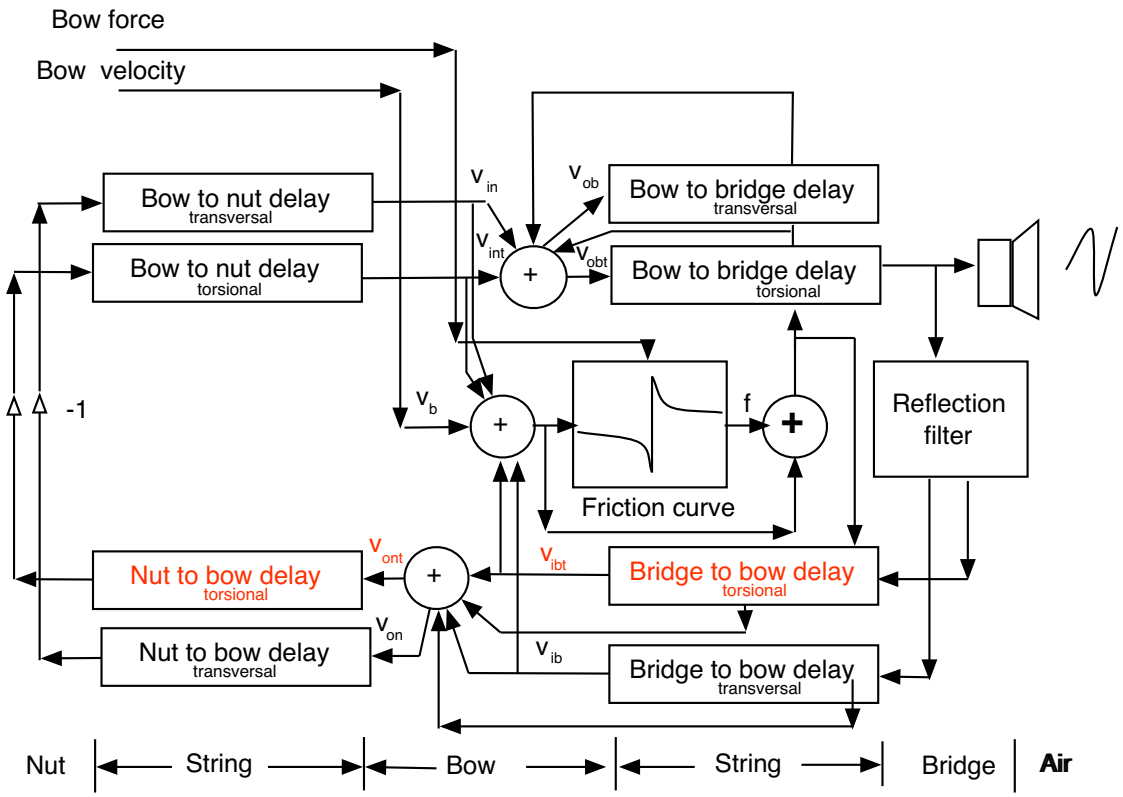

Figure 4.15: *Structure of a bowed string model that accounts for torsional waves.*

captured at the bow point (top) and at the bridge point (bottom) after steady state motion was achieved. Notice the regularity of the Helmholtz motion. Fig. 4.18 shows the time domain waveforms of a string with bending stiffness $B = 4e^{-4}$, bowed with the same parameters as the string captured in Fig. 4.17. Notice how the Helmholtz motion is not as precisely defined as before. This difference is also perceivable while listening to the two waveforms, especially in the attack portion, which is shown in Fig. 4.19. The attack in the stiff string results in a noisier and longer, which is noticeable also visually. From a perceptual point of view, however, the noisier attack makes the resulting synthetic string less *artificial* and more *realistic*.

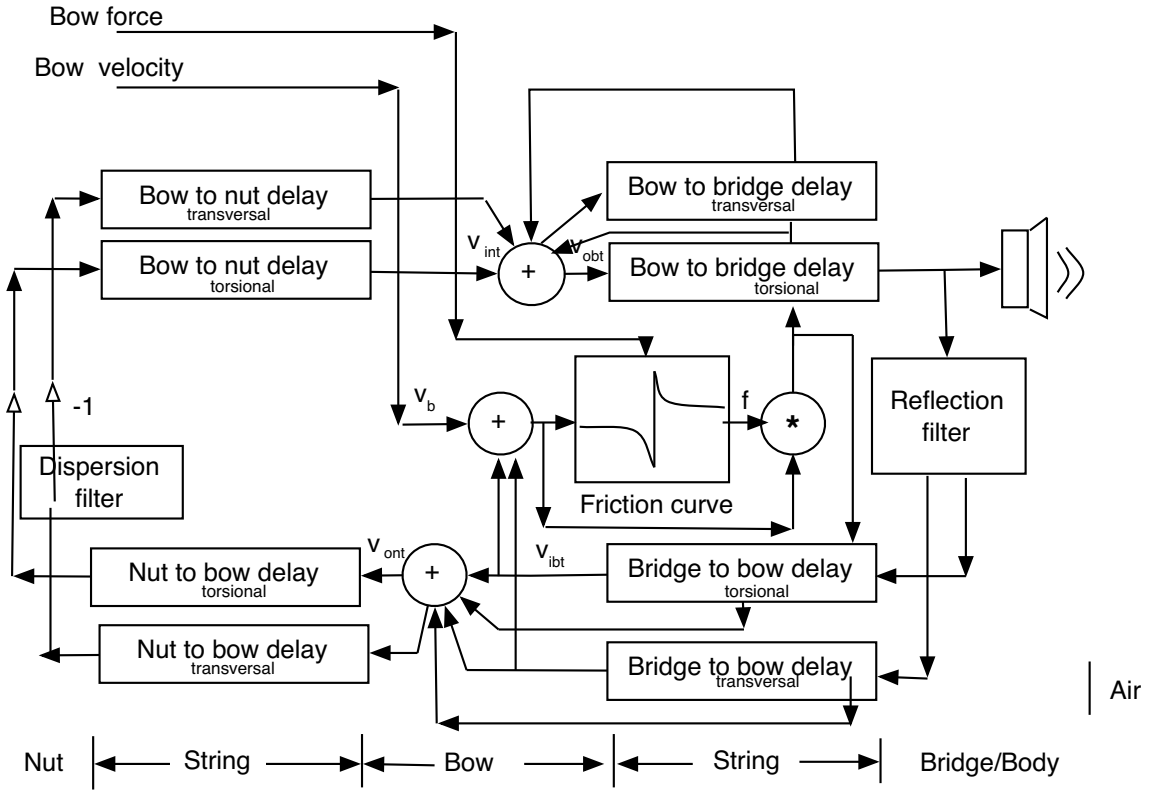

Figure 4.16: *Block diagram of a digital waveguide model of a bowed string including allpass filters for stiffness simulation.*

4.4.3 Improving the friction model

A further improvement consists of refining the friction model. Smith and Woodhouse [112] noticed that at the bow point an hysteresis loop in the velocity versus friction plot is noticeable. This loop is not taken into account by the velocity dependent friction models. They assumed that friction depends also on the temperature of the contact point.

They therefore proposed a plastic friction model given by:

$$\mu = \frac{Ak_y(T)}{N}\mathrm{sgn}(v) \tag{4.8}$$

where A is the contact area between the bow and the string, N is the normal load,

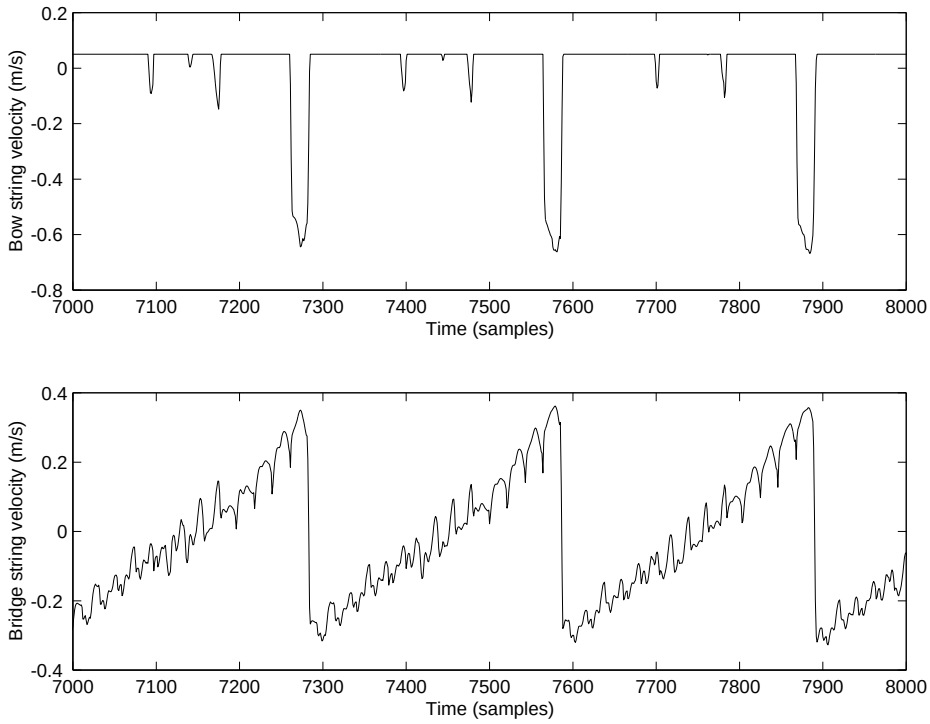

Figure 4.17: *Time domain waveforms of the basic bowed string physical model that does not account for stiffness and torsional waves. Top: string velocity at the bow point, bottom: string velocity at the bridge.*

and $k_y(T)$ is the shear yield stress as a function of temperature T. The temperature T of the shearing rosin layer can be estimated from the current sliding velocity v by passing it through an appropriate linear filter [112]. Here, the rosin is modeled as exhibiting "plastic" deformations at the bow-string contact. Such thermal friction model is calibrated so that under steady sliding conditions it matches the double exponential friction model. Since there is a time delay associated with heat flow, the plastic model exhibits *hysteresis*, unlike the other two friction models.

An example of the behavior of the plastic model is shown in Fig. 4.20. The simulations were obtained using the same cello D string as before, bowed at bow velocity $v_b = 0.05$ m/s and bow force $f_b = 0.2$ N. The top of Fig. 4.20 shows the time domain waveform at the bow point, after steady-state is achieved. The bottom shows the friction versus velocity plot. Notice the hysteresis loop. This loop does not

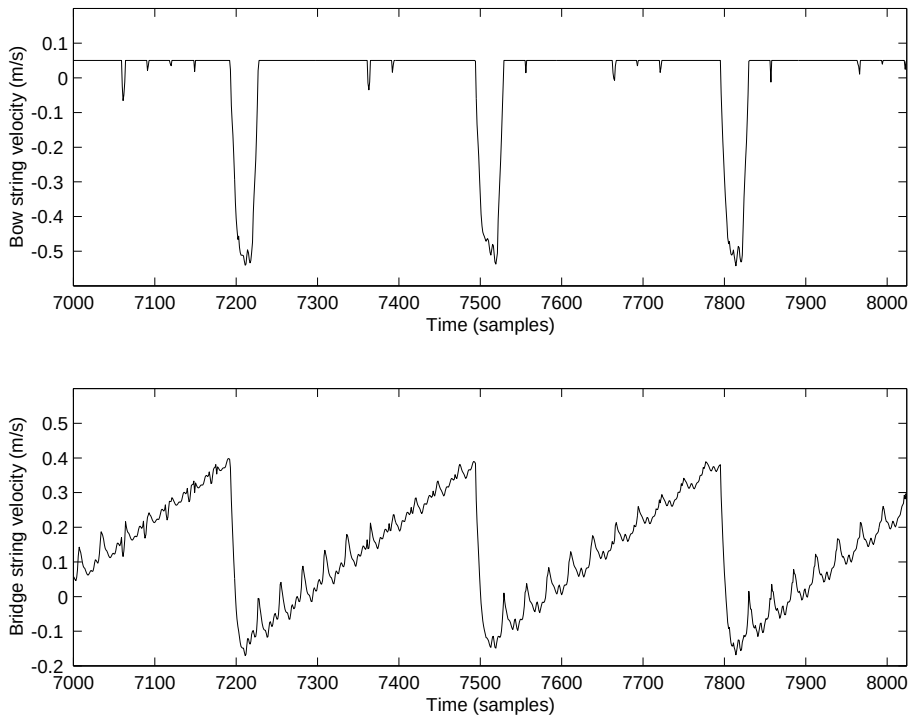

Figure 4.18: *Time domain waveforms of the basic physical model that accounts for stiffness. Top: string velocity at the bow point, bottom: string velocity at the bridge.*

correspond to the classic velocity dependent friction curve, represented in the figure by the double-exponential friction model described in Chapter 2. In Chapter 6 it is show how the plastic model improves the playability of the bowed string physical model.

4.4.4 The elasto-plastic model

In Chapter 2 the elasto-plastic friction model was introduced as one of the latest developments of dynamic friction models, in which the dependence of friction on the relative velocity between two objects in contact is expressed through a differential equation. In this section the elasto-plastic model is applied to the simulation of a bowed string, and compared to the plastic model. For steady-state, the friction curves

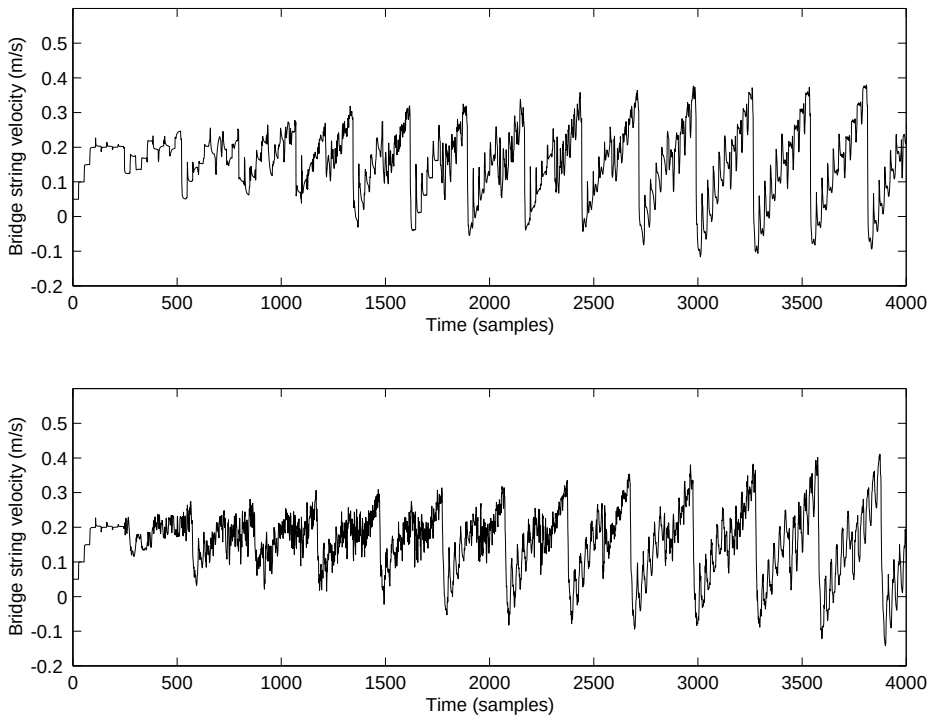

Figure 4.19: *Transient behavior of the basic physical model. The string is started from rest and excited with a constant bow velocity $v_b = 0.05$ m/s, bow force $f_b = 0.3162$ N and at a normalized bow position $\beta = 0.07$. Top: model with no stiffness, bottom: model with stiffness.*

represented in Fig. 4.21 are considered. More precisely, Fig. 4.21 shows the steady-state friction function used in [24] (solid line) and the double exponential steady-state function of Smith and Woodhouse [112].

The same waveguide resonator as before is coupled to the elasto-plastic model. Using the elasto-plastic model as the coupling mechanism between the bow and the string, the resulting system of equations for the bow becomes

$$\begin{cases} \ddot{x}_i^{(b)} + g_i^{(b)}\dot{x}_i^{(b)} + \left[\omega_i^{(b)}\right]^2 x_i^{(b)} = \dfrac{1}{m_{il}^{(b)}}(f_e^{(b)} + f) \quad , \quad (i = 1 \dots N^{(b)}) \\ \dot{z}(v,z) = v\left[1 - \alpha(z,v)\dfrac{z}{z_{ss}(v)}\right] \\ f = \sigma_0 z + \sigma_1 \dot{z} + \sigma_2 v + \sigma_3 w \quad \text{(friction force)} \end{cases} , \qquad (4.9)$$

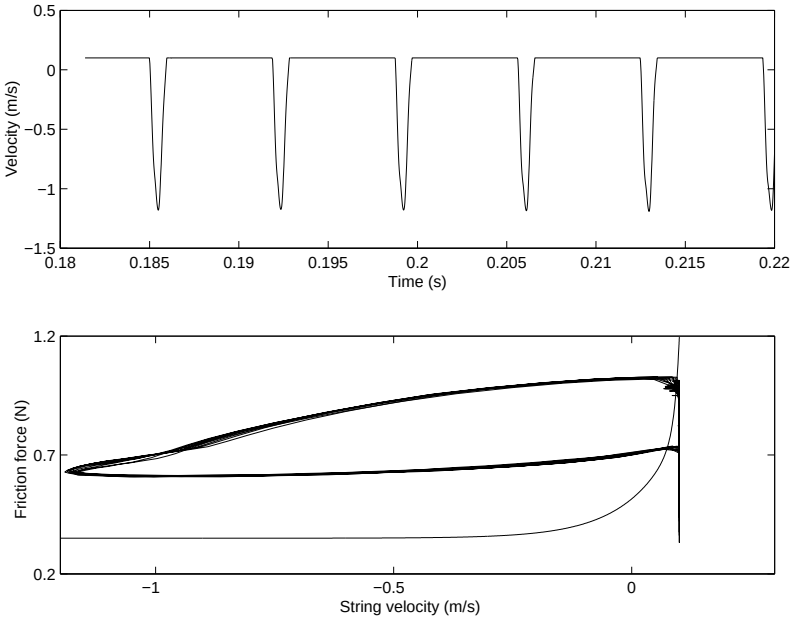

Figure 4.20: *Simulations using the plastic model. Top: string velocity at the bow point. Bottom: friction versus velocity. Notice how the plastic model produces an hysteresis loop which does not follow the traditional velocity-dependent friction model (represented in the figure by the decaying exponential in the bottom part).*

where for clarity the superscript (b) stands for "bow". The x variables represent the modal displacements for the bow, while z is the mean bristle displacement. The terms $f_e^{(b)}$ represents external forces, while the integers $N^{(b)}$ are the number of modes for the bow.

This system of equations is discretized by using the bilinear transform. Details about the discretization are described in Appendix B.

Notice how a delay-free loop appears when coupling the excitation to the resonator. This is solved by using the K-method [10], as described in Appendix B. The current $\dot{z}$ value is computed with the Newton-Raphson algorithm. Experimentally, a maximum of seven iterations is enough to achieve convergence; this allows an efficient real-time implementation.

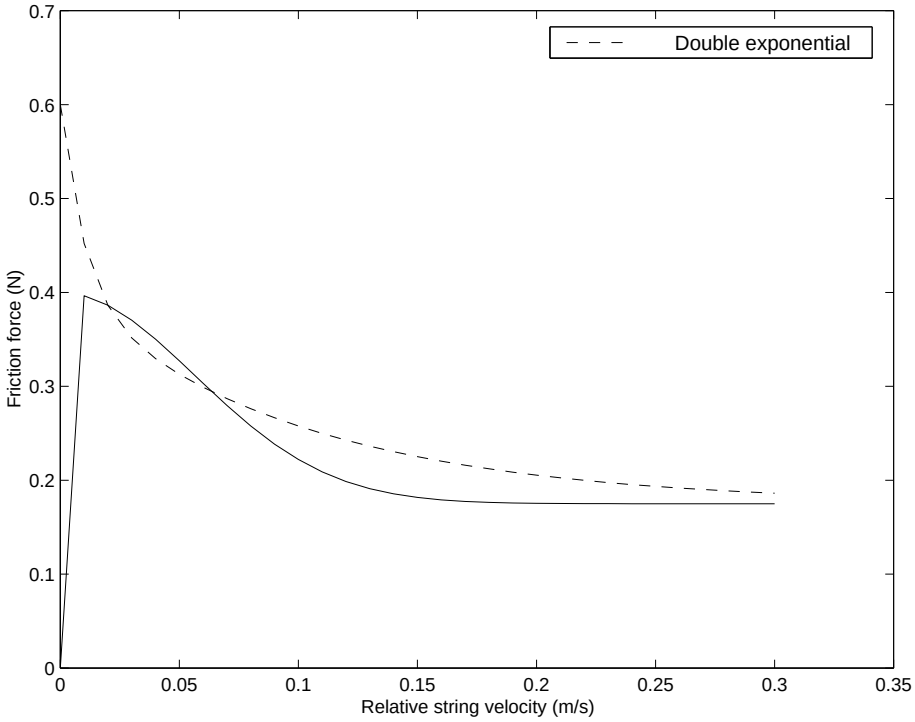

Figure 4.21: *Dotted line: double exponential friction model. Solid line: friction model of Eq. 2.14.*

About the control parameters

Since the main interest of this study is the generation of computer models which provide real-time virtual instruments with interesting musical possibilities, motivated in a general way by physical models, there is a need to describe how the physical parameters of the model have been related to high-level control parameters.

The first step consists on mapping two high-level control parameters commonly used in physical models of bowed strings, i.e., the steady-state bow velocity v_b and the normal force f_b.

The physical parameter space of the elasto-plastic model is given by the set $(f_c, f_s, v_s, \sigma_0, \sigma_1, \sigma_2, z_{ba})$.

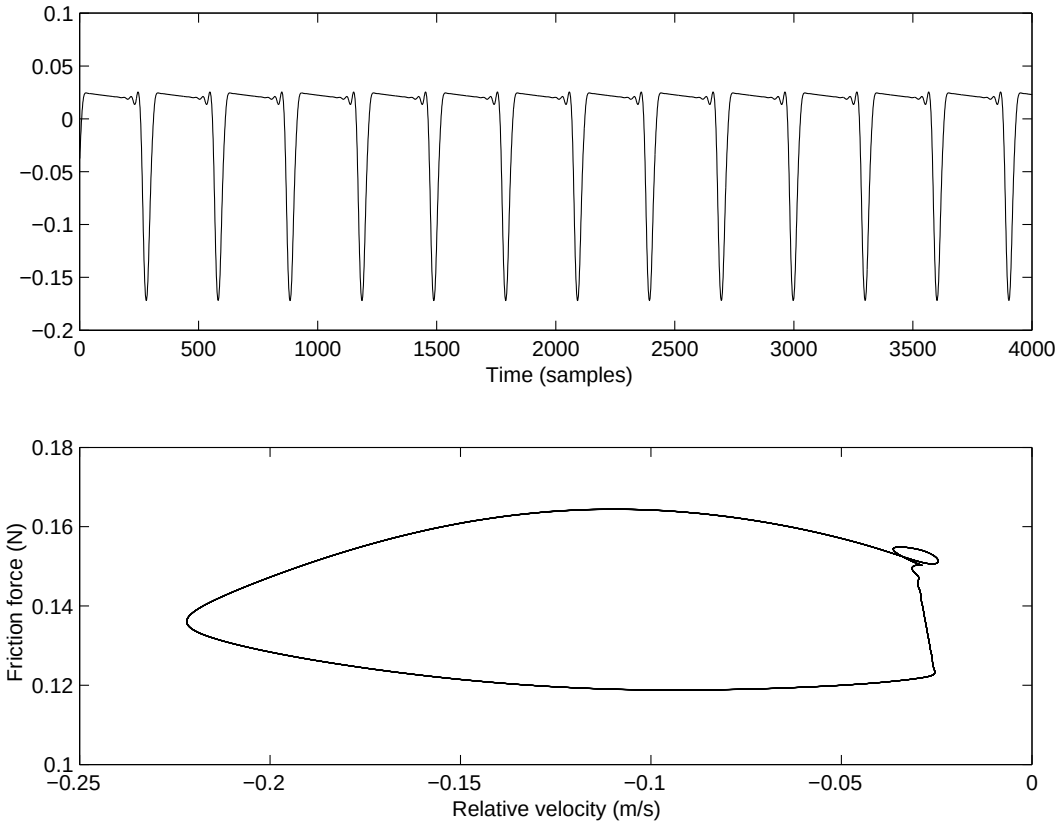

Figure 4.22: *Top: velocity at the bow point for the elasto-plastic model with friction model parameters* $\sigma_0 = 4000$*,* $\sigma_1 = 0$ *and* $\sigma_2 = 0.25$*. Bottom: velocity versus friction. Notice the hysteresis loop similar to the one obtained by using the plastic model.*

First of all, notice how in the model it is possible to set an external force f_{be} on the bow, but it not know *a priori* what the resulting bow velocity v_b will be. However, the two quantities can be easily related. At steady state, (i.e., $\dot{z} = 0$) the equality

$$v\left(1 - \alpha(v, z)\frac{z}{z_{ss}(v)}\right) = 0 \tag{4.10}$$

must hold. This means that either $v = 0$ (i.e., the external force is too weak and the bow has stopped on the string), or $v = v_b \neq 0$ and $z = z_{ss}(v_b)$ (i.e., the external force is strong enough to reach a steady-state velocity). In this latter case the total force acting on the bow is zero, i.e., $f_{be} = f_{fr}(v_b, z_{ss}(v_b))$.

Therefore choosing the value

$$f_{be} = f_{fr}(v_b, z_{ss}(v_b)) = \sigma_0 z_{ss}(v_b) + \sigma_2 v_b \tag{4.11}$$

can give two different outputs, depending on the values of the other parameters: either the bow stops after a short transient, or it reaches the desired bow velocity v_b.

Concerning the physical parameters of the friction force, the two parameters (f_c, f_s) are related to f_b through the static and dynamic friction coefficients:

$$f_s = \mu_s F_b, \qquad f_c = \mu_d F_b. \tag{4.12}$$

The breakaway displacement z_{ba} is also influenced by the normal force: note that in order for $\alpha(v, z)$ to be well defined, the inequality $z_{ba} < z_{ss}(v) \forall v$ must hold (this remark is made also in [26]). Since $\min_v z_{ss}(v) = f_c/\sigma_0$, a suitable choice for z_{ba} is

$$z_{ba} = c f_c/\sigma_0 = c\mu_d F_b/\sigma_0, \quad \text{with} \quad c < 1, \tag{4.13}$$

which states that the breakaway displacement increases with the normal force, as one would expect.

The bristle stiffness σ_0 is an interesting parameter. One would say that an increase in σ_0 results in an increase in the friction force: this is not true. Indeed, looking at the steady-state (i.e., $v = v_b$, $z = z_{ss}(v_{ss})$, and $\dot{z} = 0$) force, this does not depend upon σ_0:

$$f_{fr}\left(v_b, z_{ss}(v_b)\right) = \sigma_0 z_{ss}(v_b) + \sigma_2 v_b = f_c + (f_s - f_c)e^{-(v_b/v_s)^2} + \sigma_2 v_b, \tag{4.14}$$

which is of course the usual friction force used in static models. Therefore, σ_0 does not control the strength of the steady-state friction force, instead it defines the "degree of dynamicity" of the dynamic model; very roughly, if $\sigma_0 \to \infty$ the bristles do not move anymore. In other words, σ_0 defines the magnitude of the allowed presliding displacement.

Finally, the two parameters (v_s, σ_2) are easily deduced from the literature. The last one, σ_1, is less easily determined (it describes the internal dissipation of vibrating bristles). Canudas De Wit *et al.* [24] use the value $\sigma_1 = \sqrt{\sigma_0}$. Fig. 4.22 shows the result of applying the elasto-plastic model to a waveguide string with the same parameters as before. The friction model parameters used are $\sigma_0 = 4000$, $\sigma_1 = 0$ and $\sigma_2 = 0.25$. Notice how an hysteretic effect similar to the one produced by the plastic model is obtained with the elasto-plastic model. Moreover, notice how a realistic stick phase with ripples is obtained. The bristle internal dissipation affects micro-oscillations and is perceptually relevant. Fig. 4.23 shows the attack portion of the bridge force generated by the elasto-plastic model, with the same combinations of parameters as before. Notice how, as desirable, Helmholtz motion is achieved after the first period.

Fig. 4.24 shows the results of the simulations using the elasto-plastic model with $\sigma_2 = 0.43$. Notice how increasing the value of σ_2 makes the Helmholtz corner less sharp. This has a strong perceivable effect.

4.5 Accounting for the bow width

The previous bowed string models assume that the bow excites the string at a single point. This is a simplified assumption of reality. As a matter of fact, every bowed string player is aware that the sound quality may vary by varying the amount of bow-hair in contact with the string, which is achieved by tilting the bow.

In Chapter 3 the concept of differential slipping was introduced, and it was explained how differential slipping cannot be achieved using a model that excites the string at a single point. In this section two solutions are proposed to account for the width of the bow. The first solution consists of implementing the two-point bow-string interaction model proposed by McIntyre, Schumacher and Woodhouse in [70]. The second solution is a refined bow-width model as proposed by Pitteroff in [86], combined with the efficient waveguide implementation for the freely vibrating string.

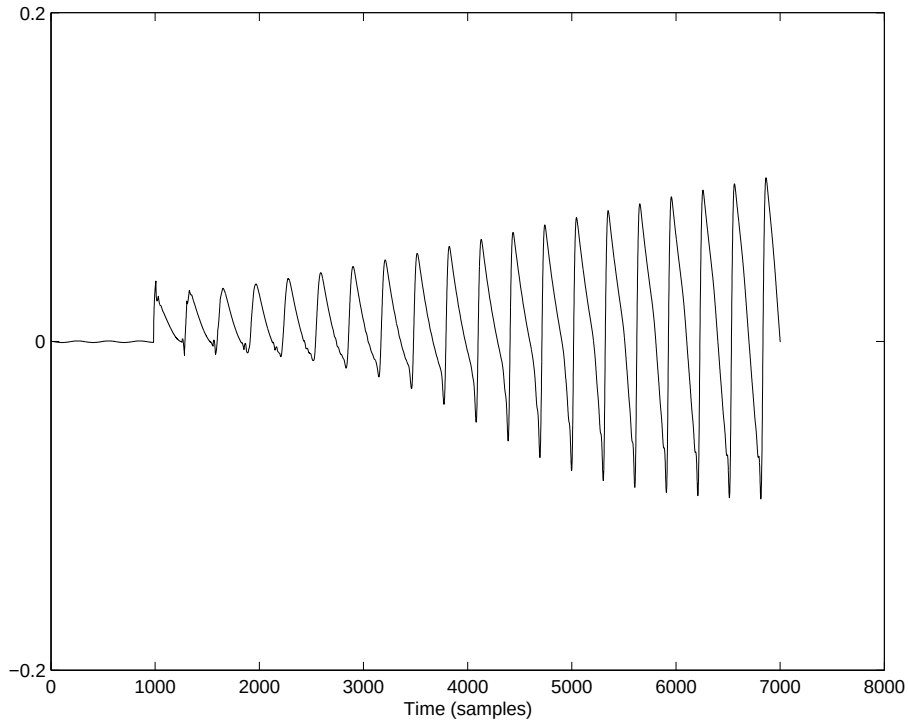

Figure 4.23: *Attack transient of the elasto-plastic model, with the same parameters as Fig. 4.22. The y axis represents the bridge force. Notice how the Helmholtz motion is achieved after the first period.*

4.5.1 A two-point bow string interaction model

Since the transitions from stick to slip are not instantaneous, different regions across the bow may have different release and capture events, and a situation called "differential-slipping events" described in [70] can occur. In differential slipping, the bow hair near the bridge may slip backward relative to the bow motion, while bow hair on the nut side may slip forward. This process can be understood as the string "straightening out" under the bow as the bowing point moves uniformly from one extreme (capture) to the other (release).

Helmholtz motion is generally not disrupted by differential slipping due in part to the damping provided by torsional string motion and the finite compliance of the bow-hair. Differential slipping can create audible events, especially when bowing closer to the bridge.

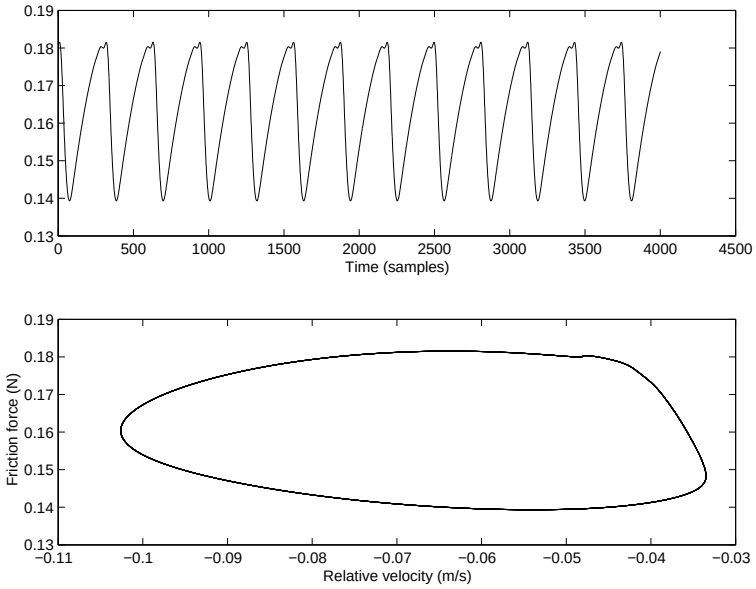

Figure 4.24: *Simulation using the elasto-plastic model with* $\sigma_2 = 0.43$. *The top portion represents the string velocity at the bow point. Notice how the sharp squarewave typical of the Helmholtz motion presents a completely different shape.*

.

To account for differential slips, a two-point model that allows to simulate efficiently the finite width of the bow was proposed in [105]. As shown in Fig. 4.25, the bow is in contact with the string in two points called v_{hl} and v_{hr}. The contact point v_{hl} on the left side of the bow is obtained summing the contribution coming from the left side of the bow, plus a filtered version of the wave coming from the right side, which is attenuated by the bow air. The same is true for the contact point on the right side, denoted by v_{hr}, so it is possible to write:

$$\begin{cases} v_{hl} = v_{i_n} * h_r + v_{i_b} \qquad v_{hr} = v_{i_n} + v_{i_b} * h_l \end{cases} \tag{4.15}$$

where h_r and h_l are two filters that model the right and left side attenuation respectively.

So two bow-string interactions have to be solved, one for each side of the bow, which give two friction values as:

$$\begin{cases} f_l &= 2\,Z\,(v_l - v_{hl}) \quad (4.17a) \\ f_l &= \mu\,(v_l - v_b) \qquad (4.17b) \end{cases} \tag{4.17}$$

and

$$\begin{cases} f_r &= 2\,Z\,(v_r - v_{hr}) \quad (4.19a) \\ f_r &= \mu\,(v_r - v_b) \qquad (4.19b) \end{cases} \tag{4.19}$$

where f_l and f_r represent the values of the friction calculated at the left and the right side of the bow respectively, and v_l and v_r represent the velocity at the left and right contact point respectively.

This allows to calculate the new outgoing velocities as follows:

$$\begin{cases} v_{o_n} &= v_{i_b} + \frac{f_r}{2Z} \qquad (4.20a) \\ v_{o_b} &= v_{i_n} + \frac{f_l}{2Z} \qquad (4.20b) \end{cases} \tag{4.20}$$

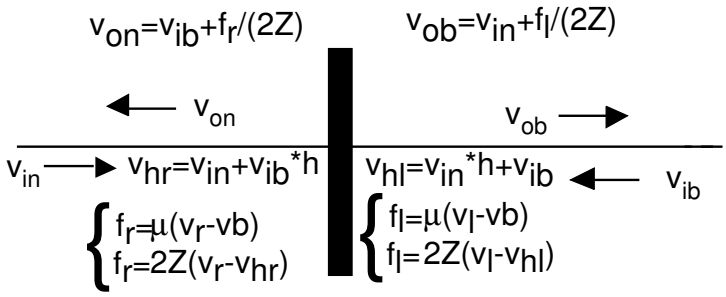

Figure 4.25: *Structure of the two point bow-string interaction model*

The bow hair

The ribbon of bow-hair on a violin bow consists of approximately 200 hairs, of which normally 50 or so are in immediate contact with the string [87]. Since the distance between the hair is smaller than the wavelength, the bow hair can be approximated as an uniform material.

Conversion of physical parameters to samples

Since the diameter of an individual bow hair is about 0.2 mm, and no more than 50 hairs are in contact with the string, the resulting bow width is about 1 cm. This means that at an audio rate of 44100 Hz the number of samples corresponding to the bow width is given by $(44100/f_0) * \delta/l$, where δ represents the width of the bow, l is the length of the string (0.69 m) and f_0 is the fundamental frequency of the string. For example, in the case of a violin G string, $f_0 = 196$ Hz, which gives a bow of three samples in contact with the string. On the other end, a violin E string ($f_0 = 659$ Hz) gives less than one sample of contact area. To cope with this problem, a multirate model is used.

Using digital fractional delays [127, 65] both a fine tuning of the sampling instants and an efficient implementation of sample rate conversion are possible. The output samples are computed with different delay values, according to the corresponding string that is played. For example, the standard audio rate of 44.1 kHz is associated to the G string, which, as explained before, gives 3.26 samples of full contact. Having

the same number of samples for the highest violin string (i.e., the E string, at 659 Hz), would require a sample rate of about 140kHz, which is way above the usual audio standards. On the other hand, imposing a sample rate of about 48 kHz would result in a single sample of bow hair contact, which reduces the two point model to the single point model. Our compromise consists of choosing a sample rate of 82 kHz for the E string, which gives about 1.8 samples of full contact, and allows to excite also the higher harmonics of the string to obtain brighter sonorities without encountering aliasing.

Simulation results

Fig. 4.27 shows the waveforms captured by the different models after reaching steady state, about 4000 samples from the attack, when the Helmholtz motion is established. These simulations show a cello G string bowed with a constant bow force of 0.2 N and a constant bow velocity of 0.05 m/s. The bow was placed at a normalized distance from the bridge of 0.1. The top figure represent the waveforms created by the basic model described at the beginning of this chapter. The second figure from the top represents the basic model with torsional waves. The third figure is the model with torsional waves and allpass filters to account for inharmonicity. Finally, the bottom figure represents the model with the same features as the previous one, but with the bow width model included. Notice how the Helmholtz waveform is somehow more "noisy" than in the previous examples. These perturbations result in audible noise, qualitatively similar to that in real bowed string instruments. Fig. 4.26 shows how the noise-generated spikes in the waveform are even more evident when bowing closer to the bridge. Maintaining the same parameters as in Fig. 4.27, the bow is moved to a normalized distance of 0.07.

Tilting the bow

Having a bow of finite width allows to reproduce the movement of the player while tilting his bow simply by changing the number of "bow samples" in contact with the string. Moreover, it is possible to simulate bows whose width is larger than that

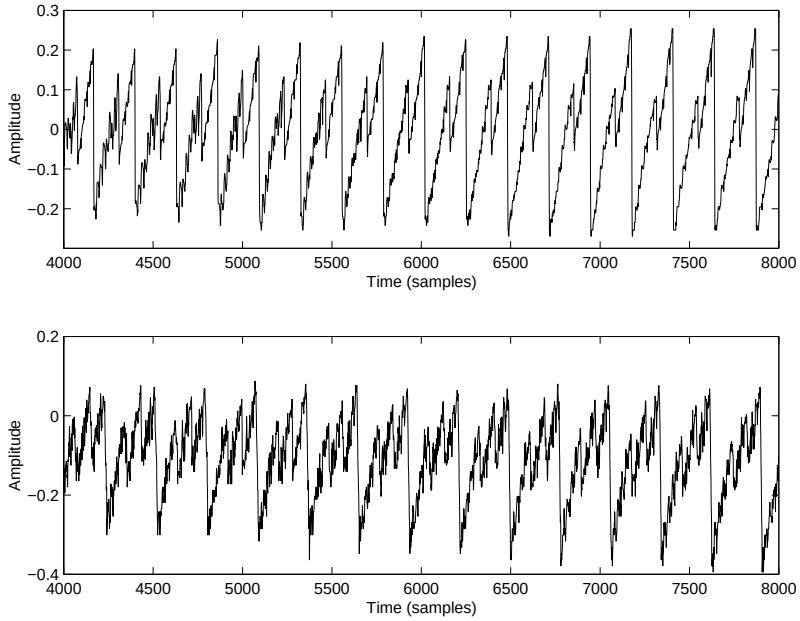

Figure 4.26: *Motion of a bowed string with the bow excited at normalized bow position of 0.07. Top: basic model, bottom: model that accounts for the bow width.*

of a real instrument, simply by increasing the amount of samples that represent the contact area.

4.5.2 A refined physical model for the bow hair

Pitteroff [86] proposes an accurate model of a bowed string which takes into account the bow width. The five equations governing the behavior of the bow under the string are given by:

$$T\frac{\partial^2\eta}{\partial x^2} + f = m\frac{\partial^2\eta}{\partial t^2}$$

$$K\frac{\partial^2\chi}{\partial x^2} - af = \Theta\frac{\partial^2\chi}{\partial t^2}$$

$$f = -s\eta_H - d\frac{\partial\eta_H}{\partial t}$$

$$v_{rel} = \frac{\partial\eta}{\partial t} - a\frac{\partial\chi}{\partial t} - \frac{\partial\eta_H}{\partial t} - v_b$$

$$v_{rel} = 0$$

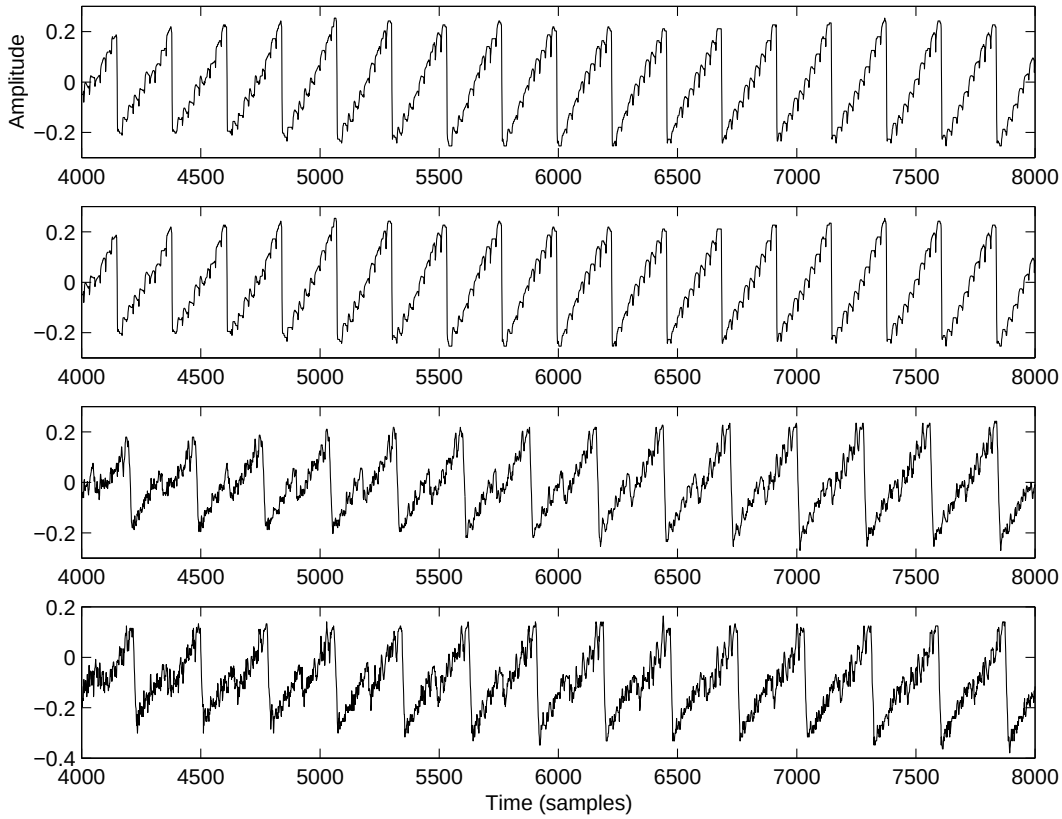

Figure 4.27: *Motion of a bowed string obtained using different models. From top to bottom: basic model, basic model with torsional waves, basic model with torsional waves and string stiffness, model with torsional waves, string stiffness and bow width.*

(stick)

$$f(v_{rel}) = \pm \left[\mu_d + \frac{(\mu_s - \mu_d)(v_b - v_{mid})}{v_b - v_{mid} \mp v_{rel}} \right] f_z \tag{4.21}$$

(slip)

where η is the string displacement, χ is the angular displacement, a denotes the radius of the string, η_H denotes the displacement of the bow hair in contact with the string.

For computational efficiency, the system of Eq. (4.21) is solved in two different ways: the portion of the freely vibrating string is solved as before using digital waveguides. For the portion of the string under the bow, finite differences are used.

A multirate implementation

The numerical schemes required for the portion of the string under the bow require a sampling rate too high for real-time and audio simulations. It was noticed, in fact, that at a sampling rate of less that about 200000 samples, depending on the fundamental frequency, the model becomes unstable. For this reason, a higher sampling rate for the samples of the string under the bow was used, while for the samples of the freely vibrating string the sampling rate of 44.1 kHz was adopted. The sampling rate conversion is performed by linear interpolation. Fig. 4.28 shows the schematic representation of the resulting model, with the two blocks for sampling rate conversion.

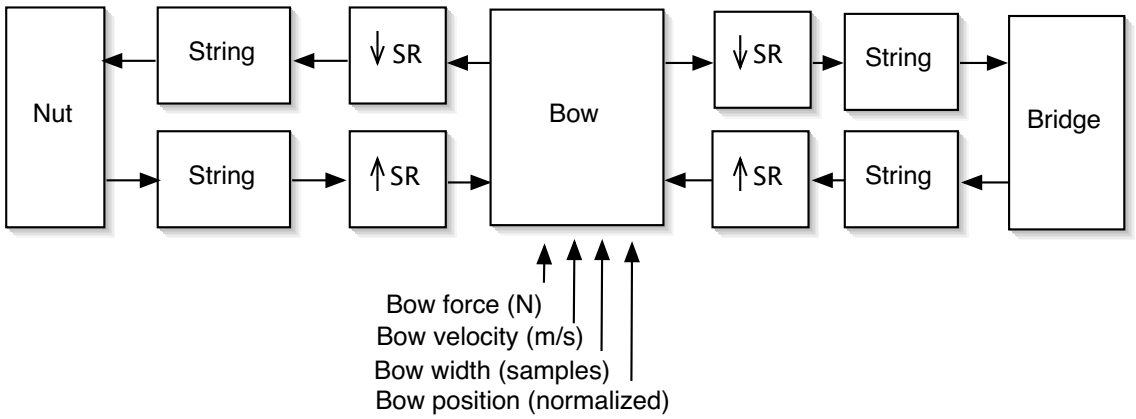

Figure 4.28: *Structure of the multirate bowed string physical model. The bow-string interaction portion of the model is downsampled by a factor of 10.*

4.6 Modeling the body of a violin

In real-time synthesis of a violin, there is some difficulty in modeling the body because of a tradeoff between accuracy and computational cost. If all the resonances of the body are accounted for, by modeling each one with its own pair of filter poles, the computational cost is too high. On the other hand, one cannot implement too few

filter poles and neglect the large number of resonances, because the complex filtering of the body contributes strongly to the characteristic timbre of the violin.

In order to solve the problem of computational cost and maintain an efficient implementation that runs in real-time, Karjalainen and Smith proposed a technique called commuted synthesis [58]. The idea behind commuted synthesis, as discussed in Chapter 3, is to combine the body resonances with the excitation mechanism.

In this section new approaches to model the body of a violin are proposed, motivated by the desire to combine an efficient real-time implementation together with a physical interpretation of the model. The high frequency resonances of the body of a violin are first simulated by using a 3D waveguide mesh [27]. Secondly, resonant filters which simulate the low frequencies resonances are added. As an alternative solution, a simulation of a trapezoidal violin is proposed.

4.6.1 The digital waveguide mesh

The digital waveguide mesh was introduced by Van Duyne and Smith [27] as an extension of the 1-D digital waveguide. The waveguide mesh is a regular array of 1-D digital waveguides arranged along each perpendicular dimension, interconnected at their crossings by scattering junctions. Examples of mesh topologies are shown in Fig. 4.29. In the canonical case, the scattering junctions are taken to be equal

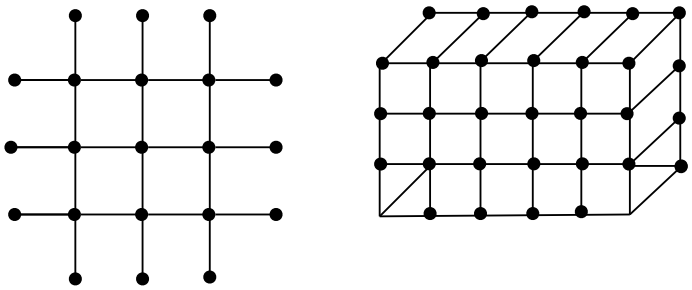

Figure 4.29: *Two examples of mesh topologies: a 2D mesh (left side), and a 3D mesh (right side).*

impedance lossless junctions and the interconnecting waveguides are of unit length. Fig. 4.30 shows a 2-D digital waveguide mesh as originally proposed in [128]. Two

conditions must be satisfied for at a lossless junction J connecting lines of equal impedance [27]:

- Sum of inputs equals the sum of outputs (flows add to zero).
- Signals at each intersecting waveguide are equal at the junction.

The first condition translates to the following equation:

$$\sum_i v^+_{il,m}(n) = \sum_i v^-_{il,m}(n) \tag{4.22}$$

where the l, m indices represent the spatial position of the junction in the mesh, the n index represents the current time sample, and $v^+_{il,m}(n)$ and $v^-_{il,m}(n)$ represent the four incoming and outgoing waves at a junction, respectively. The digital waveguide mesh algorithm can be interpreted as a difference scheme for computation of the two-dimensional wave equation [128].

4.6.2 Body modeling using the waveguide mesh

As a first attempt, the high frequency resonances of a violin body were simulated by using a 3D waveguide mesh. The 3D rectilinear mesh is an extension of the 2D mesh to 3 dimensions. It is made of 6-port scattering junctions arranged at integer valued spatial positions in each of the three axial directions.

The 3D waveguide mesh is initially chosen to correspond to a physical box with dimensions $35.5 \times 21.0 \times 3.0$ cm. Such dimensions are comparable to those of a real violin body, so it is expected for the mesh to spontaneously have a similar mode spacing at high frequencies where the air modes dominate [21]. At a sampling rate of 44.1 kHz, assuming a sound speed $c = 344$ m/s, these dimensions translate to a rectangular mesh which is approximately $26 \times 16 \times 2$ samples along each edge. [2]

[2] Using von Neumann stability analysis [27], a physical length d is converted to samples using the formula $N_d = dF_s/(c\sqrt{3})$.

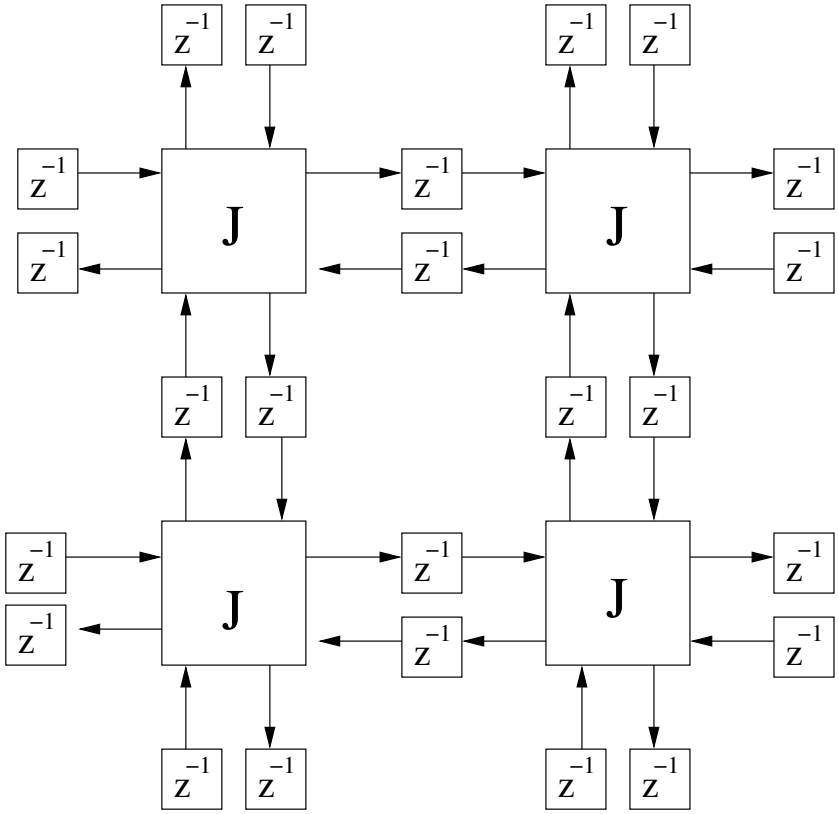

Figure 4.30: *A 2-D digital waveguide mesh. The scattering junctions J are taken to be equal impedance lossless junctions.*

Designing boundary filters for the mesh

Most of the surfaces found in everyday listening exhibit a low-pass behavior, since they absorb higher frequencies more rapidly [64]. In order to approximate such a spectral characteristic for the body of the violin, a first order spring-damper system was used, as proposed in [33] and shown in Fig. 4.31. Let us consider an unitary reflective surface, $v(t) = k_m x_m(t) + R_s \dot{x}_m(t)$, where k_m and R_s are the spring constant and damping coefficient respectively. After deriving with respect to time and performing a Laplace transform, the transfer characteristic of the system becomes:

$$\frac{V(s)}{V_m(s)} = \frac{k_m}{s} + R_s \tag{4.23}$$

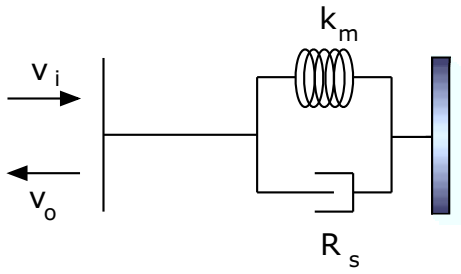

Figure 4.31: *1-st order spring/damper system.*

Since $v = v_i + v_o$, and $v_m = v_m^+ + v_m^-$, it is possible to write

$$\frac{V_o(s)}{V_i(s)} = \frac{k_m/s + R_s - Z_0}{k_m/s + R_s + Z_0} \tag{4.24}$$

By using the bilinear transformation [82], the Laplace variable can be rewritten according to the following map

$$s \leftarrow h\frac{1 - z^{-1}}{1 + z^{-1}} \tag{4.25}$$

where h is usually set to $2F_s$. Therefore the transfer function of Eq. (4.24) can be set to:

$$\frac{V_o(s)}{V_i(s)} = \frac{\frac{k_m - h(Z_0 - R_s)}{k_m + h(Z_0 + R_s)} + \frac{k_m + h(Z_0 - R_s)}{k_m + h(Z_0 + R_s)} z^{-1}}{1 + \frac{k_m - h(Z_0 + R_s)}{k_m + h(Z_0 + R_s)} z^{-1}}. \tag{4.26}$$

This formula gives the coefficients that a 1-st order filter must have to reproduce the damper/spring system. In our example, from [64] it is assumed $Z_0 = 414$, $k_m = 30$ and $R_s = 69$. The corresponding amplitude of the frequency response is shown in Fig. 4.32.

The frequency response of the 3D mesh, with the low-pass filters described above, is shown in Fig. 4.33. The mesh was excited with an unitary impulse at position $(3, 8, 2)$, which roughly corresponds to the bridge position, for a mesh of dimensions $(26, 16, 2)$. The output sound was captured at the same position.

As it can be seen from Fig. 4.33, the 3D mesh alone is not able to provide the right low-frequency resonances required to properly simulate the body of a violin. For this reason, the complete body model was enhanced by adding a combination

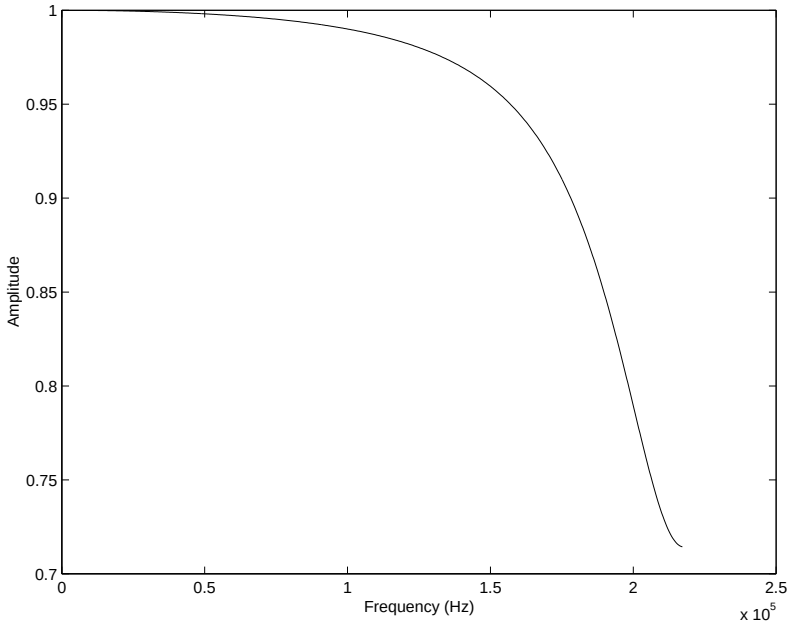

Figure 4.32: *Frequency response for the wall filters for the 2D waveguide mesh, assuming the absorption coefficients from [64].*

of second order resonant filters for low-frequencies and the same waveguide mesh for high frequencies.

The low frequency-resonances were extracted by analyzing the input admittance of an amateur made instrument, as shown in Fig.4.34.[3]

The mode extraction from the violin body response was realized using the notch filter of the form [58]

$$H_r(z) = \frac{A(z)}{A(z/r)} = \frac{1 + a_1 z^{-1} + a_2 z^{-2}}{1 + a_1 c z^{-1} + a_2^2 z^{-2}} \tag{4.27}$$

where $a_1 = -2r\cos(\omega_0)$, $a_2 = r^2$, where r is the pole radius and ω_0 is the center frequency in radians, and c is a coefficient used to flatten the magnitude response of the notch filter far away from the notch frequency.

Fig. 4.34 shows the frequency response at low frequency for the target violin, together with the location of the main low frequencies resonances. Table 4.1 reports

[3]The input admittance is courtesy of Jim Woodhouse.

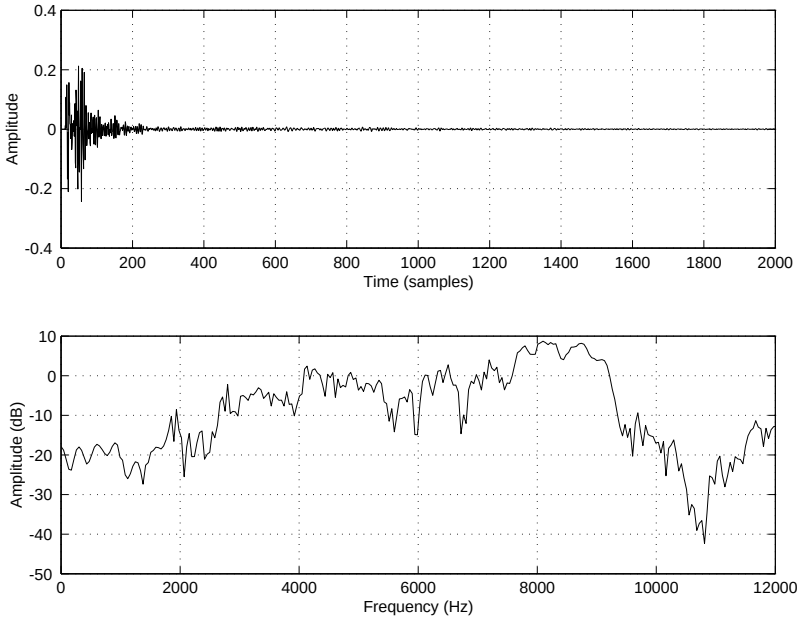

Figure 4.33: *Top: impulse response, bottom: frequency response for the 3D waveguide mesh of dimensions* $(47, 28, 8)$*,* $F_s = 44100$ *Hz, using the wall filters of Fig. 4.32.*

center frequency, Q factors and amplitude of the resonances shown in Fig. 4.34.

Fig. 4.35 shows the result of the mode extraction for the first three modes of the frequency response, Fig. 4.35 part A) shows the original frequency response. Fig. 4.35 part B) shows the frequency response after the first resonance is removed. Fig. 4.35 part C) and D) shows the frequency response after the second (part C) and third (part D) resonances are removed. Notice how the mode extraction algorithm correctly removes the targeted resonances.

The residual impulse and frequency response, containing the high frequency resonances, is shown in Fig. 4.36. Such residual is the target which needs to be compared to the designed mesh.

Due to psychoacoustic properties of hearing, instead of considering individual high-frequency modes, it is possible to consider *bands* of high-frequency modes. A reasonable choice is to group high frequency modes into *critical bands of hearing* according to the Bark [142] or ERB [74] frequency scales. Matlab software for this purpose may be found via [53].

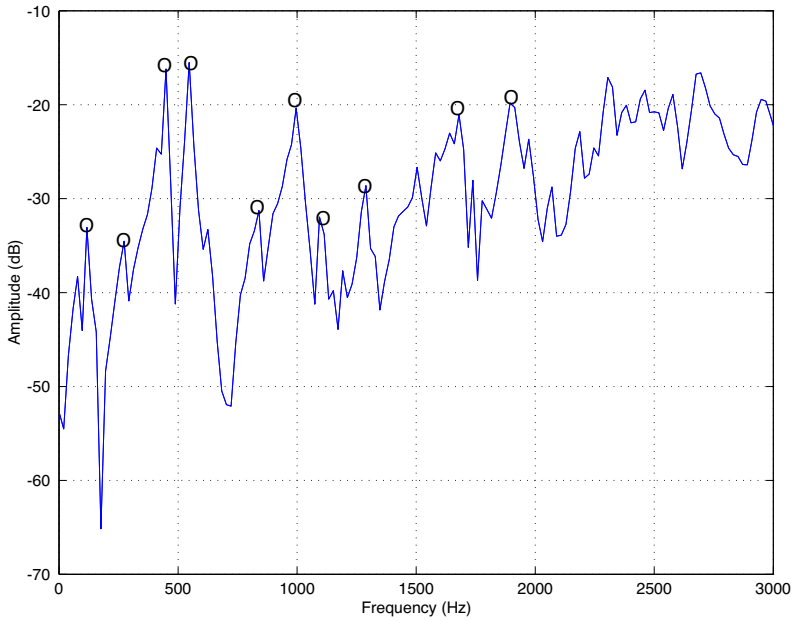

Figure 4.34: *Location of the low frequency resonances of the input admittance of an amateur violin.*

To match the mode bandwidths, the high frequencies violin body impulse response was analyzed over a Bark frequency axis to determine the average decay time for each "band of modes" in the high-frequency response.

Within each band, certain statistics of the mesh response need to be matched to those of the instrument body response. The within-band amplitude distribution was taken to be the natural amplitude fluctuation obtained when summing a set of identical modes at center frequencies chosen randomly according to the appropriate distribution. The EDR (see Sec. 4.1) was used, preferred over the more usual short-time Fourier power spectrum because it de-emphasizes beating decay envelopes due to closely tuned coupled modes (which occur often in acoustic measurements of resonating bodies). This facilitates estimating decay times for ensembles of resonators which are being characterized statistically.

The result of summing EDR in each critical band can be seen in Fig. 4.37 for the original violin response after the high frequencies have been removed, and Fig. 4.38 for the synthesized mesh response. A line is fitted to the successive values for each

Center frequency (Hz)	Q factor	Amplitude (dB)
118	18	-33
274	22	-34.5
449	10	-16
547	16	-15.5
840	50	-31
997	30	-20.4
1100	30	-34
1290	25	-29
1500	50	-28
1675	60	-22
1900	60	-20

Table 4.1: *Low-frequency resonances detected for the violin whose input admittance shown in Fig. 4.34. Resonances are shown up to 2000 Hz.*

band to estimate the average decay and initial amplitude levels for the modes in the band.[4] Notice how the average decay time between the two responses is quite similar.

Determination of crossover frequency

Simulations were carried out to determine the crossover frequency at which the synthesis model becomes perceptually equivalent to the original body impulse response. The crossover frequency is designed as the upper limit of resonant modes modeled using biquads and the lower limit at which the mesh output models the high frequency modes.

To construct the most accurate mesh impulse response with regard to the features extracted from the violin impulse response data, the average decay rate of the original impulse response was first analyzed. These data were then fit to the waveguide mesh impulse response.

To determine the lowest crossover frequency a lowpassed violin impulse response and a highpassed synthesized mesh impulse response were mixed, and the resulting sound was compared to the original violin impulse response.

[4]In the analysis, a length 30 ms Hanning window was used with 50% overlap. This maximized frequency resolution while leaving sufficiently many analysis time frames at high frequencies.

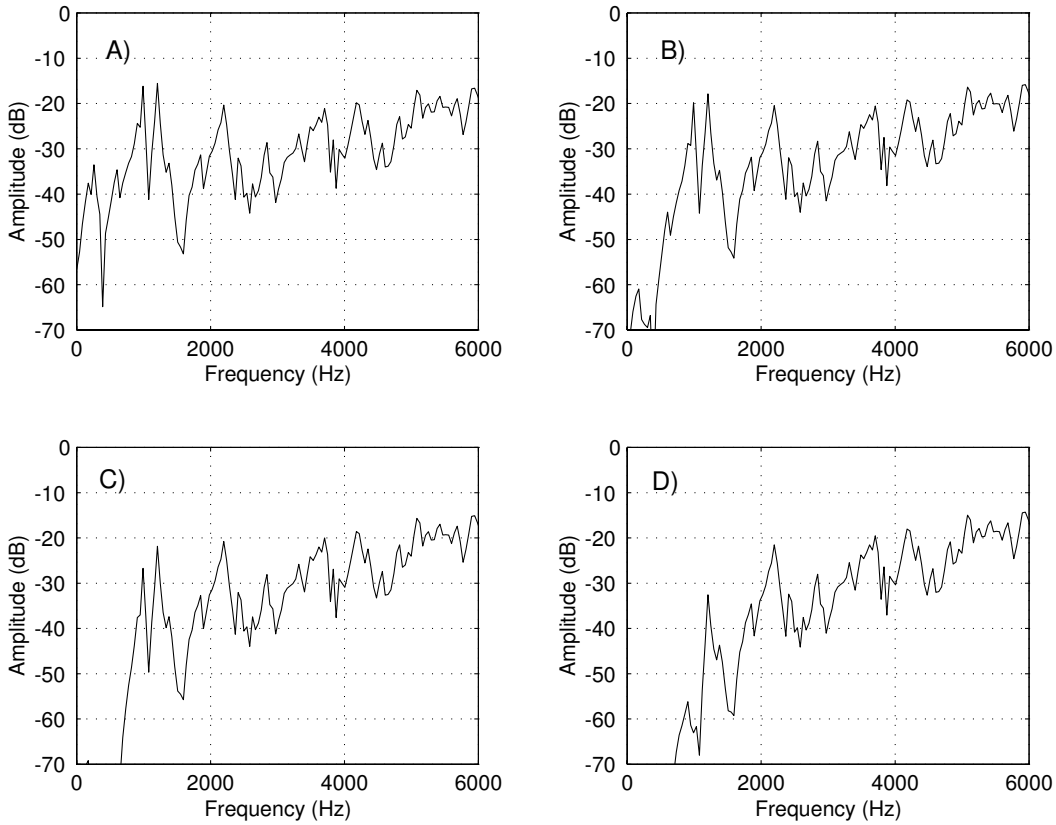

Figure 4.35: *Result of mode extraction of the first three modes of the target frequency response. A) the original frequency response, B) the frequency response after the first mode is removed, C) the frequency response after the second mode is removed, D) the frequency response after the third mode is removed.*

Tests performed show that the lowest crossover frequency at which the highpassed mesh/lowpassed violin impulse mixture is indistinguishable from the violin body impulse reference is around 1900 Hz. At this level, the number of biquad resonators needed to capture the low frequency modes is about 10. This is more computationally efficient than the crossover frequency used in the [47], which used 13 biquad resonators which went up to a crossover frequency of 3200 Hz. At a crossover frequency that was lower than the threshold, there was an audible difference in the timbre of the test signal, which could not adequately match the violin impulse response in a perceptually equivalent way.

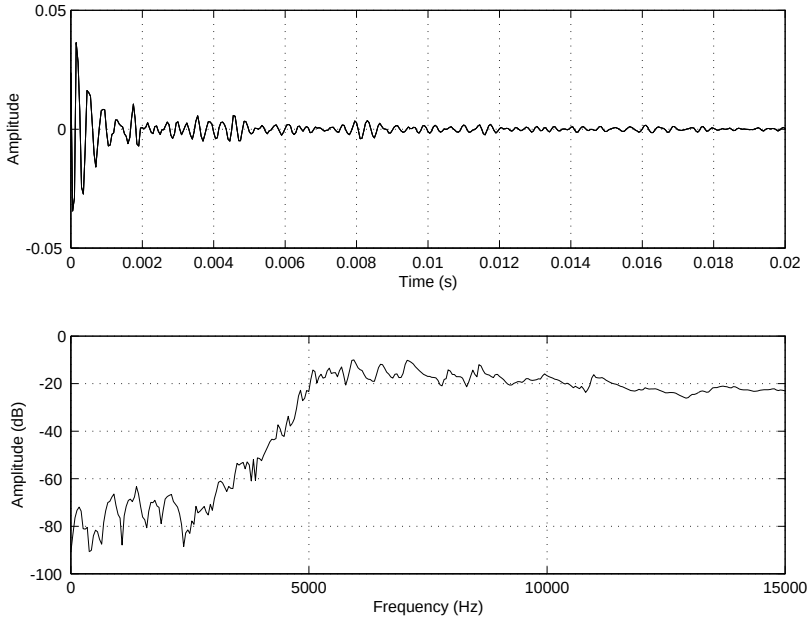

Figure 4.36: *Top: impulse response, bottom: input admittance at the bridge for the original violin, after the low frequency resonances have been removed.*

These tests show that it is perceptually possible to use a reduced number of low-frequency resonators and still provide high quality results. Connecting the mesh to these resonators produces a high quality synthetic violin impulse response. The corresponding time domain signal is shown along with that of the original violin impulse response in Fig. 4.39. The more pronounced beating of the highpassed waveguide mesh output is effectively masked by the strong, long-ringing body modes present in the original violin body impulse below 1900 Hz.

Examining smaller mesh dimensions

Since perceptual mode saturation in a critical band can be realistically achieved by a small number of resonators, it is theoretically possible that even smaller dimensions of waveguide meshes would have a distribution of mode amplitudes which can satisfy the perceptual criteria for our synthesis model described above. This would allow to build a mesh which is perceptually equivalent but whose computational cost is reduced.

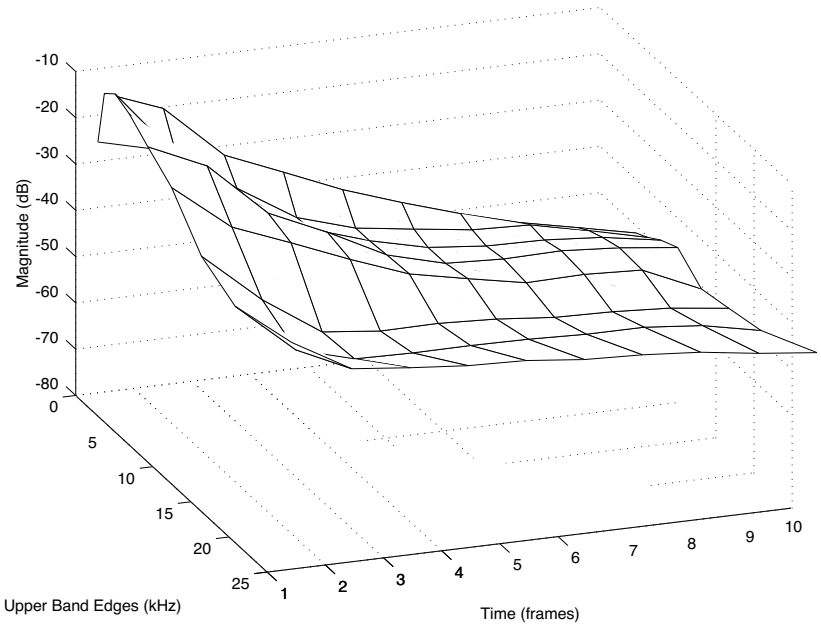

Figure 4.37: *Summed EDR for the original violin response, after low frequency resonances have been removed.*

Dimensional reductions of the 3D mesh at 44.1 kHz were also tested in the same way to determine their lowest crossover frequency, if any. At a lower sampling rate of 22.05 kHz, the desired physical dimensions translate to the 3D-mesh dimensions $13 \times 8 \times 1$ samples. With only 1 sample in the z direction, a 2D mesh at 22.05 kHz is expected to behave similarly to its 3D counterpart, at 16×9 samples. (For the 2D mesh the correction factor is $\sqrt{2}$, as opposed to $\sqrt{3}$ as it was the case in the 3D mesh. Simulation results show that this mesh has about the same crossover frequency as the 3D, 44.1 kHz mesh, at around 1900 Hz.

Using geometries which do not closely follow the physical proportions of the violin edges may result in mode distributions which are less suited for simulating high-frequency violin body resonances. For example, an $18 \times 13 \times 2$ sample 3D mesh at 44.1 kHz has its lowest crossover frequency around 2000 Hz.

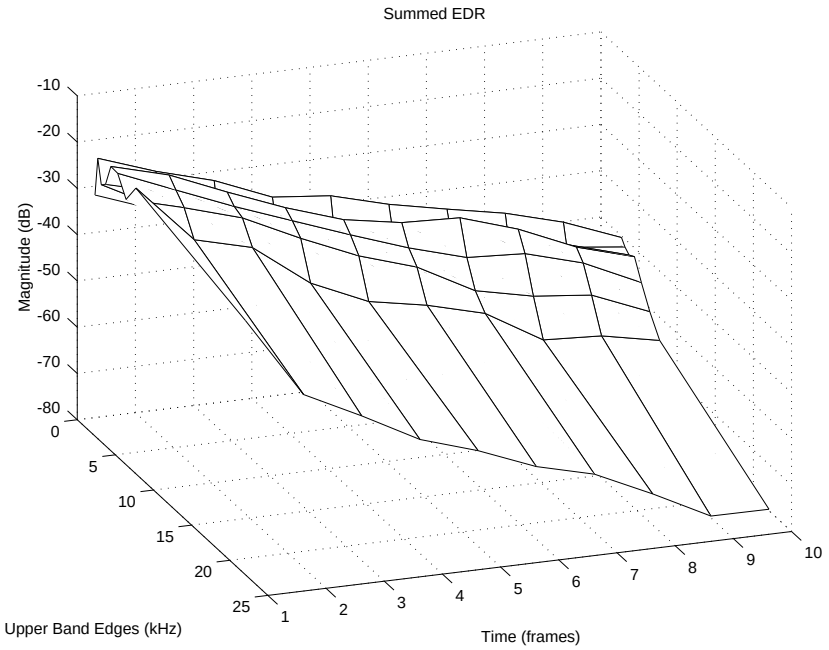

Figure 4.38: *Summed EDR for the synthesized mesh impulse response.*

Simulation results

The bridge velocity calculated by the bowed string model was fed to the resonant filters and waveguide mesh in parallel, and their outputs were added, as shown in Fig. 4.41. This is the implementation reported in [47] and [46].

Fig. 4.42 shows the results of the simulations for a violin E string ($f_0 = 659$ Hz). The top picture displays the waveforms observed at different time intervals of the outgoing velocity at the bridge point, i.e., the waveforms that are entering the mesh and the resonators.

The center of Fig. 4.42 displays the outputs of the resonant filters and the mesh respectively, while the bottom of Fig. 4.42 displays the combination of the mesh with the resonant filters.

The influence of the body model on the spectrum of the bowed string is shown in Fig. 4.43. It is noticeable how the dimensions of the mesh produce a frequency response that has a gap below 2000 Hz and above 8000 Hz. This hole is related to the fact that the mesh models the high frequency air modes of the cavity.

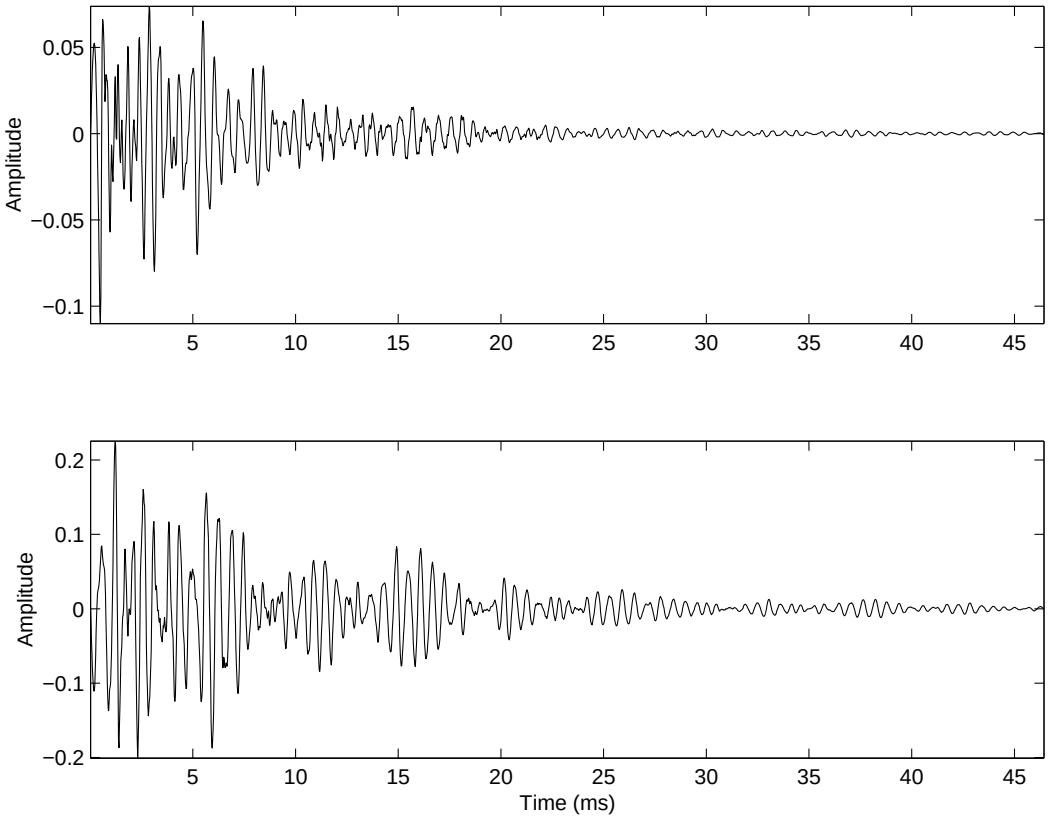

Figure 4.39: *Time responses of the violin body impulse response (top) and synthesized waveguide mesh impulse response (bottom) above 1900 Hz.*

4.6.3 Savart's trapezoidal violin

As an attempt to obtain both a body model based on waveguide meshes and a physical interpretation, the trapezoidal violin designed by Savart in the 18th century was modeled. Savart's trapezoidal violin was briefly described in Chapter 3.

To simulate such instrument, a mesh whose dimensions correspond to the ones proposed by Savart for his trapezoidal violin was chosen. In this way the mesh design was motivated and justified by historical reasons.

As shown in Fig. 4.44, the dimensions of the original violin were 600 mm of total length, 353 mm of body length, 225 mm of body width in the lower part and 85 mm of body width for the higher part of the body. This corresponds to a 3D mesh of dimensions $27 \times 17 \times 3$ for the bottom part. The violin had two rectangular holes in

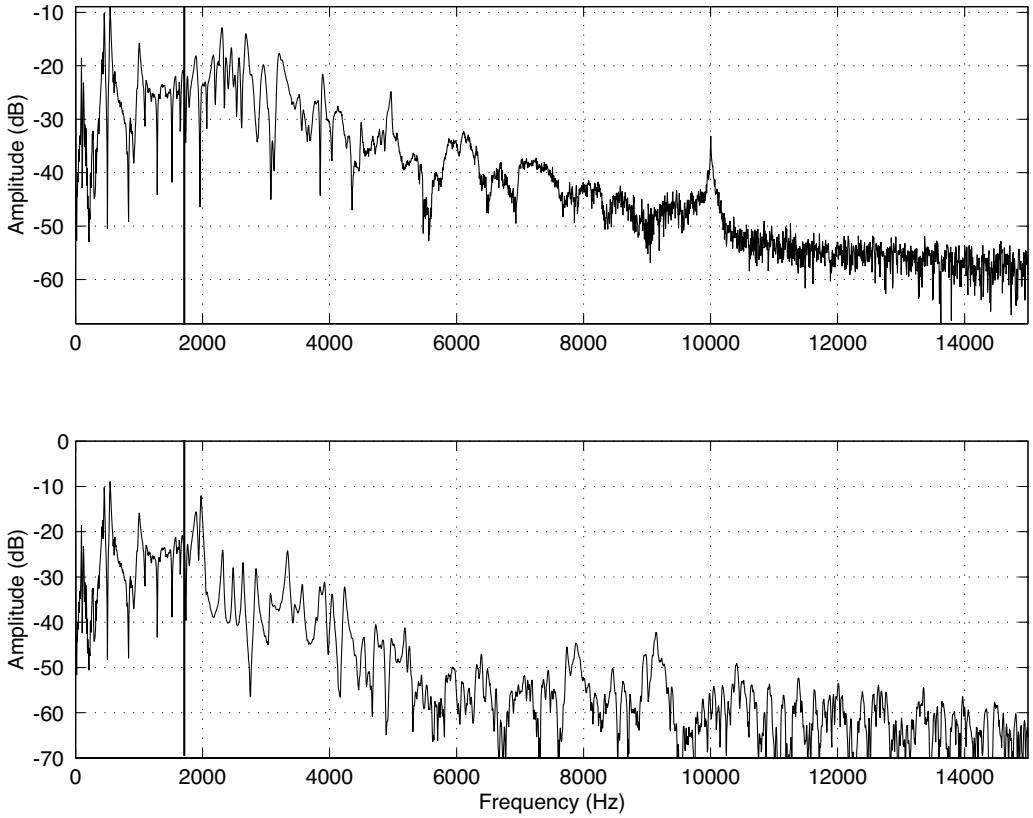

Figure 4.40: *Frequency responses of the original violin impulse response (top) and a highpassed synthesized waveguide mesh impulse response plus a lowpassed violin body impulse response (bottom). The straight vertical line at 1900 Hz shows the crossover frequency.*

each side, which correspond to the f-holes in the traditionally shaped violin.

4.6.4 Modeling Savart's trapezoidal violin

In order to create a digital model of Savart's violin a three dimensional trapezoidal waveguide mesh was chosen.

The trapezoidal mesh is an extension of the original two dimensional rectangular mesh [27] in which the horizontal dimension decreases in size from bottom to top, according to the design proposed by Savart.

The dimensions of the mesh were chosen in order to match the dimensions of

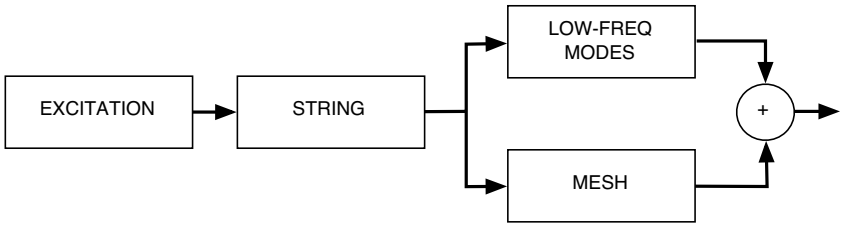

Figure 4.41: *Bowed string physical model block diagram. The outgoing velocity at the bridge is filtered in parallel through the waveguide mesh and the low-frequency resonant filters.*

Savart's violin. More precisely, the mesh had dimensions $27 \times 13 \times 3$ samples for the bottom part, and $7 \times 13 \times 3$ for the upper part.

Fig. 4.45 shows the trapezoidal mesh used to simulate Savart's violin. A model of the two violin's holes was also added. Such holes were added to the trapezoidal mesh using the same technique adopted to model toneholes in woodwind instruments [97].

Fig. 4.46 shows the impulse response (top) and frequency response (bottom) of the trapezoidal mesh. The response was obtained by exciting the mesh at position 4×1 and capturing the output waveform at 4×2. Notice the nice distribution of peaks and valleys at low frequency, which resembles to the distribution typical of a violin.

Application to the bowed string physical model

The violin body model was applied to the digital waveguide string model. The input parameters of the string model were $f_b = 0.31$ N, $v_b = 0.05$ m/s and $\beta = 0.075$. As in the case with the 3D mesh, a violin E string ($f_0 = 659$ Hz) was used.

The outgoing velocity at the bridge point v_{ob} was filtered through the resonances of the trapezoidal mesh, as shown in Fig. 4.47.

Fig. 4.48 shows the result of applying the trapezoidal mesh to the bowed string physical model. The top of Fig. 4.48 represents the outgoing velocity at the bridge v_{ob} before being filtered through the body resonances, while the bottom of Fig. 4.48 shows the output of the bowed string physical model after being filtered through the body resonances. The waveforms were captured after steady state motion was

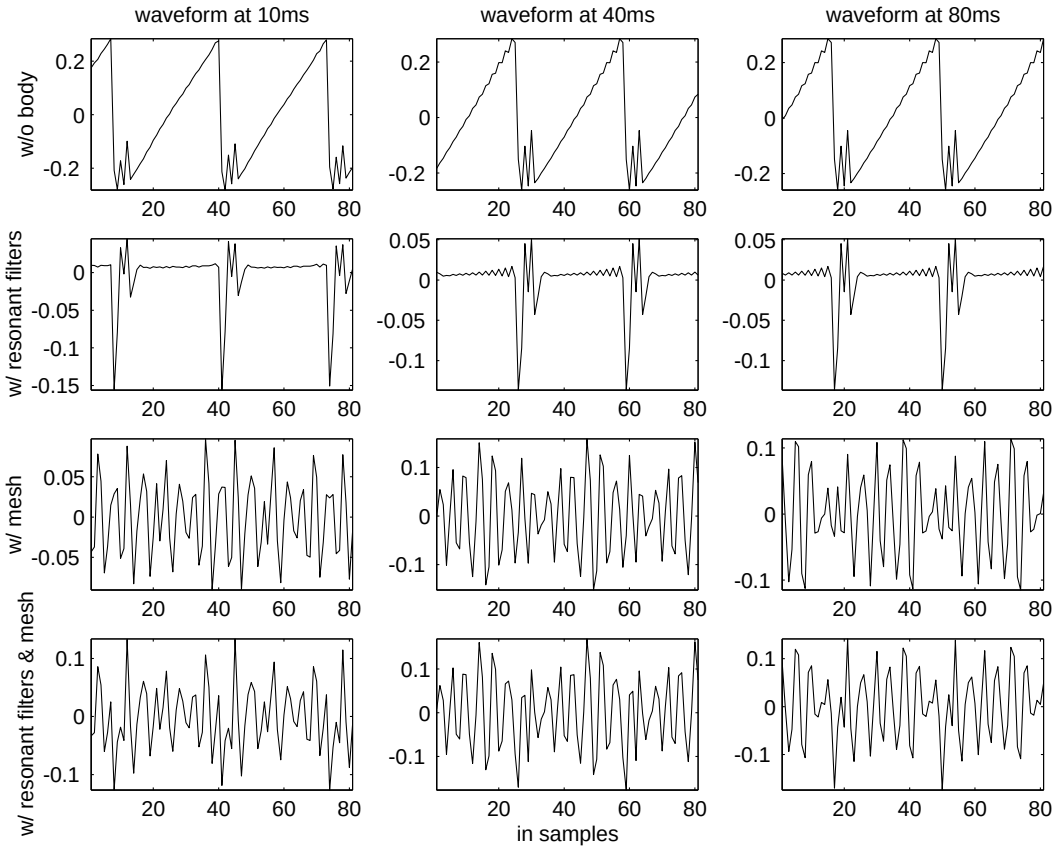

Figure 4.42: *Waveforms of the velocity captured at different locations of the model. From the top: outgoing string velocity at the bridge point, velocity output of the resonant filters, velocity output of the mesh and total final velocity.*

achieved.

As expected, the regularity of the Helmholtz motion is broken when the waves are filtered through the body. This is the same behavior that can be observed when examining the bridge waveform, with and without the role of the body. This difference can be noticed also in the spectrum of the resulting waveforms, shown in Fig. 4.49.

Final remarks

As suggested in [94], feedback delay networks (FDN) with short delay lines may be also be used to produce resonances irregularly spread over frequency such as the body of the violin.

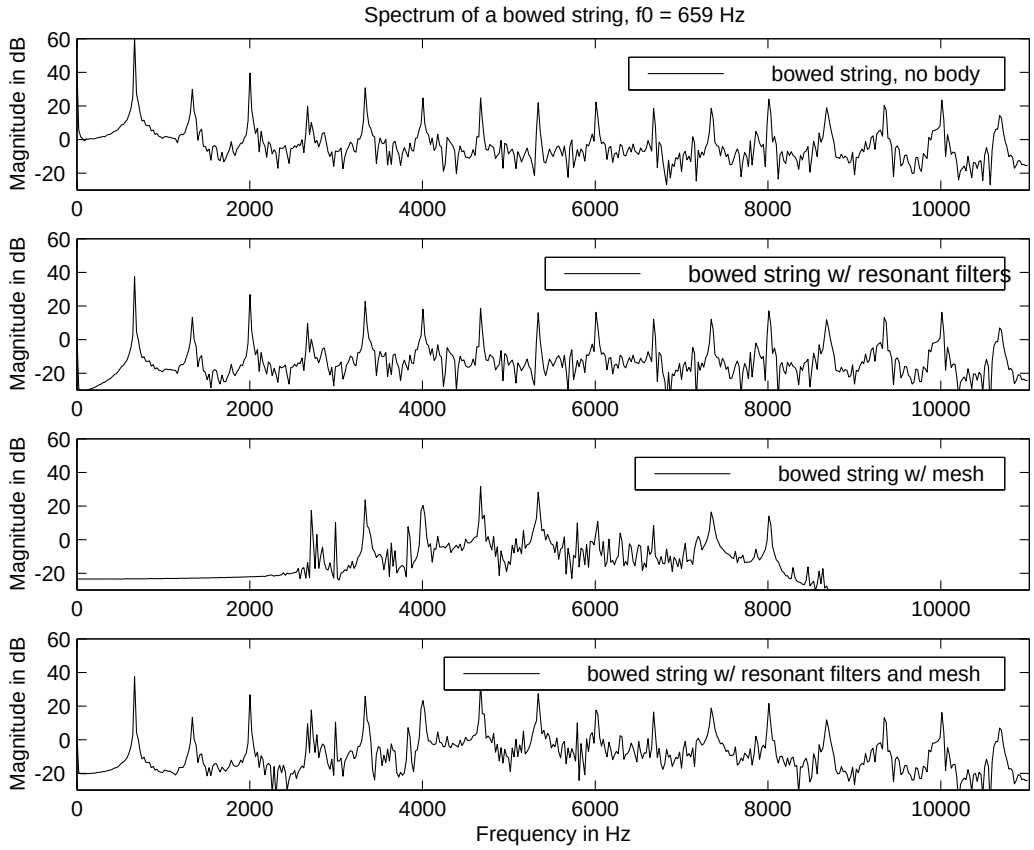

Figure 4.43: *Spectra corresponding to the waveforms of Fig. 4.42.*

Mathews and Kohut [69] showed that in simulating the violin body, the exact position and height of resonances is not usually important; on the contrary, the Q's of the resonances has to be sufficiently large and the peaks have to be sufficiently close together.

Hutchins has found that the frequency spacing Δ between the so-called A1 cavity mode (430-490 Hz) and the C3 body mode (490-590 Hz) is critical to the overall tone and playing quality of violin [49]. For example, a violin with Δ between 60 to 80 Hz is referred as suitable for soloist, while a violin with Δ between 20 to 40 Hz is suitable for chamber music players.

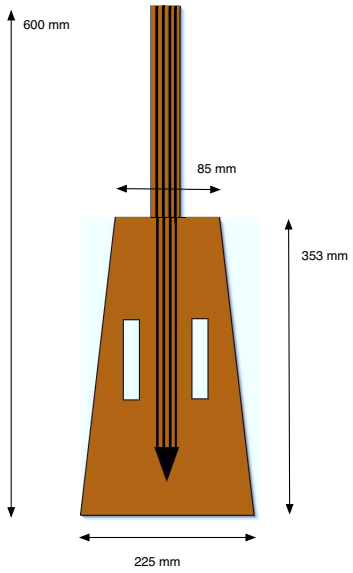

Figure 4.44: *Savart's trapezoidal violin.*

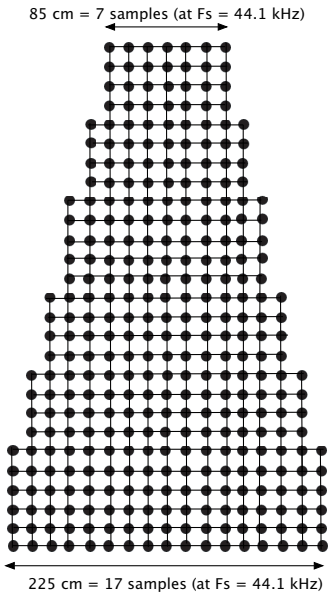

Figure 4.45: *Dimensions of the trapezoidal waveguide mesh used to simulate Savart's violin.*

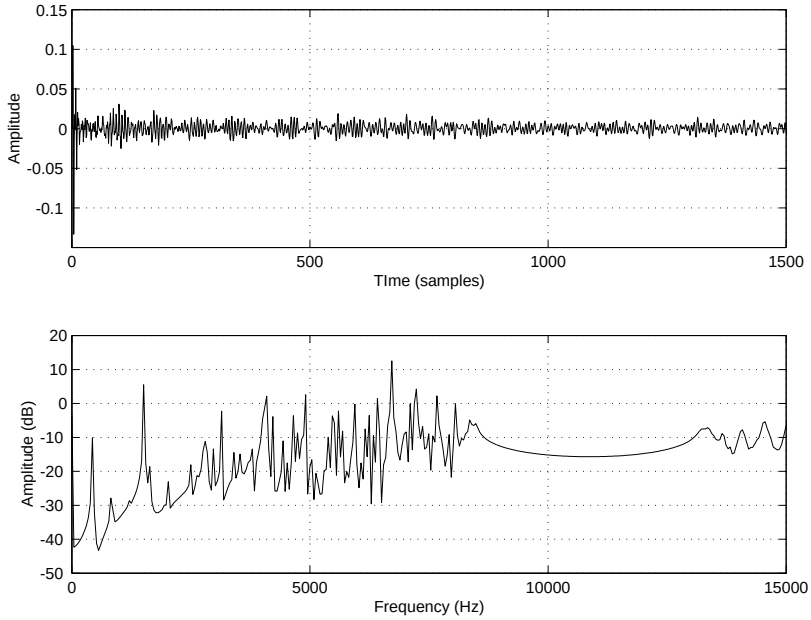

Figure 4.46: *Top: impulse response, bottom: frequency response of Savart's trapezoidal violin.*

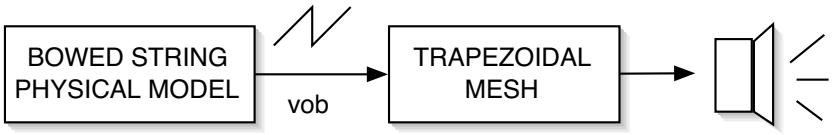

Figure 4.47: *Simplified block diagram of the combination of the physical model and the trapezoidal mesh.*

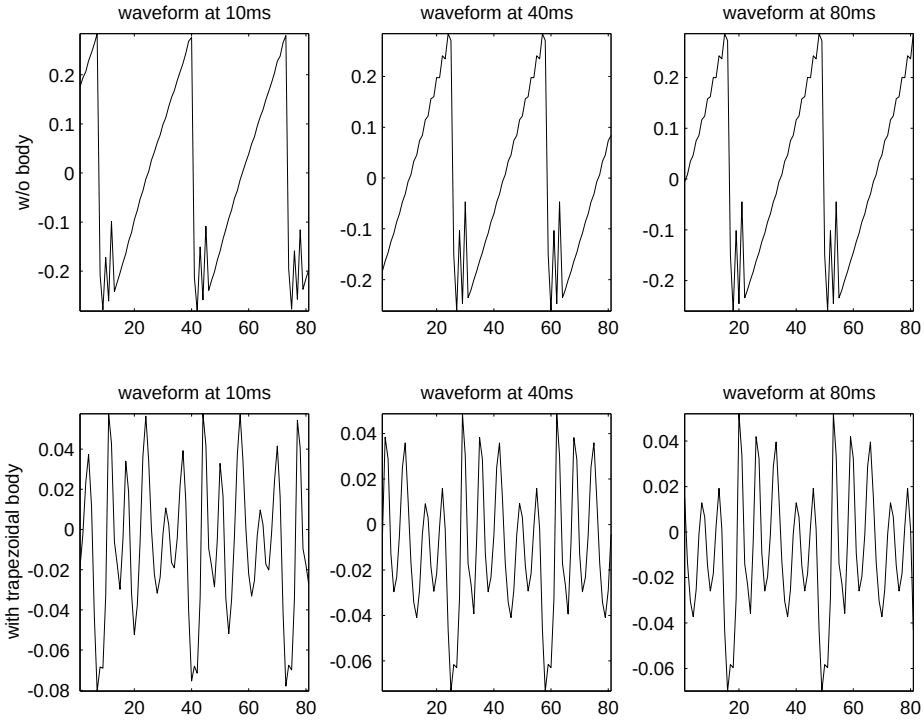

Figure 4.48: *Top: outgoing velocity at the bridge before being filtered by the resonances of the trapezoidal mesh; bottom: outgoing velocity at the bridge after being filtered by the resonances of the trapezoidal mesh.*

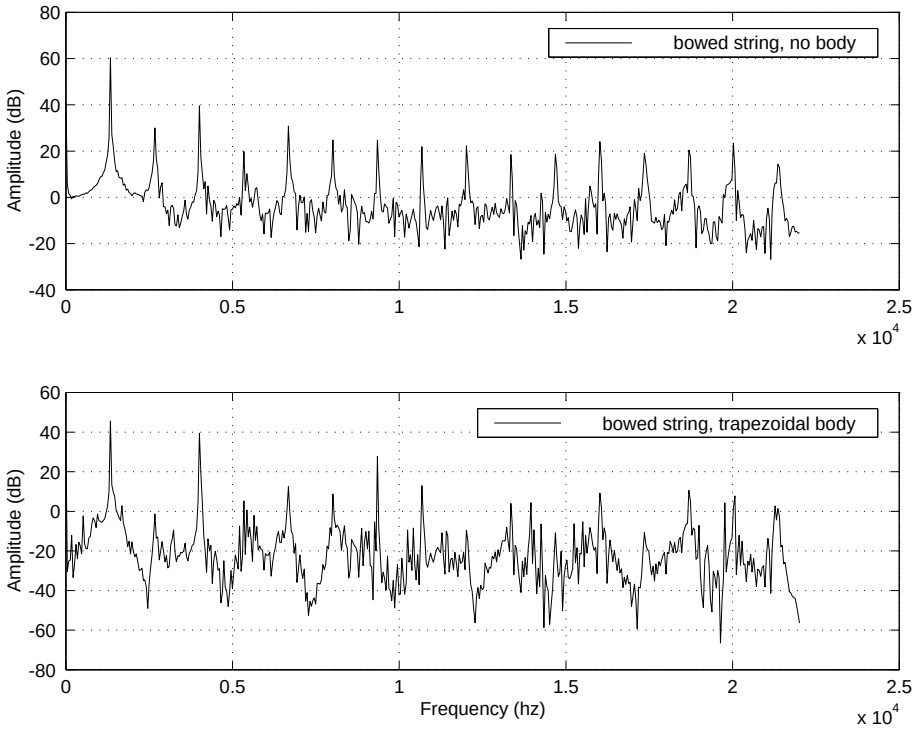

Figure 4.49: *Top: spectrum of the outgoing velocity at the bridge before being filtered by the resonances of the trapezoidal mesh; bottom: spectrum of the outgoing velocity at the bridge after being filtered by the resonances of the trapezoidal mesh.*

Chapter 5

Other instruments driven by friction

In the previous chapter an efficient yet accurate model of a bowed string instrument was proposed. The string was simulated using one dimensional digital waveguides, and the body of the instruments was simulated using waveguides meshes.

In this chapter other instruments whose main excitation mechanism is friction, such as the musical saw, the glass harmonica, the Tibetan bowl and bowed cymbals are examined. As contemporary music adopts lots of these instruments, efficient computer simulations of them become an interesting tool for interactive computer music, providing to composers and performers different new sonorities to explore.

Moreover, friction driven sonorities appear also in everyday life. The sound of a squeaky door, the noise of a brake and a chalk on a board are few examples of the variety of sonorities that interaction between rubbed dry surfaces can produce. Simulations of such everyday sonorities are also proposed. Starting by examining a musical saw, whose characteristic pure tone is suitable for an efficient implementation, more complex instruments such as bowed cymbals and plates are modeled.

Simulations in this chapter use banded waveguides, a synthesis technique first introduced in [29, 28], which can be interpreted as an hybrid between modal synthesis and digital waveguides.

The first part of this chapter provides an analysis of the differences between banded

waveguides and modal synthesis. The second part describes synthesis techniques to simulate unusual friction driven musical instruments.

5.1 Modal synthesis versus banded waveguides

The most elementary banded waveguide structure is depicted in Fig. 5.1. Compared to the waveguide structure of Fig. 3.7, the low-pass filter has been replaced by a band-limited operation represented by the block BP.

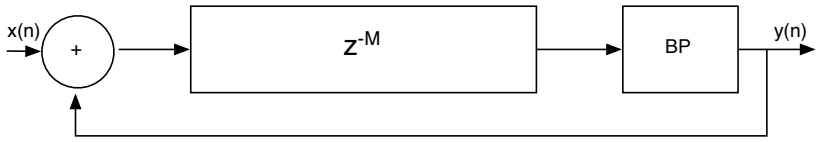

Figure 5.1: *Block diagram structure of one banded waveguide.*

The idea behind banded waveguides is to adopt a filtered delay-line loop to model a mode of a resonating system. The loop contains a bandpass filter which eliminates energy at frequencies other than the desired mode. The band-limiting operation is achieved by using second-order bandpass filters, for their efficiency and simplicity [123]. Considering the following transfer function

$$H_2(z) = \frac{1 - z^{-2}}{1 - (2R\cos\theta)z^{-1} + R^2 z^{-2}} \tag{5.1}$$

where R and θ are free parameters which relate to bandwidth B, center frequency ψ and gain A_0, the following equations result [123]

$$R \approx 1 - B/2 \tag{5.2}$$

$$\cos\theta = \tfrac{2R}{1+R^2}\cos\psi \tag{5.3}$$

$$A_0 = (1 - R^2)\sin\theta. \tag{5.4}$$

Notice how the filter of Eq. (5.1) has the same peak gain for all tunings.

As shown by Smith in [115], it is possible to normalize exactly the resonant gain. In this case, the transfer function of the bandpass filter becomes

$$H_2(z) = \frac{1 - Rz^{-2}}{1 - (2R\cos\theta)z^{-1} + R^2 z^{-2}} \tag{5.5}$$

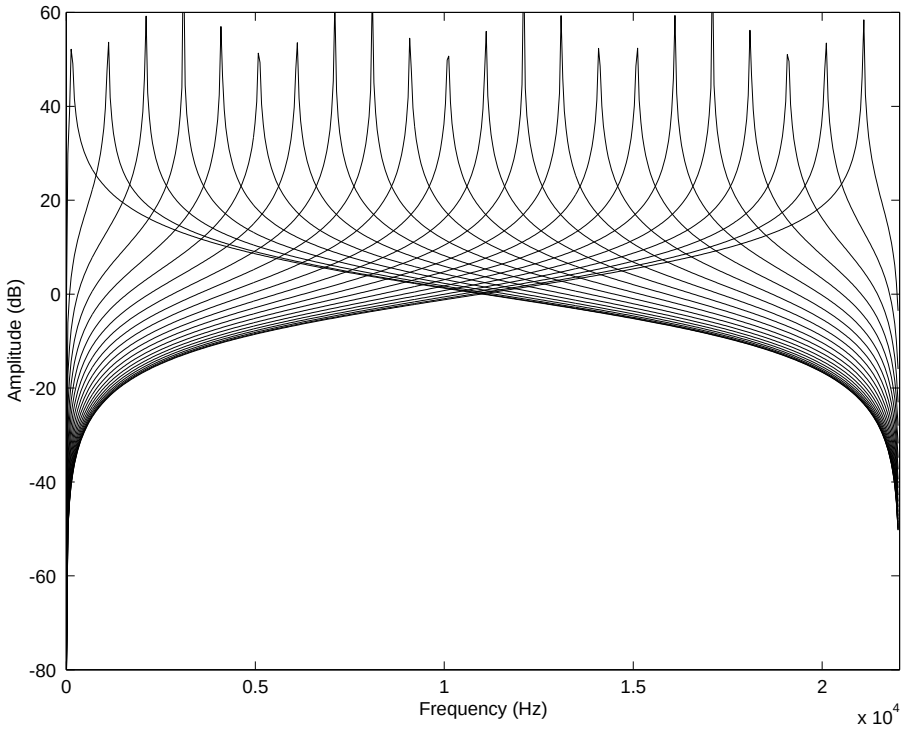

Figure 5.2: *Frequency response overlays for the bandpass filter of Eq. 5.5.*

Fig. 5.2 shows the frequency response overlay for the filters or Eq. 5.5, obtained by varying the resonant frequency, keeping a constant value $R = 0.99$. Notice the regularity of the amplitude of the frequency response as a function of tuning. The same plot can also be found in [115].

As a further improvement, as suggested in [115], the resonator input is scaled by a gain $g = (1 - R^2)/2$, in such a way that the output signal power equals the input signal power.

Using the bandpass filter just described, the free parameters of a banded waveguides are length of the delay-line d, resonance frequency of the band-pass R and

bandwidth B. The length of the delay-line is tuned to the frequency f_m of a mode to be modeled. The relationship between f_m, sampling frequency F_s and delay-line length d is given by

$$d = F_s/f_m \tag{5.6}$$

To calculate the band-pass parameter R the same modal frequency f_m is used and converted into radians:

$$\psi = 2\pi f_m/F_s \tag{5.7}$$

Among these parameters, only the bandwidth B does not have a strict physical interpretation. It is usually chosen to sufficiently reject other modes of the comb response of a feedback delay-line filter.

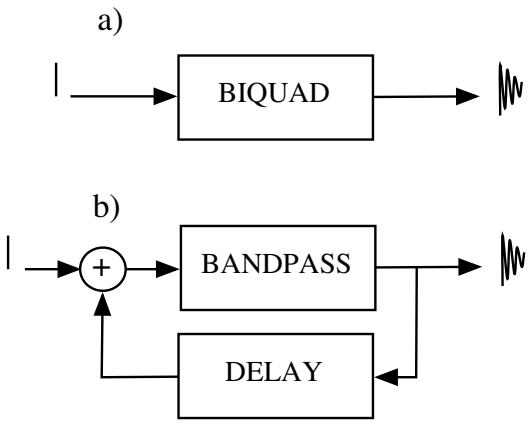

Figure 5.3: *Block diagram structure of a) one modal resonator, b) one banded waveguide.*

It is interesting to understand what is the advantage of using banded waveguides versus modal synthesis, a synthesis technique described in Chapter 3. In the interpretation of modal synthesis as a cascade of second order bandpass filters, as described in [83] and shown in Fig. 5.3, part a), the bandpass filter of Eq. (5.5) is used. In this

way, the only difference among modal synthesis and banded waveguides is the role of the feedback delay line.

To understand the effect of such delay line, an unitary impulse is fed into one modal resonator and one banded waveguide. The parameters of the resonant filter are $f_m = 440$ Hz, and $R = 0.9977$, and the simulations run at $F_s = 44100$. The delay line has F_s/f_m samples. The time domain output is shown in Fig. 5.4. In it, the solid line represents the time domain simulation obtained by using the modal resonator, while the dotted line represents the simulation obtained by using the one dimensional digital waveguide.

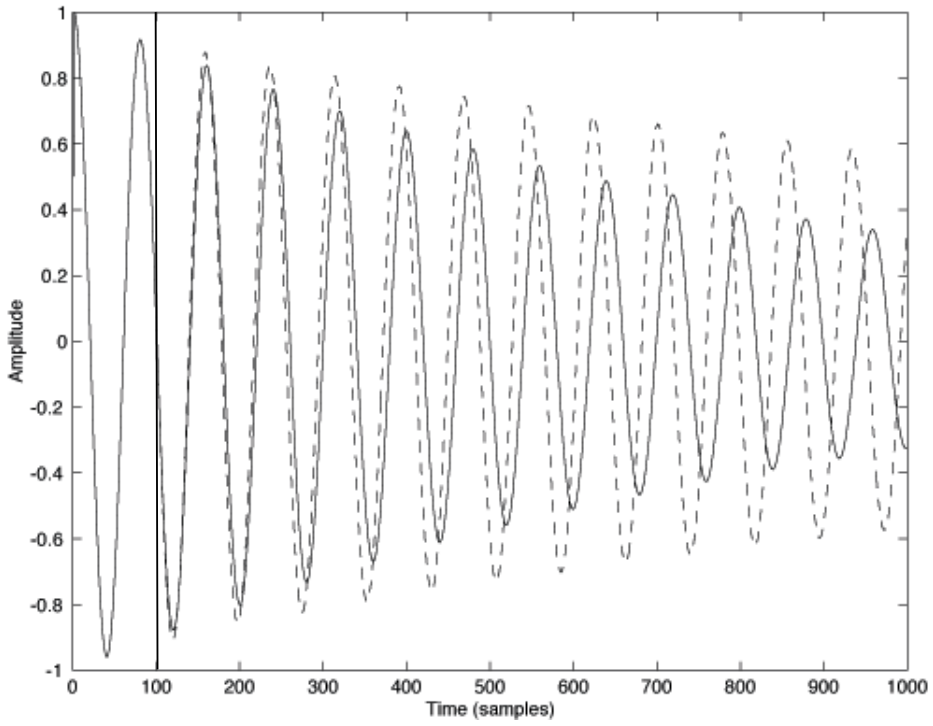

Figure 5.4: *Solid line: time domain simulation of an unitary impulse fed through a bandpass filter; dotted lines: time domain simulation of an unitary impulse fed thorugh one banded waveguide.*

As expected, up to F_s/f_m, i.e., up to about 100 samples, the two systems behave the same way. Once the delayed samples are fed back into the bandpass filter, the behavior of the two systems starts to change.

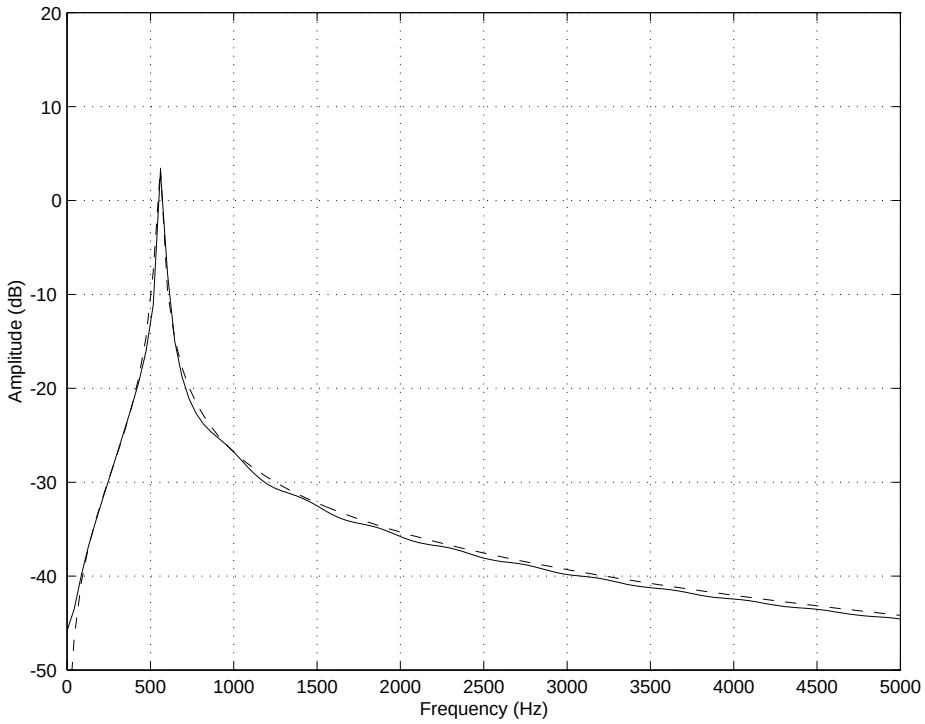

Figure 5.5: *Solid line: frequency response of a second order bandpass filter; dotted lines: frequency response of one banded waveguide. The vertical line represents the position in which the two systems start to behave differently.*

In Fig. 5.4, this is apparent by noticing the higher amplitude of the simulation using banded waveguides, which is due to the fact that rebouncing contributions are added to the incoming waves. Notice how the slight pitch difference is due to the fact that in this simulation integer delay lines are used.

Fig. 5.5 shows the frequency response of the two systems. As before, dotted lines represent the frequency response of one banded waveguide, while solid lines represent the frequency response of one modal resonator. The frequency response was obtained by calculating the FFT of the first 4096 samples of the time domain waveform. Notice how the two frequency responses are almost equivalent.

It is interesting to wonder if the slight difference on the behavior provides any advantage from a simulation point of view. Having a feedback system such as in banded waveguide enables a more natural simulations of interactions between exciters and

resonators. Moreover, modal synthesis does not retain any spatial information about the wavetrains that propagate along a resonating object. In modal synthesis, spatial information is not contained in the resonating structure, as in banded waveguides, but it is imposed by varying the amplitude and phase of the different resonant modes.

As Fig. 5.6 shows, this is particularly relevant in the case of circular resonators, where waves propagating from the excitation point along the two sides of the rim vary their amplitude according to the excitation position. Maintaining both a spatial and spectral representation of the modes, it is possible to produce a synthesis technique which preserves a physical interpretation in terms of space and is also computational efficient.

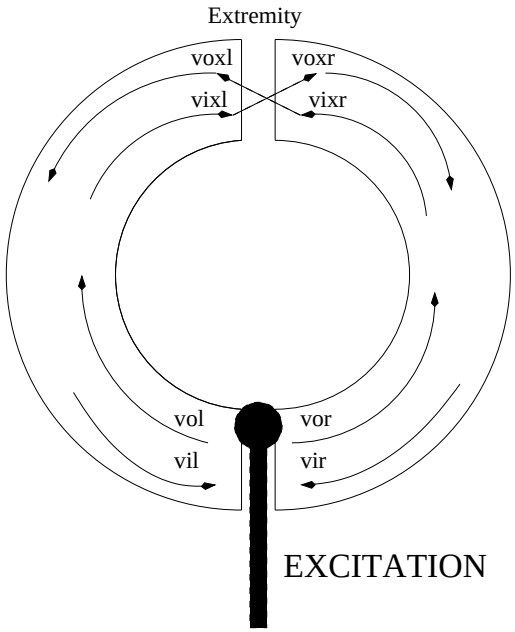

Figure 5.6: *Waves propagating around a circular resonator.*

Considering the more accurate physical interpretation of banded waveguides, which provides also better results in the quality of the synthesis, this technique is adopted in the rest of this chapter to simulate a musical saw and other unusual friction driven instruments.

5.2 The musical saw

When an ordinary handsaw is bent into an S-shape, as shown in Fig. 5.7, an interesting acoustical effect can occur. Tapping the blade of the saw reveals that beyond a certain critical degree of curvature, a very lightly damped vibration mode appears which is confined to the middle region of the S. This confined mode can be excited by a violin bow, to produce the pure sound of the "musical saw".

The origins of the musical saw go back to the early 20th century, thanks in particular to Leon Weaver. Later on, June Weaver started playing the saw using a violin bow in a lap style, as shown in Fig. 5.7.

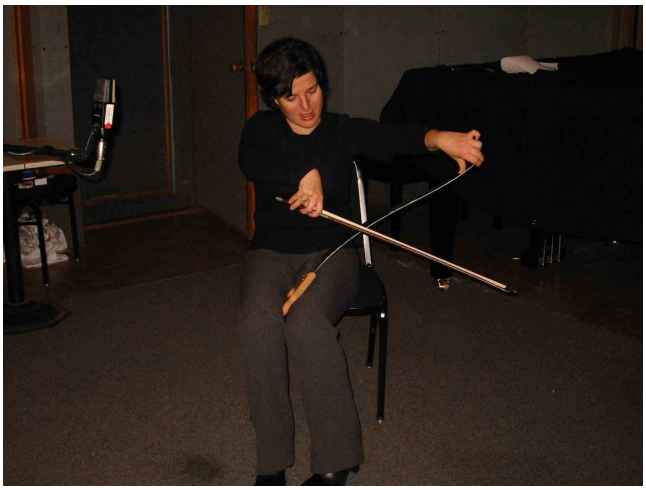

Figure 5.7: *The author playing an ordinary handsaw.*

5.2.1 Acoustics of the musical saw

Fig. 5.9 shows the spectrogram of the sound obtained from a Stanley 26 inches crosscut saw bowed at the curvature. The saw was blocked in one side using a clamp, and bent as shown in Fig. 5.8. This S-shape allows certain modes to be confined to the vicinity of the inflection by a process of reflection from points of critical curvature. The tone produced is almost sinusoidal, and the player controls the pitch by changing the curvature of the blade. Increasing the curvature gives rise to a higher pitch. The

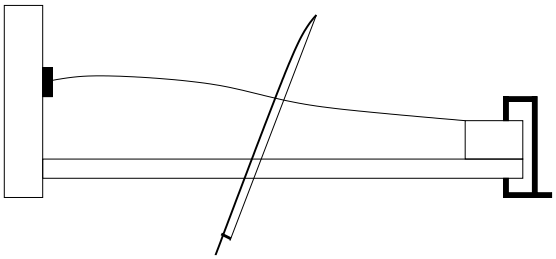

Figure 5.8: *Configuration of a saw fixed at both ends.*

vibrato is obtained by slightly moving the extremity of the saw in the hand of the player.

While the saw is bowed many partials appear in the spectrum, but when the bow is released mainly the fundamental frequency resonates.

Scott and Woodhouse in [101] propose a detailed description of the vibrational behavior of an elastic strip with varying curvature. Their analysis considers a parallel-sided strip, whereas a normal saw blade has a tapering width. Since the research presented in this dissertation has as main purpose the development of efficient physically inspired models which run in real-time and reproduce the sonorities created by the real instrument, a different approach from the one proposed in [101] is therefore needed.

5.2.2 Modeling a musical saw

Since the spectrum of a musical saw shows one strong mode, this instrument can be modeled using one banded waveguide excited by the same friction driven mechanism explained in the previous chapter and used for the bowed string simulation.

The spectrum of the simulated saw is shown in Fig. 5.10. Notice how, as in the recordings of the real instrument shown in Fig. 5.9, when the saw is sustained by the bow a rich spectrum appears, but when it is released only the fundamental frequency has a strong perceivable amplitude.

Notice also how the starting transient appears faster than in the recorded version. This is due to the switch on bowing gesture used in the simulated model.

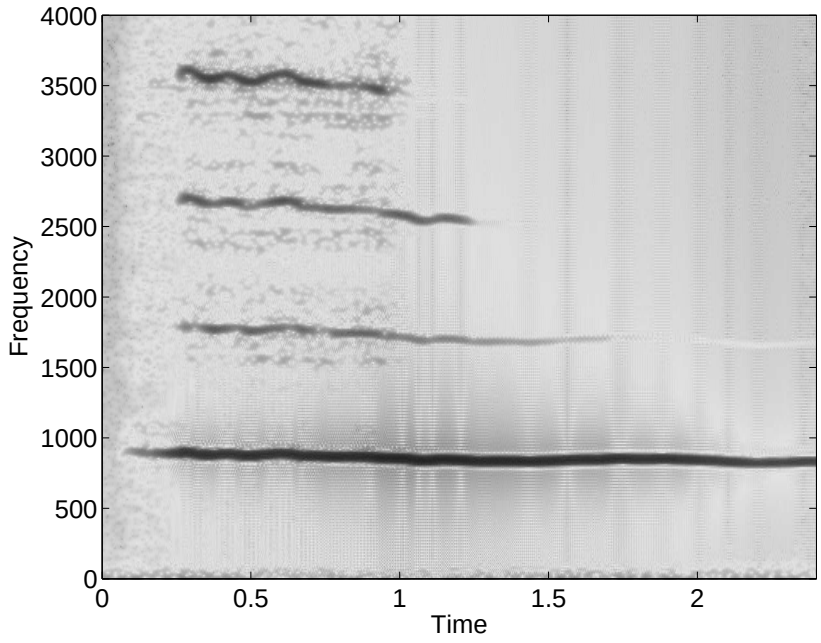

Figure 5.9: *Sonogram of a bowed saw tone. The saw is bowed for about one second and then left to resonate. While the fundamental has a long decay time, the higher harmonics are quickly damped.*

5.3 The glass harmonica

Glass harmonicas are musical instruments of two kinds. The first one, invented by Benjamin Franklin in 1757 and shown in Fig. 5.11, adopts glass bowls turned by a horizontal axis so that one side of the bowl dips into a trough of water. The second one is a combination of wineglasses similar to the ones shown in Fig. 5.12. Different melodies can be played on a set of tuned glasses (filled with appropriate amounts of water or carefully selected by size), simply by rubbing the edge of the glass with a moist finger. Rubbing rims of glasses in order to produce music became very popular in Europe during the 18th century. Music on glasses has been successfully composed by Mozart, Beethoven, and many others.

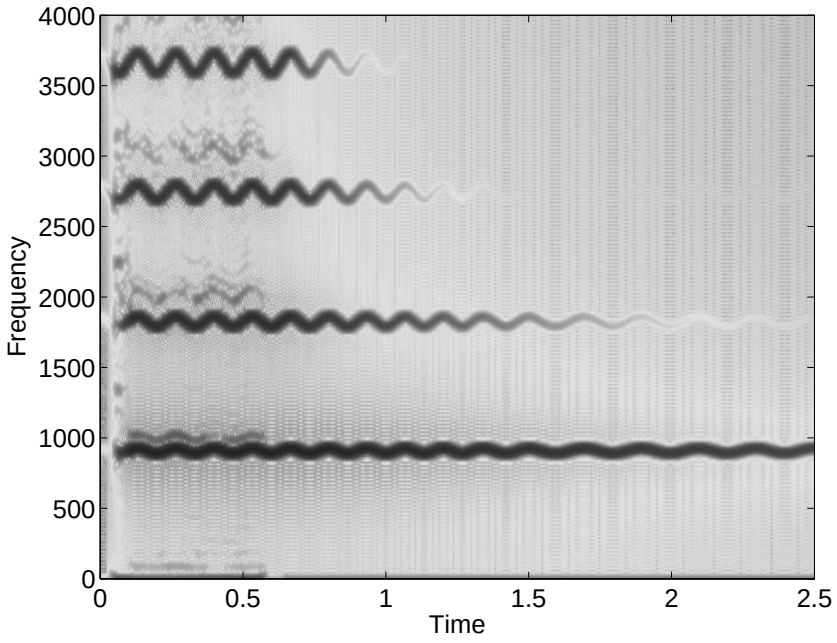

Figure 5.10: *Sonogram of a synthetic bowed saw tone. The saw is bowed for about 1.5 seconds and then left to resonate. Notice how, as in the real instrument, while the fundamental has a long decay time, the higher harmonics are quickly damped. The vibrato is also strongly noticeable.*

5.3.1 Acoustics of wineglasses

The main vibrational modes of a wineglass resemble those of a large church bell. The modes can be described with the label (m, n), where $2m$ is the number of nodes around the rim and n is the number of nodes around the circumference of the glass. The wineglass modes are generally of the form $(m, 0)$, and the resonance frequencies are nearly proportional to m^2 [95].

During the recordings two wineglasses of diameter 6.7 and 6.0 cm, respectively, and of height 10.3 and 9.5 cm were used. A microphone was positioned about 1 meter from the glasses. The wineglasses were tapped with an impulse hammer, rubbed with a wet finger, and bowed with a cello bow. Tapping the glass excites a number of "bell modes", while rubbing or bowing it strongly excites the $(2, 0)$ mode and its harmonics, and to a lesser degree the other modes as well.

Figure 5.11: *Benjamin Franklin's glass harmonica, which he called "armonica", as seen in the Franklin Institute Science Museum in Philadelphia. Picture courtesy of Ed Gaida.*

5.3.2 Analysis of the recordings

Fig. 5.14 shows the analysis and synthesis steps performed in order to model the glass harmonica as well as the Tibetan bowl described in the following section. From the recorded impulse response, the frequencies of the main resonances of the instruments were extracted, together with their damping factors, using spectral analysis. The fundamental frequency of each mode was extracted in order to build the digital waveguide network, each digital waveguide representing one mode. Moreover, the decay time of each mode was used to build the low-pass filters that model the decay characteristics of each mode. Each mode was used to build the digital waveguide network.

Fig. 5.15 shows spectra of the steady-state portion of bowed and rubbed tones of

Figure 5.12: *Young performers playing the glass harmonica.*

Mode	Freq.(Hz)	Amp. (dB)	Decay (dB/sec)
(2,0)	676	-16.669	-19.474
(3,0)	1625	-18.207	-52.477
(4,0)	3185	-10.582	-86.801
(5,0)	5111	0	-153.23
(6,0)	7127	-12.963	-172.42

Table 5.1: *Frequencies, relative magnitudes (normalized to 0 dB), and decay rates for the first few major modes of a large wineglass.*

the larger glass when played at medium volume, as well as its impulse response. Table 5.1 summarizes the resonance behavior of the same glass; here the mode frequencies are proportional to $m^{2.17}$.

5.3.3 Modeling a glass harmonica

A wineglass is a three-dimensional object and disturbances travel along the object in all dimensions. The object is however axially symmetrical, and the dominant modes are essentially circular modes [95]. Energy travels along the rim of the glass creating a closed path. Essentially the rim represents a bar being bent into a circular shape, closing onto itself at both ends. Hence the path is quasi one-dimensional.

For this reason, to model waves propagating along the rim of a wineglass we use

Figure 5.13: *A crystal wineglass.*

a network of circular banded waveguides (CBW), each waveguide being tuned to the fundamental frequency of the corresponding mode. A CBW is a connection of two waveguides bandlimited by a bandpass filter. The output of each waveguide is connected to the input of the other waveguide in a loop, as Fig. 5.16 shows.

Fig. 5.16 illustrates the situation in which only one mode is present. In the simulated instrument many modes appear, which are connected to the excitation model as shown in Fig. 5.17.

5.4 The Tibetan bowl

Oral tradition dates the singing bowl back to 560-180 B.C. in Tibet. These bowls have been found in temples, monasteries, and meditation halls throughout the world. Singing bowls are said to be made out of five to seven metals such as gold, silver, mercury, copper, iron, metal and tin, each representing a celestial body. Each of these metals is said to produce an individual sound, including partials, and together these sounds produce the exceptional singing sound of the bowl. Each bowl is hand hammered round to produce beautiful harmonic tones and vibrations. Today they are used in music, relaxation, meditation, and healing. The bowl used as a starting point for the simulations is shown in Fig. 5.18.

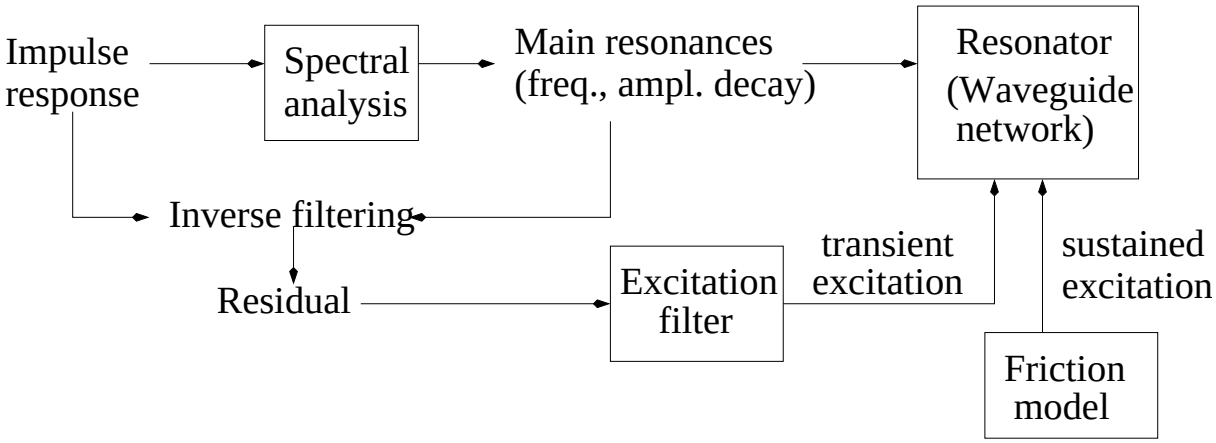

Figure 5.14: *Analysis and synthesis steps to obtain the bowl and wineglass models.*

5.4.1 Acoustics of the Tibetan bowl

From a perceptual point of view, the sound of a Tibetan bowl has two main characteristics: long sustained partials and a strong characteristic beating. Beatings are due to the slight asymmetries of the shape of the bowl. Without these asymmetries, a phenomenon called *degeneracy* would appear, i.e., a phenomenon in which different modes have the same frequency.

The impulse response of a Tibetan bowl while hit at eight different positions shown in Fig. 5.19 was recorded. The bowl was hit using a hard mallet, and the radiated sound was captured by a microphone placed at about 40 cm above the center of the bowl, as shown in Fig. 5.20.

The frequency responses corresponding to the eight different positions of Fig. 5.19 are shown in Fig. 5.21. In the topmost plot, the location of the eight modes is also represented. Notice the evolution of the modes according to the hitting positions. Notice also how the location of the modes strongest modes is clearly visible in the spectrum.

Fig. 5.22 shows the results of the peak detection algorithm obtained by performing a spectral analysis of the evolution of the partials of the Tibetan bowl. The impulse response of the instrument was analyzed performing an STFT of the sustained portion of the tone. The signal was windowed using an Hamming window of 2048 points. The

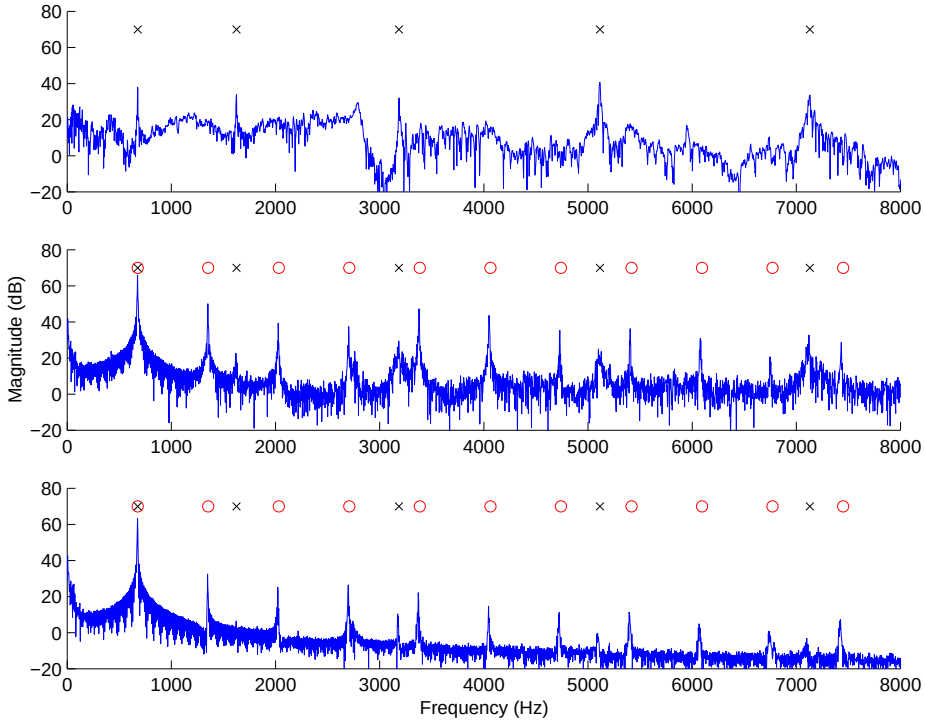

Figure 5.15: *Spectrum of a large wineglass. Top: hitting the glass with a hard mallet; center: bowing with a cello bow; bottom: rubbing with a wet finger. The circles indicate harmonics of the* $(2,0)$ *mode, and the x's indicate the* $(m,0)$ *modes for* $m = 2$ *to 6.*

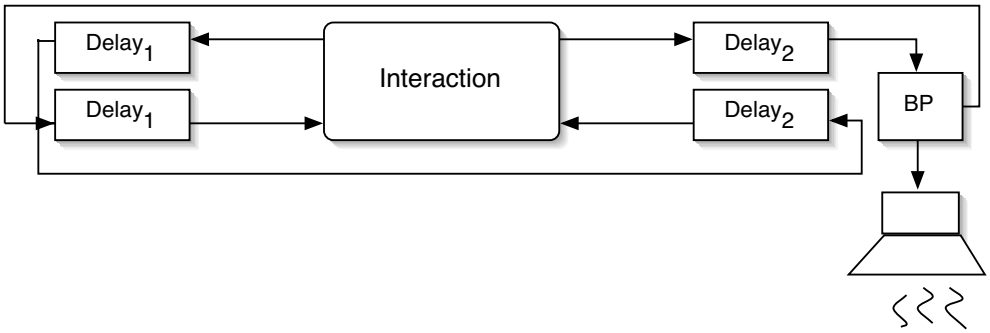

Figure 5.16: *Digital waveguide network structure of the bowl resonator. Representation of one mode. Each bi-directional delay line contains the waves propagating in the two sides of the bowl.*

size of the overlap between windows was of 256 points. On the top of the plot the two modes at lowest frequency is displayed. Notice the slow decay time of the three main modes. Notice also how the pitch detection algorithm is able to identify the characteristic beating of the instrument.

5.4.2 Modeling a Tibetan bowl

Considering the strong similarities between the structure of the bowl and the one of the wineglasses, circular banded waveguides were used to implement the bowl model. Beatings were implemented using detuned banded waveguides, i.e., banded waveguides made of a slight different length [107].

The spectrum of the synthetic bowl is shown in Fig. 5.23. Notice how the two main characteristics of the spectrum of the Tibetan bowl, i.e. the long decay time and the beatings, are present.

5.5 Bowed cymbals and plates

Contemporary music performances have seen a wide use on stage of bowed percussion instruments. It is therefore interesting to create computer simulations of such instruments, to be used in interactive performances.

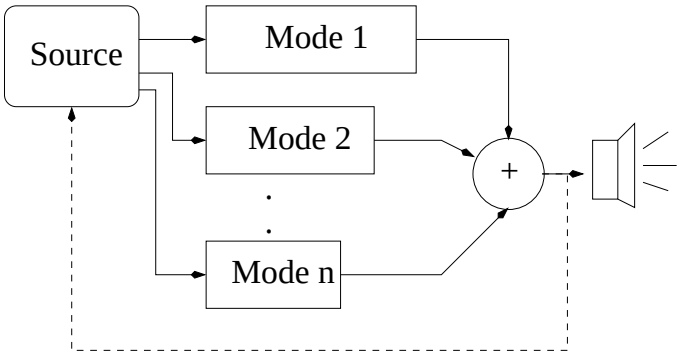

Figure 5.17: *Complete model, connecting the exciter and the resonator. Each mode is modeled as shown in Fig. 5.16. The dotted connection between the source and the resonator is due to the fact that they can be connected with either a feedback or a feed-forward loop.*

Figure 5.18: *The Tibetan singing bowl used for the analysis.*

Gongs and cymbals with shallow curvature exhibit a range of striking auditory effects such as pitch glide and energy cascade towards high frequencies, which are commonly used in Eastern music. These effects all depend upon dynamic nonlinearity, and in some cases upon chaotic vibration [31]. In instruments such as gongs and cymbals, while the modes are clearly distinguishable at low frequencies, at high frequencies they often mix with one another.

The nonlinear coupling between vibrational modes, moreover, is pretty strong, which makes many partials appear quickly in the spectrum. This is true no matter how the cymbal is excited.

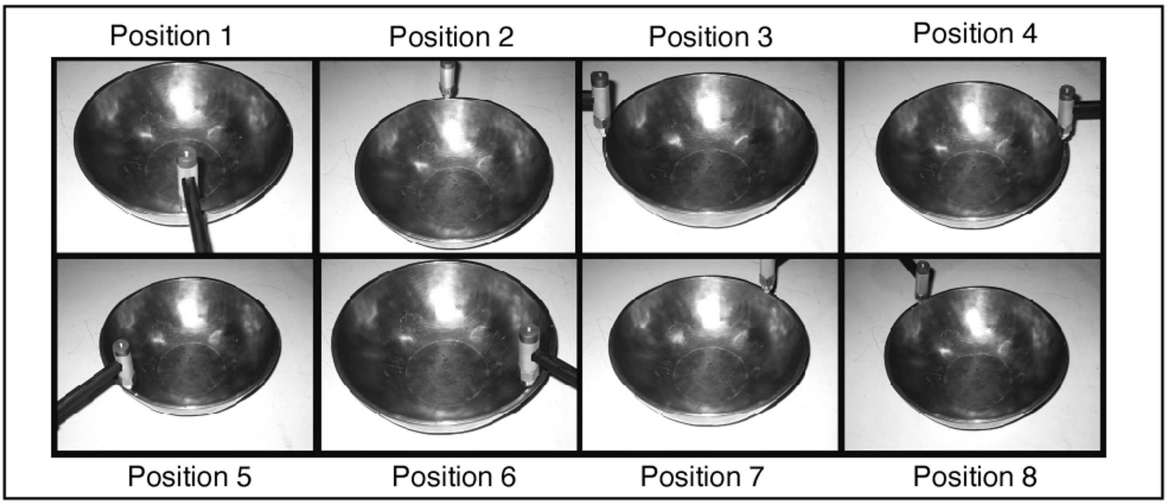

Figure 5.19: *The figure shows the eight different positions in which the bowl was hit during the recordings.*

5.5.1 Acoustics of bowed cymbals and plates

Fletcher in [31] proposes an investigation of nonlinearities in cymbals. The result of exciting a cymbal with a sinusoidal shaker shows that, while at low amplitudes the radiated sound is concentrated at the fundamental of the exciting frequency, increasing the amplitude enhances also the relative levels of all the partials. At a critical excitation amplitude the spectrum develops a complete set of subharmonics, and transitions to fully chaotic behavior can appear.

The mathematical problem of analyzing cymbal behavior in detail is rather complex. The frequency response of a bowed cymbal presents a large number of potentially active modes.

Fig. 5.27 shows the frequency response of an orchestral cymbal of diameter 41 cm bowed with a violin bow. The recording was made in a quiet room and the microphone placed about .3 meters from the cymbal. Some prominent peaks comprise the more steady oscillation of the cymbal, and there is still much energy at high frequencies, where modes are very dense.

Figure 5.20: *Position of the microphone used to record the impulse responses of the Tibetan bowl.*

5.6 Banded waveguide mesh

In the previous chapters, digital waveguides were introduced as an efficient synthesis technique to model quasi-harmonic resonating objects. Moreover, the digital waveguide mesh was used to simulate bodies of complex resonators such as the violin. In this chapter, the banded waveguide approach was adopted to simulate unusual friction driven musical instruments such as the musical saw and the Tibetan bowl.

The solutions proposed until now work well for resonators which present a rather limited amount of modes. For more complex resonators such as cymbals and plates, a different approach is more suitable. Since the ultimate goal is to create efficient sound synthesis models which run in real-time and perceptually reproduce sonorities of real instruments, a new solution is necessary.

In this dissertation a new resonator structure called *banded waveguide mesh* is proposed. The banded waveguide mesh is an extension to multiple dimensions of the banded waveguide, in order to allow a real-time implementation. The spectrum of a

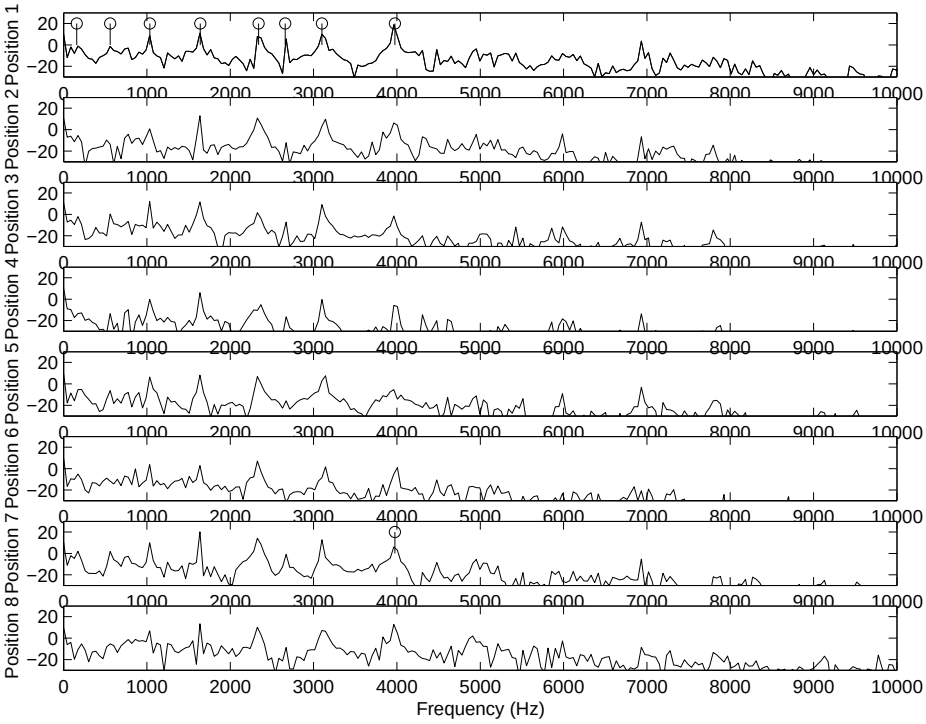

Figure 5.21: *Spectra resulting from varying the excitation position of the bowl. From top to bottom the plots represent positions from one to eight respectively, according to Fig. 5.19. In the topmost plot the location of the eight modes is also represented. Notice the evolution of the modes according to the hitting positions.*

vibrating system is split into frequency bands. For frequency bands where a single resonance is present, a one-dimensional digital waveguide is used. For bands where resonances are more complex, a 3D digital waveguide mesh is used, whose dimensions are chosen in order to match statistically and psychoacoustically the resonances of the high frequencies of the modeled object. More precisely, let f_c be the cutoff frequency above which an adequately high concentration of modes appear in the spectrum. For frequencies below f_c, banded waveguides simulate the modes of the resonators with higher amplitude. For frequencies above f_c, a 3D mesh simulates statistically and perceptually the high frequencies modes of the resonator. Let f_{0m} be the fundamental frequency of the mesh, i.e., the lowest mode generated by the mesh. Notice that the higher the value of f_{0m}, the smaller the dimensions of the waveguide mesh and the more efficient the implementation. The choice of f_{0m}, therefore, is an important

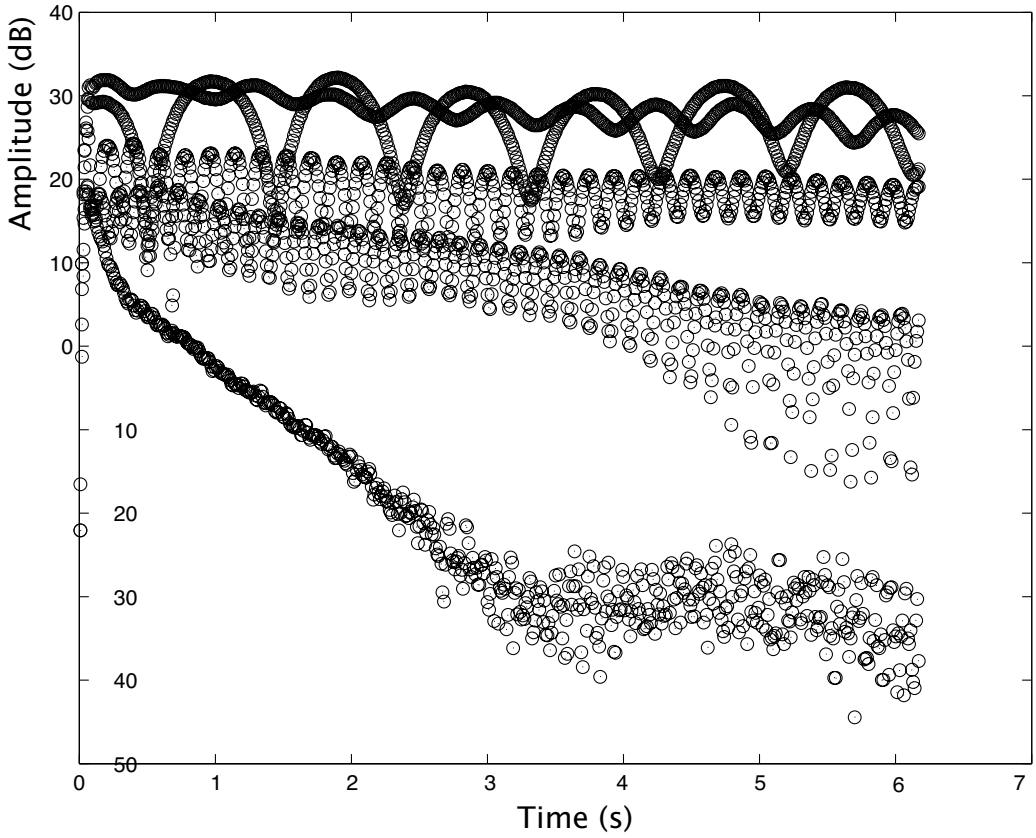

Figure 5.22: *Results of the peak detection algorithm on the Tibetan bowl's impulse response. Notice how the algorithm correctly detects the beating, which appear as amplitude modulation of the modes of the instrument with the longer decay time.*

decision for the resulting computational cost. As an example, the spectrum of a cymbal while hit at one extremity with a hard mallet is shown in Fig. 5.25. Notice how, up to about 8000 Hz, it is possible to identify bands where strong resonances are present. Above 8000 Hz modes are more dense and overlap. In this case, banded waveguides simulates mode up to 8000 Hz, while a 3D mesh simulates the dense concentration of modes above 8000 Hz.

The banded waveguide mesh is therefore a parallel connection of banded waveguides and one 3D mesh for high frequencies. The structure of a banded waveguide mesh is shown in Fig. 5.26. As in the case of banded waveguides, reflection filters are

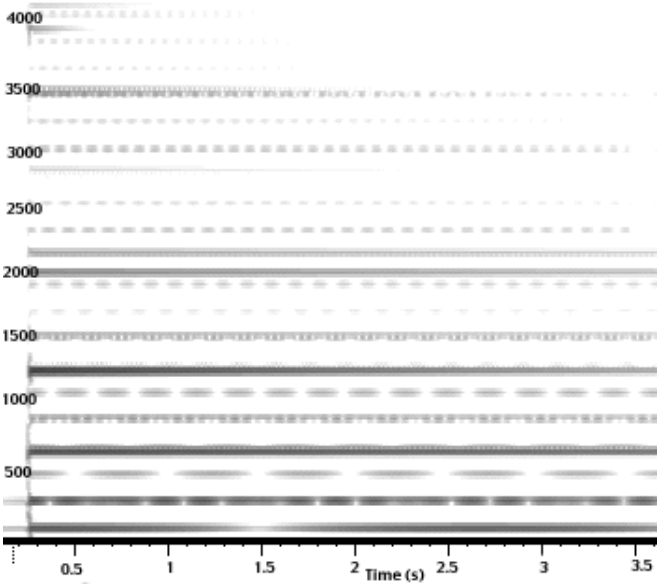

Figure 5.23: *Spectrogram of the synthetic Tibetan bowl.*

included in the structure in order to achieve desired decay characteristics.

Notice how the goal of the banded waveguide mesh is to obtain a small reverberator which statistically and perceptually behaves like the physical instrument which the mesh is simulating. In this case, the banded waveguide mesh does not retain any physical interpretation concerning the stucture of the modeled object. However, the development of such a modally dense small box reverberator allows to faithfully reproduce complex sonorities such as the ones produced when bowing plates or percussion instruments.

5.6.1 Modeling bowed cymbals

As an application of a complex resonator which is suitable to be simulated using a banded waveguide mesh, a model of bowed cymbal is proposed. Bowed cymbals lend themselves well to being modeled with a banded waveguide mesh structure. Low modes are excited by the bowing and energy is transfered to high-frequency modes which are chaotically coupled. The manner of excitation of these strong lower modes

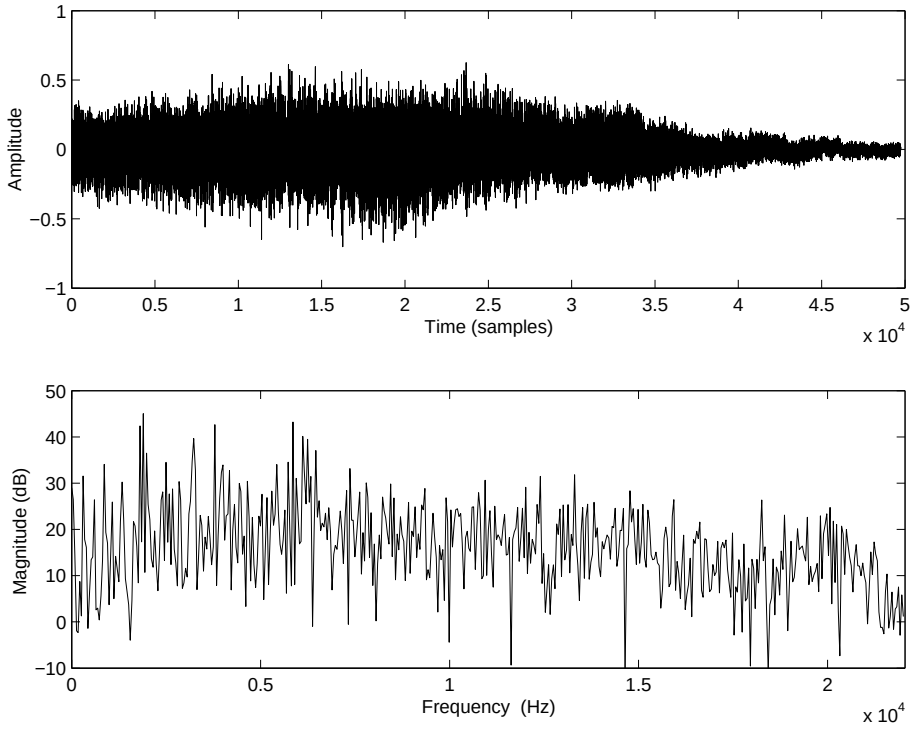

Figure 5.24: *An example of a bowed cymbal. Top: time domain waveform (sustain, decay and release). Bottom: frequency response; notice the density of high frequency modes.*

rely on the detailed mechanical interaction of the bow and the rim, and thus an interface between the bowing and the resonating plate is needed which preserves the spatiality of the bow/cymbal contact. Banded waveguides allow individual modes to be controlled in time, frequency and space. The shimmery, noiselike high-frequency modes are not a direct consequence of the bow excitation, so a banded waveguide mesh can be used as an approximation of a dense modal region.

Bowed cymbals can produce a wide range of sonorities with only small variations in bowing force, velocity and position. In certain cases the cymbal produces a very noisy growl and modes are very dense throughout the spectrum. In this case, a waveguide mesh with sufficient mode density at the lower frequency range would be too large to be implemented in real-time.

For low frequencies, banded waveguide structures allows for exact tuning of partial

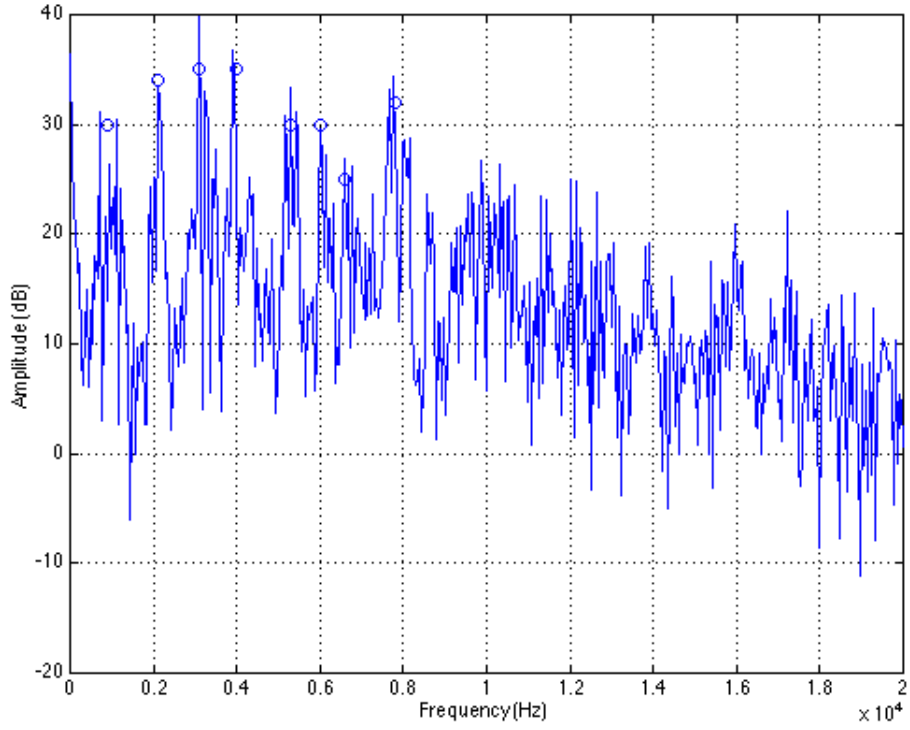

Figure 5.25: *Spectrum of a cymbal while hit with a hard mallet at one extremity. The circles represent the locations of the strongest low-frequency resonances.*

frequencies and hence avoids problems of waveguide meshes with grid dispersion and the related difficulty of tuning modes exactly [27].

In this application, due to the density of modes in the range modeled by the mesh, these difficulties can be neglected. The spectrum of the simulated bowed cymbal is shown in Fig. 5.27. The resonator was bowed with bow force $f_b = 0.31$ N and bow velocity $v_b = 0.035$ m/s, at one extremity of the mesh. The top part of Fig. 5.27 represents the frequency response of the bowed low-frequencies banded waveguides. The plot in the center represents the frequency response of the bowed 3D mesh. The bottom plot represents the complete resonator model, i.e., the combination of the banded waveguides and the 3D mesh. Notice how the nonlinearity of the friction driven excitation mechanism allows several modes to appear in the spectrum. Notice also how the spectrum of the 3D mesh is, as expected, rather weak at low

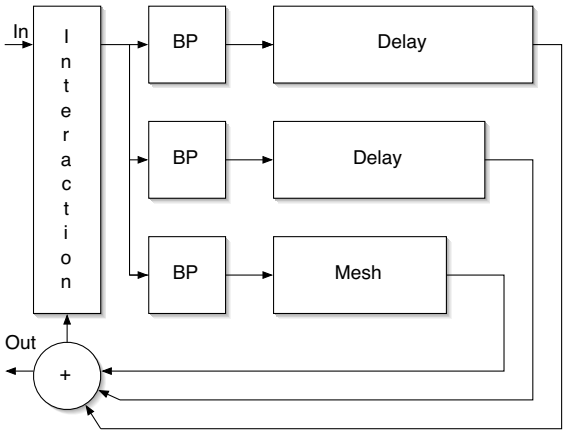

Figure 5.26: *A banded waveguide mesh with an arbitrary number of one-dimensional digital waveguides and a digital waveguide mesh.*

frequencies. From a perceptual point of view, the simulation results obtained by bowing the parallel connection of the banded waveguide plus the 3D mesh provide much more satisfactory results.

The resulting time and frequency domain simulations are shown in Fig. 5.28. Notice the complexity of the time domain as well as of the frequency domain waveform.

5.7 Other instruments

In addition to the instruments presented in the previous section, interesting sonorities are produced also by other unusual friction driven musical instruments such as the cuica and the guiro.

The cuica is a single-headed Brazilian friction drum, in which sound is produced by rubbing a short stick attached to the membrane on the inside of the instrument. It produces an unearthly sound and exceptional pitch range: hence its popularity as a solo instrument. The pitch is altered by pressing the thumb against the skin near the node of the friction stick.

The guiro is a percussion instrument from Panama made from a gourd. A stick is scraped across the guiro's notched surface to produce its sound. Modern guiros

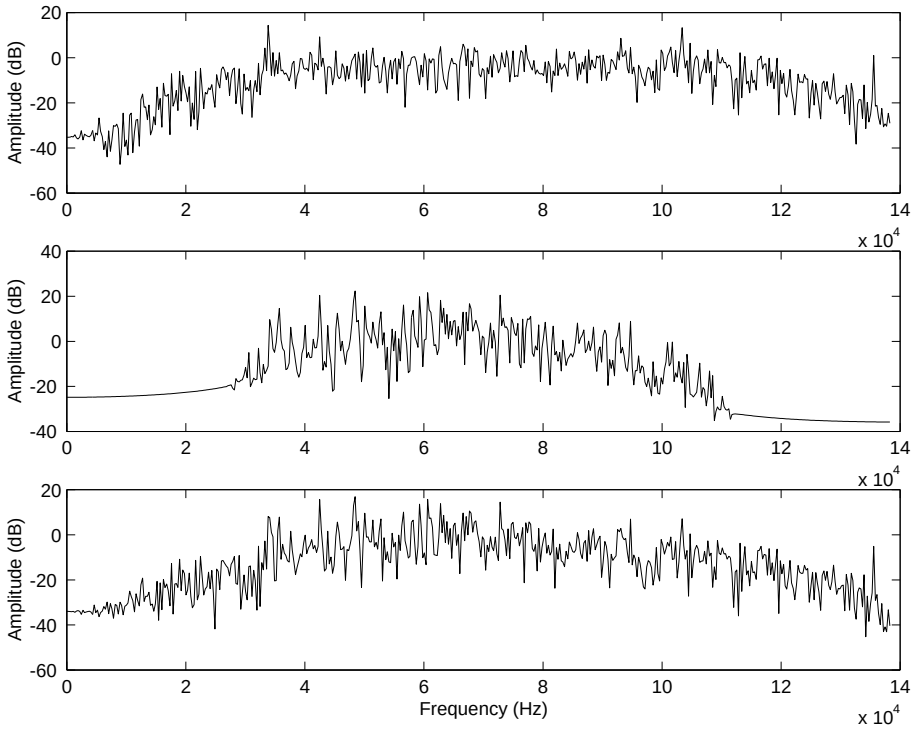

Figure 5.27: *Spectrum of a synthetic bowed cymbal. Top: bowed low-frequency resonators, center: bowed 3D mesh, bottom: the complete model.*

are made from wood or plastic. Models of such instruments are not described in this dissertation. However, it is interesting to observe that their sonorities can be simulated by using the same friction driven excitation mechanism.

5.8 Friction in everyday life

In everyday life, the awareness of friction as an acoustic phenomenon is mostly related to such unpleasant situations as squeaks and squeals in automotive environments, or rail-wheel noise. However, as described before, friction affects the sonic environment in different ways, and sometimes friction induced vibrations are also desirable. Among the many everyday examples of friction sounds, a bowed string and brake noise represent probably the extremes in terms of acoustic output [3]. No matter which is the degree of appreciation of friction sounds, their ubiquitous presence in our everyday

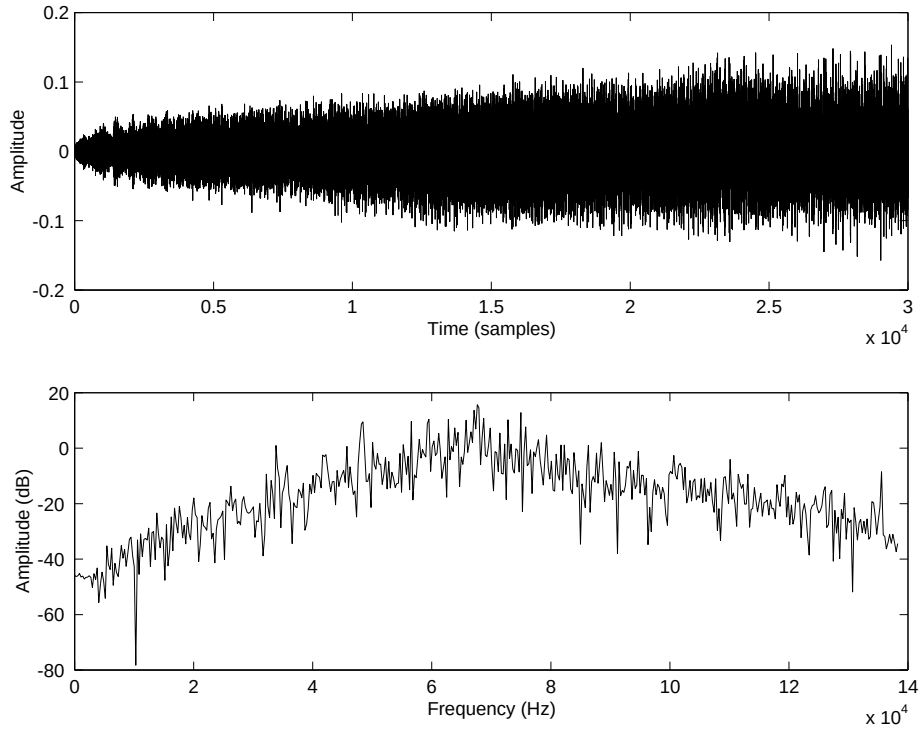

Figure 5.28: *Top: time domain waveform of a synthetic bowed cymbal. Bottom: frequency domain waveform of a synthetic bowed cymbal.*

life makes them an interesting research topic not only in robotics and haptics but also in virtual reality simulations. In a collaboration with Federico Avanzini and Davide Rocchesso, several animations using external graphical libraries of `pd`, such as the OpenGL-based `gem`[1] were designed. The applications are highly interactive and use a standard mouse as the input device for controlling high-level parameters. Namely, x- and y-coordinates of the pointer are linked to the external forces f_{ee} and the normal force f_b, respectively.

The elasto-plastic friction model described in Chapter 2 was used to produce the sound connected to such animations. The parameters of the elasto-plastic friction model, together with a phenomenological description, are described in the following section.

[1] http://gem.iem.at/

5.8.1 Control parameters

High-level interactions between the user and the audio objects rely mainly upon three interaction parameters. These are the external forces acting on each of the two objects, which are tangential to the sliding direction, and the normal force f_N between the two objects. It must be noticed that treating f_N as a control parameter is a simplifying assumption, since oscillatory normal force components always accompany the friction force in real systems [3]. The remaining parameters belong to a lower level control layer, as they are less likely to be touched by the user and have to be tuned at the sound design level.

Such low-level parameters can be grouped into two subsets, depending on wether they are related to the resonators' internal properties or to the interaction mechanism. Each mode of the two resonating objects is tuned according to its center frequency and decay time. It has been shown [62] that these parameters are strictly related to the perception of material. Additionally, a modal gain (which is inversely proportional to the modal mass) can be set for each resonator mode, and controls the extent to which the mode can be excited during the interaction. The implementation allows position dependent interaction by giving the option to choose any number of interaction points. A different set of modal gains can be set for each point.

A second subset of low-level parameters relates to the interaction force specification. The triple $(\sigma_0, \sigma_1, \sigma_2)$ (see Eq. (2.13)) defines the bristle stiffness, the bristle internal dissipation, and the viscous friction, and therefore affects the characteristics of signal transients as well as the ease in establishing stick-slip motion. The triple (f_c, f_s, v_s) (see equation (2.14)) specifies the shape of the steady state Stribeck curve. Specifically, the Coulomb force and the stiction force are related to the normal force through the equations $f_s = \mu_s f_N$ and $f_c = \mu_d f_N$, where μ_s and μ_d are the static and dynamic friction coefficients. Finally, the breakaway displacement z_{ba} (see equation (2.15)) is also influenced by the normal force. In order for the function $\alpha(v, z)$ to be well defined, the inequality $z_{ba} < z_{ss}(v)\ \forall v$ must hold. Since $\min_v z_{ss}(v) = f_c/\sigma_0$, a suitable mapping between f_N and z_{ba} is

$$z_{ba} = c f_c/\sigma_0 = c\mu_d f_N/\sigma_0, \quad \text{with} \quad c < 1. \tag{5.8}$$

One approach to determine the low-level model parameters is "hand and hear" direct manipulation. Since many "knobs" are available, the phenomenological description of model parameters given in Table 5.2 can be a helpful starting point for the sound designer. Besides direct empirical search, modal parameters can be sometimes found in closed form (only for simple geometries), they can be obtained from analysis of recorded sounds of real objects [84], or derived from finite element object modeling [78]. Interaction parameters can also be found from analysis of real signals. Parameter estimation techniques are the subject of many studies in automatic control, an extensive discussion of such issues is provided in [4]. In certain cases typical parameter values can be found from the literature (see e.g., [8] for bowed string instruments).

Symbol	**Physical Description**	**Phenomenological Description**
σ_0	bristle stiffness	affects the evolution of mode lock-in
σ_1	bristle dissipation	affects the sound bandwidth
σ_2	viscous friction	affects the speed of timbre evolution and the sound pitch
σ_3	noise coefficient	affects the perceived surface roughness
μ_d	dynamic friction coeff.	high values reduce the sound bandwidth
μ_s	static friction coeff.	affects the smoothness of sound attack
v_s	Stribeck velocity	affects the smoothness of sound attack
f_N	normal force	high values give rougher and louder sounds

Table 5.2: *A phenomenological guide to the variables of the elasto-plastic friction model.*

Braking effects Through several mechanisms, different kinds of vibrations and sonorities develop within brakes. In the case of rotating wheels slipping sideways

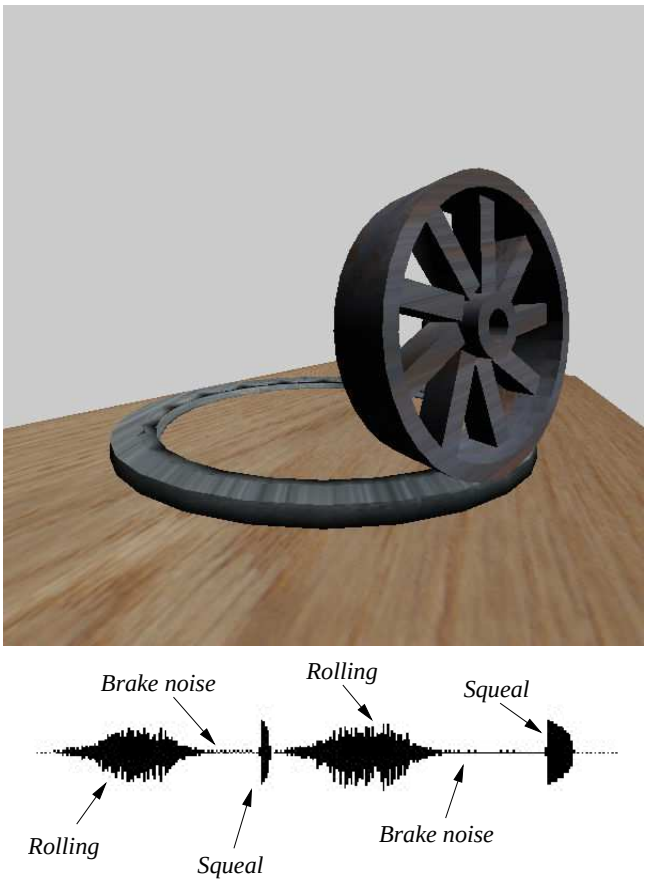

Figure 5.29: *3D animation and waveform: a wheel which rolls and slides on a circular track.*

across the rails, the friction forces acting at the wheel rim excite transverse vibrations. In order to test the ability of the model to simulate brake noise, the simulation depicted in Fig. 5.29 has been designed, where a wheel driven by the external force f_{ee} rolls on a circular track. The rolling sound is obtained as the result of a sequence of micro-impacts [93].

When a positive normal force is applied, the wheel is blocked from rolling and the friction model is triggered. Neat stick-slip is established only at sufficiently low velocities, and brake squeals are produced in the final stage of deceleration. The resulting effect convincingly mimics real brake noise.

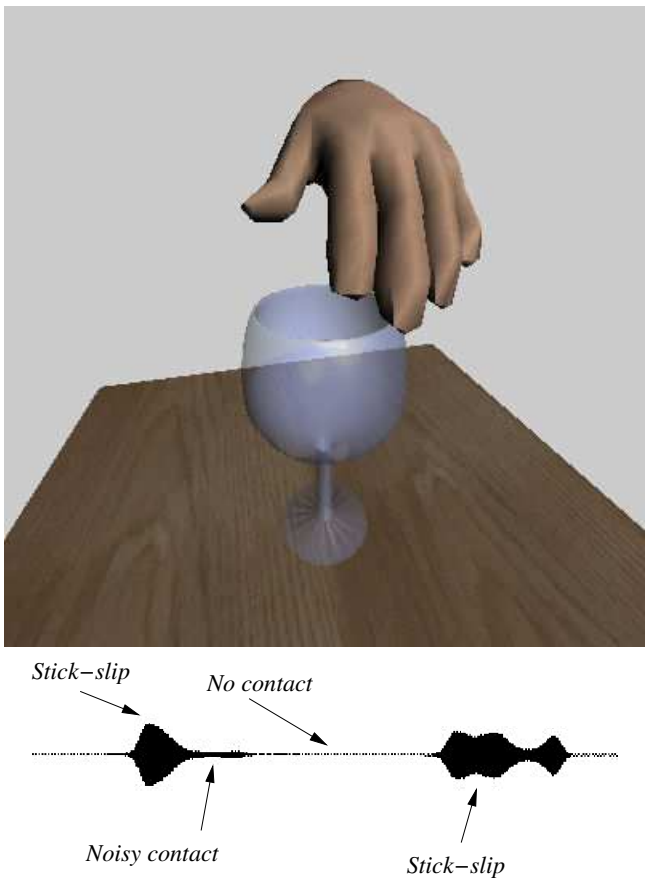

Figure 5.30: *3D animation and waveform: a moisty finger rubbing a crystal glass.*

Wineglass rubbing An animation of a rubbed wineglass was furthermore designed, using the wineglass model previously described in this chapter. As in the previous example, the rubbing finger is controlled through mouse input. Interestingly, setting the glass into resonance is not a trivial task and requires some practice and careful control, just as in the real world.

Door squeaks The third everyday sound which was simulated is the squeak produced by the hinges of a swinging door. In this situation, different combinations of transient and continuous sliding produce many squeaks which create a broad range of sonic responses. The example depicted in Fig. 5.31 uses two exciter-resonator pairs,

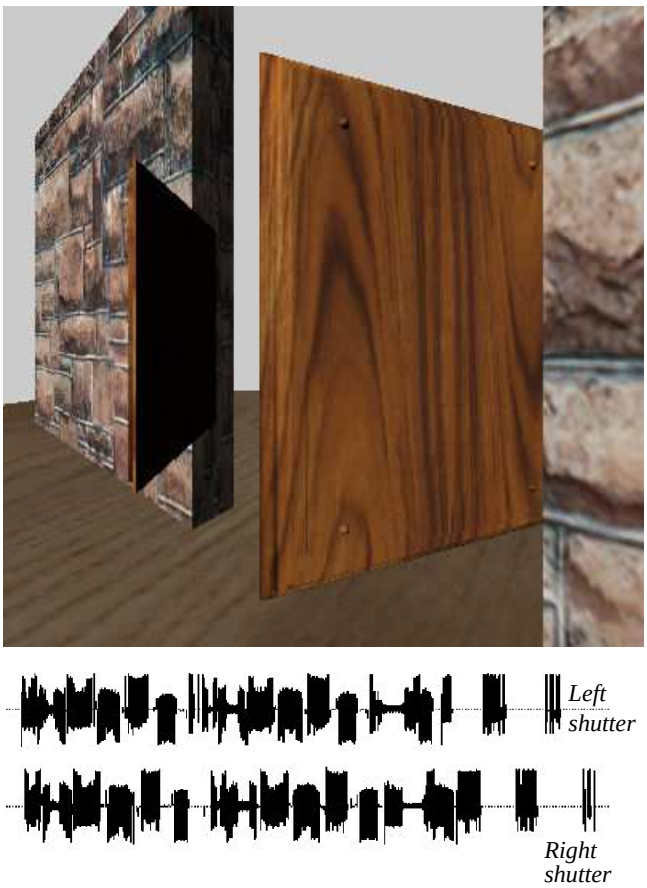

Figure 5.31: *3D animation and waveform: a swinging door, each of the two shutters is linked to a friction module.*

one for each of the shutters. In this case the modal frequencies of the objects have been chosen by hand and hear tuning on the basis of recorded sounds. The results are especially convincing in reproducing complex transient and *glissando* effects which are typically found in real door squeaks.

5.9 Final remarks

In this chapter computer models of different friction driven systems based on several flavours of banded waveguides have been proposed. An overview which summarizes

the available literature on physics based models of friction driven musical instrument is given in Table 5.3.

Instrument	**Characteristics**	**Modeling technique**
bowed string	quasi-harmonic modes	digital waveguides [71, 120, 117]
bowed bar	few inharmonic modes	banded waveguides [29] and modal synthesis [54]
musical saw	one strong mode	banded waveguides [104]
Tibetan bowl	few inharmonic modes	banded waveguides [28, 107]
wineglass	few inharmonic modes	banded waveguides [28, 107] and modal synthesis [93]
squeaking doors	few inharmonic modes	modal synthesis [93]
guiro	few inharmonic modes; combination of stick-slip and transient excitation	PhiSM [18]
bowed cymbals	many inharmonic modes	banded waveguide mesh [103]

Table 5.3: *Summary of physical modeling techniques used to simulate different friction driven musical instruments.*

For a given instrument, the choice of a particular synthesis technique which simulates it, is given by different factors. As shown in Table 5.3, digital waveguides are an efficient synthesis technique to simulate quasi-harmonic resonators such as strings.

For systems with few inharmonic modes, usually modal synthesis or banded waveguides are preferred. Physically informed sonic models (PhiSM) are a synthesis technique introduced by Cook in [18]. The idea behind PhiSM is to use particle synthesis models, in which each particle is a modal object with a certain frequency and decay time. A probability function describes how such particles interact. PhiSM algorithms are particularly useful to simulate sounds of shakers, and maracas, although they have also been used in [18] to reproduce friction driven instruments such as a guiro.

Since none of the previous solutions is suitable to simulate sonorities produced when bowing complex resonators such as a cymbal, in this dissertation a new resonator structure called the banded waveguide mesh was introduced.

Fig. 5.32 shown the block diagram of the different exciter-resonator structures adopted in this dissertation. For simplicity, the excitation is placed at one side of

the waveguide and losses are not represented. Fig. 5.32 part A) represents a one dimensional waveguide (1D WG) excited in a feedback loop by a nonlinear mechanism (NL). In this dissertation, the nonlinear mechanism is represented by the friction model. Notice how, in all the different configurations, the friction model is also the only nonlinearity present in the system. Fig. 5.32 part B) represents the same digital waveguide as before, with a model for the body resonances as proposed in Sec. 4.6. Fig. 5.32 part C) represents one banded waveguide (1D BW) such as the one used to simulate a musical saw, while Fig. 5.32 part D) represents a connection of several banded waveguides (in this case two) which was the model adopted to simulate, for example, the Tibetan bowl and the rubbed wineglass. Fig. 5.32 part E) represents the banded waveguide mesh, i.e. the structure proposed to simulate complex bowed resonators.

Notice how an automatic technique which analyzes a resonating object, and determines the most suitable synthesis technique to simulate such object, does not exist yet. This issue is left for further research.

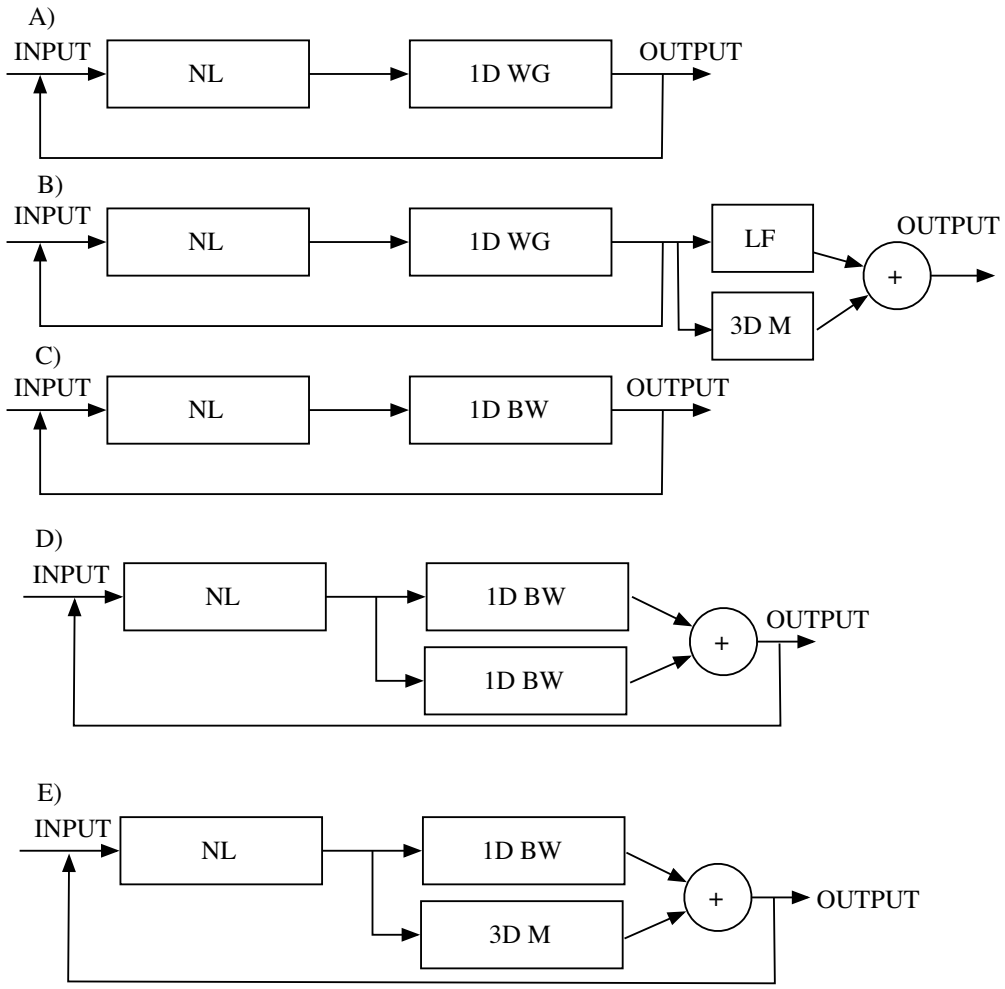

Figure 5.32: *Block diagrams of the different waveguide-based data structures developed in this chapter and in the previous one. For simplicity, it is assumed that the excitation point is placed at one extremity of the waveguide, and losses are not represented. A) a one dimensional digital waveguide, B) a one dimensional digital waveguide filtered through the body model described in Sec. 4.6, C) one banded waveguide, D) a connection of two banded waveguides, E) a banded waveguide mesh.*

Chapter 6

Playability studies

It is well known by bowed string players that some instruments are easier to play than others, although defining what makes an instrument more or less playable is not an easy and absolute task. Usually, skilled players are able to compensate for the lack of quality of their instrument and manage to still produce pleasant sonorities.

An advantage of the availability of computer simulated bowed strings is the possibility of carefully controlling all the parameters that influence the resulting sonorities of such instruments and investigate their role on the playability of the model. Although bowed string physical models are not yet at the state to compete with traditional instruments, much progress in the last decades has been obtained both regarding computer simulations, some of which have been discussed in Chapter 4, and also to create interfaces able to play such computer simulated instruments [76, 139].

In [100], Schumacher and Woodhouse mention four classes of parameters that are related to a bowed string instrument. The first class, which is shown in Table 6.1, represents the parameters related to the physical properties of the string itself, such as the string's length l, its tension T and mass per unit length M, and its Q-factor. The second class of parameters, described in Table 6.2, refers to the parameters that the player controls, such as the bow velocity, bow position, bow force and amount of bow hair in contact with the string. Other parameters considered important for the resulting sonorities are the parameters of the body of the instrument (i.e., the resonances of the body of the instrument) and the friction parameters. In the case

of a synthetic bowed string, friction parameters mean the particular friction model used and the friction coefficients chosen for that particular model. A description of the role of friction parameters for the elasto-plastic model described in Chapter 2 was shown in Table 5.2.

Symbol	**Physical description**	**Phenomenological description**
B	bending stiffness	affects the string's harmonicity
l, m, T	string length, mass and tension	affects the frequency
Q	Q-factor	affects the decay time of the string

Table 6.1: *Physical parameters of a bowed string and their effect on the resulting sonorities.*

Symbol	**Physical description**	**Phenomenological description**
f_b	bow pressure	affect amplitude, affects the timbre
v_b	bow velocity	affects the amplitude and the timbre
β	bow position	affects the timbre
dw	bow width	affects the timbre

Table 6.2: *Player's control parameters of a bowed string and their effect on the resulting sonorities.*

Fig. 6.1 shows three different spectra of the same violin tone bowed at three different dynamic levels: pianissimo, mezzo forte and fortissimo. The combination of the different input parameters of the violin allows to obtain these different dynamic levels. Moreover, a change of dynamic does not simply mean that the amplitude of the partials changes linearly, but creates also a significant variation in the timbre of the instrument. As an example, an increase in bow pressure increases the overall amplitude of the resulting tone, but also varies significantly the timbre.

In this chapter the role of the control parameters of different friction models is explored when applied to a waveguide string resonator. The focus is on Woodhouse's playability definition [134], which is described in the following section.

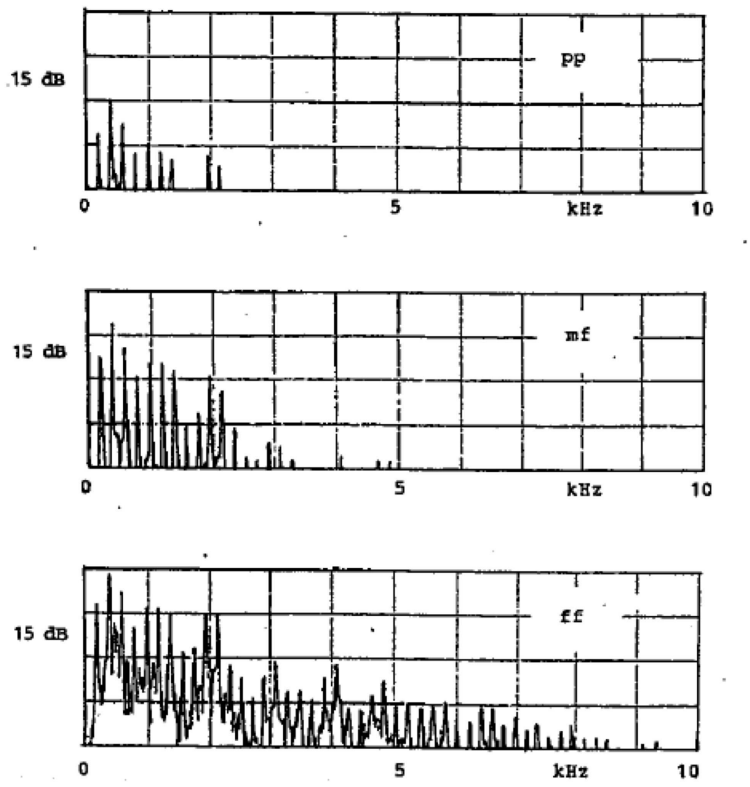

Figure 6.1: *Spectral differences obtained by bowing a violin pianissimo, mezzo forte and fortissimo, from [50].*

6.1 Quality Measures

The quality of a bowed-string instrument is more reliably determined by the player than the listener [99]. While the "tone" is clearly an important component of quality, a "poor tone" can be compensated in many ways. A more intrinsic quality which is less easily compenated is the "playability" of the instrument.

6.1.1 Evaluating playability

"Playability" can be loosely defined as the "volume" of the multidimensional parameter space in which "good tone" is produced.

The "playability" evaluation technique, described in [134, 100, 99], includes two high-level components: (1) a bowed-string software model [71] which is calibrated by measured and/or inferred physical data, and (2) an algorithm for evaluating the quality of the model's output [134, p. 149],[99].

In this particular study, we define playability in terms of the minimum and maximum bowing force over a range of bowing positions for steady bowing (constant bow force and velocity). The type of bowed-string motion is automatically classified [134] for a reasonable range of bow forces and positions along the string, and these are used to produce a kind of empirical "Schelleng diagram" [135]. As discussed in the following subsection, a Schelleng diagram displays at a glance the region of "good behavior" for the bowed string model, *i.e.*, the region of the parameter space in which simple "Helmholtz motion" is obtained.

6.1.2 Schelleng Diagram

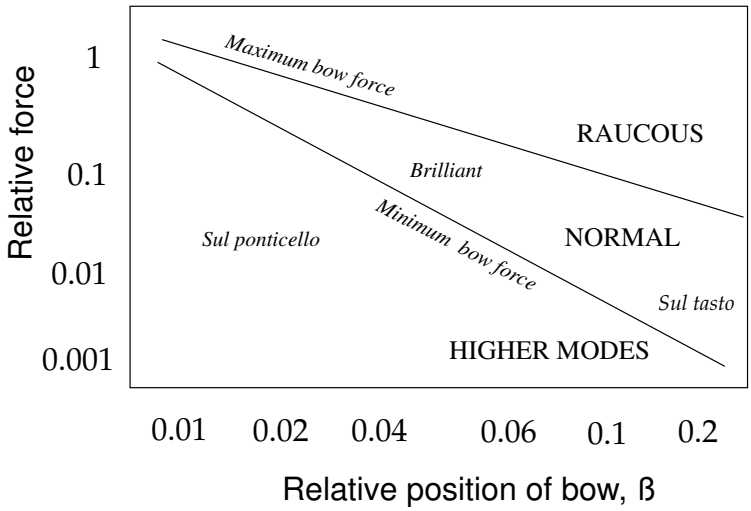

Figure 6.2: *Theoretical Schelleng diagram.*

Fig. 6.2 shows the classical "Schelleng diagram" [98] indicating the theoretical minimum and maximum bow force as a function of bow position along the string. Between the bow-force limits, "Helmholtz motion" is possible. Helmholtz motion is characterized by a single "corner" traveling back and forth on the string under

an approximately parabolic envelope. While the corner is between the bow and the nut or finger, the string is sticking to the bow. When the corner is on the shorter part of its journey, between the bow and the bridge, the string is slipping under the bow. This fundamental picture of normal bowed-string behavior was first discovered and described by Helmholtz in the mid-nineteenth century [130]. Further details of possible bowed-string motion are summarized in [99], and a review of theoretical models can be found in [133].

Schelleng's formula for maximum bow force is given by:

$$f_{max} = \frac{2v_b}{Y_0\beta(\mu_s - \mu_d)} \tag{6.1}$$

where, as before, v_b is the bow velocity, Y_0 is the characteristic string admittance, μ_s and μ_d are the static and dynamic friction coefficients respectively and β is the bow position. Minimum bow force is given by:

$$f_{min} = \frac{v_b}{2RY_0^2\beta^2(\mu_s - \mu_d)} \tag{6.2}$$

where R is the assumed dashpot rate of the bridge.

Below the minimum bow force, a second Helmholtz corner is likely to appear (or more), due physically to *multiple slips* per period. This regime is is often referred to as "surface sound" and is common in "sul ponticello" playing.

Above the maximum bow-force, the Helmholtz corner may not be strong enough to initiate slipping when passing the bow toward the bridge. In this case, the time-keeping function of the traveling corner may be disrupted, leading to aperiodic, even "raucous" sound.

Part of the "playability" of a bowed-string instrument is the ease with which Helmholtz motion can be achieved. Skilled players strive to achieve Helmholtz motion as quickly as possible in "smooth" playing [40, 8]. It is even possible to hit Helmholtz motion immediately on the first period, which is especially desirable on a double bass for which a single period can be tens of milliseconds long.

All the simulations in this chapter examine a cello D string with bending stiffness

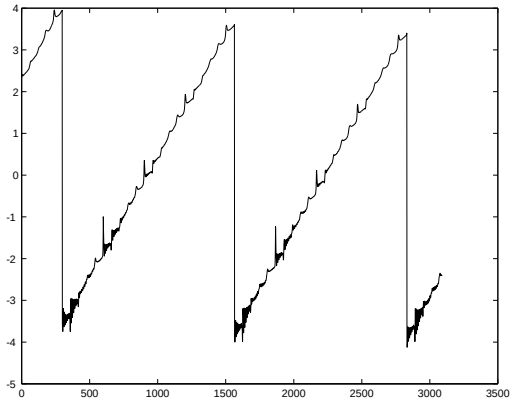

Figure 6.3: *An example of anomalous low frequency motion.*

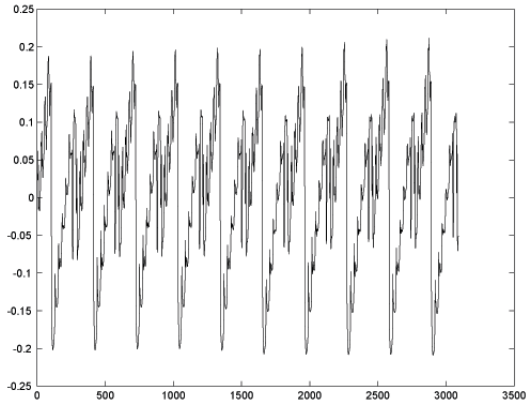

Figure 6.4: *An example of multiple slips motion.*

$B = 0.0004$, where B is the coefficient of the fourth derivative of string displacement with respect to position in the wave equation for stiff vibrating strings [134, p. 133], a violin A string and a violin G string with no stiffness. The sampling rate in all cases is set to 44.1 kHz.

In all simulations the string, starting from rest, is excited by a constant bow velocity v_b of 0.05 m/s.

In each computed Schelleng diagram, the bow force f_b is varied between 0.005 and 5 N, and the normalized distance β of the bow from the bridge is varied between 0.02 and 0.4 (where 0.5 would be at the string midpoint).

The torsional wave speed is 5.2 times the transverse wave speed; the transversal

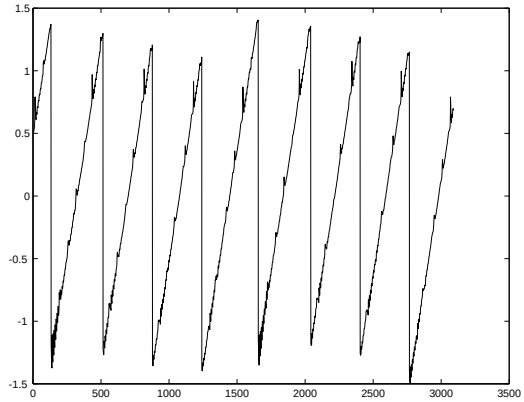

Figure 6.5: *An example of raucous motion.*

and torsional impedances are 0.55 and 1.8 kg/s, respectively. At the nut and bridge side, transversal and torsional wave losses are modeled by low-pass filters as described in the previous sections.

In running such simulations, there is the desire to prove the following two statements:

- the efficient implementation of the bow-string physical model described in Chapter 4 produces similar playability regions as the ones described by Woodhouse in [136].

- The elasto-plastic friction model behaves better than the "classic" friction models.

For this reason, as done in [136], we do not consider the role of the body, as well as of the finite bow width.

6.2 Simulation results

The simulation results are summarized as follows. First, we consider the effect of torsional waves for the plastic friction model (which is believed to be the most physically accurate). Next, we look at the other choices of friction models and we examine presence or absence of torsional waves as well as presence or absence of stiffness.

6.2.1 Effect of Torsion-Wave Simulation on Playability

Fig. 6.6 shows the empirical Schelleng diagram obtained by running the simulation with the plastic friction model installed.[1] The darker shaded region including the squares is defined as the "playable" region of the parameter space, where Helmholtz motion is established. The region including the circles is the one in which multiple slips are established. We see that there is good qualitative agreement with the theoretical Schelleng diagram, as desired and expected.

Fig. 6.7 shows the same case of Fig. 6.6 except without including simulation of torsional waves. We find that the playability region is not altered very much when torsional waves are removed. Looking only at the Helmholtz region, there are 65 pixels of Helmholtz-motion in Fig. 6.6, and 63 in Fig. 6.7. On the whole, the results are fairly comparable. However, the Helmholtz region is more contiguous without torsional waves. Evidently, torsional waves can reflect at a "bad time" so as to disturb the Helmholtz motion, as indicated by the '$\circ$' amidst the '$\Box$'s in Fig. 6.6.

The good news for synthesizer builders is that the added expense of torsional wave simulation (which basically adds a coupled "second string") does not appear to improve playability. Since torsional waves are not prominent in the radiated sound either, it seems warranted to leave them out of synthesis models, even in the highest quality instances.

It is well known that string losses are required for stability of the Helmholtz motion [34, 135, 100]. The transduction of transverse waves into (more highly damped) torsional waves represents a significant loss on the string. It is therefore natural to ask whether the preceding results might be improved by including only the (real) losses corresponding torsional wave creation, since this costs little or nothing extra in the simulation. In other words, the model generates torsional waves realistically, but they are treated as if they are fully absorbed by the string terminations. This simplified torsional wave simulation was suggested as a possibility in [100, p. 512]. It turns out as a surprise the fact that simulating the plastic model without torsional waves, but maintaining losses generated by torsional waves at the bow, collapses the

[1] The automatic evaluation technique which estimates the quality of waveforms is courtesy of Jim Woodhouse.

playability region to zero pixels. The reason why this happens is not completely clear and left to further investigation.

Fig. 6.8 shows the Schelleng plot obtained by running the plastic friction model with torsional waves and the same parameters as before. The string, instead of starting from rest, starts from an already established Helmholtz motion. Notice that, as somehow expected, the playability region in increased.

6.2.2 Effect of the Bow-String Friction Model

Up to now we have only looked at the plastic friction model which is believed to be the most accurate physically. We now look at the effect of using the older simpler models labeled "exponential" and "hyperbolic" in the previous chapters.

Exponential Friction Model

Fig. 6.9 shows the Schelleng diagram obtained using the classic exponential friction model with torsional wave simulation included. We see that the plastic friction model (see Fig. 6.6) "plays better" close to the bridge, and it has a larger region of Helmholtz motion, especially when bowing somewhat away from the bridge. The combined areas of Helmholtz and multiple-slipping motion, however, are somewhat larger with the exponential friction model.

Fig. 6.10 shows the exponential friction case with torsional wave simulation removed (completely). As in the plastic friction-model case, the playability is comparable, and arguably even improved. Note the greater "reliability" of playing near the upper bow-force limit. While there are 48 Helmholtz pixels in the full-simulation case, and only 42 in the case without torsional simulation, the Helmholtz region is more contiguous and solid, having fewer interior pitfalls.

Hyperbolic Friction Model

Fig. 6.11 and Fig. 6.12 show the Schelleng diagram obtained by running the simulation using the hyperbolic friction model, with and without torsional waves respectively. The results are quite similar to the preceding exponential model case.

6.2.3 Effect of string stiffness

To examine if stiffness affects playability, Fig. 6.13 represents the simulated Schelleng plot for a cello D string without stiffness. The simulation is run using the exponential friction model. As expected, stiffness does not affect the playability of the model. The same playability region as the one of Fig. 6.9 is obtained. As explained in Chapter 4, the role of stiffness is to round the sharp Helmholtz corners. Stiffness, however, does not affect the quality of the resulting waveform.

6.2.4 Velocity versus force playability region

It is also possible to examine if it exists a delimited playability region also in the velocity versus force plane. Fig. 6.14 represents the simulated Schelleng plot for a cello D string with stiffness and without torsional waves. The simulation is run using the exponential friction model, and the plot is made in the velocity versus force plane, maintaining a constant normalized bow position $\beta = 0.07$. Notice how it exists a limited region in which the Helmholtz motion is achieved. As before, this region is represented by the darker squares. Fig. 6.15 shows the simulated Schelleng diagram for a cello D string with stiffness and with torsional waves. As in Fig. 6.14, the plot is represented in the velocity versus force plane. Notice how the playability region is somehow enhanced when torsional waves are taken into account. In this case the role of torsional waves, i.e., to add losses which facilitates the establishment of the Helmholtz motion, is apparent.

6.2.5 Three dimensional playability plots

In order to evaluate the playability for all variations of parameters, we represented the playability in a 3 dimensional space. This is represented in Fig. 6.16. The simulation is run using a cello D string with the exponential friction model and torsional waves. In Fig. 6.16, only the region in which Helmholtz motion is achieved, i.e., the region with dark squares, is represented. The z-axis represents bow velocity in a linear scale between 0 to 1 m/s, while the x and y axis represent bow position and bow force in a logarithmic scale respectively. For a given bow velocity of 0.05 m/s, the

playability plot reads like the one shown in Fig. 6.9. Notice how the Helmholtz region is concentrated in a limited portion of the space, as desired and expected. As a final comparison, the playability of the elasto-plastic model described in Chapters 2 and 4 is examined. The simulation was run using the same string parameters as before, and keeping a constant bow velocity $v_b = 0.05$ m/s. The elasto-plastic friction model parameters were $\sigma_0 = 4000$, $\sigma_1 = 0$ and $\sigma_2 = 0.25$. Fig. 6.17 shows the results. Notice how the elasto-plastic friction models behaves better than the hyperbolic and exponential friction models. Notice also how the playability of the elasto-plastic friction model is strongly comparable to the one of the plastic friction model (see Fig. 6.6). This means that, by choosing appropriate values for the elasto-plastic friction model parameters, a wide playability region can be obtained.

6.3 Conclusion

In this chapter we used playability plots as a way to investigate the role of the parameters of the physical model to achieve good tone. Results run on a cello D string, running in real-time at a sampling rate of $F_s = 44.1$ kHz, excited by the exponential, hyperbolic and plastic friction models are comparable to the ones reported in [136]. Moreover the playability of the elasto-plastic friction model was examined, and it was shown that the elasto-plastic friction model behaves better than the "classic" friction models.

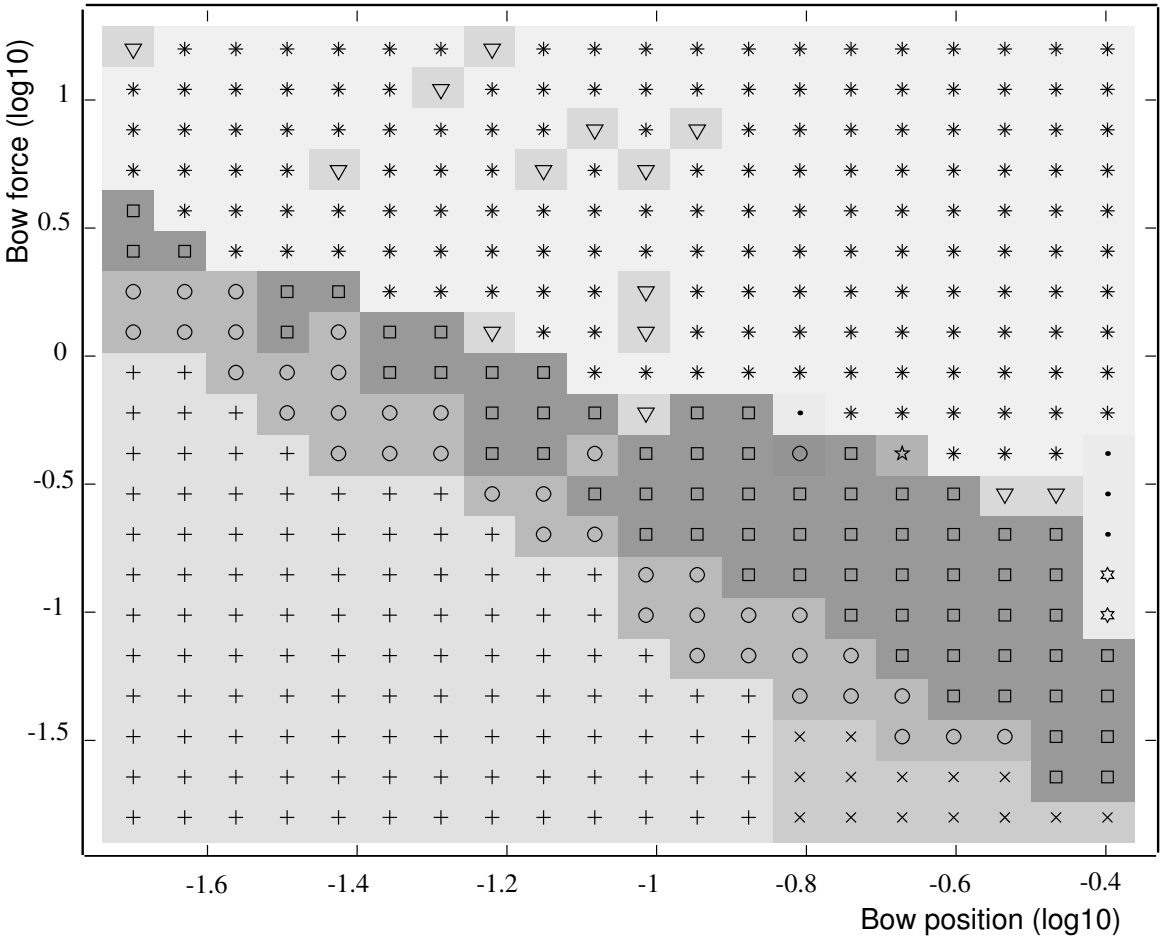

Figure 6.6: *Simulated Schelleng diagram for the plastic friction model case. High quality Helmholtz motion is indicated by open squares, and multiple slipping is plotted using open circles. All other symbols denote generally less desirable modes of string motion. A cello D string ($f_0 = 147$ Hz) is excited with a constant bow velocity $v_b = 0.05$ m/s. Bow force and position are varied as shown in the figure.*

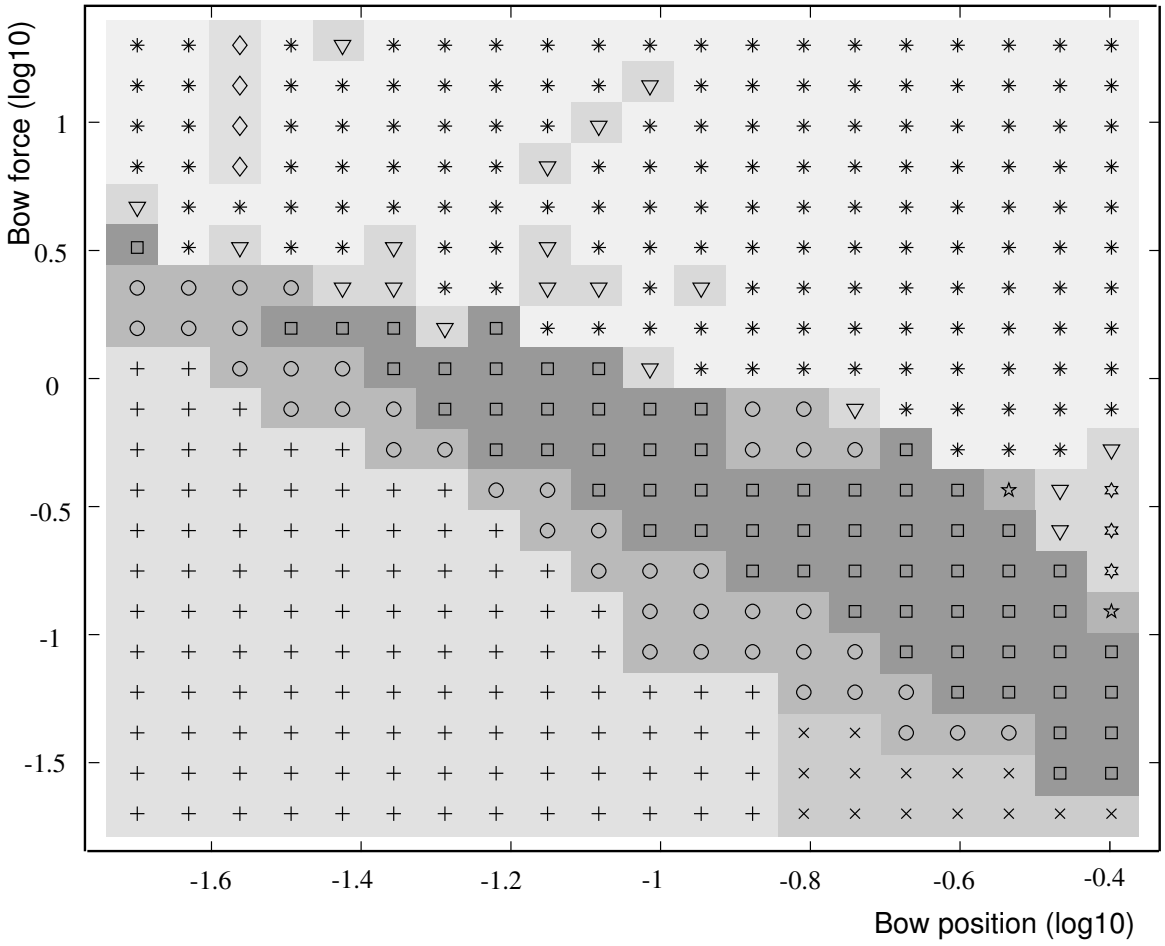

Figure 6.7: *Simulated Schelleng diagram for the plastic friction model case, with torsional wave simulation removed. As before, classic Helmholtz motion is indicated by '□', and multiple slipping by '○'.*

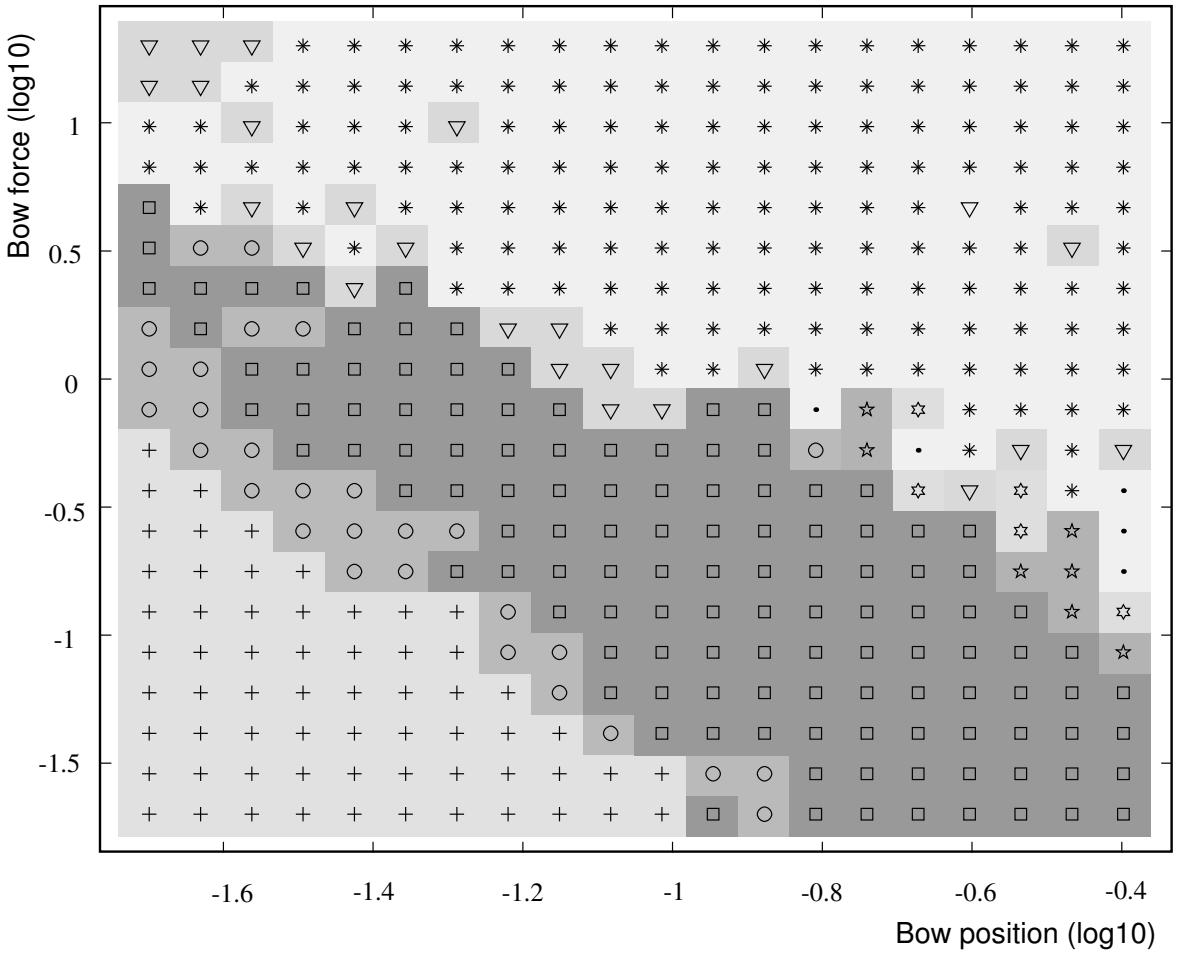

Figure 6.8: *Simulated Schelleng diagram for the plastic friction model case. A cello D string ($f_0 = 147$) Hz is excited with a constant bow velocity v_0.05 m/s. Bow force and position are varied as shown in the figure. The string is initialized with an already established Helmholtz motion.*

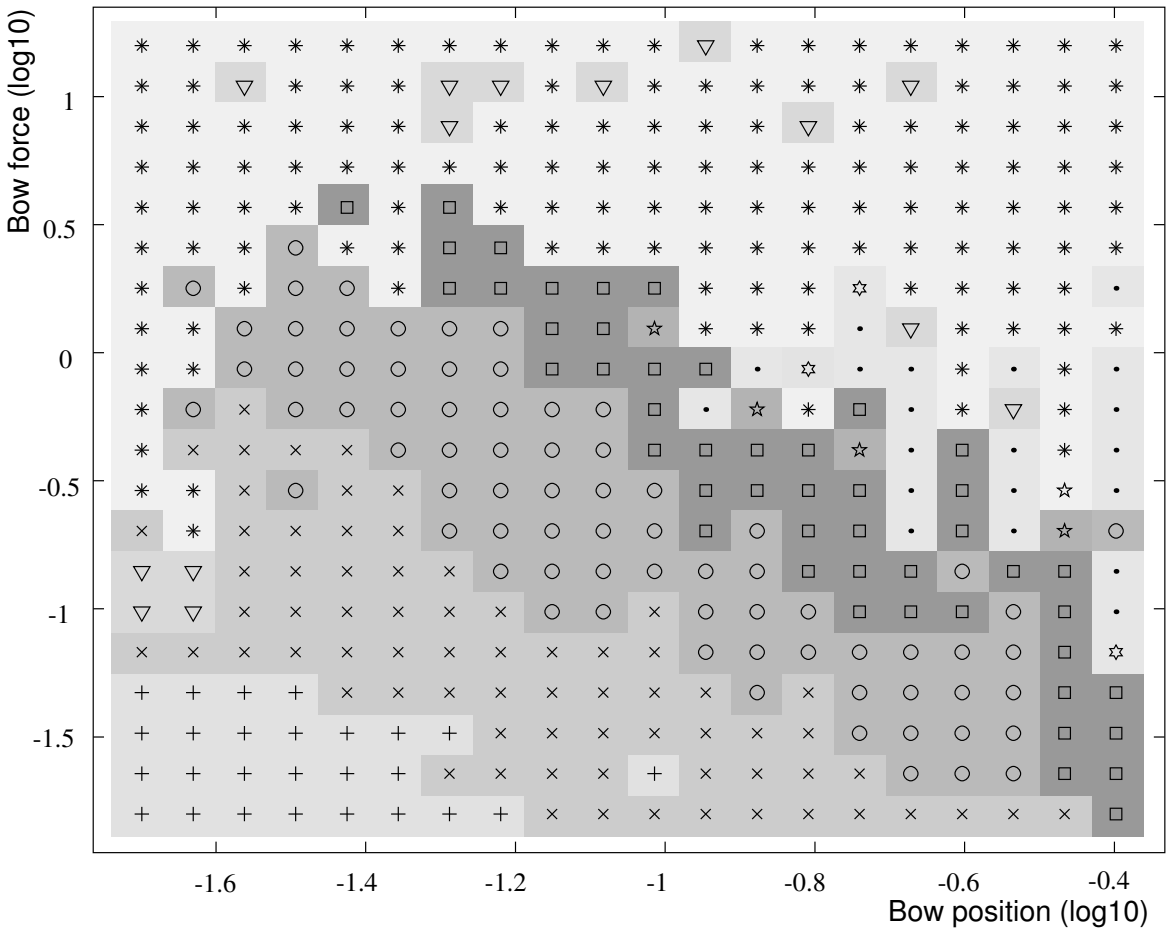

Figure 6.9: *Simulated Schelleng diagram for the exponential friction model case, with torsional waves.*

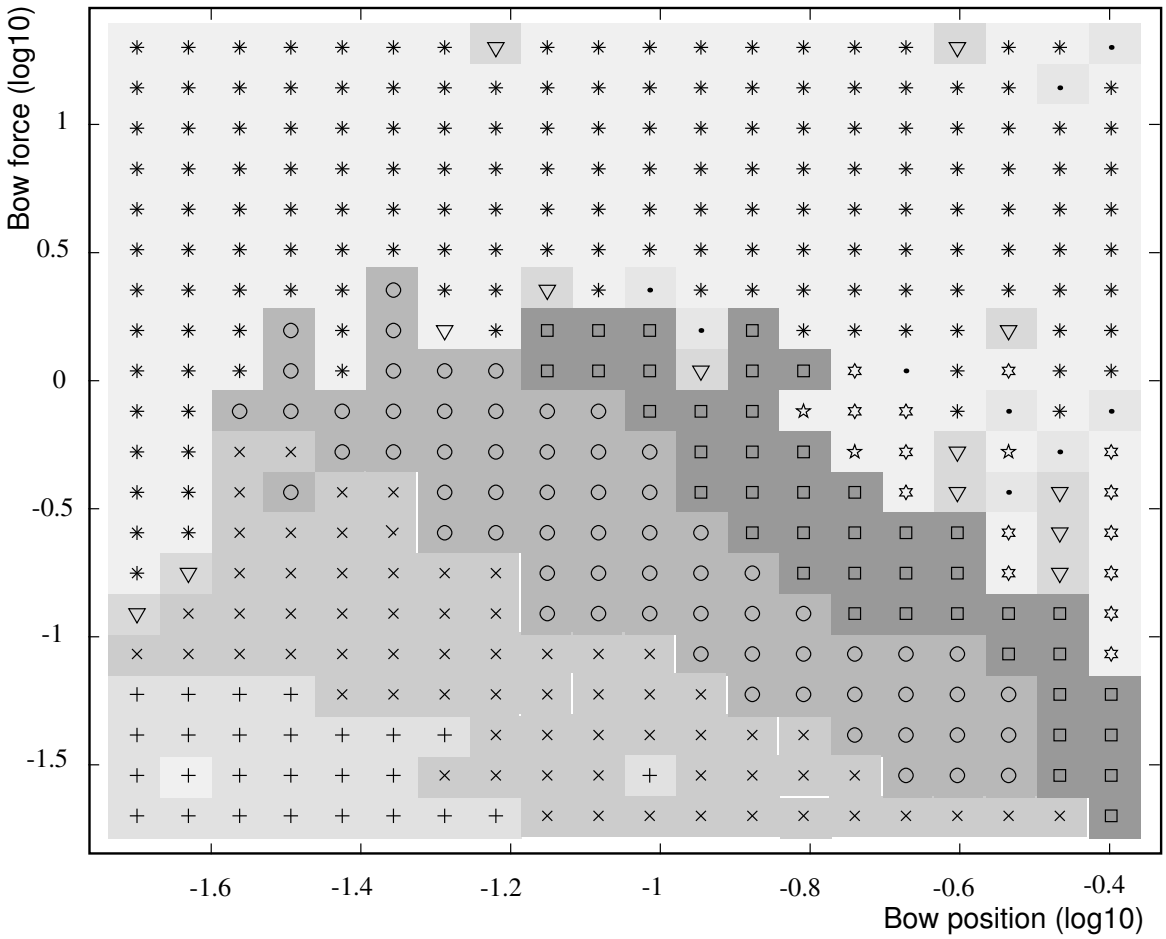

Figure 6.10: *Simulated Schelleng diagram for the exponential friction model case, with torsional waves completely removed.*

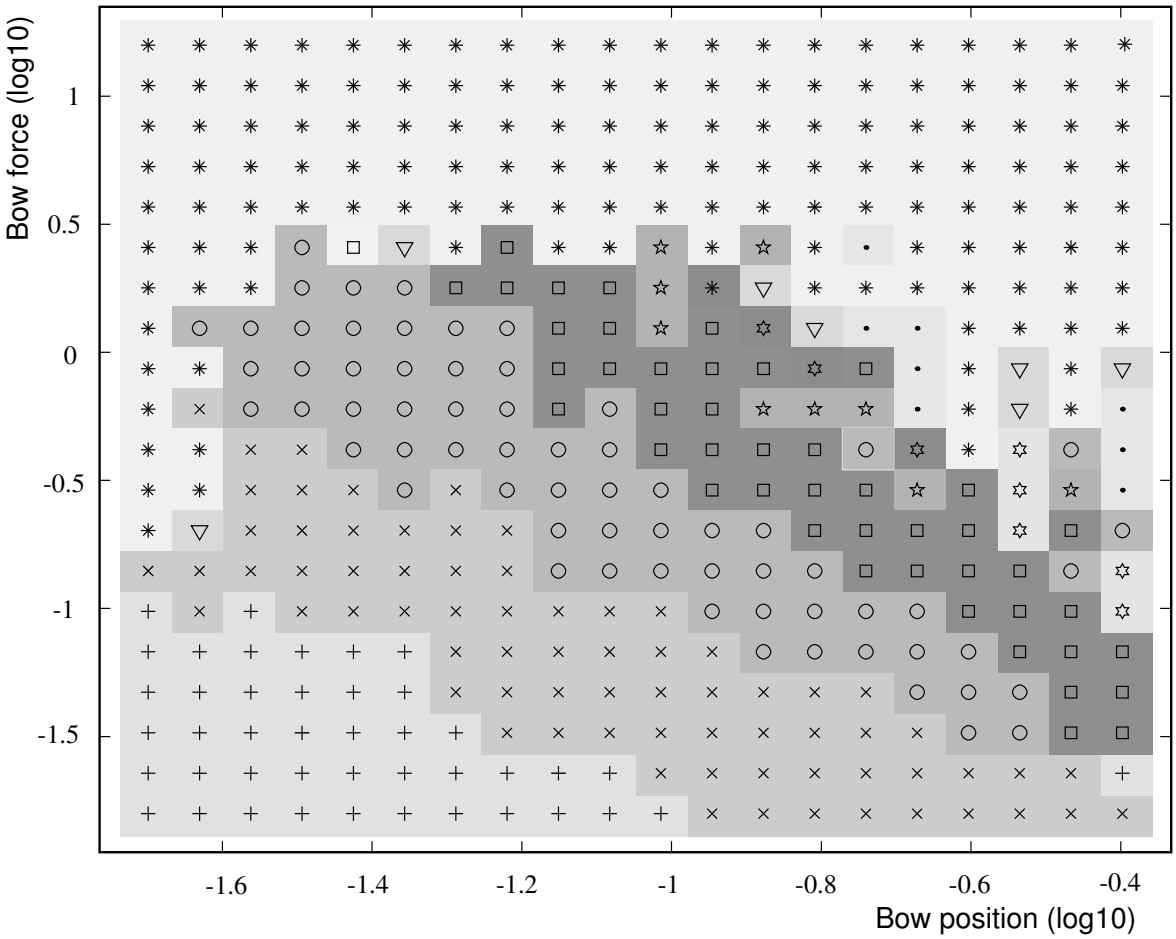

Figure 6.11: *Simulated Schelleng diagram for the hyperbolic friction model case, with torsional waves simulations.*

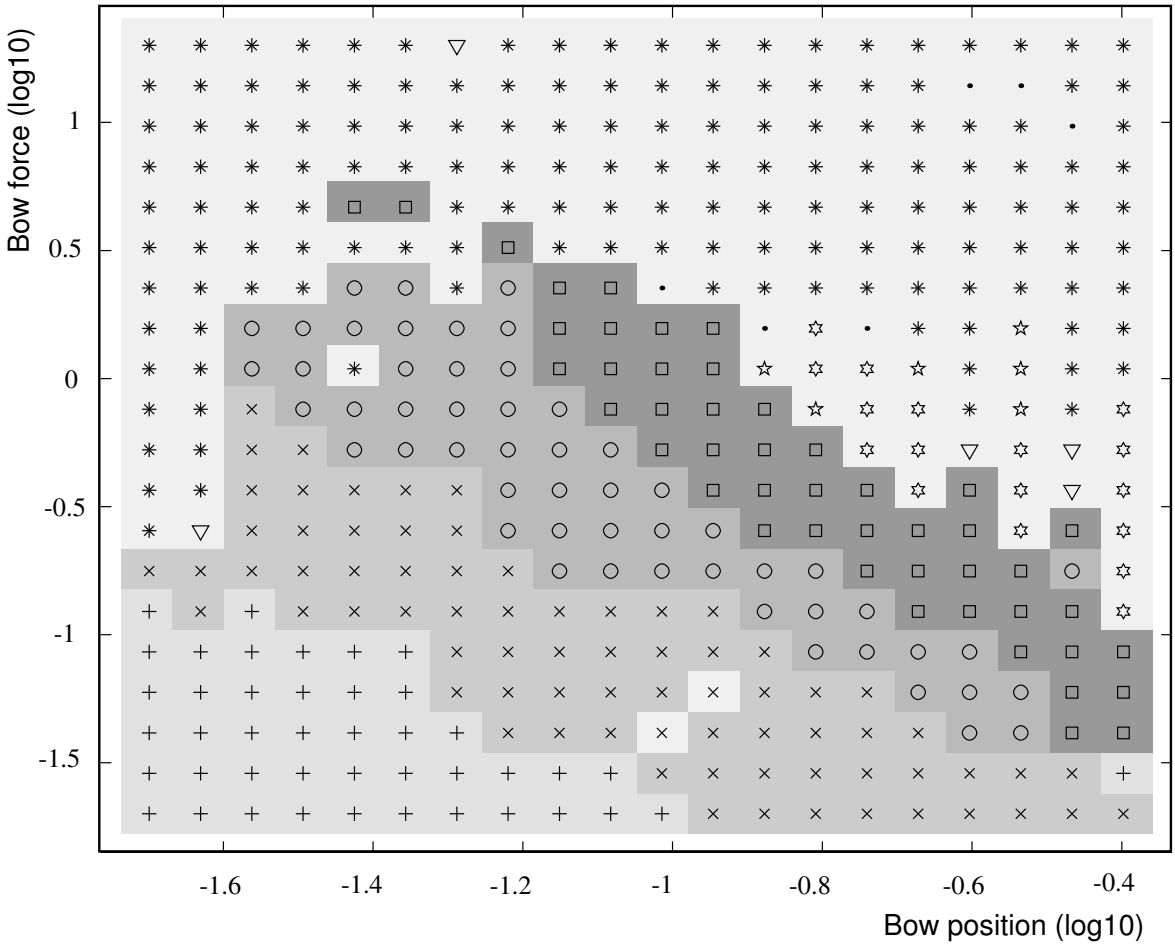

Figure 6.12: *Simulated Schelleng diagram for the hyperbolic friction model case, with torsional waves completely removed.*

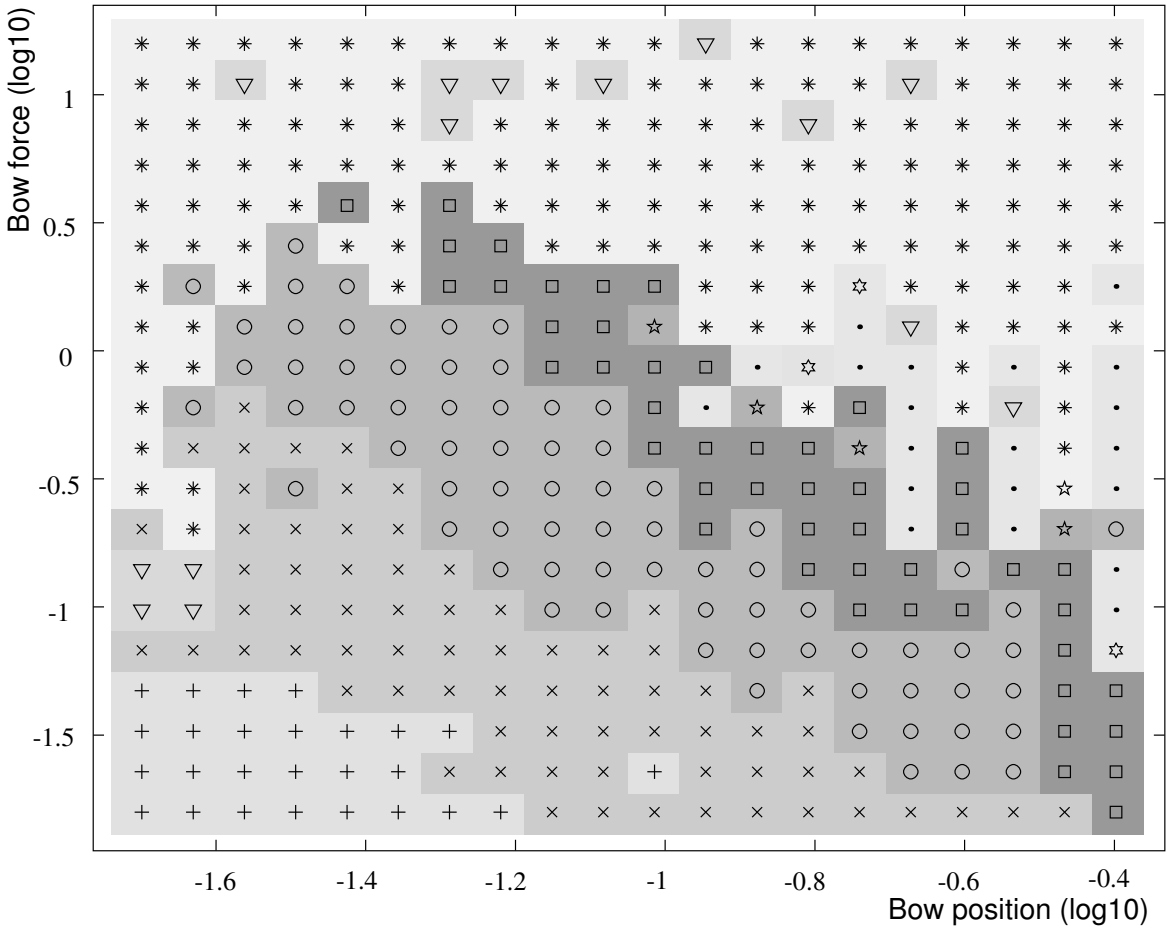

Figure 6.13: *Simulated Schelleng diagram for the exponential friction model case, without string stiffness.*

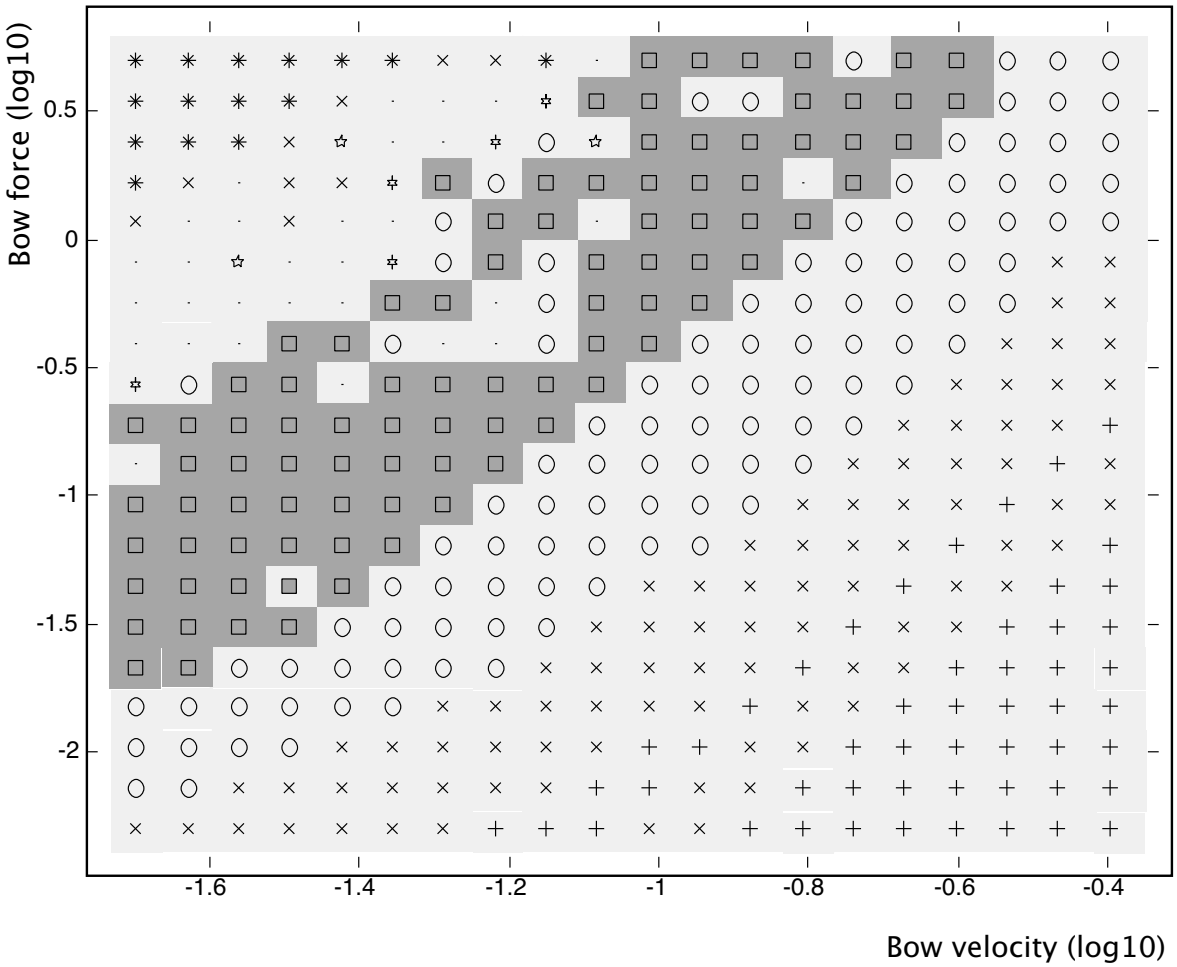

Figure 6.14: *Simulated Schelleng diagram for the exponential friction model case, in the velocity versus force plane, without torsional waves.*

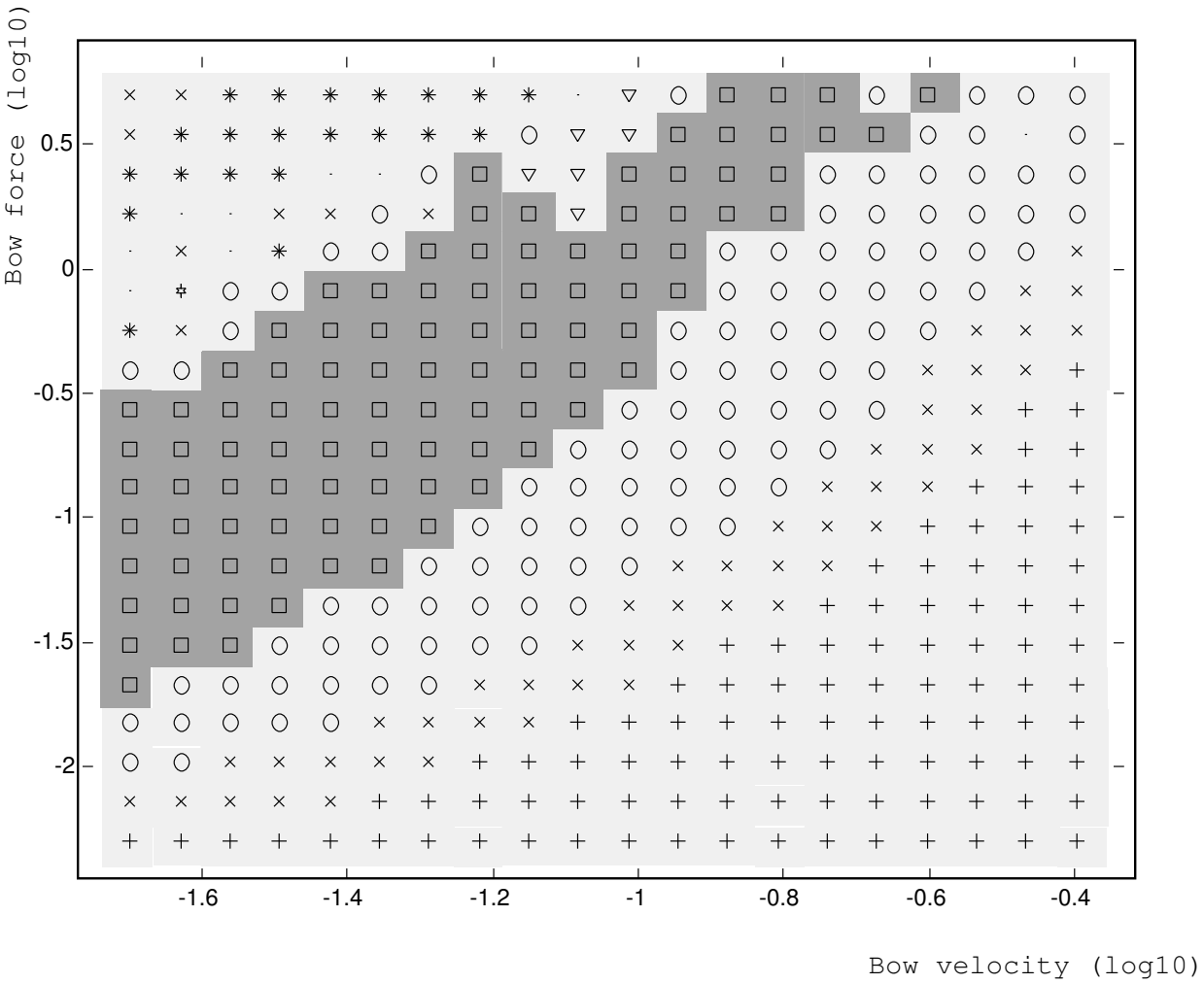

Figure 6.15: *Simulated Schelleng diagram for the exponential friction model case, in the velocity versus force plane, with torsional waves.*

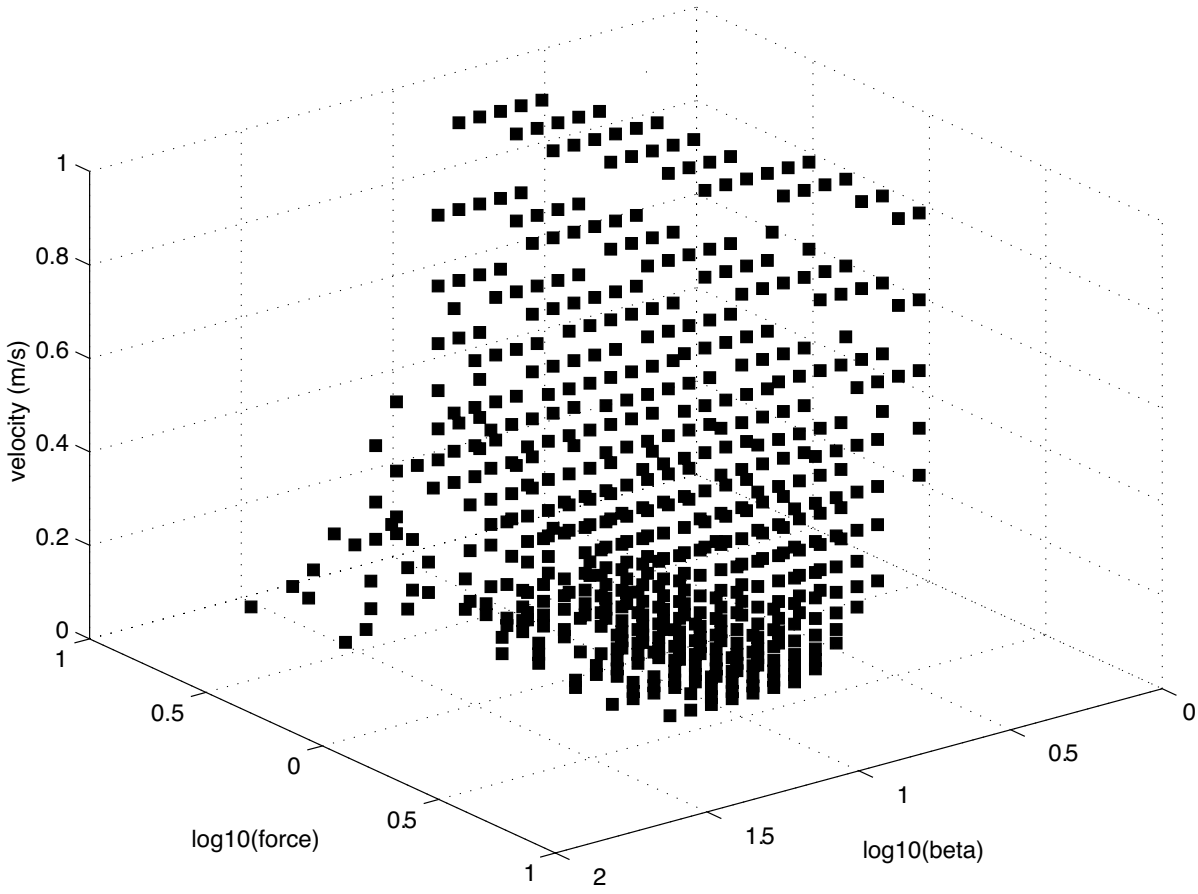

Figure 6.16: *3D playability plot of the basic physical model with torsional waves.*

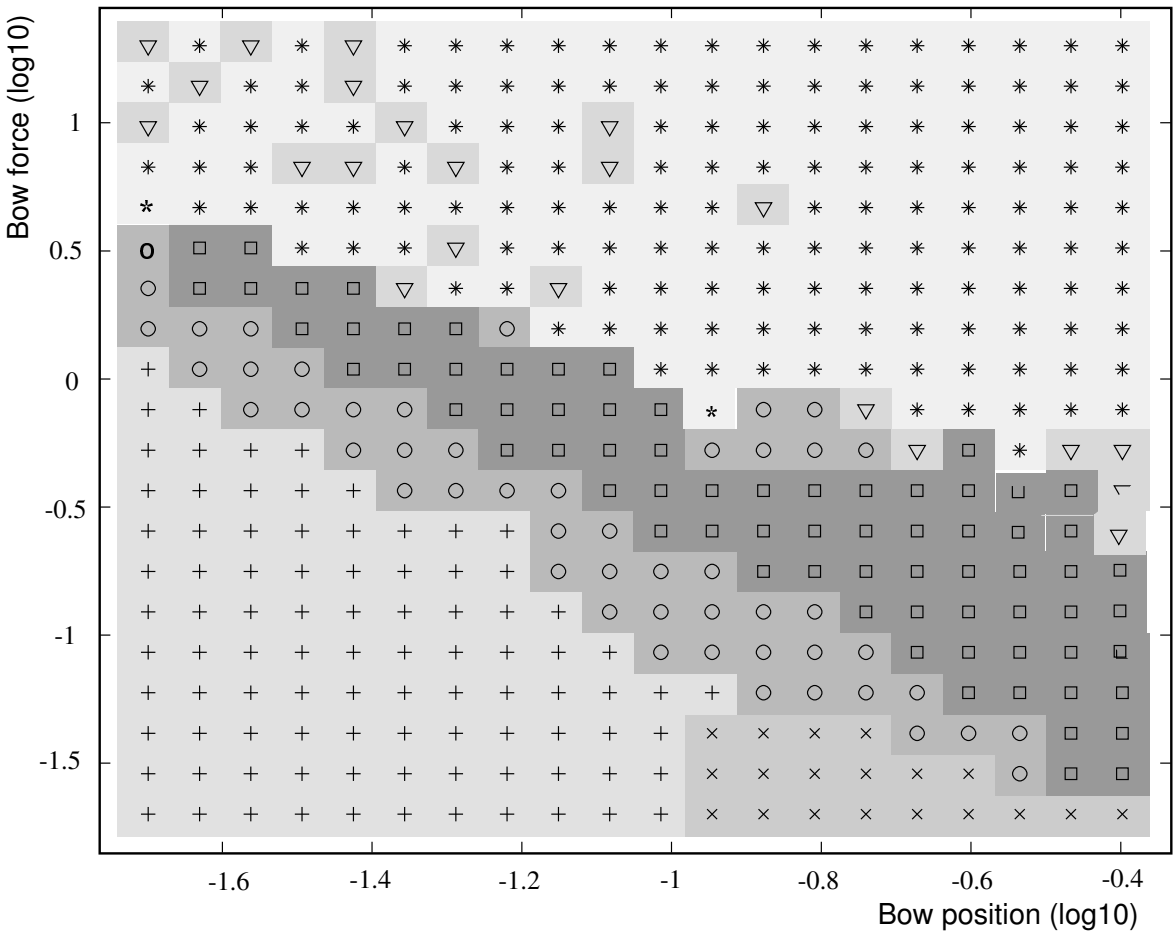

Figure 6.17: *Playability plot for the elasto-plastic friction model, using the same string parameters as before, with elasto-plastic parameters* $\sigma_0 = 4000$, $\sigma_1 = 0$ *and* $\sigma_2 = 0.25$ *(see Chapters 2 and 4).*

Chapter 7

Friction models in interactive performances

In the previous chapters we examined friction sonorities with the goal of building efficient real-time physical models. We studied the behavior of these models and analyzed how input parameters affect their playability. We focused mainly on an acoustical analysis of playability, i.e., we did not analyze the role of the interaction between the human performer and the computer. During the past decade, lots of improvement has been made both on computer models of bowed strings and on building input devices that allow to play such models. These devices are important in order for the models to be playable in real-time, i.e. to be usable in an interactive performance. This chapter describes research aimed to achieve such goals.

7.1 Playability and human computer interaction

The development of real-time modeling of musical instruments has exposed the problems of their gestural control. When a suitable device is attached to the physical model, the natural interaction that exists between a musician and his instrument is preserved, enabling the parameters of the model to evolve following the gestures of the performer.

7.2 Bow Strokes

Our first goal was the real-time simulation of highly skilled bowed string instrument performance. In particular, we were interested in studying the model's behaviour when submitted to different bow strokes, such as *detaché*, *balzato*, *staccato*, *flying staccato* and so on.

The basic gestural parameters which can be used to define bow strokes include: a specific precision grip in which all five fingers are in contact with the bow, a variable length linear displacement in the axis of the bow, a rotational movement relative to the strings' axes in order to choose the string to be played, the pressure of the bow against the string, and the bow velocity. Other important variables include the bow position relative to the string and the amount of bow hair in contact with the string, i.e., a rotation with respect to the bow's axis.

One must also be aware that the technical demands required to perform many of these bow strokes are typically obtained by musicians only after years of practice. Furthermore, in addition to the performer's skilled motor behaviour, these bow strokes heavily rely upon physical properties of both the string and the bow, such as the elasticity of the bow hair, tension of the string, etc.

7.2.1 Controlling the model using a graphical tablet

In order to obtain an accurate simulation of the bow strokes mentioned above, it is necessary to have a flexible input controller at one's disposition. We have therefore decided to use an input device that provides both the means to reproduce the fundamental characteristics of the performer's gestural control and which is sufficiently generic in order to be able to extrapolate the typical violin technique. Other important considerations for our choice of input device were availability, accuracy, precision, resolution and affordability.

Among the commonly available standard input devices that match the above requirements, the one that appeared to best suit our needs was a WACOM graphic tablet equipped with a stylus transducer. One of the main factors in our decision was the number of control parameters simultaneously available [132]. More specifically,

the stylus can provide control for five variables: horizontal and vertical position in a plane, pressure perpendicular to the plane, and angle relative to both plane axes.

STYLUS-TABLET	BOW-VIOLIN
1 Y POSITION ON THE TABLET	BOW POSITION
2 DERIVATIVE OF THE X POSITION	BOW VELOCITY
3 Z POSITION	BOW PRESSURE
4 ANGLE IN THE X AXIS	STRING PLAYED
5 ANGLE IN THE Y AXIS	AMOUNT OF BOW HAIR

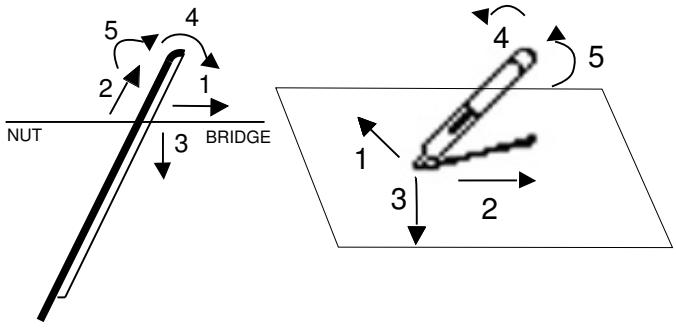

Figure 7.1: *Comparison between the degrees of freedom of the bow-string and the ones of the pen-tablet interaction.*

The stylus is then used to control bow force, bow velocity, distance from the bridge and inclination of the bow. One can notice from Fig. 7.1 that the stylus provides roughly the same control possibilities as those of a real bow, and that there is also a direct correspondence between the physical parameters of the stylus and those of the bow (e.g., position in x and y axis, force in the z axis and angle in both x and y).

Extending the Tablets Capabilities

The ability to use two devices on the same tablet simultaneously seems optimal for simulating both hands of a bowed string instrument's player. This allows the performer to control bowing with one hand, while controlling pitch changes, *vibrati* and *glissandi* with the other, either using a second stylus or a puck transducer.

After experiments with both devices, we noticed that the fact that they do not provide the same physical interaction that exists between the fingers of the player and the bow restrains optimal control. We coped with this problem by fitting the tablet with sensors that can measure position and force simultaneously. These are shown in Fig. 7.2.

Figure 7.2: *WACOM tablet fitted with additional pressure and position sensors (on the left side of the tablet).*

Although positioning these sensors on the tablet does not provide the same tactile feedback as the fingerboard of a violin or other stringed instrument, the left hand finger position and pressure on a string of a real instrument may nonetheless be simulated. The main advantage in using these extra sensors is that, when compared to a stylus or a puck, they are operated using similar motor skills.

Simulation of Bow Strokes using the Tablet

Using the stylus, we were able to reproduce most of the bow strokes (such as staccato, balzato, martellato, and so on) without resorting to any special non-linear mapping of stylus output parameters to model input parameters. In particular, even bow strokes obtained by skilled musicians could be reproduced immediately and intuitively from the use of the stylus in place of a bow. For example, to obtain a *balzato* the player rubs the string quickly with the bow backward and forward, "jumping" on the string using both his wrist and his forearm, and taking advantage of the elasticity of both the string and the bow [102].

In order to examine the behavior of the model when submitted to fast repeated balzatos, the player simply needs to rub the tablet with the pen backward and forward and then release it. The evolution of the resulting parameters, shown in Fig. 7.3, corresponds to measurements made by Askenfelt [7] on an actual violin.

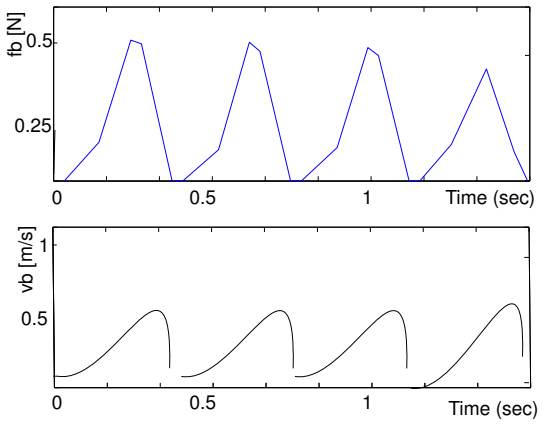

Figure 7.3: *Top: pressure of the stylus on the tablet during balzato. Bottom: velocity of the pen.*

Note that in this bow stroke, while the hand that holds the stylus reproduces with fidelity the movement performed using a bow, the behaviour of the controller is quite different. An important characteristic of the balzato stroke is the fact that the player takes advantage of the elasticity of both the string and the bow hair to facilitate the bouncing of the bow. Since this elasticity is absent in both the tablet and stylus, the performer must use a slightly modified gesture in order to furnish all the energy

necessary for the stylus to rebound. A similar situation is observed in other bow strokes that are completely based on physical properties of the instrument, the more remarkable example of which is the *gettato*. In it the player simply allows the bow to fall and freely rebound against the string. The rigid surfaces of the tablet and of the stylus do not provide the same elastic feedback felt by the violinist.

The bow strokes shown so far have the common characteristic that the bow is not in constant contact with the string, which is not always the case with other bow strokes. For example, to play *detaché* the stylus simply moves back and forth along the horizontal axis of the tablet, at an almost constant velocity and pressure, as shown in Fig. 7.4. Another example would be *staccato*, in which the performer exerts a high initial force and velocity and then stops the stylus almost immediately, as can be seen in Fig. 7.5.

It is remarkable that, while learning to hold a bow and perform skilled bow strokes requires a considerable amount of time, the familiarity with a device like a pen allows the performer to obtain immediately a confidentiality with the controller.

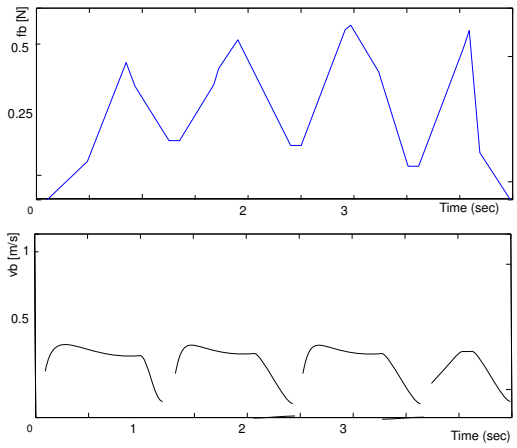

Figure 7.4: *Top: pressure of the stylus on the tablet during detaché. Bottom: velocity of the stylus.*

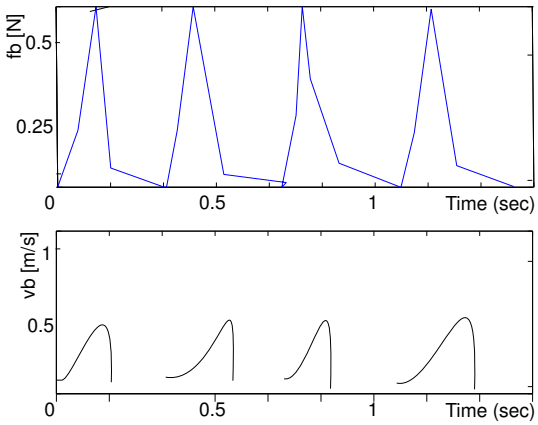

Figure 7.5: *Top: pressure of the stylus on the tablet during staccato. Bottom: velocity of the stylus.*

7.3 Bowed string physical models and haptic feedback

The tablet appeared to be a convenient device to control the bowed string physical model, for its availability in the market and for the ease to use. Despite the fact that the table is an instrument easy to learn how to play, it shows some limitations such as the ergonomics different from traditional bowed string instruments and its lack of haptic feedback. By incorporating haptic feedback into the controller for the virtual bowed string, it is possible to take advantage of the player's existing sensitivity to the relationship between their instrument's feel and its sound in order to create a wider range of parameters that can be sensed and controlled during performance.

Sile O'Modhrain in her PhD dissertation [81] discovered that haptic feedback greatly increases the playability of virtual instruments. In this context, playability is referred to as the ability of bowed string players to consistently perform different bow strokes that produce violin sounds that are judged as perceptually acceptable by professional bowed string players and also have waveforms that reside within the playability region as defined in the previous chapter.

In order to introduce both force feedback and ergonomics that are reminiscent of a traditional violin interface, Charles Nichols built the vBow [76, 77], a haptic feedback

controller. The goal of the vBow is to be able to introduce a new violin interface that addresses the limitations of MIDI violins as well as to provide a controller that can also play other real-time synthesis tools.

The bowed string physical model described in chapter 4 has been successfully used in connection with the vBow [77].

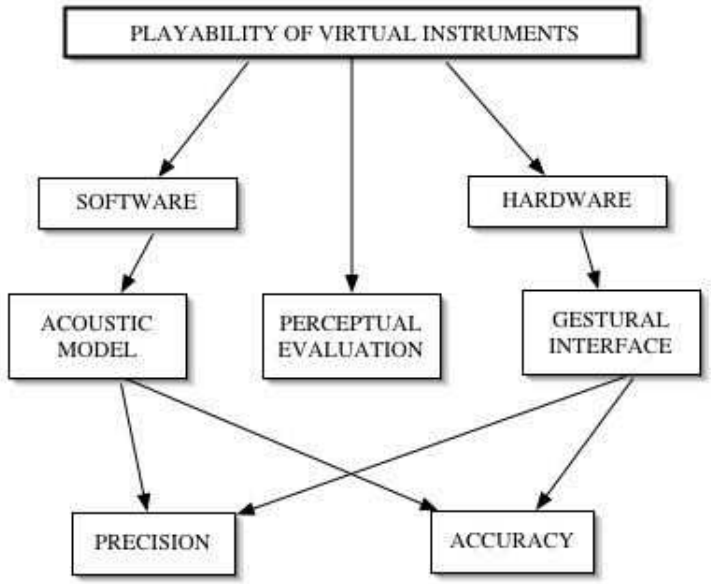

Figure 7.6: *Playability chart of a virtual musical instrument*

Another more general definition of playability is the ability of the virtual instrument to be ergonomically playable, that is the player should be able to physically manipulate the interface freely and with ease.

A chart that summarizes all the playability issues mentioned above is shown in Fig. 7.6.

In order to explore all the previous definitions of playability and extend them, we are currently interested in analyzing the possibility of reproducing traditional bowing techniques using a bow controller that behaves in a manner as closely related to that of a traditional violin bow as possible. This allows us to validate both the model and the controller by comparing it to the behavior of the traditional instrument.

7.3.1 The virtual violin project

The real-time bowed string physical model is currently used together with a wireless bow controller developed by Diana Young [140, 108, 109]. The aim is to reproduce the bow strokes that are most fundamental to the right hand technique of an accomplished bowed string player.

The ultimate goal of this research is to create a bowed string instrument able to reproduce the behavior of a traditional instrument as well as to create extended performance techniques for bowed string players.

The bow controller used is a commercial carbon fiber bow, adapted by adding a custom measurement system. The system is comprised of an electric field sensor for measuring bow position (tip-frog / bow-bridge distance), commercial accelerometers for detecting 3D acceleration, and foil strain gauges for measuring the strain in the bow stick proportional to normal force on the string and the orthogonal force corresponding to flexion toward and away from the scroll.

From these sensors, the parameters of bow velocity, bow-bridge distance, downward force, and bow width (using tilt information provided by the accelerometers and the second strain sensor) may be isolated from bowing gestures and used as input to the physical model. For a detailed description of the bow controller, see [139].

In preliminary experiments we used a Macintosh G4 computer to run the Max/MSP implementation of the bowed string physical model. The gestural data from the bow controller was connected via a serial/USB converter to a USB port of the computer.

Recordings of both the violin audio and the bow controller data were made simultaneously within the Max/MSP environment. The gesture data was then used to drive the physical model, which produced waveforms that were also recorded.

This setup was simple enough to allow fast and easy recording and testing, and was used to reproduce bow strokes. The waveforms of the violin were then qualitatively compared to those produced by the model using both time and spectral domain evaluation and perceptual evaluation.

The integration of the bow controller hardware with the software model was addressed one input parameter at a time. In the first trial the downward strain sensor was used to control the downward force parameter for the bowed string model.

With the model parameters of bow-bridge distance, bow velocity, bow width, and frequency held constant, the downward force was varied between 0 and 5 N.

Other than setting a threshold appropriate for the sensor range, it was unnecessary to perform any adjustments to this mapping. Using the bow controller to play a single string on the test violin, it was possible to compare the sound produced by the model with that of the test violin. Sonorities which sounded appropriate for the amount of pressure applied to the bow were produced.

Interestingly, the model produced sounds that seemed perceptually correct for long sustained strokes as well as for short strokes with sharp attacks and decays.

7.3.2 Adding Velocity and Bow-Bridge Distance

Next, the bow velocity and bow-bridge distance controls were added by using the data from the bow position sensor. By taking the data values corresponding to the tip and the frog, the transverse bow position was determined, and from this the velocity value was derived. The bow-bridge distance was taken as the sum of the tip and the frog values.

It was possible to change the sound of the tones produced by the model by adjusting bow pressure, speed, bow-bridge distance, and by simply changing the bow direction. As the sound of the test violin offered an easy comparison to the model, playing two open strings (of the test violin) while controlling a single tone of the model tuned to different intervals above and below the higher string was experimented. Playing the small duet between real and virtual violins it was possible to make small adjustments to the mappings so that the timbres sounded as though they were all three emanating from the test violin.

7.3.3 Complete mapping

In order to build an expressive virtual musical instrument, the capture of the gesture of the performance is as important as the manner in which the mapping of gestural data onto synthesis parameters is done. In the case of physical modeling synthesis, a one-to-one mapping approach of control values to synthesis parameters makes sense

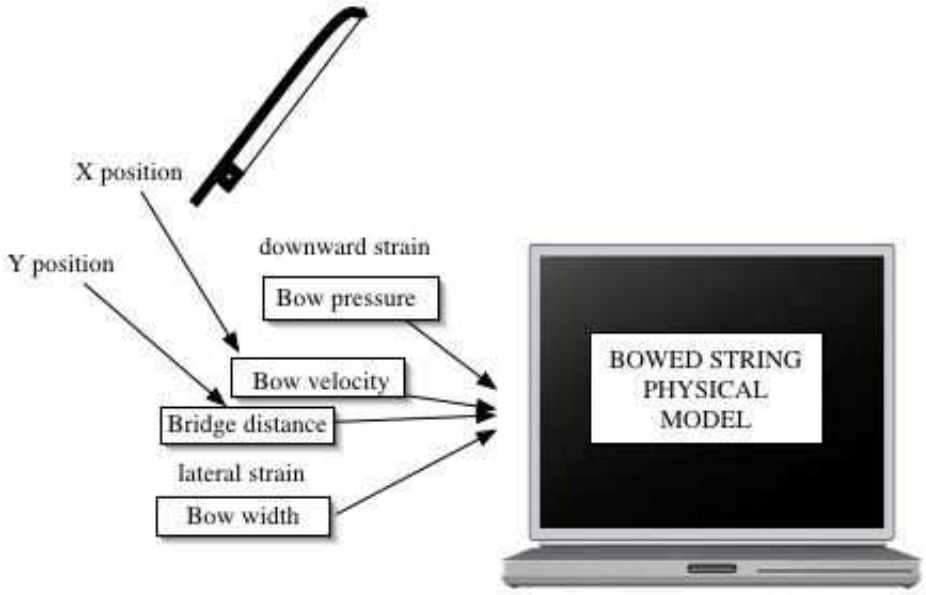

Figure 7.7: *Mapping of the bow controller to the bowed string physical model.*

due to the fact that the relationship between gesture input and sound production is often hard-coded inside the synthesis model [48]. Because both the physical model and the bow controller are developed according to physical input and output parameters, the complete mapping between the two is straightforward. Fig. 7.7 shows how all the data sent by the bow controller were mapped to the input parameters of the physical model. Downward bow force of the controller is directly mapped into bow force in the physical model. Bow velocity and bow-bridge distance were captured by measuring the horizontal and vertical position of the bow respectively. Moreover, lateral strain sensors were mapped onto the amount of bow hair in contact with the bow.

7.4 Recreating a virtual violin

In recent experiments [140, 109, 108], playability and bow strokes were explored by using the wireless bow controller able to capture all the subtle nuances of bowing gestures. Playing the bowed string physical model and an electric violin with the same input parameters, it was possible to compare the resulting waveforms both

perceptually and acoustically, and therefore validate the model.

7.5 Extended techniques for physical models

Up to this point, this dissertation has merely focused on the description of how existing musical instruments can be digitally reproduced. From a musical perspective, physical models become interesting when sonorities that cannot be achieved with real instruments are created. Such extensions may not have scientific relevance, but are noneless interesting from an artistic point of view.

Recent work has involved exploring extended techniques for physical models using instrumental controller subsititution [12]. Instrumental controller substitution utilizes the virtually disembodied nature of physical models as a means of exploring their unique acoustic nature. The decoupling of the instrumental controller and the audio synthesis is used as a compositional opportunity to expand the musical possibilities of physical models.

Although such extensions are not described in this dissertation, it is important to stress their existance which opens new possibilities for interactive compositions, virtual reality and augmented sonic environments.

Chapter 8

Conclusions and future work

In this thesis different models of friction driven sonorities have been examined. The importance of friction in musical applications and everyday life sonorities has been outlined and examined, and state-of-the-art friction models have been applied to a musical context.

The models developed in this dissertation have been implemented in real-time under the Max/MSP and Pd platform, as described in Appendix A, and are downloadable from the website http://www-ccrma.stanford.edu/∼serafin.

These models have already been, in our opinion, successfully used in many real-time interactive performances. In making such models available, the author wishes that more composers and sound artists will find the sound of friction inspiring.

8.1 Future work

There are still many interesting applications related to friction driven physical models, which are outlined in the following section.

8.1.1 A generalized friction controller

The idea behind a generalized friction controller is to have a device able to play all the friction driven musical instruments. So far, many controllers for bowed strings

have been developed, and some of them have been described in Chap. 7.

However, there does not yet exist a controller able to drive in real-time all friction driven instruments. In the previous chapter different controllers which offer many possibilities to performers due to their traditional feel, appearance, and function have been discussed. It is legitimate to ask whether in many scenarios a less traditional interface may be more beneficial. Specifically, together with Diana Young a general interface for the control of all friction-driven instrument models is under development [110].

Such a device would likely share some of the physical qualities of a bow, but having characteristics that imply different playing techniques. The challenges on the design of this device are due to the fact that friction sounds are produced in different ways such as perpendicular motion of the exciter on the resonator (like in the case of the bowed string and the musical saw), or circular motion (like in the Tibetan bowl and glass harmonica). We are currently experimenting with having a pressure sensor, a combination of different types of position sensors (Hall technique), strain/bend sensors like the ones used in the bow controller, accelerometers, and gyros for angular velocity.

Such an instrument will give composers and performers great possibilities to explore and extend the sound of friction.

8.1.2 Perception of chilling sounds

Another interesting research direction is a perceptual investigation of the properties of friction sounds. As outlined in this dissertation, different sonorities can be produced by the same excitation mechanism.

However, it is not yet clear which is the mechanism which makes the human brain perceive such sounds as belonging to different sources, or what makes those sounds pleasant or unpleasant. This is an interesting topic which can be further explored.

8.1.3 Friction models and graphical user interfaces

Another interesting issue is related to the use of friction models in human-computer interfaces. Enhancing information in human-computer interfaces by using different senses is a natural choice motivated by our daily interaction with the world. In everyday life humans communicate and interact by using multiple channels which are interdependent. Especially in applications that present a direct manipulation interaction (e.g., icon dragging), typical visual feedback techniques tend to give the impression that manipulation is happening on a surrogate object rather than a real one. In order to provide *substance* to the manipulated objects, physical reality must be mimicked more closely. In particular real objects tend to resist to motion due to their inertial properties, friction, and so on.

Many kinds of haptic devices providing force feedback have been proposed and manufactured as a direct solution to this kind of requirements. However, there are many practical cases where it is desirable to substitute haptic feedback with other modalities. One possible reason is that these devices are in most cases cumbersome and expensive, another is that they provide a strictly personal display (e.g., a user cannot share a sensation of effort with an audience). A number of alternatives have therefore been proposed. Approaches based on purely visual feedback have been demonstrated to be effective in some cases. Cartoon animation techniques applied to widget components and graphical object manipulation do enhance the interaction [126]. Force-feedback has also been visually simulated via cursor displacement [129] and pseudo-haptic feedback [67].

However, in many applications the visual display does not appear to be the best choice as a replacement of kinesthetic feedback. Touch and vision represent different priorities [63], with touch being more effective in conveying information about "intensive" properties (material, weight, texture, and so on) and vision emphasizing properties related to geometry and space (size, shape). Moreover, the auditory system tends to dominate in judgments of temporal events, and intensive properties strongly affect the temporal behavior of objects in motion, thus producing audible effects at different time scales. In the light of these remarks, audition appears to be an ideal candidate modality to support *illusion of substance* [126] in direct manipulation of

virtual objects, and indeed Massimino and Sheridan [68] have shown that audition is an effective *sensorial substitute* for some typical manipulation tasks.

Together with Federico Avanzini and Davide Rocchesso, we are currently investigating the use of friction sounds for sensorial substitution, to examine if auditory feedback can facilitate the development of a more user friendly human computer interface, especially when a tactile force feedback is not available.

8.1.4 Friction models in multimedia and virtual reality

While sound synthesis techniques have until now been adopted mainly in the computer music community, recently their interest has increased also in virtual reality, computer animation and computer games [20]. The availability of parametric models whose quality is constantly improving makes such models desireable for sound designers in the entartainment industry.

As outlined in this dissertation, many sounds that are produced by musical instruments and everyday objects derive from interaction between rubbed surfaces. It is therefore an interesting application to use such models in other fields where sound plays an important factor. In this way high quality computer generated sounds would be appealing not only to composers but to those who are interested in sound design from different perspectives.

Appendix A

Implementation

The models proposed in this thesis have been implemented as extensions to the Max/MSP [141] environment.

The bowed string physical model has also been developed in the Synthesis Toolkit (STK) platform [17]. Figure A.1 shows the interface developed. The objects implemented in Max/MSP are a bowed string physical model, a rubbed wineglass, a musical saw a bowed cymbal and a singing bowl.

The squeaking doors, rotating wheels and rubbed wineglasses have been implemented in Pd [89] and are available from the Sounding Object website.[1].

The friction models described in this dissertation have been used in different applications. Some examples are the following:

1. PhD dissertation of Sile OModhrain: Playing by Feel: Incorporating Haptic Feedback into Computer-Based musical Instruments, (bowed string physical model in STK), see [81].

2. PhD dissertation of Charles Nichols: The vbow: an expressive musical controller haptic human-computer interface, (bowed string physical model in STK), see [77].

3. Compositions *S-Trance-S*, *(Dis)appeances* and *S-Morphe-S* by Matthew Burtner (extended bowed string physical model and singing bowl respectively, in

[1](http:///www.soundobject.org)

Figure A.1: *The Max/MSP interface for the friction models.*

Max/MSP).

4. Hyperbow controller by Diana Young (bowed string physical model in Max/MSP). See, for example, [108, 109, 140].

5. *Requiem* by Ching-Wen Chao, Stanford DMA dissertation, 2002 (tibetan bowl physical model, in Max/MSP).

.

Appendix B

Numerical issues

In Chapter 2 we have shown that the elasto-plastic friction models are represented through different non-linear coupling between the resonating objects. When the continuous-time systems are discretized and turned into numerical algorithms, the non-linear terms introduce computational problems that require to be solved adequately. This is the topic of this Appendix.

B.1 Discretization

As described in Chap .4, the string resonator is represented by using a one dimensional digital waveguide. In this section we describe how the interaction force $f(n)$ for the elasto-plastic model is computed at each time step, and coupled to the waveguide resonator. At each time step n the variables $[x(n), v(n)]$, representing the relative position and velocity, and $f(n)$, the friction force, have instantaneous mutual dependence. That is, a delay-free non-computable loop has been created in the discrete-time equations and, since a non-linear term is involved in the computation, it is not trivial to solve the loop. This is a known problem in numerical simulations of non-linear dynamic systems. An accurate and efficient solution, called K method, has been recently proposed by Borin, De Poli and Rocchesso [10] and will be adopted here. First, the instantaneous contribution of $f(n)$ in the computation of vector $[x(n), v(n)]$ can

be isolated as follows:

$$\begin{bmatrix} x(n) \\ v(n) \end{bmatrix} = \begin{bmatrix} \tilde{x}(n) \\ \tilde{v}(n) \end{bmatrix} + \boldsymbol{K} f(n) \tag{B.1}$$

where $[\tilde{x}(n), \tilde{v}(n)]$ is a computable vector (i.e., it is a linear combination of past values. Second, substituting the previous expression in the non-linear contact force equation, and applying the implicit function theorem, $f(n)$ can be found as a function of $[\tilde{x}(n), \tilde{v}(n)]$ only:

$$f(n) = f\left(\begin{bmatrix} \tilde{x}(n) \\ \tilde{v}(n) \end{bmatrix} + \boldsymbol{K} f(n) \right) \quad \overset{\text{K method}}{\longmapsto} \quad f(n) = h(\tilde{x}(n), \tilde{v}(n)) \quad . \tag{B.2}$$

Summarizing, if the map $f(n) = h(\tilde{x}(n), \tilde{v}(n))$ is known, then the delay-free loop in the computation can be removed by rewriting the algorithm as

```
for    n = 1... samplelength
       Assign    f(n) = 0
       Compute   x_i^(b)(n)  (i = 1...N^(h)),
       Compute      v_h
       Compute   x̃(n), ṽ(n),
             and f(n) = h(x̃(n), ṽ(n))
       Update    x_i^(b)(n) = x_i^(b)(n) + b_i^(h) f(n)  (i = 1...N^(h))
       Update string velocity
end
```

The dynamic equation for $\dot{z}$ is discretized using the bilinear transformation. Since this is a first order equation, discretization by the trapezoid rule is straightforward:

$$\begin{aligned} z(n) = &\quad z(n-1) + \int_{(n-1)T_s}^{nT_s} \dot{z}(\tau) d\tau \quad \Rightarrow \\ z(n) \approx &\quad z(n-1) + \frac{T_s}{2}\dot{z}(n-1) + \frac{T_s}{2}\dot{z}(n) \quad . \end{aligned} \tag{B.3}$$

Therefore, equations in the coupled numerical system for the friction force become:

$$\begin{cases} z(n) = z(n-1) + \frac{T_s}{2}\dot{z}(n-1) + \frac{T_s}{2}\dot{z}(n) \\ \dot{z}(n) = \dot{z}(v(n), z(n)) \\ f(n) = f(z(n), \dot{z}(n), v(n), w(n)) \end{cases} , \tag{B.4}$$

where $\dot{z}(v, z)$ and $f(z, \dot{z}, v, w)$ are given in Eq. (2.13). It can be seen that at each time step n the variables $[v(n), z(n)]$ and $\dot{z}(n)$ have instantaneous mutual dependence. The K method [10] is adopted in order to solve this problem. The instantaneous contribution of $\dot{z}(n)$ in the computation of vector $[x(n), v(n)]$ must be isolated so that the K method can be applied on the non-linear function $\dot{z}(v, z)$:

$$\begin{bmatrix} v(n) \\ z(n) \end{bmatrix} = \begin{bmatrix} \tilde{v}(n) \\ \tilde{z}(n) \end{bmatrix} + \boldsymbol{K}\dot{z}(n) \quad , \tag{B.5}$$

then

$$\dot{z}(n) = \dot{z}\left(\begin{bmatrix} \tilde{v}(n) \\ \tilde{z}(n) \end{bmatrix} + \boldsymbol{K}\dot{z}(n) \right) \quad \overset{\text{K method}}{\longmapsto} \quad \dot{z}(n) = h(\tilde{v}(n), \tilde{z}(n)) \quad . \tag{B.6}$$

where $\tilde{v}$ and $\tilde{z}$ are –as above– computable quantities. From Eq. (B.3), the element $\boldsymbol{K}(2)$ is easily found as $\boldsymbol{K}(2) = T_s/2$, while $\tilde{z}(n) = z(n-1) + T_s/2 \cdot \dot{z}(n-1)$. Finding $\boldsymbol{K}(1)$ is less straightforward, since the friction force itself depends explicitly upon v. Recalling that

$$v(n) = v_s(n) - \sum_{j=1}^{N^{(b)}} t_{mi}\dot{x}_i^{(b)}(n) \quad , \tag{B.7}$$

where $v_s(n)$ represents the string velocity, and substituting here the discrete-time equations for $\dot{x}_i^{(b)}(n)$, a little algebra leads to the result.

Having determined the $\boldsymbol{K}$ matrix, the K method can be applied and the algorithm can be rewritten as

```
for    n = 1... samplelength
       Assign    f(n) = 0
       Compute   x_i^(b)(n) (i = 1...N^(b)),
            and v_s(n)
       Compute   ṽ(n), z̃(n), and ż(n) = h(ṽ(n), z̃(n))
       Compute   v(n) = ṽ(n) + K(1)ż(n),
            z(n) = z̃(n) + K(2)ż(n), and f(n)
       Update    x_i^(b)(n) = x_i^(b)(n) + b_i^(b) f(n) (i = 1...N^(b))
       Update v_s(n)
end
```

B.1.1 The Newton-Raphson algorithm

Two choices are available for efficient numerical implementation of the K method. The first choice amounts to pre-computing the new non-linear function h off-line and storing it in a look-up table. One drawback is that when the control parameters (and thus the $\boldsymbol{K}$ matrix) are varied over time, the function h needs to be re-computed at each update of $\boldsymbol{K}$. In such cases, an alternative and more convenient approach amounts to finding h iteratively at each time step, using the Newton-Raphson method. This latter approach is adopted here. Since most of the computational load in the numerical system comes from the non-linear function evaluation, the speed of convergence (i.e. the number of iterations) of the Newton-Raphson algorithm has a major role in determining the efficiency of the simulations.

Using the Newton-Raphson method for computing h means that at each time step n the value $h(n)$ is found by searching a local zero of the function

$$g(h) = \dot{z}\left(\begin{bmatrix} \tilde{v} \\ \tilde{z} \end{bmatrix} + \boldsymbol{K}h\right) - h \tag{B.8}$$

The Newton-Raphson algorithm operates the search in this way:

$h_0 = h(n-1)$
$k = 1$
`while (err <` $<$ `Errmax)`
`Compute` $g(h_k)$ `from Eq. (B.8)`
`Compute` h_{k+1} `as` $h_{k+1} = h_k - \frac{g(h_k)}{g'(h_k)}$
`Compute` `err = abs`$(h_{k+1} - h_k)$
$k = k + 1$
`end`
$h(n) = h_k$

Therefore, not only the function $g(h)$ but also its derivative $g'(h)$ has to be evaluated at each iteration. The computation of $g'(h)$ is done in successive steps as a composite derivative. First step:

$$\frac{dg}{dh} = \frac{\partial \dot{z}}{\partial v}\boldsymbol{K}(1) + \frac{\partial \dot{z}}{\partial z}\boldsymbol{K}(2) - 1 \quad . \tag{B.9}$$

Second step (recalling Eq. (2.13)):

$$\begin{aligned} \frac{\partial \dot{z}}{\partial v} &= 1 - z\left[\frac{(\alpha + v \cdot \partial\alpha/\partial v) z_{ss} - \alpha \cdot v \cdot dz_{ss}/dv}{z_{ss}^2}\right] \quad , \\ \frac{\partial \dot{z}}{\partial z} &= -\frac{v}{z_{ss}}\left[z\frac{\partial \alpha}{\partial z} + \alpha\right] \quad . \end{aligned} \tag{B.10}$$

Third step (recalling Eqs. (2.15, 2.16)):

$$\frac{\partial \alpha}{\partial v} = \begin{cases} \dfrac{\pi}{2}\cos\left(\pi\dfrac{z - \frac{z_{ss}+z_{ba}}{2}}{z_{ss} - z_{ba}}\right)\dfrac{\frac{dz_{ss}}{dv}(z_{ba} - z)}{(z_{ss} - z_{ba})^2} & , \quad \begin{array}{l}(z_{ba} < |z| < z_{ss})\ \& \\ (\mathrm{sgn}(v) = \mathrm{sgn}(z))\end{array} \\ 0 \quad , & \text{elsewhere} \end{cases} \tag{B.11}$$

$$\frac{\partial \alpha}{\partial z} = \begin{cases} \dfrac{\pi}{2}\cos\left(\pi\dfrac{z - \frac{z_{ss}+z_{ba}}{2}}{z_{ss} - z_{ba}}\right)\dfrac{1}{z_{ss} - z_{ba}} & , \quad \begin{array}{l}(z_{ba} < |z| < z_{ss})\ \& \\ (\mathrm{sgn}(v) = \mathrm{sgn}(z))\end{array} \\ 0 \quad , & \text{elsewhere} \end{cases} \quad . \tag{B.12}$$

Last step (recalling Eq. (2.14)):

$$\frac{dz_{ss}}{dv} = -\text{sgn}(v)\frac{2v}{\sigma_0 v_s^2}(f_s - f_c)e^{-(v/v_s)^2} \quad . \tag{B.13}$$

Computing these terms from the last step to the first step, the derivative $g'(h)$ can be obtained.

In order to develop a real-time model, it is essential that the number of iterations for the Newton-Raphson algorithm remains small in a large region of the parameter space. To this end, analysis on the simulations has to be performed, where model parameters are varied over a large range. Such analysis shows that in every conditions the algorithms exhibit a high speed of convergence. Empirical results show that the number of iterations remains smaller than seven.

Appendix C

Publications

The following is a list of the publications related to this dissertation, ordered by topic.

C.1 Bowed string physical model

1. S. Serafin, J. O. Smith, III, and J. Woodhouse. An investigation of the impact of torsion waves and friction characteristics on the playability of virtual bowed strings. IEEE Workshop on Signal Processing to Audio and Acoustics, New Paltz, NY, New York, Oct. 1999, IEEE Press.

2. S. Serafin, C. Vergez, and X. Rodet. Friction and application to real-time physical modeling of a violin. Proc. ICMC 99: International Computer Music Conference 1999, Bejing, China, October 99 .

3. S. Serafin, J.O. Smith III Modeling stiffness in virtual bowed-string instruments (abstract) ASA meeting, Atlanta may 2000.

4. S. Serafin, J.O.Smith III Influence of the Attack Parameters on the Playability of a Virtual Bowed String Instrument. Proc. ICMC 2000: International Computer Music Conference 2000, Berlin, Germany, august 2000.

5. P. Huang, S. Serafin, J.O.Smith III. A 3D Waveguide Mesh Model of High-Frequency Violin Body Resonances. Proc. ICMC 2000: International Computer

Music Conference 2000, Berlin, Germany, august 2000.

6. S. Serafin, J.O.Smith III. A multirate, finite-width, bow-string interaction model. Proc.DAFX 2000, Digital Audio Effects, Verona, Italy December 2000.

7. P. Huang, S. Serafin, J.O.Smith III. Modeling High-Frequency Modes of Complex Resonators Using a Waveguide Mesh. Proc. DAFX 2000, Digital Audio Effects, Verona, Italy December 2000.

8. Serafin and J. O. Smith. Impact of string stiffness on digital waveguide models of bowed strings. Catgut Acoustical Society Journal, vol. 4, no. 4, 2001.

9. F. Fontana, S. Serafin. Modeling Savart 's trapezoidal violin using a digital waveguide mesh. Proc. SMAC 2003, Stockholm, August 2003.

10. S. Serafin, F. Avanzini, D. Rocchesso. Bowed string simulation using an elasto-plastic friction model. Proc. SMAC 2003, Stockholm, August 2003.

C.2 Other friction driven musical instruments

11. S. Serafin, P. Huang, J.O.Smith III. The banded digital waveguide mesh. Proc. Mosart meeting, Barcelona, November 2001.

12. S. Serafin, P. Huang, S. Ystad, C. Chafe, J.O. Smith III. Analysis and Synthesis of Unusual Friction Driven Musical Instruments. Proc. ICMC 2002, Gotheborg, Sweden, September 2002.

13. S. Serafin, C. Wilkerson, J.O. Smith III. Modeling bowl resonators using circular waveguide networks. Proc. DAFX 2002, Hamburg, Germany, September 2002.

14. F. Avanzini, S. Serafin, D. Rocchesso. Modeling Interactions between Rubbed Dry Surfaces Using an Elasto-Plastic Friction Model. Proc. DAFX 2002, Hamburg, Germany, September 2002.

15. G. Essl, S. Serafin, P.Cook, J.Smith. Theory of banded waveguides, Computer Music Journal, Spring 2004.

16. G. Essl, S. Serafin, P.Cook, J.Smith. Musical applications of banded waveguides, Computer Music Journal, Spring 2004.

C.3 Control of physical models

17. S. Serafin, R. Dudas. An alternative controller for a virtual bowed string instrument. In M. Wanderley and M. Battier (eds): Trends in Gestural Control of Music- Ircam.

18. S. Serafin, R. Dudas, M. Wanderley, X. Rodet. Gestural control of a real-time physical model of a bowed string instrument. Proc. ICMC 99: International Computer Music Conference 1999, Bejing, China, October 99 .

19. S. O'Modhrain, S. Serafin, C. Chafe, J.O.Smith III. Qualitative and quantitative assessment on the playability of a virtual bowed string instrument. Proc. ICMC 2000: International Computer Music Conference 2000, Berlin, Germany, August 2000.

20. S. Serafin, J.O.Smith III, H. Thornburg. A pattern recognition approach to invert a bowed string physical model. Proc. ISMA 2001, Perugia, Italy September 2001.

21. S. Serafin, J.O. Smith III, H. Thornburg, F. Mazzella, A. Tellier and G. Thonier. Data driven identification and computer animation of a bowed string. Proc. ICMC 2001, La Havana, Cuba September 2001.

22. S. Serafin, M. Burtner, S. O'Modhrain, C. Nichols. Expressive controllers for bowed string physical models. Proc. DAFX 2001, Limerick, Ireland December 2001.

23. S. Serafin, D. Young. Bowed string physical model validation through use of a bow controller and examination of bow strokes. Proc. SMAC 2003, Stockholm, August 2003.

24. D. Young, S. Serafin. Playability evaluation of a bowed string physical model. Proc. NIME 2003, Montreal, CA, May 2003.

25. S. Serafin, D. Young. Investigation of the playability of virtual bowed strings. Proc. CIM 2003, Florence, Italy, May 2003.

C.4 Musical applications

26. M. Burtner, S. Serafin. Extended Performance Techniques for a Virtual Instrument. Proc.DAFX 2000, Digital Audio Effects, Verona, Italy December 2000.

27. M. Burtner, S. Serafin. Real time extended physical models for the composer and performer Proc. ICMC 2001, La Havana, Cuba September 2001.

28. M. Burtner, S. Serafin. Extended techniques for physical models using instrumental controller substitution Proc. ISMA 2001, Perugia, Italy September 2001.

29. M. Burtner, S. Serafin, D. Topper. Real-Time Spatial Processing and Transformations of a Singing Bowl. Proc. DAFX 2002, Hamburg, Germany, September 2002.

Bibliography

[1] J. Adrien. The missing link: Modal synthesis. In Giovanni De Poli, Aldo Picialli, and Curtis Roads, editors, *Representations of Musical Signals*, pages 269–297. MIT Press, Cambridge, MA, 1991.

[2] J.M Adrien, R. Causse, and E. Ducasse. Dynamic modeling of stringed and wind instruments, sound synthesis by physical models. In *Proc. ICMC*, 1988.

[3] A. Akai. Acoustics of Friction. *Journal of the Acoustical Society of America*, 111(4):1525–1548, Apr. 2002.

[4] F. Altpeter. *Friction Modeling, Identification and Compensation.* PhD thesis, École Polytechnique Fédérale de Lausanne, 1999.

[5] J. Antunes, M. Tafasca, and L. Henrique. Simulation of the bowed string dynamics. In *5eme Conference Francaise d'Acoustique*, 2000.

[6] Aristotle. *Physics.* Oxford University Press, 1936.

[7] A. Askenfelt. Measurement of bow motion and bow force in violin playing. *Journal of the Acoustical Society of America*, 80(4):1007–1015, Oct. 1986.

[8] A. Askenfelt. Measurement of the bowing parameters in violin playing. II: Bow-bridge distance, dynamic range, and limits of bow force. *Journal of the Acoustical Society of America*, 86(2):503–516, Aug. 1989.

[9] P.J. Blau. *Friction science and technology.* Marcel Dekker, 1996.

[10] G. Borin, G. De Poli, and D. Rocchesso. Elimination of delay-free loops in discrete-time models of nonlinear acoustic systems. *IEEE Transactions on Speech and Audio Processing*, 8(6):717–727, 2000.

[11] W.F. Brace and J.D.Byerledd. Stick slip as a mechanism for earthquakes. *Science*, 153:990–992, 1966.

[12] M. Burtner and S. Serafin. The exbow-metasax: Compositional applications of bowed string physical models using instrument controller subsitution. *Journal of New Music Research*, 32(4), December 2003.

[13] C. Cadoz, J.-L. Florens, and S. Gubian. Bowed string synthesis with force feedback gestural interaction. In *Proc. International Computer Music Conference*, La Havana, Cuba, 2001.

[14] C. Chafe. Simulating performance on a bowed instrument. Technical report, CCRMA, 1988.

[15] C. Chafe. Pulsed noise in self-sustained oscillations of musical instruments. In *In Proc. ICASSP, Albuquerque*. IEEE Press, 1990.

[16] E.F. Chladni. *Traité d'acoustique*. Imprimeur-Libraire pour les Mathématiques, 1809.

[17] P. R. Cook. Synthesis toolkit in C++, version 1.0. In *SIGGRAPH Proceedings*. Assoc. Comp. Mach., May 1996.

[18] P. R. Cook. Physically Informed Sonic Modeling (PhISM): Synthesis of Percussive Sounds. *Computer Music Journal*, 21(3):38–49, 1997.

[19] P. R. Cook and G. Scavone. The synthesis toolkit (stk). In *Proc. ICMC*. International Computer Music Association, October 1999.

[20] P.R. Cook. *Real Sound Synthesis for Interactive Applications*. AK Peters, 2002.

[21] L. Cremer. *The Physics of the Violin*. MIT Press, Cambridge, MA, 1984.

[22] P. Dahl. A solid friction model. Technical report, The Aerospace Corporation, 1968.

[23] J.L. d'Alembert. Investigation of the curve formed by a vibrating string, 1747. In *Acoustics: Historical and Philosophical Development.* Dowden, Hutchinson and Ross, 1973.

[24] C. Canudas de Wit, H. Olsson, K. J. Åström, and P. Lischinsky. A new model for control of systems with friction. *IEEE Trans. Autom. Control*, 40(3):419–425, 1995.

[25] J. Dieterich. Time dependent friction and the mechanics of stick slip. *Pure Appl. Geophys.*, 116:790–806, 1978.

[26] P. Dupont, V. Hayward, B. Armstrong, and F. Altpeter. Single State Elasto-Plastic Friction Models. *IEEE Trans. Autom. Control*, 2002.

[27] S. Van Duyne and J. O. Smith III. Physical modeling with the 2d waveguide mesh. In *Proc. International Computer Music Conference (ICMC)*, pages 40–47, The Hague, 1993. ICMA.

[28] G. Essl. *Physical Wave Propagation Modeling for Real-Time Synthesis of Natural Sound.* PhD thesis, Princeton University, November 2002.

[29] G. Essl and P. Cook. Measurements and efficient simulation of bowed bars. *Journal of the Acoustical Society of America*, 108(1):379–388, July 2000.

[30] B. Feeny, A. Guran, N. Hinrichs, and K. Popp. A historical review on dry friction and stick-slip phenomena. *Appl. Mech. Rev.*, 51(5), 1998.

[31] N. Fletcher. Nonlinearity, complexity and the sounds of musical instruments. In *16th International Congress on Acoustics*, June 1998.

[32] N. H. Fletcher and T. D. Rossing. *The Physics of Musical Instruments, Second Edition.* Springer Verlag, New York, 1998.

[33] F. Fontana. *Physics-Based Models for the Acoustic Representation of Space in Virtual Environments.* PhD thesis, University of Verona, 2002.

[34] F. G. Friedlander. On the oscillations of the bowed string. *Proc. Cambridge Philosophy Society*, 49:516–530, 1953.

[35] G. Galilei. *Dialogues.* University of California Press, 1967. Reprinted and translated by Drake.

[36] C.S. Gillmor. *Charles Augustin Coulomb: Physics and Engineering in Eighteen century France.* Princeton, N.J., 1971.

[37] K. Guettler. Personal communications, SMAC 2003.

[38] K. Guettler. The bowed string computer simulated — some characteristic features of the attack. *Catgut Acoustical Society Journ.*, 2(2):22–26, Nov 1992. Series II.

[39] K. Guettler. *The bowed string. On the development of the Helmholtz motion and on the Creations of Anomalous Low Frequencies.* PhD thesis, Royal Institute of Technology, 2002.

[40] K. Guettler and A. Askenfelt. On the kinematics of spiccato and ricochet bowing. *Catgut Acoustical Society Journal*, 3(6):9–15, Nov. 1998. (Series II).

[41] D.A. Haessig and B. Friedland. On the modeling and simulation of friction. In *Transactions of the ASME*, 1991.

[42] V. Hayward and B. Armstrong. A new computational model of friction applied to haptic rendering. In P. Corke and J. Trevelyan, editors, *Experimental Robotics VI*, pages 403–412. Springer-Verlag, 2000.

[43] V. Hayward and B. Armstrong. A new computational model of friction applied to haptic rendering. In *Experimental Robotics*, pages 404–412. Springer NY, 2000.

[44] L. Hiller and P. Ruiz. Synthesizing musical sounds by solving the wave equation for vibrating objects. Part I. *Journal of the Audio Engineering Society*, 19(6), June 1971. Part II: vol. 19, no. 7, July/Aug. 1971.

[45] M. Holm. From real to virtual violin. the process in development of an artificial model of violin. In *5th National Symposium on Music Research.*, 2001.

[46] P. Huang, S. Serafin, and J. O. Smith III. Modeling High-Frequency Modes of Complex Resonators Using a Waveguide Mesh. In *Proceedings of the COST G-6 Conference on Digital Audio Effects (DAFX-00)*, Verona, Italy, December 7-9 2000.

[47] P. Huang, S. Serafin, and J. O. Smith III. A waveguide mesh model of high-frequency violin mode resonances. In *International Computer Music Conference, Berlin*. Computer Music Association, 2000.

[48] A. Hunt, M. Wanderley, and M. Paradis. The importance of parameter mapping in electronic instrument design. *Journal of New Music Research*, 3(2), June 2003.

[49] C.M. Hutchins. Tonal effects of interactions between the two lowest cavity modes and three body modes of violin. In *Stockholm Musical Acoustics Conference (SMAC-93)*, pages 373–378, Stockholm, August 1993. Royal Swedish Academy of Music.

[50] J. O. Smith III. Music applications of digital waveguides. Technical Report STAN-M-39, CCRMA, 1987.

[51] J. O. Smith III. Music applications of digital waveguides. Technical Report STAN–M–39, CCRMA, Music , Stanford University, 1987.

[52] J. O. Smith III. Nonlinear commuted synthesis of bowed strings. In *Proc. ICMC 97, Greece*. Computer Music Association, 1997.

[53] J. O. Smith III and J. S. Abel. Bark and ERB bilinear transforms. *IEEE Trans. Speech and Audio Processing*, pages 697–708, November 1999.

[54] O. Inacio, L. Henrique, and J. Antunes. Dynamical analysis of bowed bars. In *ICSV8*, Hong-Kong, July 2001.

[55] E. Jansson. Acoustics for violin and guitar makers. Technical Report 3, KTH, 2002.

[56] H. Järveläinen, V. Välimäki, and M. Karjalainen. Audibility of inharmonicity in string instrument sounds, and implications to digital sound synthesis. In *Proc. ICMC*. Computer Music Association, 1999.

[57] J.M. Jot. An analysis/synthesis approach to real-time artificial reverberation. In *Proc. Int. Conf. on Acoustics Speech and Signal Processing (ICASSP)*, pages II.221–II.224, New York, 1992. IEEE Press.

[58] M. Karjalainen and J. O. Smith III. Body modeling techniques for string instrument synthesis. In *International Computer Music Conference, Hong Kong*, pages 232–239. Computer Music Association, Aug. 1996.

[59] M. Karjalainen, V. Välimäki, and Z. Jánosy. Towards high-quality sound synthesis of the guitar and string instruments. In *Proc. 1993 Int. Computer Music Conference, Tokyo*, pages 56–63. Computer Music Association, Sept. 10–15 1993.

[60] J. B. Keller. Bowing of violin strings. *Comm. Pure Applied Math.*, 6:483–495, 1953.

[61] D. Klatt. Software for a cascade/parallel formant synthesizer. *Journal of the Acoustical Society of America*, 67:13–33, 1980.

[62] R. L. Klatzky, Pai D. K., and E. P. Krotov. Perception of Material from Contact Sounds. *Presence, 4, 399–410.*, 2000.

[63] R. L. Klatzky and S. J. Lederman. Touch. In A. F. Healy and R. W. Proctor, editors, *Experimental Psychology*, pages 147–176. Wiley, New York, 2002.

[64] H. Kuttroff. *Room Acoustics*. Elsevier Science, Essex, England, 1991.

[65] T. I. Laakso, V. Välimäki, M. Karjalainen, and U. K. Laine. Splitting the Unit Delay—Tools for Fractional Delay Filter Design. *IEEE Signal Processing Magazine*, 13(1):30–60, January 1996.

[66] M. Lang. Allpass filter design and applications. *IEEE Transactions on Signal Processing*, 46(9):2505–2514, 1998.

[67] A. Lécuyer, S. Coquillart, A. Kheddar, P. Richard, and P. Coiffet. Pseudo-haptic feedback: Can isometric input devices simulate force feedback? In *Proc. IEEE Int. Conf. on Virtual Reality*, pages 83–90, 2000.

[68] M.J. Massimino and T.B. Sheridan. Sensory substitution for force feedback in teleoperation. *Presence*, 2(4):344–352, 1993.

[69] M. Mathews and J. Kohut. Electronic simulation of violin resonances. *Journal of the Acoustical Society of America*, 53(6):1620–1626, 1973.

[70] M. E. McIntyre, R. T. Schumacher, and J. Woodhouse. Aperiodicity in bowed-string motion. *Acustica*, 49(1):13–32, Sept. 1981.

[71] M. E. McIntyre, R. T. Schumacher, and J. Woodhouse. On the oscillations of musical instruments. *Journal of the Acoustical Society of America*, 74(5):1325–1345, Nov. 1983.

[72] M. E. McIntyre and J. Woodhouse. On the fundamentals of bowed string dynamics. *Acustica*, 43(2):93–108, Sept. 1979.

[73] J. L. McKechnie, editor. *Webster's New Universal Unabridged Dictionary.* Simon ans Schuster, New York, 1983.

[74] B.C. J. Moore. *An Introduction to the Psychology of Hearing.* Academic Press, New York, 1997.

[75] A.J. Morin. New friction experiments carried out at metz in 1831-1833. In *Proceedings of the French Royal Academy of Sciences*, volume 4, pages 1–128, 1833.

[76] C. Nichols. The vbow: A virtual violin bow controller for mapping gesture to synthesis with haptic feedback. *Organized Sound*, 7(2), 2003.

[77] C. Nichols. *The vbow: an expressive musical controller haptic human-computer interface.* PhD thesis, Stanford University, 2003.

[78] J. O'Brien, P. R. Cook, and G. Essl. Synthesizing sounds from physically based motion. *Proceedings of ACM SIGGRAPH, ACM Press/ACM SIGGRAPH, Los Angeles, CA*, pages 529–536, 2001.

[79] H. Olsson, K. J. Åström, C. Canudas de Wit, M. Gäfwert, and P. Lischinsky. Friction models and friction compensation. *European J. of Control*, 4:176–195, 1998.

[80] H. Olsson, K.J. Astrom, C. Canudas de Wit, and M. Gafvertand P. Lischinsky. Friction models and friction compensation. Technical report, Lund Institute of Technology, 1997.

[81] S. O'Modhrain. *Playing by Feel: Incorporating Haptic Feedback into Computer-Based musical Instruments.* PhD thesis, Music Dept., Stanford University (CCRMA), 2000.

[82] Alan V. Oppenheim and R. W. Schafer. *Discrete Time Signal Processing.* Prentice-Hall, Inc., Englewood Cliffs, NJ, 1989.

[83] D. Pai. *Modal synthesis for Vibrating Objects.* Audio Anecdotes. AK Peters, 2004.

[84] D. Pai, K. Van Den Doel, D. L. James, J. Lang, J. E. Lloyd, J. L. Richmond, and S. H. Yau. Scanning physical interaction behavior of 3d objects. *Proceedings of ACM SIGGRAPH, ACM Press/ACM SIGGRAPH, Los Angeles, CA.*, pages 87–96, 2001.

[85] M. Palumbi and L. Seno. Metal string. In *Proc. International Computer Music Conference*, Beijing, China., 1999.

[86] R. Pitteroff. *Contact mechanics of the bowed string.* PhD thesis, Cambridge University, 1995.

[87] R. Pitteroff. Mechanics of the contact area between a violin bow and a string. part I: Reflection and transmission behaviour. part II: Simulating the bowed string. part III: Parameter dependance. In *Acustica-Acta Acustica*, pages 543–562, 1998.

[88] K. Popp and P. Stelter. Stick-slip vibrations and chaos. *Philosophical Transactions*, 332:89–105, 1990.

[89] M. Puckette. Pure Data. In *Proceedings of the International Computer Music Conference (ICMC).* International Computer Music Association (ICMA), 1996.

[90] C. V. Raman. On the mechanical theory of vibrations of bowed strings and of musical instruments of the violin family, with experimental verification of results. *Indian Assoc. Cult. Sci. Bull.*, 15:1–158, 1918.

[91] J.W. Rayleigh. *The Theory of Sound.* Dover, New York, 1976.

[92] O. Reynolds. On the theory of lubrication and its application to mr. beauchamp tower's experiments, including an experimental determination of the viscosity of olive oil. *Phil. Trans. Royal Soc.*, 177:157–234, 1886.

[93] D. Rocchesso and F. Fontana, editors. *The Sounding Object.* Mondo estremo, 2003.

[94] D. Rocchesso and J. Smith. Circulant and elliptic feedback delay networks for artificial reverberation. *IEEE Transactions on Speech and Audio Processing*, 5(1):51–63, 1997.

[95] T. D. Rossing. Acoustics of the glass harmonica. *Journal of the Acoustical Society of America*, 95(2), 1994.

[96] S. Sastry, editor. *Nonlinear systems: analysis, stability and control.* Springer Verlag, 1999.

[97] G. Scavone and J. O. Smith III. Digital waveguide modeling of woodwind toneholes. *132nd meeting of the Acoustical Society of America, Honolulu*, Dec. 1996.

[98] J. C. Schelleng. The bowed string and the player. *Journal of the Acoustical Society of America*, 53(1):26–41, Jan. 1973.

[99] R. T. Schumacher and J. Woodhouse. Computer modelling of violin playing. *Contemporary Physics*, 36(2):79–92, 1995.

[100] R. T. Schumacher and J. Woodhouse. The transient behavior of models of bowed-string motion. *CHAOS*, 5(3):509–523, 1995.

[101] J.F.M. Scott and J. Woodhouse. Vibration of an elastic strip with varying curvature. *Philosophical Transactions*, 1992.

[102] S. Serafin and R. Dudas. *An alternative controller for a virtual bowed string instrument.* Trends in Gestural Control of Music. M. Wanderley and M. Battier, 2000.

[103] S. Serafin, P. Huang, and J. O. Smith III. The Banded Digital Waveguide Mesh. In *Proc. Workshop on Future Directions of Computer Music (Mosart-01)*, Barcelona, Spain, November 2001.

[104] S. Serafin, P. Huang, S. Ystad, C. Chafe, and J.O. Smith III. Analysis and synthesis of unusual friction driven musical instruments. In *Proceedings of the International Computer Music Conference (ICMC-02)*, Gotheborg, 2002.

[105] S. Serafin and J. O. Smith. A multirate, finite width bow string interaction model. In *Proceedings of Cost-DAFX, Verona, Italy*, 2000.

[106] S. Serafin, J. O. Smith III, and J. Woodhouse. An investigation of the impact of torsion waves and friction characteristics on the playability of virtual bowed strings. In *Proc. IEEE Workshop on Appl. of Signal Processing to Audio and Acoustics, New Paltz, NY*, New York, Oct. 1999. IEEE Press.

[107] S. Serafin, C. Wilkerson, and J. O. Smith III. Modeling Bowl Resonators Using Circular Waveguide Networks. In *Proceedings of the COST G-6 Conference on Digital Audio Effects (DAFX-02)*, Hamburg, Germany, 2002.

[108] S. Serafin and D. Young. Bowed string physical model validation through use of a bow controller and examination of bow strokes. In *Proc. Stockholm Musical Acoustics Meeting (SMAC)*, 2003.

[109] S. Serafin and D. Young. Investigation of the playability of virtual bowed strings. In Italy Centro Tempo Reale, Florence, editor, *Proc. XIV Colloquium Musical Informatics*, 2003.

[110] S. Serafin and D. Young. A generalized controller for friction driven musical instruments. In *Proc. NIME*, 2004.

[111] X. Serra. A computer model for bar percussion instruments. In *Proc. 1986 Int. Computer Music Conf., The Hague*. Computer Music Association, 1986.

[112] J. H. Smith and J. Woodhouse. The tribology of rosin. *J. Mech Phys.Solids*, 48:1633–1681, 1999.

[113] J. O. Smith. A new approach to digital reverberation using closed waveguide networks. In *1985 Computer Music , Vancouver*, pages 47–53. Computer Music Association, 1985. also available in [51].

[114] J. O. Smith. *Physical Audio Signal Processing: Digital Waveguide Modeling of Musical Instruments and Audio Effects*. available online at `http://-ccrma.stanford.edu/~jos/pasp/`, 2004.

[115] J.O. Smith. *Introduction to Digital Filters*. available online at `http://www-ccrma.stanford.edu/~jos/filters/`, February 11, 2002.

[116] J.O. Smith. Selected tutorials, papers, programming examples, (some) sound samples, and related links. *Digital Waveguide Synthesis Home Page*, 2003. `http://ccrma.stanford.edu/~jos/wg.html`.

[117] Julius O. Smith. Physical modeling using digital waveguides. *Computer Music Journal*, 16(4):74–91, Winter 1992. special issue: Physical Modeling of Musical Instruments, Part I. Available online at http://www-ccrma.stanford.edu/~jos/pmudw/.

[118] Julius O. Smith. *Acoustic Modeling Using Digital Waveguides*. Curtis Roads and Stephen Travis Pope and Aldo Piccialli and Giovanni De Poli editors. Swets and Zietlinger, Netherlands, 1997.

[119] J. O. Smith III. Synthesis of bowed strings. In *Proc. ICMC*. Computer Music Association, 1982. essentially fully contained in [120].

[120] J. O. Smith III. *Techniques for Digital Filter Design and System Identification with Application to the Violin*. PhD thesis, Elec.Eng. Dept., Stanford University (CCRMA), June 1983.

[121] J. O. Smith III. Efficient simulation of the reed-bore and bow-string mechanisms. In *Proc. 1986 Int. Computer Music Conf., The Hague*, pages 275–280. Computer Music Association, 1986. also available in [51].

[122] J. O. Smith III. Efficient synthesis of stringed musical instruments. In *Proc. 1993 Int. Computer Music Conference, Tokyo*, pages 64–71. Computer Music Association, 1993.

[123] K. Steiglitz. *Digital Signal Processing Primer: With Applications to Digital Audio and Computer Music*. Benjamin Cummings, 1996.

[124] T. Takala, J. Hiipakka, M. Laurson, and V. Valimaki. An expressive synthesis model for bowed string instruments. In *Proc. International Computer Music Conference*, Berlin, Germany., 2000.

[125] T. Takala and V. Valimaki. Virtual musical instruments. natural sounds using physical models. *Organised Sound*, 1996.

[126] B. H. Thomas and P. Calder. Applying Cartoon Animation Techniques to Graphical User Interfaces. *ACM Trans. on Computer-Human Interaction*, 8(3):198–222, Sept 2001.

[127] V. Välimäki, M. Karjalainen, and T. I. Laakso. Fractional delay digital filters. In *Proc. Int. Symp. Circuits and Systems (ISCAS-93), Chicago*, New York, May 1993. IEEE Press.

[128] S. A. Van Duyne and J. O. Smith. The 2-D digital waveguide mesh. In *Proc. IEEE Workshop on Appl. of Signal Processing to Audio and Acoustics, New Paltz, NY*, New York, Oct. 1993. IEEE Press.

[129] K van Mensvoort. What you see is what you feel. In *Proc. DIS*, pages 345–348, London, UK, 2002.

[130] H. L. F. von Helmholtz. *On the Sensations of Tone as a Physiological Basis for the Theory of Music*. Dover, New York, 1954. English translation of 1863 (German) edition by A. J. Ellis.

[131] J. Wawrzynek, C. Mead, T. Lin, H. Liu, and L. Dyer. A VLSI approach to sound synthesis. In *Proc. ICMC 1984*, pages 53–64. Computer Music Association, 1984.

[132] D. Wessel and M. Wright. Problems and prospects for intimate musical control of computers. *Computer Music Journal*, (2):44–56, Summer 2002.

[133] J. Woodhouse. Idealised models of a bowed string. *Acustica*, 79:233–250, 1993.

[134] J. Woodhouse. On the playability of violins. Part I: Reflection functions. Part II: Minimum bow force and transients. *Acustica*, 78:125–136,137–153, 1993.

[135] J. Woodhouse. On the stability of bowed string motion. *Acustica*, 80:58–72, 1994.

[136] J. Woodhouse. Bowed string simulations using a thermal friction model. *Acustica - Acta Acustica*, 89:355–368, 2003.

[137] J. Woodhouse and A. R. Loach. The torsional behavior of cello strings. *Acustica - ACTA Acustica*, 85, 1999.

[138] J. Woodhouse, R. Schumacher, and S. Garoff. Reconstruction of bowing point friction force in a bowed string. *J. Acoust. Soc. Am.*, 108, 2000.

[139] D. Young. The hyperbow controller: Real-time dynamics measurement of violin performance. In *Proc. NIME*, 2001.

[140] D. Young and S. Serafin. Playability evaluation of a virtual bowed string instrument. In *Proc. NIME*, Montreal, Quebec, May 2003.

[141] D. Zicarelli. An Extensible Real-Time Signal Processing Environment for Max. In *Proc. ICMC*, Ann Arbour, Michigan, 1998.

[142] E. Zwicker and H. Fastl. *Psychoacoustics, Facts and Models*. Springer Verlag, Berlin, 1990. See also later 1999 edition.